Modelling the Diverse Population of Hot Jupiter Dynamical Atmospheres



DPhil Thesis

Submitted in partial fulfillment of the
requirements for the degree of

Doctor of Philosophy

in

Atmospheric, Oceanic & Planetary Physics

Author: Alexander B. Roth
Supervisors: Prof. V. Parmentier & Prof. R. T. Pierrehumbert
Examiners: Prof. T. D. Komacek & Prof. J-M. Desért

Oxford, United Kingdom, October 2024

Modelling the Diverse Population of Hot Jupiter Dynamical Atmospheres

Alexander B. Roth

Department of Physics, University of Oxford
Clarendon Laboratory, Parks Road, Oxford, OX1 3PU, United Kingdom

October 2024

DPhil Thesis

Contents

1 Introduction **1**
- 1.1 Exoplanets 1
- 1.2 Hot Jupiters 3
- 1.3 Motivation for Studying Atmospheres 5
- 1.4 Observing Transiting Planet Atmospheres 7
  - 1.4.1 Spectral Features 7
  - 1.4.2 Phase Curves 9
  - 1.4.3 The Inherent 3D-ness of Hot Jupiters 10
  - 1.4.4 The Future of Exoplanet Observations 12
- 1.5 Thesis Outline 13

2 Hot Jupiter Atmospheres: Theoretical Approach **17**
- 2.1 Hot Jupiter Atmospheres: Overview 17
- 2.2 Heating & Cooling Through Radiation 18
  - 2.2.1 Albedo 18
  - 2.2.2 Temperature Inversions 20
- 2.3 Methods to Model Radiative Heating & Cooling 21
- 2.4 Dynamical Equations in Spherical Coordinates 22
  - 2.4.1 Common Approximations 24
  - 2.4.2 Dynamical Equations in Pressure Coordinates 25
- 2.5 Dynamics 26
  - 2.5.1 Super-rotation & Formation of the Jet 27
  - 2.5.2 Drag Mechanisms 29
  - 2.5.3 Length Scales 29
  - 2.5.4 Timescales 31
- 2.6 Overall Redistribution of Heat 32
  - 2.6.1 Expected Scaling of Heat Redistribution 32
- 2.7 Further Complications to Energy Balance 33

3 Creating a Large GCM Model Grid **39**
- 3.1 Introduction 39
- 3.2 Important Results from 3D Modelling Studies 40
- 3.3 The SPARC/MiTgcm 41
  - 3.3.1 Radiative Transfer with EGP 42
  - 3.3.2 Geometric & Bond Albedos 42
  - 3.3.3 Dissipation 42
  - 3.3.4 Model Limitations 44
- 3.4 Creating a Large GCM Model Grid 44
  - 3.4.1 Spectral Calculations for the Grid 45
  - 3.4.2 Chemistry 46
  - 3.4.3 Model Convergence 47
- 3.5 Grid Parameters 47
  - 3.5.1 Equilibrium Temperature 49
  - 3.5.2 Orbital Period 50

3.5.3 Metallicity 51
3.5.4 Surface Gravity 51
3.5.5 TiO & VO 51
3.5.6 Drag Timescale 52

4 A Large Grid of GCM Models: Atmospheric Diversity 57
4.1 Introduction 57
4.2 Atmospheric Characteristics for a Range of Planetary Parameters 58
4.3 Heat Redistribution 60
4.3.1 Geometric & Bond Albedo 61
4.3.2 Expected Scaling for the Heat Redistribution Factor with the Jet 62
4.3.3 Overall Model Distribution 63
4.3.4 Specific Trends with Parameters 65
4.3.5 Combined Parameter Trends: Heat Redistribution 66
4.4 Bolometric Phase Curves 67
4.4.1 Offset 67
4.4.2 Offset Trend with Period 68
4.4.3 Combined Parameter Trends: Offset 71
4.4.4 Amplitude 72
4.4.5 Amplitude and Offset are Set by Different Mechanisms 72
4.5 Temperature Contrast Between the Limbs 75
4.6 Summary & Conclusion 76

5 A Large Grid of GCM Models: Spectra and the Onset of TiO/VO Revealed 79
5.1 Introduction 79
5.2 Spitzer Band Secondary Eclipse 80
5.3 Spectral Feature Strength 83
5.4 Spitzer Phase Curve Offset & Amplitude 86
5.4.1 Spitzer 3.6 micron Phase Curve Data Comparison 86
5.5 Summary & Conclusion 87

6 A Large Grid of GCM Models: The Effects of Dynamic Drag 91
6.1 Introduction 91
6.2 General Atmospheric Characteristics for a Range of Drag Strengths 92
6.3 The Effects of Drag on Emission Spectra & Phase Curves 95
6.3.1 Emission Spectra 95
6.3.2 Phase Curve Offset 97
6.3.3 Non-Monotonically Decreasing Offset 99
6.3.4 Drag Dependent Phase Curve Offset & Amplitude Relationship 100
6.3.5 Spectral Indices 102
6.4 The Effects of Drag on Planetary Heat Redistribution 103
6.5 Summary & Conclusion 107

7 A Large Grid of GCM Models: Comparison with 1D Radiative-Convective Thermochemical Equilibrium Models 109
7.1 Introduction 109
7.2 1D Model Grid 110

7.3 Benchmarking of the 1D Grid 110
7.3.1 Adjustment for TiO Opacities 111
7.3.2 Total Flux Integral 114
7.4 Overview of 1D v 3D 115
7.4.1 Special Case: 1400K TiO/VO 117
7.5 Spectral Indices 118
7.6 Spectral Dependence of the Flux Residuals 120
7.6.1 Overall RMS of the Residuals 122
7.6.2 Parameter Dependence in the RMS of Residuals 122
7.6.3 Dilution Factor Slope 123
7.7 Summary & Conclusion 126

8 Summary & Outlook 129
8.1 Thesis Summary 129
8.2 Potential for Future Work 131
8.2.1 Deconstruction of the Circulation 131
8.2.2 Grid as a Fast Characterisation Tool 132
8.2.3 Grid as a Machine Learning Tool 132
8.2.4 Post-Processing of the Grid 133
8.3 Sliders and Data Availability 133

Acknowledgements 135

Chapter 1

Introduction

The material in this chapter is based on Roth et al. (2024):
– Roth A., Parmentier V., Hammond M., 2024, MNRAS, 531, 1056

1.1 Exoplanets

In 1992 the first exoplanet was discovered around the pulsar PSR B1257+12 (Wolszczan & Frail 1992), which was confirmed in 1994 (Wolszczan 1994). Then, the following year, 51 Peg b was discovered. This was the first exoplanet known to be orbiting a main sequence star (Mayor & Queloz 1995). Since that time, the number of exoplanets that have been found has increased by many orders of magnitude. There are now 5,766 (as of October 10th 2024) confirmed planets residing in stellar systems beyond our own. This population of extra-solar planets that have been discovered displays huge diversity, with extremes ranging from high temperature 'lava-worlds' with surfaces covered by molten lava, to sub-zero temperature planets coated in ice, and from small rocky worlds to gas giants many times the size of Jupiter. Despite this boom in exoplanet discovery, a true solar system analogue is still yet to be found. The commonality of some planets is clearly due to observational biases, such as hot Jupiters - which are, contrary to our high detection rate, in fact quite rare. However, the prevalence of others, such as sub-Neptunes, appears to be the result of natural planetary formation mechanisms.

The first exoplanet orbiting a main sequence star, and many since then, was detected using the radial velocity (RV) technique (Mayor & Queloz 1995). This method relies on the gravitational interaction between a planet and its host star. Both the planet and star will orbit the combined centre of mass for the system. The star will therefore periodically move towards and away from Earth, with this small 'wobble' depending on the relative mass of the planet to the star, the star-planet separation and the orbital inclination. When the stellar spectrum is observed at a high resolution, this can be seen as a Doppler shift in the absorption lines. Due to the complex, and therefore heavy, spectrographs that this method relies upon, RV measurements are taken from ground based instruments. The most prolific of these are HARPS, at the La Silla observatory in Chile (Pepe et al. 2000), and HIRES, aboard the Keck telescope in Hawaii (Vogt et al. 1994). To date, 1,093 confirmed exoplanets have been discovered using RVs, equating to $\sim$19% of the current total population.

In 2002, transit photometry was then suggested as a viable method for exoplanet detection (Mandel & Agol 2002). When the emission of the combined star and planet system is monitored, the brightness will decrease if the planet transits across the stellar disk as seen from Earth. When monitored over a large enough time period, this decrease in brightness will be periodic in nature as the planet orbits. With the launch of the Kepler mission (Batalha et al. 2013; Borucki et al. 2011; Koch et al. 2010) (a large scale 'planet-hunting' transit survey observing over 500,000 stellar systems between the original Kepler mission (2009 and 2013) and extended following mission K2 (2013-2018)), the number of exoplanets detected via this method began to quickly outpace the RV method. This can be clearly seen in the lower panel of Figure 1.1. The natural successor to this mission was the Transiting Exoplanet Sur-

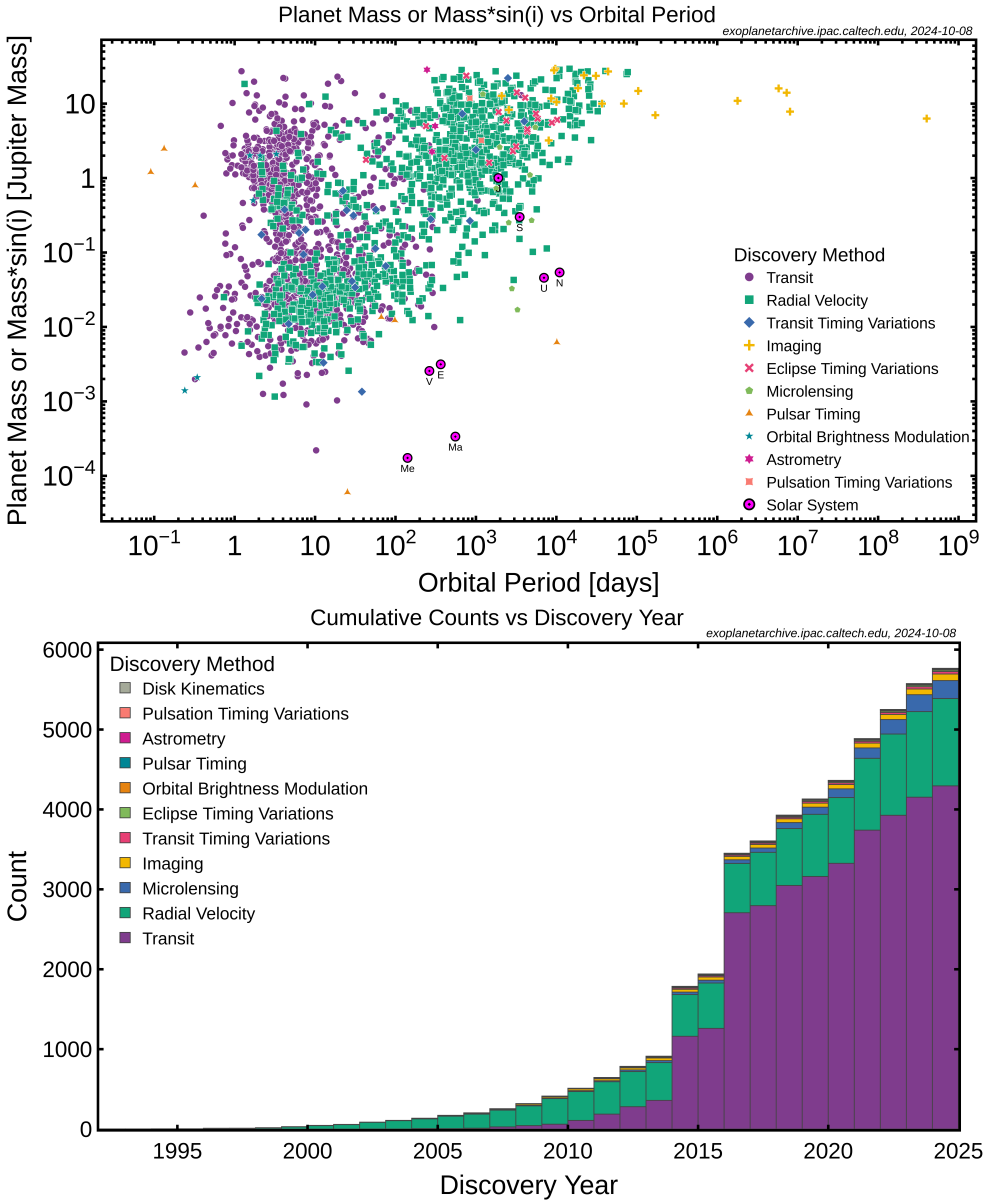


Figure 1.1: Population of confirmed exoplanets. **Top Panel:** Displays the planet mass as a function of orbital period. **Bottom Panel:** Displays the number of detections by method for each year since 1992. In both plots the colour and markers indicate the different detection techniques used to confirm each planet. Full credit for these plots goes to the NASA Exoplanet Archive `https://exoplanetarchive.ipac.caltech.edu/exoplanetplots/`.

vey Satellite (TESS) (Ricker et al. 2015), which launched in 2018 with the goal of finding nearby planets that could be characterized. This detection technique can also be performed via ground based instruments. Transit surveys using ground based instruments include WASP (Butters et al. 2010; Pollacco et al. 2006), KELT (Pepper et al. 2007), and MASCARA (Talens et al. 2017). With 4,295 confirmed planets discovered via transit spectroscopy (∼75% of the current total population), this method has detected the most planets to date.

Whilst these two detection techniques are very different in their approach, they do share one commonality - both favour the detection of high mass planets orbiting close to their

host star. The larger a planet's mass is relative to a star, the larger the induced Doppler signal will be (typically of the order $\sim 100 ms^{-1}$). This Doppler signal will also occur with a lower periodicity for shorter orbital periods. Close-in orbits also increase the likelihood of a planet occulting the stellar disk when viewed from the observer, which the transit method relies on. Additionally, larger planets will induce larger and more regular drops in the stellar flux (typically of order $\sim$1%), making them easier to identify. As a result of these detection biases, the population of confirmed exoplanets is biased towards these particular regions within the parameter space, as displayed in the upper panel of Figure 1.1. Due to this, a disproportionate amount of the high quality exoplanet data that we currently have is for a class of planets known as 'hot Jupiters'. It is these planets that we will focus on in this work.

1.2 Hot Jupiters

Hot Jupiters are gas giant planets, with radii and masses analogous to their namesake, Jupiter, within our own solar system. However, these planets, unlike Jupiter, orbit very close to their host star ($<$0.1 AU), with periods on the order of $\sim$1 day. Because of this they receive much more stellar irradiation than Jupiter, giving them a much higher temperature in comparison, with equilibrium temperatures varying from $\sim$1000 to 2000K. Because of this, although the occurrence rate for hot Jupiters around sun-like-stars is actually very low (estimated to be $\sim$1% (Beleznay & Kunimoto 2022; Wright et al. 2012), many have been observed due to either the biases in detection techniques discussed in Section 1.1 or from biases in atmospheric observation. From detection, transit probability depends on orbital semi-major axis, making it more likely to find hot Jupiters at short periods, and larger radii result in larger signals. From atmospheric observation, transit spectrum spectral features are proportional to planetary radii and atmospheric scale height ($R_p H / R_s^2$), so large radii, temperature and low gravity result in larger transmission features. Emission spectra are proportional to planet temperature and radii (R_p^2 / R_s^2), again meaning higher temperatures and radii result in larger features. Slightly cooler gas giant planets are aptly called 'warm Jupiters', whereas hotter ones are often called 'ultra-hot Jupiters'. Many of these planets have been observed during secondary eclipse (Baxter et al. 2020; Deming et al. 2023; Garhart et al. 2020), with a smaller number viewed over full orbits to provide phase curves (Parmentier & Crossfield 2018). Due to their short-period orbits, strong gravitational interactions are thought to cause tidal locking (Lubow et al. 1997; Rasio et al. 1996; Showman & Guillot 2002), leading to rotation periods synchronised with orbital periods. This means that all the incident stellar irradiation is deposited into the day-side hemisphere, with a night-side hemisphere receiving none. Day-side temperatures typically range between $\sim$1500-3000K, with night-side temperatures usually at $\sim$1000K. Because of this vast temperature contrast between the hemispheres, steep day-night temperature contrasts form, making these planets' atmopsheres intrinsically 3-dimensional in nature and driving strong winds (Showman & Guillot 2002). These winds facilitate energy transport from the hot day-side onto the cold night-side (Komacek & Showman 2016; Komacek & Tan 2018), in the form of either a super-rotating equatorial jet which can reach speeds of up to several kms^{-1} or direct day-to-night divergent flow (Hammond & Lewis 2021). The winds and day-to-night flow have been measured in these atmospheres (Brogi et al. 2016; Snellen et al. 2010). The jets, first theorized by modelling (Cooper & Showman 2005; Dobbs-Dixon & Agol 2013; Heng et al. 2011; Mayne et al. 2014; Menou & Rauscher 2009; Perna et al. 2012; Rauscher & Menou 2012;

Showman & Guillot 2002; Showman et al. 2008, 2015; Tan & Komacek 2019), have also been inferred through observation (Charbonneau et al. 2008; Cowan et al. 2007; Crossfield et al. 2010; Knutson et al. 2007, 2009a; Louden & Wheatley 2015; Seidel et al. 2020; Snellen et al. 2010). However, these winds are often not strong enough to transport energy from day-to-night before it is radiated back to space, leading to large horizontal contrasts in temperature (Knutson et al. 2007; Stevenson et al. 2010), chemistry (Helling et al. 2019; Parmentier et al. 2018), and cloud coverage (Helling et al. 2019; Parmentier et al. 2021).

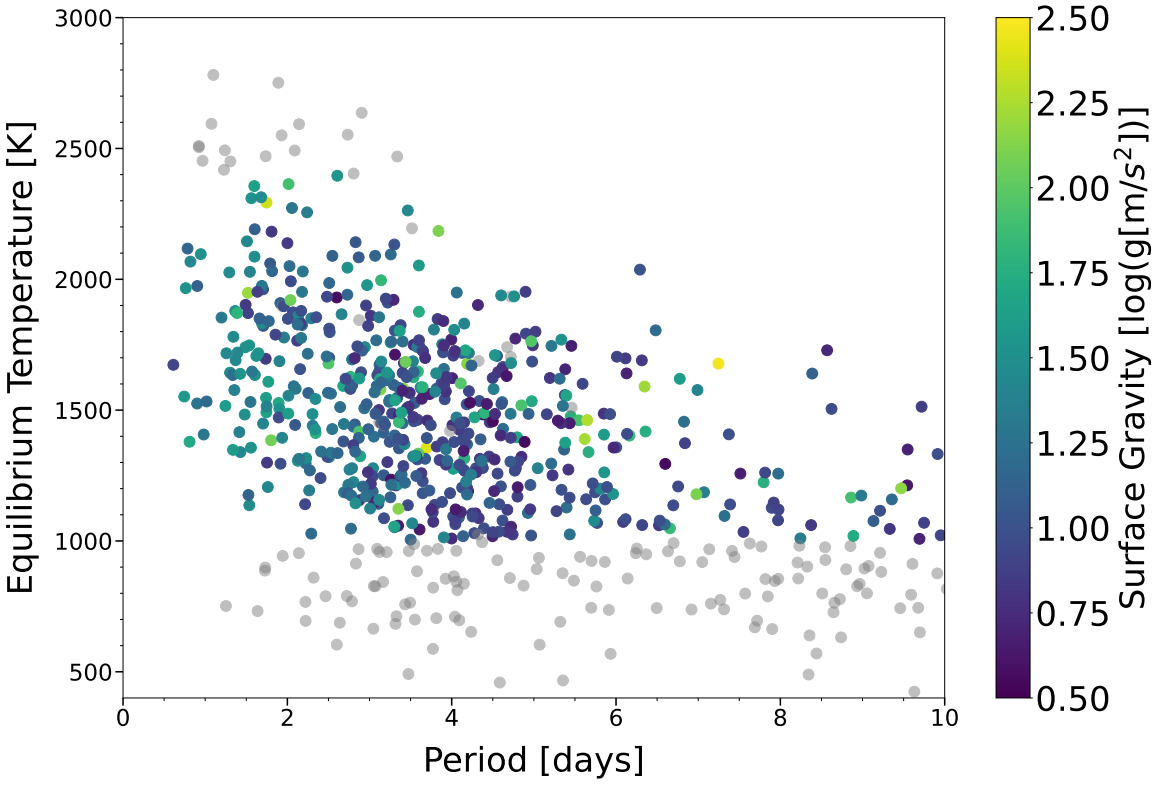


Figure 1.2: Distribution of known exoplanets ($0.3 < R_p < 3R_j$) with equilibrium temperature as a function of orbital period. Exoplanets with surface gravities between $0.5 < log(g) < 2.5$ are colour coded and those outside this range are displayed in grey.

Even within this class of planets, the population is extremely diverse. The range of equilibrium temperatures corresponds to an instellation received varying by more than an order of magnitude. In addition to this, gravity and rotation periods also vary by an order of magnitude within the population, as displayed in Figure 1.2. Composition-wise, observations of their spectra have shown that atmospheric metallicity can also have an order of magnitude variation (Welbanks et al. 2019). There are multiple known correlations between these parameters at the population level which can significantly boost the spectral diversity we observe and introduce trends in their atmospheres. For example, because of tidal locking, equilibrium temperature and rotation are expected to be intrinsically linked. Additionally, many hot Jupiters have an inflated radius (Baraffe et al. 2014; Fortney & Nettelmann 2010), leading to a correlation between equilibrium temperature and surface gravity. Finally, a correlation between atmospheric metallicity and planet mass is observed in the solar-system and could also be present in giant exoplanets (Welbanks et al. 2019).

1.3 Motivation for Studying Atmospheres

From observation of exoplanets we now have constraints on many physical properties for both the systems and planets themselves, including the orbital periods, planet masses and radii. However, if we wish to characterise individual exoplanets, and in particular gain a better understanding of their atmospheric conditions, then these measurements alone are not sufficient. For this, we need detailed observations of a planet's atmosphere. Interpreting these observations requires a theoretical understanding of the complex thermo-chemical processes that shape their atmospheres.

Additionally, which formation pathway is responsible for the observed exoplanet population remains a largely unanswered question. Planets form from the local material in the stellar disk via two methods:

- Core accretion, when a planet core forms and then accretes gas from the proto-planetary disk (Chabrier et al. 2014; Fortney et al. 2021; Perri & Cameron 1974; Pollack et al. 1996).
- Formation via gravitational instability, when a portion of the disk fragments away and subsequently collapses under gravity to form a planet (Boss 1997; Durisen et al. 2007; Fortney et al. 2021).

There are three viable migration mechanisms which have been suggested to produce the observed population of hot Jupiters:

1. **In-situ formation**, where a planet is formed via core accretion at their present location within the stellar disc, without any subsequent migration.
2. **Disk migration**, where a planet would form, via core accretion or gravitational instabilities, further out in the stellar disc and subsequently migrate to its present location after formation has occurred.
3. **High eccentricity migration**, where, after dissipation of the stellar disk, a planet could be disturbed into an elliptical orbit and then migrate towards the star due to tidal interactions circularising the orbit.

All of these formation mechanisms will leave an imprint on the planetary properties. The fact that hot Jupiters seem to be found closer to their stars than expected, given the difficulty of core accretion very close to a star, has often been suggested as a constraint on in situ formation (Fortney et al. (2021) for a review). However, Batygin et al. (2016) show that Super-Earth type planets can instigate rapid gas accretion within the central regions of protoplanetary disks, potentially leading to a large fraction of the hot Jupiter population being formed via this pathway. Batygin et al. (2016) additionally propose that hot Jupiters formed in this way are likely to have low-mass companion planets, which could be detected via high precision radial velocity measurements.

The location of formation, or subsequent migration after formation has occurred, will also affect the atmospheres of giant planets (Bitsch et al. 2022; Fortney et al. 2013). Perhaps the most important factor linking atmospheric abundances to formation mechanisms is the C/O ratio. The major carbon and oxygen bearing molecules, such as H_2O, CH_4, CO_2 and CO, condense at different locations within the stellar disk, based on the local temperature.

(Bitsch et al. 2022; Booth et al. 2017; Cridland et al. 2020; Lothringer et al. 2021; Madhusudhan et al. 2017; Mollière et al. 2022; Öberg et al. 2011; Schneider & Bitsch 2021). The C/O ratio is therefore highly dependent on the location of planet formation with respect to the condensation temperatures of these species.

Additionally, nitrogen is a useful marker for planets which form further out in the disk. The C/N, N/O and C/O ratios can be jointly used to determine if a planet's metallicity is due mainly to accretion of solids, due to the relative volatility of these species (Turrini et al. 2021). Sulphur can further be useful as a direct probe of atmospheric metallicity, as the S/N ratio can be used to determine the amount of solid material a planet accretes, in the form of planetesimals. Due to the volatility of S and N within the stellar disk, sulphur will be solid, whereas nitrogen is likely to be gaseous (Turrini et al. 2021). In HST observations, H2O, Na and K could be used to directly trace the atmospheric metallicity (Welbanks et al. 2019). Many more molecules and atomic species can be used to trace the metallicity in high-resolution and JWST observations. This M/H ratio is key to determining the timing of a planet's migration in relation to dissipation of the stellar disk (Madhusudhan et al. 2014; Mordasini et al. 2016; Öberg et al. 2011; Thorngren et al. 2016). Consequently, measuring the chemical abundances of these important refractory and volatile species in planetary atmospheres can inform us of their formation and migration history (Cridland et al. 2019; Madhusudhan et al. 2014; Öberg et al. 2011).

In addition to providing information on the formation history of planets, the chemical composition of an atmosphere can strongly alter its thermal structure. In particular, the presence of TiO and VO, two strong optical absorbers that exist in M dwarfs, have been postulated to create a thermal inversion in hot Jupiter day-sides (Fortney et al. 2008; Hubeny et al. 2003), meaning that the temperature would increase with decreasing pressure. TiO condensation marks the transition between L and M dwarfs, which lead Fortney et al. (2008) to propose two distinct classes of planets (pL and pM). However, clear absorption features in observations of HD 209458 b (Line et al. 2016), and WASP-43 b (Kreidberg et al. 2014), have shown the definitive lack of a thermal inversion (Kreidberg et al. 2014; Line et al. 2016), despite having equilibrium temperatures above the TiO condensation boundary. More recently, such thermal inversions have been observed by the presence of emission features in the thermal emission spectra of the hottest planets (Cont et al. 2022; Coulombe et al. 2023; Mikal-Evans et al. 2020; van Sluijs et al. 2023), and TiO has been directly observed at high resolution (Cont et al. 2022; Prinoth et al. 2022). Therefore, the exact point at which the population transitions from a TiO/VO rich atmosphere with a thermal inversion towards a TiO/VO poor atmosphere without an inversion is still unclear. Direct detection of TiO and VO through observation is complex, as its spatial distribution is shaped by multiple processes. Condensation of these chemicals in the deep layers (Spiegel et al. 2009), or on the night-side (Merritt et al. 2020; Parmentier et al. 2013), could deplete these chemicals from the planet's day-side atmosphere (Powell et al. 2018). Furthermore, atmospheres that are hot enough to suppress condensation can be too hot for TiO and VO to be stable against thermal dissociation (Parmentier et al. 2018).

However, abundance measurements in exoplanet atmospheres have to rely on a thorough understanding of their 3D thermo-chemical structure to avoid bias in atmospheric retrievals (Arcangeli et al. 2018; Taylor et al. 2020). Particularly, at the population level, we wish to separate the part of the observed trends and scatter that is due to the diversity of the planetary parameters (e.g. temperature or rotation period) and the one that is due to intrinsic, formation related, parameters (such as metallicity). Additionally, it is not only the trend

of chemical abundances with parameters, but also their scatter around the mean population value that can inform us on the planetary formation mechanisms and their stochastic nature (Fortney et al. 2013).

With rapidly increasing numbers of high quality exoplanet observations, large scale population studies (e.g Baxter et al. 2020; Deming et al. 2023; Garhart et al. 2020; May et al. 2022a) are now possible. With this in mind, hot Jupiters provide the best opportunities for characterising exoplanet atmospheres. Due to their short periods, high emission and large atmospheres, they offer optimal targets for transit observations and provide an invaluable window into the thermo-chemical composition of exoplanets.

1.4 Observing Transiting Planet Atmospheres

As the number of high-quality exoplanet observation increases, with the James Webb Space telescope (Greene et al. 2016), and upcoming Ariel mission (Tinetti et al. 2017), providing wide wavelength coverage and ground-based telescopes supplying high resolution data (Ehrenreich et al. 2020), hot Jupiters will continue to provide the best targets for atmospheric characterisation.

There are essentially three primary methods used for observing transiting exoplanet atmospheres. Transmission spectroscopy, emission spectroscopy and phase curves. As a planet transits across the stellar disk, light from the star will pass through the limbs of the planet and interact with the atmosphere through scattering and absorption. At different wavelengths, the light will be more or less attenuated as it passes through the atmosphere, based on the chemistry at the limbs. Therefore, by measuring the attenuation of this light at different wavelengths we can build up a picture of a planet's apparent size and determine the chemical structure at the planet's limbs. This is known as transmission spectroscopy and was the first method used to characterise exoplanet atmospheres, suggested theoretically in Brown (2001); Hubbard et al. (2001); Seager & Sasselov (2000), and observed in Charbonneau et al. (2002), for HD 209458 b.

Emission spectroscopy is another important tool for characterizing exoplanet atmospheres, as it gives not only information on the chemical abundances but also the thermal structure of an atmosphere. In a transiting system, during secondary eclipse the thermal emission from the planet is blocked by the star. By observing the system before, during and after the secondary eclipse we can therefore measure the thermal emission from the combined star-planet system and from the star alone, to discern the planetary contribution. Due to the geometry of a transit, the transit photosphere will be at lower pressures than the emission photosphere, meaning that emissions spectroscopy allows us to probe deeper layers in the atmosphere than enabled through transmission spectroscopy. Therefore, by observing the secondary eclipse at multiple wavelengths, the atmospheric pressure-temperature structure can be determined. The albedo can also be measured by estimating the proportion of reflected stellar flux. This method was first used for exoplanets in Deming et al. (2005) for HD 209458 b and Charbonneau et al. (2005), for TrES-1 b.

1.4.1 Spectral Features

The flux emitted from a planet's atmosphere at a particular frequency, ν, is given by the thermal emission of the pressure level where the optical depth $\tau(\nu) = 2/3$ at that frequency

(Parmentier 2014). In the absence of chemistry, the resulting planetary eclipse spectra will therefore appear as blackbody emission at the temperature of the photosphere. However, in a real atmosphere the emitted light will be imprinted by molecular features as it travels out of the atmosphere. If the low pressure regions above the photosphere are cooler than the emitting layer, molecules will absorb the light, thus creating absorption features in the spectra. Conversely, if the low pressure regions are hotter than the photosphere, the molecular features will appear in emission. The resulting planetary eclipse spectrum is therefore shaped by a combination of the vertical temperature structure and the chemical composition. By observing the emitted flux over a range of frequencies, it is therefore possible to recover this information from secondary eclipse observations. However, as the flux is sensitive to both the temperature profile and chemical abundances, their effects are somewhat degenerate on the final spectrum. For example, the effects of a vertical shift in the temperature profile cannot necessarily be distinguished from an increase of molecular abundance which vertically shifts the photosphere.

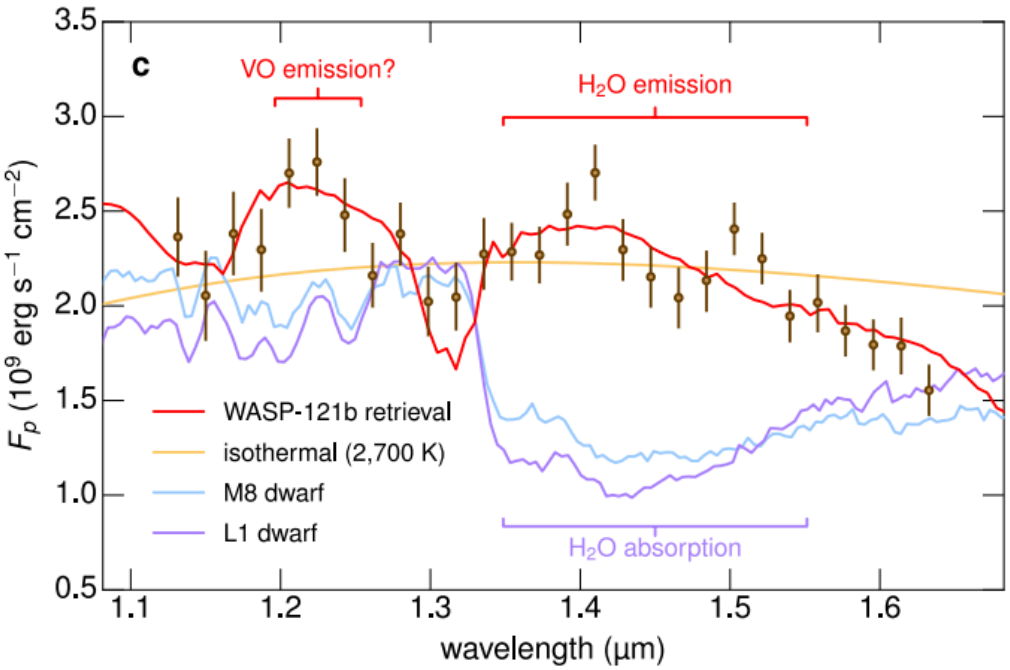


Figure 1.3: This figure is taken from Evans et al. (2017) (see their Figure 2), showing the planetary emission spectrum for WASP-121 b in the HST/WFC3 band-pass. The brown circles display the observed data points. A best-fit retrieval is also displayed, alongside example spectra for an M8 and L1 dwarf, displaying absorption in the same band-pass, and a blackbody spectrum at 2700K.

Importantly, the presence of temperature inversions mentioned in Section 1.3 significantly impact the planetary eclipse spectra. As the temperature increases with altitude above the photosphere, molecular features are expected to appear primarily in emission in this case. As such, detection of emission features in observed secondary eclipse is often

ascribed to the presence of temperature inversions (Baxter et al. 2020; Mansfield et al. 2021), and has driven much of the research into the presence of high pressure optical absorbers. Figure 1.3, for example, shows the detection of water emission and tentative detection of VO emission in the HST/WFC3 band-pass for ultra-hot Jupiter WASP-121 b (Evans et al. 2017), which indicates the presence of a stratospheric temperature inversion for this planet.

The spectral features present in eclipse spectra have also been used to asses trends in the population of hot Jupiters. For instance, Baxter et al. (2020) use the warm Spitzer/IRAC band-passes at 3.6 and 4.5 μm to study trends in the near infrared, where CH_4 and CO features are expected to be present depending on the planets equilibrium temperature.

1.4.2 Phase Curves

A phase curve can be obtained by observing the total flux of a transiting system over the course of a full orbit. From this, the component of stellar flux can then be removed, leaving the hemispherically averaged brightness of the planet - a combination of thermal emission and reflected starlight. Showman & Guillot (2002) first suggested that exoplanet phase curves would be a useful diagnostic tool to determine day-night temperature contrast and hotspot offset for hot Jupiters, as the shape and amplitude of the phase curve will be dependent on the inhomogeneous nature of the atmosphere's contrasting hemispheres. Therefore, through observation of these phase curves, it is possible to determine the longitudinal structure for a tidally locked exoplanet.

From observations of phase curves, three important parameters can be retrieved which relate to the atmospheric state of the planet (Cowan & Agol 2008; Demory et al. 2013; Knutson et al. 2009b, 2012), see Parmentier & Crossfield (2018) for a review. Figure 1.4 shows a diagram of these key parameters for the 3.6µm phase curve of HD 189733 b, observed with the Spitzer Space Telescope by Knutson et al. (2012).

From the secondary eclipse depth the brightness temperature of the day-side atmosphere can be calculated. This can then be used as a reference point from which to calculate the amplitude, the difference between the minimum and maximum of the flux emitted by a planet. The amplitude holds information on the relative temperatures of the day and night-side atmospheres, and therefore on the efficiency of heat redistribution in an atmosphere.

The phase curve offset is a measure of the longitudinal offset of the brightest hemisphere from the substellar point. This has a *positive* value if offset *eastward* (respective to the direction of planetary rotation) from the substellar point, meaning that the brightest hemisphere would be observed before secondary eclipse. If the brightest hemisphere is observed after secondary eclipse then the offset is *westwards* of the substellar point and therefore *negative*. Figure 1.4, therefore, displays a positive phase curve offset.

Observing phase curves has proven more challenging than observing transits and eclipses. This is due to the much longer timescale that observations must be carried out over, requiring a full (and sometimes multiple) orbital period. Because of this, only a limited number of full phase curve observations have been carried out to date. A summary of the observed hot Jupiter phase curves can be found in Table 1.1. The majority of phase curve observations so far have been performed with Spitzer, and a limited number with Kepler and HST. Additionally, a small number of phase curve observations have already been taken with JWST. Although a handful of phase curves were observed in the Spitzer 8 and 24 micron band-passes, these were mostly found to be compromised by systematics (Knutson et al. 2007, 2012), and instrument errors (Crossfield et al. 2012), so we do not include them here.

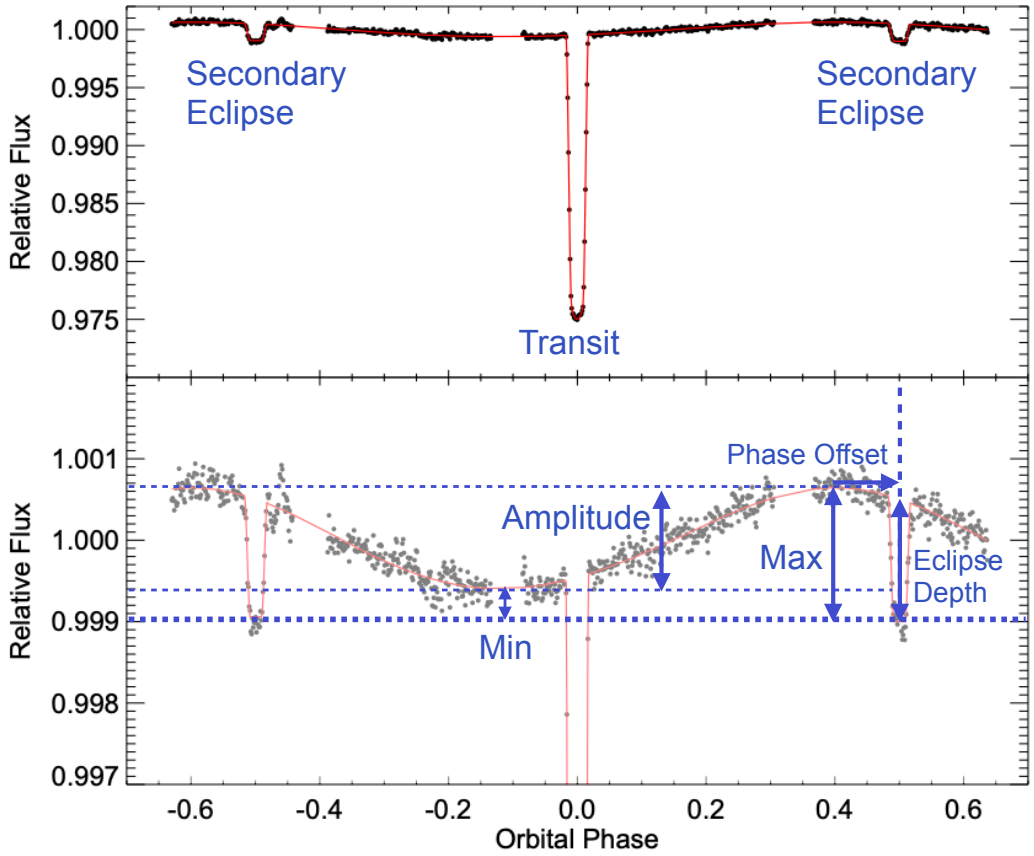


Figure 1.4: This figure is an adapted version of Figure 1 in Parmentier & Crossfield (2018). It shows the phase curve of HD 189733 b observed at 3.6μm with the Spitzer Space Telescope by Knutson et al. (2012), with key parameters which can be extracted from observed phase curves overlaid.

1.4.3 The Inherent 3D-ness of Hot Jupiters

As we have already mentioned, the vast inequality in stellar irradiation between the hemispheres of hot Jupiters makes their atmospheres inherently 3D. Energy is deposited into the atmosphere most intensely at the substellar point (most commonly denoted as being at 0° latitude and longitude). The intensity of this irradiation then decreases due to the geometry of the planet at both further latitudes and longitudes from the substellar point, leading to both latitudinal and longitudinal inhomogeneities in the thermal and chemical structure of the atmosphere. Additionally, the hemispherical temperature contrast between day and night-side (and resulting strong advective heat redistribution) acts to shift the hottest point in the atmosphere away from the substellar point and towards the evening limb. This means that the atmosphere is not longitudinally symmetrical.

Additionally, the 3D structure of hot Jupiters makes it challenging to measure the chemical abundances from their spectra. Indeed, observations, either in transit or eclipse, are usually sensitive to the spatially averaged spectra. Information from different parts of the atmosphere, which can have very different properties, are mixed together. 1D retrieval models can have strong biases when applied to hot Jupiter data sets, for both emission (Blecic et al. 2017; Feng et al. 2016; Taylor et al. 2020), and transmission (Caldas et al. 2019; Lacy

Table 1.1: Hot Jupiter phase curve observations with Kepler, Spitzer, HST and JWST.

Planet	Instrument & Band-pass	Reference
HAT-P-7b	Kepler 0.6	Esteves et al. (2015)
	Spitzer 3.6 & 4.5	Wong et al. (2016)
HD189733b	Spitzer 3.6 & 4.5	Knutson et al. (2012)
HD209458b	Spitzer 4.5	Zellem et al. (2014)
WASP-12b	Spitzer 3.6 & 4.5	Cowan et al. (2012)
WASP-14b	Spitzer 3.6 & 4.5	Wong et al. (2016)
WASP-18b	Spitzer 3.6 & 4.5	Maxted et al. (2013)
	HST/WFC3	Arcangeli et al. (2018, 2019)
WASP-19b	Spitzer 3.6 & 4.5	Wong et al. (2016)
WASP-43b	Spitzer 3.6 & 4.5	Stevenson et al. (2017)
	HST/WFC3	Stevenson et al. (2014)
	JWST MIRI/LRS	Bell et al. (2023)
WASP-103b	Spitzer 3.6 & 4.5	Kreidberg et al. (2018)
	HST/WFC3	Kreidberg et al. (2018)
WASP-121b	JWST NIRSpec G395H	Mikal-Evans et al. (2023)
HD149026	Spitzer 3.6 & 4.5	Zhang et al. (2018)
WASP-33b	Spitzer 3.6 & 4.5	Zhang et al. (2018)
KELT-16b	Spitzer 4.5	Bell et al. (2021)
MASCARA-1b	Spitzer 4.5	Bell et al. (2021)
Qatar-1b	Spitzer 4.5	May et al. (2022b)
Qatar-2b	Spitzer 3.6 & 4.5	May et al. (2022b)
WASP-52b	Spitzer 3.6 & 4.5	May et al. (2022b)
WASP-34b	Spitzer 4.5	May et al. (2022b)
CoRoT-2b	Spitzer 4.5	Dang et al. (2018)
KELT-1b	Spitzer 3.6 & 4.5	Beatty et al. (2019)
KOI-13b	Kepler 0.6	Esteves et al. (2015)
TrES-2b	Kepler 0.6	Esteves et al. (2015)
Kepler-5b	Kepler 0.6	Esteves et al. (2015)
Kepler-6b	Kepler 0.6	Esteves et al. (2015)
Kepler-7b	Kepler 0.6	Demory et al. (2013)
Kepler-8b	Kepler 0.6	Esteves et al. (2015)
Kepler-12b	Kepler 0.6	Esteves et al. (2015)
Kepler-41b	Kepler 0.6	Esteves et al. (2015)
Kepler-43b	Kepler 0.6	Esteves et al. (2015)
Kepler-76b	Kepler 0.6	Esteves et al. (2015)
Kepler-91b	Kepler 0.6	Esteves et al. (2015)
Kepler-412b	Kepler 0.6	Esteves et al. (2015)

& Burrows 2020; Line & Parmentier 2016; MacDonald & Madhusudhan 2017; MacDonald et al. 2020; Pluriel et al. 2020). This is due to the spatially varying cloud coverage (Line & Parmentier 2016), thermal structure (Caldas et al. 2019; Feng et al. 2016; Taylor et al. 2020), or chemical abundance maps (MacDonald et al. 2020; Pluriel et al. 2020). This problem becomes even greater at higher spectral resolutions, as the spectral line shapes, depths and positions (which are heavily dependent on the chemical, thermal and dynamical structure in the atmosphere) become increasingly resolved (Beltz et al. 2021; Keles 2021; Kempton et al. 2014; Miller-Ricci Kempton & Rauscher 2012; Showman et al. 2013; Wardenier et al.

2021; Zhang et al. 2017). This has been shown to cause heavily asymmetric features in transmission (Ehrenreich et al. 2020; Kesseli & Snellen 2021; Kesseli et al. 2022; Savel et al. 2022; Wardenier et al. 2021). These effects can lead to biases when inferring abundances because of the non-linear nature of radiative transfer: the spatially averaged spectra is different from the spectra of the spatially averaged thermal structure of the planet. This is particularly true when spatial correlations between physical quantities are present in the planet (e.g. clouds forming in the cooler parts of the atmosphere, or chemical abundances being determined by the local temperature). Consequently, to obtain robust chemical abundances from observed spectra, we must understand how planetary parameters influence the physical processes in hot Jupiter atmospheres. Therefore, to draw conclusions on observational trends arising from planet formation processes, we must first understand expected trends due to planetary properties.

1.4.4 The Future of Exoplanet Observations

We are currently in a period of transition for exoplanet characterisation, as the quantity and precision of 3D atmospheric information we have for hot Jupiters will drastically increase over the coming years due to a number of space missions and an influx of ground based high resolution data. The James Webb Space Telescope (JWST) (Greene et al. 2016), launched in December 2021, has already begun to provide wavelength coverage between 0.6 - 28.8 μm with a much higher spectral resolution and precision than its predecessor, the Hubble Space Telescope. The Atmospheric Remote-sensing Infrared Exoplanet Large-survey (ARIEL) (Tinetti et al. 2017) mission aims to survey a wide range of $\sim$ 1,000 transiting exoplanets and will use transit, eclipse and phase-curve spectroscopy with a wavelength coverage of 0.5 - 7.8 μm, and is due to launch in 2029. One of the most beneficial aspects of the ARIEL mission will be its capacity to perform a population study alongside more detailed analysis for specific planets. Additionally, the Transiting Exoplanet Survey Satellite, (TESS) (Ricker et al. 2015), is currently observing hundreds of thousands of main sequence dwarf stars to identify transiting exoplanets.

High-resolution spectroscopy (HRS), using ground-based instruments, provides a further approach to studying the structure of Exoplanets (Birkby 2018; Brogi et al. 2012; Snellen et al. 2010). HRS can probe atmospheric physics and chemistry which is not accessible for lower resolution observations (i.e via JWST). In HRS, individual spectral lines can be resolved. As these spectral lines are periodically Doppler shifted during the planets orbit, the planetary signal can be isolated from the stellar signal and telluric absorption. Because of this, HRS is able to perform local measurements of specific chemical species (due to their unique set of absorption frequencies). HRS observations in the optical range can target alkali and refractory species, such as TiO, VO and Fe (Ehrenreich et al. 2020; Hoeijmakers et al. 2015; de Regt et al. 2022), whereas infrared observations can target volatile molecules such as H_2O, CO and OH (Tennyson & Yurchenko 2012).

Overall, as the number of high quality exoplanet observations rapidly increases, hot Jupiters will continue to provide the best targets for atmospheric characterisation, and so improvements to our understanding and modelling of their atmospheres will continue to be a focus of the exoplanet community.

1.5 Thesis Outline

The overall goal of this work is to better understand how the intrinsic planetary parameters of hot Jupiters influence their atmospheres, and to what extent the '3D-ness' of these planets needs to be accounted for in the current observation climate. The outline of this thesis is as follows:

Chapter 2: Here, we outline the existing theory on hot Jupiter atmospheres. This includes radiative energy propagation, dynamics and formation of large scale dynamical structures and the redistribution of heat. We also present the dynamical equations, and common approximation to these equations, which are used to describe three-dimensional atmospheres. Additionally we define key time and length scales which apply to these atmospheres.

Chapter 3: Here, we introduce the global circulation model SPARC/MiTgcm, which is the primary modelling tool used in this work. We also include an overview of existing three dimensional modelling studies, and their key findings in relation to hot Jupiters. We discuss the specific setup of our models, describing our methods to compute dynamics and radiative transfer and energy dissipation. We also discuss the limitations of our model, in relation to this work. We go on to describe the creation of a large GCM model grid, spanning a wide range of systematically and jointly varied planetary parameters. We describe how this model grid is split into drag-free models, and those with a prescribed Rayleigh drag timescale. We then further discuss the input parameters to our model grid, and their expected effects on an atmosphere.

Chapter 4: Here, we detail the diversity of atmospheric characteristics on display within our drag-free GCM model grid. In particular, we highlight the range of atmospheric heat redistribution efficiency which arises from our parameter space. We also investigate both the phase curve offset and amplitude within the model grid, in addition to the temperature contrast between the planetary limbs.

Chapter 5: Here, we describe a comparison between our grid of drag-free GCM models and observations from Spitzer and HST. We highlight the effects of optical absorbing molecules TiO and VO on observed brightness temperatures within the Spitzer band-passes, and the strength of water absorption in the HST/WFC3 band-pass. We also perform a population level comparison between all phase curves taken with the Spitzer instrument and the model grid.

Chapter 6: Here, we focus on our GCM model grid over a range of atmospheric Rayleigh drag timescales. We describe the general effects of increasing drag strength on large scale dynamical atmospheric structures. We go on to show the effects of drag on the emission spectra and phase curves of these atmospheres. Additionally, we discuss the effects of magnetic drag on heat redistribution efficiency within an atmosphere.

Chapter 7: Here, we present a comparison between our drag-free GCM model grid and an equivalent 1D radiative-convective-thermochemical equilibrium model grid. We describe the setup and benchmarking of the 1D model grid. We use this comparison to discuss the impact of modelling inherently three-dimensional atmospheres with lower dimensionality models. We highlight differences between the pressure-temperature structures and spectra of the 1D and 3D models over a wide range of parameters. We also discuss the use of a dilution factor in exoplanet retrievals with 1D models.

Chapter 8: Here we present a summary for all the findings within this work, and some additional avenues for potential future research relating to the topics discussed.

Bibliography

Arcangeli J., et al., 2018, ApJ, 855, L30
Arcangeli J., et al., 2019, A&A, 625, A136
Baraffe I., Chabrier G., Fortney J., Sotin C., 2014, in Beuther H., Klessen R. S., Dullemond C. P., Henning T., eds, Protostars and Planets VI. pp 763–786 (arXiv:1401.4738), doi:10.2458/azu˙uapress˙9780816531240-ch033
Batalha N. M., et al., 2013, ApJS, 204, 24
Batygin K., Bodenheimer P. H., Laughlin G. P., 2016, ApJ, 829, 114
Baxter C., et al., 2020, A&A, 639, A36
Beatty T. G., Marley M. S., Gaudi B. S., Colón K. D., Fortney J. J., Showman A. P., 2019, AJ, 158, 166
Beleznay M., Kunimoto M., 2022, MNRAS, 516, 75
Bell T. J., et al., 2021, MNRAS, 504, 3316
Bell T. J., et al., 2023, arXiv e-prints, p. arXiv:2301.06350
Beltz H., Rauscher E., Brogi M., Kempton E. M. R., 2021, AJ, 161, 1
Birkby J. L., 2018, arXiv e-prints, p. arXiv:1806.04617
Bitsch B., Schneider A. D., Kreidberg L., 2022, A&A, 665, A138
Blecic J., Dobbs-Dixon I., Greene T., 2017, ApJ, 848, 127
Booth R. A., Clarke C. J., Madhusudhan N., Ilee J. D., 2017, MNRAS, 469, 3994
Borucki W. J., et al., 2011, ApJ, 736, 19
Boss A. P., 1997, Science, 276, 1836
Brogi M., Snellen I. A. G., de Kok R. J., Albrecht S., Birkby J., de Mooij E. J. W., 2012, Nature, 486, 502
Brogi M., de Kok R. J., Albrecht S., Snellen I. A. G., Birkby J. L., Schwarz H., 2016, ApJ, 817, 106
Brown T. M., 2001, ApJ, 553, 1006
Butters O. W., et al., 2010, A&A, 520, L10
Caldas A., Leconte J., Selsis F., Waldmann I. P., Bordé P., Rocchetto M., Charnay B., 2019, A&A, 623, A161
Chabrier G., Johansen A., Janson M., Rafikov R., 2014, in Beuther H., Klessen R. S., Dullemond C. P., Henning T., eds, Protostars and Planets VI. pp 619–642 (arXiv:1401.7559), doi:10.2458/azu˙uapress˙9780816531240-ch027
Charbonneau D., Brown T. M., Noyes R. W., Gilliland R. L., 2002, ApJ, 568, 377
Charbonneau D., et al., 2005, ApJ, 626, 523
Charbonneau D., Knutson H. A., Barman T., Allen L. E., Mayor M., Megeath S. T., Queloz D., Udry S., 2008, ApJ, 686, 1341
Cont D., et al., 2022, A&A, 668, A53
Cooper C. S., Showman A. P., 2005, ApJ, 629, L45
Coulombe L.-P., et al., 2023, arXiv e-prints, p. arXiv:2301.08192
Cowan N. B., Agol E., 2008, ApJ, 678, L129
Cowan N. B., Agol E., Charbonneau D., 2007, MNRAS, 379, 641
Cowan N. B., Machalek P., Croll B., Shekhtman L. M., Burrows A., Deming D., Greene T., Hora J. L., 2012, ApJ, 747, 82
Cridland A. J., Eistrup C., van Dishoeck E. F., 2019, A&A, 627, A127
Cridland A. J., van Dishoeck E. F., Alessi M., Pudritz R. E., 2020, A&A, 642, A229
Crossfield I. J. M., Hansen B. M. S., Harrington J., Cho J. Y. K., Deming D., Menou K., Seager S., 2010, ApJ, 723, 1436
Crossfield I. J. M., Knutson H., Fortney J., Showman A. P., Cowan N. B., Deming D., 2012, ApJ, 752, 81
Dang L., et al., 2018, Nature Astronomy, 2, 220
Deming D., Seager S., Richardson L. J., Harrington J., 2005, Nature, 434, 740
Deming D., Line M. R., Knutson H. A., Crossfield I. J. M., Kempton E. M. R., Komacek T. D., Wallack N. L., Fu G., 2023, arXiv e-prints, p. arXiv:2301.03639
Demory B.-O., et al., 2013, ApJ, 776, L25
Dobbs-Dixon I., Agol E., 2013, MNRAS, 435, 3159
Durisen R. H., Boss A. P., Mayer L., Nelson A. F., Quinn T., Rice W. K. M., 2007, in Reipurth B., Jewitt D., Keil K., eds, Protostars and Planets V. p. 607 (arXiv:astro-ph/0603179), doi:10.48550/arXiv.astro-ph/0603179
Ehrenreich D., et al., 2020, Nature, 580, 597
Esteves L. J., De Mooij E. J. W., Jayawardhana R., 2015, ApJ, 804, 150
Evans T. M., et al., 2017, Nature, 548, 58
Feng Y. K., Line M. R., Fortney J. J., Stevenson K. B., Bean J., Kreidberg L., Parmentier V., 2016, ApJ, 829, 52

Fortney J. J., Nettelmann N., 2010, Space Sci. Rev., 152, 423
Fortney J. J., Lodders K., Marley M. S., Freedman R. S., 2008, ApJ, 678, 1419
Fortney J. J., Mordasini C., Nettelmann N., Kempton E. M. R., Greene T. P., Zahnle K., 2013, ApJ, 775, 80
Fortney J. J., Dawson R. I., Komacek T. D., 2021, Journal of Geophysical Research (Planets), 126, e06629
Garhart E., et al., 2020, AJ, 159, 137
Greene T. P., Line M. R., Montero C., Fortney J. J., Lustig-Yaeger J., Luther K., 2016, ApJ, 817, 17
Hammond M., Lewis N. T., 2021, Proceedings of the National Academy of Science, 118, 2022705118
Helling C., et al., 2019, A&A, 631, A79
Heng K., Frierson D. M. W., Phillipps P. J., 2011, MNRAS, 418, 2669
Hoeijmakers H. J., de Kok R. J., Snellen I. A. G., Brogi M., Birkby J. L., Schwarz H., 2015, A&A, 575, A20
Hubbard W. B., Fortney J. J., Lunine J. I., Burrows A., Sudarsky D., Pinto P., 2001, ApJ, 560, 413
Hubeny I., Burrows A., Sudarsky D., 2003, ApJ, 594, 1011
Keles E., 2021, MNRAS, 502, 1456
Kempton E. M. R., Perna R., Heng K., 2014, ApJ, 795, 24
Kesseli A. Y., Snellen I. A. G., 2021, ApJ, 908, L17
Kesseli A. Y., Snellen I. A. G., Casasayas-Barris N., Mollière P., Sánchez-López A., 2022, AJ, 163, 107
Knutson H. A., et al., 2007, Nature, 447, 183
Knutson H. A., et al., 2009a, ApJ, 690, 822
Knutson H. A., Charbonneau D., Cowan N. B., Fortney J. J., Showman A. P., Agol E., Henry G. W., 2009b, ApJ, 703, 769
Knutson H. A., et al., 2012, ApJ, 754, 22
Koch D. G., et al., 2010, ApJ, 713, L79
Komacek T. D., Showman A. P., 2016, ApJ, 821, 16
Komacek T. D., Tan X., 2018, Research Notes of the American Astronomical Society, 2, 36
Kreidberg L., et al., 2014, ApJ, 793, L27
Kreidberg L., et al., 2018, AJ, 156, 17
Lacy B. I., Burrows A., 2020, ApJ, 905, 131
Line M. R., Parmentier V., 2016, ApJ, 820, 78
Line M. R., et al., 2016, AJ, 152, 203
Lothringer J. D., Rustamkulov Z., Sing D. K., Gibson N. P., Wilson J., Schlaufman K. C., 2021, ApJ, 914, 12
Louden T., Wheatley P. J., 2015, ApJ, 814, L24
Lubow S. H., Tout C. A., Livio M., 1997, ApJ, 484, 866
MacDonald R. J., Madhusudhan N., 2017, MNRAS, 469, 1979
MacDonald R. J., Goyal J. M., Lewis N. K., 2020, ApJ, 893, L43
Madhusudhan N., Amin M. A., Kennedy G. M., 2014, ApJ, 794, L12
Madhusudhan N., Bitsch B., Johansen A., Eriksson L., 2017, MNRAS, 469, 4102
Mandel K., Agol E., 2002, ApJ, 580, L171
Mansfield M., et al., 2021, Nature Astronomy, 5, 1224
Maxted P. F. L., et al., 2013, MNRAS, 428, 2645
May E., et al., 2022a, arXiv e-prints, p. arXiv:2203.15059
May E. M., et al., 2022b, AJ, 163, 256
Mayne N. J., et al., 2014, A&A, 561, A1
Mayor M., Queloz D., 1995, Nature, 378, 355
Menou K., Rauscher E., 2009, ApJ, 700, 887
Merritt S. R., et al., 2020, A&A, 636, A117
Mikal-Evans T., Sing D. K., Kataria T., Wakeford H. R., Mayne N. J., Lewis N. K., Barstow J. K., Spake J. J., 2020, MNRAS, 496, 1638
Mikal-Evans T., et al., 2023, ApJ, 943, L17
Miller-Ricci Kempton E., Rauscher E., 2012, ApJ, 751, 117
Mollière P., et al., 2022, ApJ, 934, 74
Mordasini C., van Boekel R., Mollière P., Henning T., Benneke B., 2016, ApJ, 832, 41
Öberg K. I., Murray-Clay R., Bergin E. A., 2011, ApJ, 743, L16
Parmentier V., 2014, PhD thesis, LAGRANGE - Joseph Louis LAGRANGE - Université Nice Sophia Antipolis (UNS); Observatoire de la Côte d'Azur CNRS : UMR7293
Parmentier V., Crossfield I. J. M., 2018, Exoplanet Phase Curves: Observations and Theory. p. 116, doi:10.1007/978-3-319-55333-7_116

Parmentier V., Showman A. P., Lian Y., 2013, A&A, 558, A91
Parmentier V., et al., 2018, A&A, 617, A110
Parmentier V., Showman A. P., Fortney J. J., 2021, MNRAS, 501, 78
Pepe F., et al., 2000, in Iye M., Moorwood A. F., eds, Society of Photo-Optical Instrumentation Engineers (SPIE) Conference Series Vol. 4008, Optical and IR Telescope Instrumentation and Detectors. pp 582–592, doi:10.1117/12.395516
Pepper J., et al., 2007, PASP, 119, 923
Perna R., Heng K., Pont F., 2012, ApJ, 751, 59
Perri F., Cameron A. G. W., 1974, Icarus, 22, 416
Pluriel W., Zingales T., Leconte J., Parmentier V., 2020, A&A, 636, A66
Pollacco D. L., et al., 2006, PASP, 118, 1407
Pollack J. B., Hubickyj O., Bodenheimer P., Lissauer J. J., Podolak M., Greenzweig Y., 1996, Icarus, 124, 62
Powell D., Zhang X., Gao P., Parmentier V., 2018, ApJ, 860, 18
Prinoth B., et al., 2022, Nature Astronomy, 6, 449
Rasio F. A., Tout C. A., Lubow S. H., Livio M., 1996, ApJ, 470, 1187
Rauscher E., Menou K., 2012, ApJ, 750, 96
Ricker G. R., et al., 2015, Journal of Astronomical Telescopes, Instruments, and Systems, 1, 014003
Roth A., Parmentier V., Hammond M., 2024, MNRAS, 531, 1056
Savel A. B., et al., 2022, ApJ, 926, 85
Schneider A. D., Bitsch B., 2021, A&A, 654, A71
Seager S., Sasselov D. D., 2000, ApJ, 537, 916
Seidel J. V., Ehrenreich D., Pino L., Bourrier V., Lavie B., Allart R., Wyttenbach A., Lovis C., 2020, A&A, 633, A86
Showman A. P., Guillot T., 2002, A&A, 385, 166
Showman A. P., Cooper C. S., Fortney J. J., Marley M. S., 2008, ApJ, 682, 559
Showman A. P., Fortney J. J., Lewis N. K., Shabram M., 2013, ApJ, 762, 24
Showman A. P., Lewis N. K., Fortney J. J., 2015, ApJ, 801, 95
Snellen I. A. G., de Kok R. J., de Mooij E. J. W., Albrecht S., 2010, Nature, 465, 1049
Spiegel D. S., Silverio K., Burrows A., 2009, ApJ, 699, 1487
Stevenson K. B., et al., 2010, Nature, 464, 1161
Stevenson K. B., et al., 2014, Science, 346, 838
Stevenson K. B., et al., 2017, AJ, 153, 68
Talens G. J. J., Spronck J. F. P., Lesage A. L., Otten G. P. P. L., Stuik R., Pollacco D., Snellen I. A. G., 2017, A&A, 601, A11
Tan X., Komacek T., 2019, in AAS/Division for Extreme Solar Systems Abstracts. p. 326.03
Taylor J., Parmentier V., Irwin P. G. J., Aigrain S., Lee E. K. H., Krissansen-Totton J., 2020, MNRAS, 493, 4342
Tennyson J., Yurchenko S. N., 2012, MNRAS, 425, 21
Thorngren D. P., Fortney J. J., Murray-Clay R. A., Lopez E. D., 2016, ApJ, 831, 64
Tinetti G., et al., 2017, in European Planetary Science Congress. pp EPSC2017–713
Turrini D., et al., 2021, ApJ, 909, 40
Vogt S. S., et al., 1994, in Crawford D. L., Craine E. R., eds, Society of Photo-Optical Instrumentation Engineers (SPIE) Conference Series Vol. 2198, Instrumentation in Astronomy VIII. p. 362, doi:10.1117/12.176725
Wardenier J. P., Parmentier V., Lee E. K. H., Line M. R., Gharib-Nezhad E., 2021, MNRAS, 506, 1258
Welbanks L., Madhusudhan N., Allard N. F., Hubeny I., Spiegelman F., Leininger T., 2019, ApJ, 887, L20
Wolszczan A., 1994, Science, 264, 538
Wolszczan A., Frail D. A., 1992, Nature, 355, 145
Wong I., et al., 2016, ApJ, 823, 122
Wright J. T., Marcy G. W., Howard A. W., Johnson J. A., Morton T. D., Fischer D. A., 2012, ApJ, 753, 160
Zellem R. T., et al., 2014, ApJ, 790, 53
Zhang J., Kempton E. M. R., Rauscher E., 2017, ApJ, 851, 84
Zhang M., et al., 2018, AJ, 155, 83
de Regt S., Kesseli A. Y., Snellen I. A. G., Merritt S. R., Chubb K. L., 2022, A&A, 661, A109
van Sluijs L., et al., 2023, MNRAS, 522, 2145

Chapter 2

Hot Jupiter Atmospheres: Theoretical Approach

The material in this chapter is based on Roth et al. (2024):
– Roth A., Parmentier V., Hammond M., 2024, MNRAS, 531, 1056

2.1 Hot Jupiter Atmospheres: Overview

The atmosphere of a planet can generally be thought of as a large scale heat engine (Koll & Komacek 2018). Energy is deposited into the atmosphere by stellar irradiation incident at the top of the atmosphere and by thermal radiation generated within the planet's core. A portion of this energy is then lost through radiation to space, whilst the rest is transformed into heat which permeates through the atmosphere and shapes the vertical temperature profile. This heat is then transformed into kinetic energy, which drives dynamical processes within the atmosphere such as convection and advection to redistribute the energy resulting in an atmosphere that exists out of its local mean radiative equilibrium state. In hot Jupiters, parcels of gas are moved from the day to the night-side. In this way the atmosphere drives the redistribution of energy deposited into the atmosphere towards a state of global thermal equilibrium.

Due to their short period orbits, the incident stellar flux received by hot Jupiters is many orders of magnitude higher than that received by gas giants within our solar system. There is still no clear consensus on the exact power generated within the interior of hot Jupiters, although it must be large given their inflation. Initially, cooling models suggested that the interior temperature should decrease over time to a value similar to that of Jupiter's, ∼100K (Burrows et al. 2004; Fortney et al. 2007; Showman & Guillot 2002). However, the inflated radii of hot Jupiters suggests that the internal temperature could be much larger (Fortney et al. 2007; Miller & Fortney 2011). Thorngren et al. (2019) for instance suggest that values of up to $T_{int} \sim 800K$ are much more reasonable. This higher value of internal temperature could shift the radiative-convective boundary (RCB) to much lower pressures, thus significantly altering the thermo-chemical and flow structure of the atmosphere (Carone et al. 2020; Komacek et al. 2022b; Thorngren et al. 2019). However, as increasing equilibrium temperature *increases* the pressure of the RCB, and the exact scaling relation between internal and equilibrium temperatures is still unknown, many modelling efforts continue to assume an internal temperature matching Jupiter's. As the irradiation and internal fluxes combine via T^4 scaling, the energy budget at the photosphere can therefore be considered to be determined mostly by the incident flux from the host star (Cowan & Agol 2011).

Additionally, the atmospheric dynamics for tidally locked exoplanets behave very differently to the atmospheres within our own solar system. The primary forcing on the atmosphere from the host star is the huge disparity in irradiation received between the day and night-side hemispheres, and the resulting temperature contrast drives large scale planetary wide circulation in the form of a super-rotating jet at the equator, reaching many kms^{-1}, divergent direct day-night flows over the poles and wave adjustment mechanisms.

Observing close orbiting giant planets can give us insights into the thermal structure and atmospheric circulation. The day-side brightness temperature can be determined from secondary eclipse observations, in addition to providing constraints on the overall atmospheric heat redistribution. The longitudinal thermal structure can be determined from phase curve observations and the albedo of the atmosphere can be determined from optical eclipses. High spectral resolution transit spectroscopy can also provide constraints on the wind speed at the limbs of the planet.

When building numerical models to describe these planets, it is important that we understand the relevant processes that determine the atmospheric state. In this chapter, we begin by discussing radiative heating and cooling in atmospheres (Section 2.2), including the methods used to model this. We then describe the dynamical equations used to model atmospheres in three-dimensions, including common approximations to these equations (Section 2.4). We then give an overview of the dynamics observed in hot Jupiters, including discussion on the formation of super-rotating jets, drag mechanism and relevant time and length scales (Section 2.5). We give an overview of the redistribution of heat throughout a tidally locked planet's atmosphere (Section 2.6), before highlighting some complications to the energy budget in these planets (Section 2.7).

2.2 Heating & Cooling Through Radiation

The incident stellar flux on a planet's atmosphere has two main pathways. It is either reflected back into space, the portion of which can be determined by the bond albedo, or it is deposited in the day-side atmosphere where it can either be re-radiated or partially advected onto the night-side before being re-radiated (Cowan & Agol 2011). The timescale upon which this re-radiation occurs is therefore incredibly important in shaping the three dimensional, thermo-chemical structure of an atmosphere. The radiative timescale, the time it takes for a parcel of gas to lose its energy to space, can be approximated as:

$$\tau_{\rm rad} \sim \frac{P_{\rm photo} c_p}{4\sigma g T^3}, \tag{2.1}$$

where g is the surface gravity, P is the pressure, c_p is the specific heat capacity and T is the equilibrium temperature (Showman & Guillot 2002). This timescale can range from a few seconds to thousands of years at deeper pressure levels, as seen for HD 209458 b in Figure 2.1. In a typical hot Jupiter, the photosphere is found at ∼0.1 bars, with a radiative timescale of $\sim 10^4$s. As a consequence of the strong dependence between the radiative timescale and equilibrium temperature, whilst the observed day-side temperatures of hot Jupiters scale fairly linearly with equilibrium temperature, the night-sides show a flat trend with values of ∼ 1000K (Beatty et al. 2019; Bell et al. 2021; Keating et al. 2019).

2.2.1 Albedo

The portion of incident stellar flux reflected back space contains information about the atmospheric structure, chemical composition and cloud properties. Through transit and direct imaging observations, the component of reflected light can be measured and computed in the form of planetary albedo. The geometric albedo, which is a measure of the reflected light in the direction of an observer, can be calculated from:

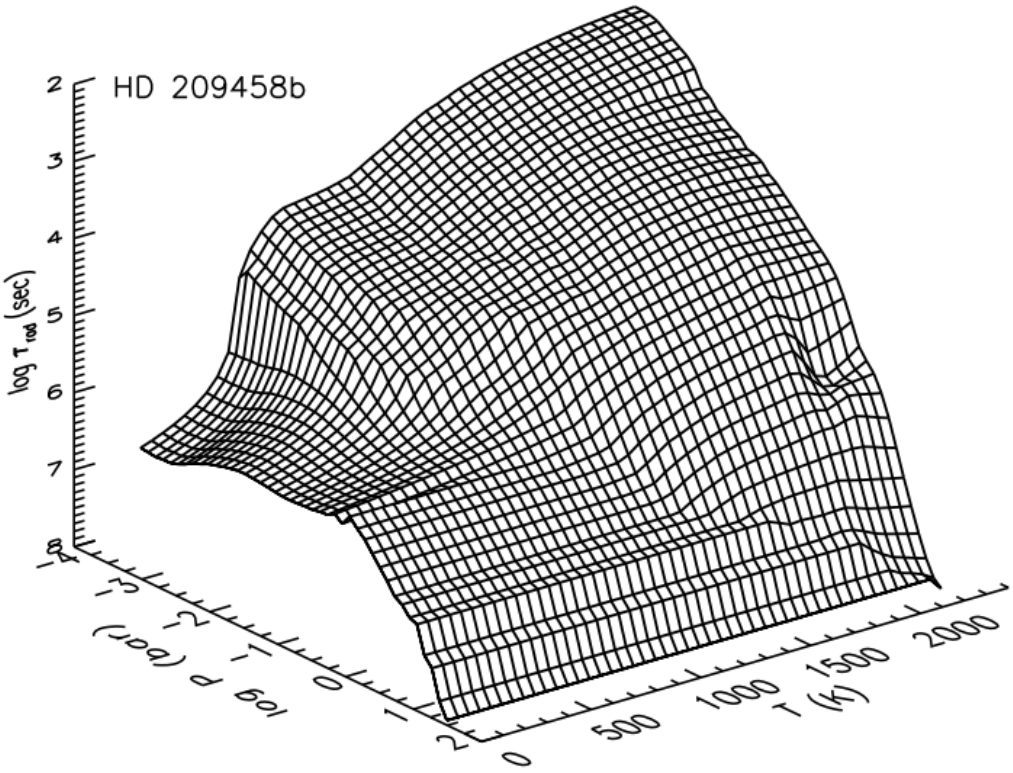


Figure 2.1: This Figure is taken from Showman et al. (2008), and displays the radiative timescale for the hot Jupiter HD 209458 b as it varies with atmospheric pressure and temperature.

$$\frac{F_p}{F_s} = A_g \left(\frac{R_p}{a}\right)^2 \phi(\alpha), \tag{2.2}$$

where F_p and F_s are the planet and star flux, A_g is geometric albedo, R_p is the planet radius, a is the semi-major axis and $\phi(\alpha)$ is the phase function at phase α where, for the emergent flux $j(\alpha)$:

$$\phi(\alpha) = \frac{j(\alpha)}{j(0)}. \tag{2.3}$$

A_g is calculated analytically in Madhusudhan & Burrows (2012) as a function of single-scattering albedo, see Figure 2.2.

We can also calculate a spherical albedo, A_s for a planet, which is a measure of the ratio of total reflected to incident flux on a planet's atmosphere over all angles but only at one wavelength. This is very similar to the bond albedo, which is measured over all wavelengths. The spherical albedo is related to the geometric albedo through the phase integral q:

$$A_s = qA_g. \tag{2.4}$$

Extending the work from Madhusudhan & Burrows (2012), Heng et al. (2021) calculate the spherical and geometric albedos analytically for isotropic, Lambertian, Rayleigh and

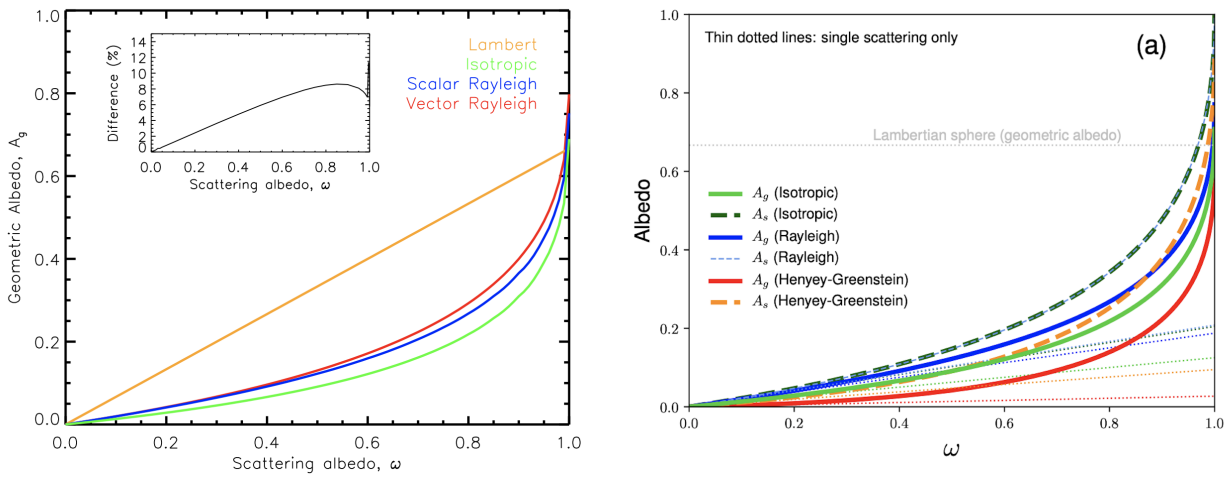


Figure 2.2: Left Panel: Plot from Madhusudhan & Burrows (2012), showing analytical variation of geometric albedo with single scattering albedo for Lambertian, isotropic and Rayleigh scattering. **Right Panel:** Plot from Heng et al. (2021), showing the analytical variation in both spherical and geometric albedo for isotropic, Rayleigh and Henyey-Greenstein scattering.

Henyey-Greenstein reflection, see Figure 2.2. The analytical predictions show that both the geometric and spherical albedo will increase with single scattering albedo, but that the geometric albedo always remain smaller than the spherical albedo.

In a real planet, the single scattering albedo of the atmosphere will be determined by the competition between absorbing material (molecular and atomic absorption) and the scattering material (Rayleigh scattering of the gas and cloud scattering).

2.2.2 Temperature Inversions

Typically, temperature should be expected to decrease with altitude in an atmosphere. As the pressure decreases with altitude, the atmospheric gas will expand and the opacity therefore decreases. This means a lower portion of the incoming stellar irradiation will be absorbed, and that which is will be re-radiated to space very quickly. However, if strong UV/optical absorbers are present in the upper atmosphere, a portion of the incident stellar irradiation will be intercepted creating an area of local heating - which causes a temperature inversion, where the temperature *increases* with decreasing pressure.

This has a significant impact on the radiative equilibrium state of the atmosphere. In addition to drastically increasing the temperature at the photosphere, the layer of high temperature absorbing gas will also induce an anti-greenhouse effect at higher pressures, reducing the temperature below the inversion.

In Earth's atmosphere this effect is caused by ozone in the stratosphere. In hot Jupiter atmospheres, the primary chemicals thought to be responsible for these temperature inversion are gaseous titanium oxide (TiO) and vanadium oxide (VO) (Fortney et al. 2008; Hubeny et al. 2003). These species are predicted by chemical equilibrium to be present in sufficient quantities to produce a strong thermal inversion above temperatures of $\sim$ 1400K, creating two distinct regimes in which hot Jupiter atmospheres can be classified (Fortney et al. 2008; Parmentier et al. 2015; Piette et al. 2020).

TiO and thermal inversions have indeed been detected in the hottest hot Jupiters, such as

WASP-33 b ($T_{\rm eq}$ = 2781K) (Cont et al. 2022), WASP-121 b ($T_{\rm eq}$ = 2450K) (Evans et al. 2016), WASP-189 b ($T_{\rm eq}$ = 2636K) (Prinoth et al. 2022), and WASP-18 b (T_{eq} = 2505K) (Coulombe et al. 2023), and VO was recently detected in WASP-76 b ($T_{\rm eq}$ = 2182K) (Pelletier et al. 2023). However, TiO, VO nor thermal inversions, have been detected in cooler planets, such as HD 209458 b ($T_{\rm eq}$ = 1477K) (Line et al. 2016), or WASP-43 b ($T_{\rm eq}$ = 1379K) (Kreidberg et al. 2014), even though these planets are hot enough to have a gaseous TiO in their atmospheres. It is therefore not yet clear at which equilibrium temperature the population of planets transitions from TiO/VO dominated atmospheres to atmospheres devoid of TiO/VO (Mansfield et al. 2021). The main mechanisms through which to deplete TiO/VO from the day-side atmosphere are condensation processes that can either happen in the deep layers of the atmosphere (Parmentier et al. 2016; Spiegel et al. 2009), or in the planet's night-side (Beatty et al. 2017; Parmentier et al. 2016; Pelletier et al. 2023). The actual strength of these cold-trap processes depends on poorly constrained microphysical parameters (such as the size of the condensates) and the strength of the atmospheric mixing (Parmentier et al. 2013; Powell et al. 2019; Spiegel et al. 2009).

It should be noted that TiO and VO are not the only explanation for temperature inversion, however. For example Mollière et al. (2015) show that, for planets with C/O ratios $\sim$1 and $T_{eff} \geq$1500K, a temperature inversion can be present without the need for additional atmospheric absorbers as the main atmospheric coolants are depleted. Furthermore, in ultra-hot Jupiters it has also been shown that atomic metals, such as Fe, could produce temperature inversions (Arcangeli et al. 2018; Lothringer et al. 2018). Atomic iron has been detected in the day-side thermal emission spectra of multiple ultra-hot Jupiters (Cont et al. 2021; Kasper et al. 2021; Nugroho et al. 2020; Pino et al. 2020; Yan et al. 2020, 2022). However, the strength of currently observed inversions in hot Jupiters are hard to obtain without TiO and VO.

2.3 Methods to Model Radiative Heating & Cooling

The simplest way to parameterise the heating and cooling of an atmosphere is with a Newtonian heating scheme, in which the temperature is considered to relax towards an assumed radative-equilibrium state over time. Of course, despite being computationally very inexpensive, this method is a drastic over-simplification. It requires a guess at the radiative-equilibrium pressure-temperature profile of an atmosphere and, more crucially, is not energy conserving.

A far more rigorous way to determine the heating and cooling rates is via modelling the propagation of radiation, and therefore energy, including the effects of emission, absorption and scattering processes within the atmosphere. The radiative transfer equation describes this process:

$$-\mu \frac{dI_{\mu\nu}}{dm} = \kappa_\nu I_{\mu\nu} - \kappa_\nu B_\nu(T). \tag{2.5}$$

In the above equation, for a specific frequency ν and direction μ, κ is the opacity, B(T) is the Planck function at temperature T, $dm = \rho dz$ is the mass contained along the path of irradiation and I is the specific intensity of the irradiation which propagates with angle $\theta = 1/\cos(\mu)$.

This equation can be simplified depending on the choice of opacity modelling. In the

simplest form, the opacity can be considered constant with wavelength, known as a 'grey' modelling. This is a valid approximation in the deep layers, where the diffusion limit applies to emitted photons (Mihalas & Mihalas 1984; Parmentier 2014). A further step is to differentiate between the visible opacity, corresponding to the absorption of incident stellar irradiation, and thermal opacity, corresponding to the thermal emission from the atmosphere. This is known as 'semi-grey' modelling (Guillot 2010; Hansen 2008; Robinson & Catling 2012). However, opacity itself is highly dependent on the temperature structure due to pressure and temperature broadening of spectral lines, and changing chemistry (Arcangeli et al. 2018; Parmentier et al. 2018). Because of this, 'non-grey' opacity modelling (modelling the full spectral variation of opacity in an atmosphere) is important for realistic modelling to ensure that energy is conserved when calculating the spectrum of a planet from the modelled temperature field (e.g. as in (Parmentier & Guillot 2014; Parmentier et al. 2015)).

In GCM modelling, non-grey opacities are often modeled through the correlated-k distribution method (Goody & Yung 1989; Lacis & Oinas 1991). This method allows many individual spectral lines to be reorganised and compressed into a smaller number of spectral bins, which can then be used as k-coefficients. This is done by re-mapping the the absorption coefficients from spectral space (i.e $k(\nu)$, where ν is the frequency) to a space where k varies with a variable g. g(k) is then referred to as the cumulative distribution where:

$$g_i = \int_0^k f_i(k^{'})dk^{'}. \tag{2.6}$$

Here, $f_i(k)$ is the cumulative distribution function for the absorption coefficient, k, in a layer of atmosphere, i, over a spectral interval of $\delta\nu$ (Goody & Yung 1989; Kataria et al. 2013; Lacis & Oinas 1991). The full frequency space can then be split up into a number of smaller frequency intervals. Within each frequency interval, the absorption coefficients can be sorted by their occurrence and a cumulative distribution, g, derived. Radiative transfer calculations can then be carried out for each of the frequency intervals, using the derived cumulative distribution for that interval. Within each window, a number, n, of different monochromatic absorption coefficients (i.e k-coefficients) are computed at n Gauss points to integrate over k(g).

2.4 Dynamical Equations in Spherical Coordinates

The evolution of an atmosphere is governed by a complete set of conservation equations (Kalnay 2002), these being:

(i) Conservation of momentum (Newton's second law)

There are three equations for the three components of velocity (u, v, w). When written in spherical coordinates, ϕ for longitude, θ for latitude and r for radial distance, the velocities can be expressed as:

$$u = r\cos\theta\frac{D\phi}{Dt}, \tag{2.7}$$

$$v = r\frac{D\theta}{Dt}, \tag{2.8}$$

$$w = \frac{Dr}{Dt}. \tag{2.9}$$

The momentum conservation equations in spherical coordinates are then (Mayne et al. 2014):

$$\frac{Du}{Dt} = \frac{uv\tan\theta}{r} + \frac{uw}{r} + fv + f^{'}w - \frac{1}{\rho r\cos\theta}\frac{\partial P}{\partial\phi} + D_{\phi}, \tag{2.10}$$

$$\frac{Dv}{Dt} = -\frac{u^2\tan\theta}{r} - \frac{vw}{r} - uf - \frac{1}{\rho r}\frac{\partial P}{\partial\theta} + D_{\theta}, \tag{2.11}$$

$$\frac{Dw}{Dt} = \frac{u^2+v^2}{r} + uf^{'} - g(r) - \frac{1}{\rho}\frac{\partial P}{\partial r}, \tag{2.12}$$

where f is the coriolis parameter, $f = 2\Omega\sin\theta$, and therefore $f^{'} = 2\Omega\cos\theta$. $g(r)$ is the radially dependent gravity, $g(r) = g_{r=R_p}\left(\frac{R_p}{r}\right)^2$.

(ii) Conservation of mass (or the continuity equation)

$$\frac{D\rho}{Dt} = -\rho\left(\frac{1}{r\cos\theta}\frac{\partial u}{\partial\phi} + \frac{1}{r\cos\theta}\frac{\partial(v\cos\theta)}{\partial\theta} + \frac{1}{r^2}\frac{\partial(r_2 w)}{\partial r}\right). \tag{2.13}$$

In addition to overall mass conservation, conservation equations for individual atmospheric constituents can also be added as in (Kalnay 2002), as long as their sources (evaporation) and sinks (condensation) are accounted for.

(iii) Conservation of energy (first law of thermodynamics)

$$\frac{D\Theta}{Dt} = \frac{Q\Theta}{T} + D(\Theta), \tag{2.14}$$

where Q is a term for the heating rate, $D(\Theta)$ is a term for the dissipation and Θ is the potential temperature at pressure, P, and temperature, T, compared to some reference pressure, P_o:

$$\Theta = T\left(\frac{P_o}{P}\right)^{\frac{R}{c_p}}, \tag{2.15}$$

where c_p is the specific heat capacity and R the ideal gas constant.

(iv) Equation of state for the gas

This is usually the ideal gas law:

$$P = \frac{k_B}{\mu}\rho T. \tag{2.16}$$

where k_B is the Boltzmann constant and μ the mean molecular weight of the atmosphere.

2.4.1 Common Approximations

In order to simplify the dynamical equations to a set which can be more quickly numerically solved, a number of approximations are applied. The name given to the reduced equation set is determined by which approximations are used. A full breakdown of the approximation sets and resulting names can be seen in Table 2.1. The commonly used approximations are (Mayne et al. 2014):

- **Constant Gravity:** The gravity can be approximated as constant throughout an atmosphere if $R_p \geq z$, where z is the vertical height of the atmosphere. This approximation encompasses the approximation of no self-gravity, i.e the mass of the atmosphere does not contribute towards the gravity of the planet, which is valid if $M_{\text{atm}} << M_{\text{p}}$. It also naturally assumes the spherical geopotentials approximation. i.e that a planet can be considered as a perfect sphere in which the gravity does not vary latitudinally, as it would due to tidal deformation, (White et al. 2008).

- **The Shallow-Fluid Approximation:** By approximating that $r \rightarrow R_p$ and therefore $\frac{\partial}{\partial r} \rightarrow \frac{\partial}{\partial z}$, we can write the vector invariant form of the momentum equation. This approximation holds if $R_p \gg z$.

- **The Traditional Approximation:** When the shallow-fluid approximation is applied in spherical coordinates the resulting equations no longer conserve angular momentum. We deal with this by assuming that terms proportional to $1/\text{r}$ and $df/d\theta$ are negligible in the full momentum equations. This assumption requires $N^2 > \Omega^2$, where N is the Brunt-Väisälä frequency.

- **The Hydrostatic Approximation:** We assume that the vertical pressure gradient is balanced by the gravitational term in the vertical momentum equation, $\frac{dp}{dr} = -\rho g$. This is valid for atmospheres where the horizontal length scale is much larger than the vertical length scale, $L >> H$.

Table 2.1: Common approximation sets in dynamic atmospheric modelling (Mayne et al. 2014).

Name	Assumptions
Full	Spherical Geopotentials, No Self Gravity
Deep	″ + Constant Gravity
Shallow	″ + Shallow Fluid Approximation
Primitive	″ + Traditional Approximation

2.4.2 Dynamical Equations in Pressure Coordinates

When solving the dynamical equations for a hydrostatic atmosphere, it is a much more natural choice to work in pressure coordinates. This simplifies the equations of motion and most atmospheric processes scale with pressure rather than height. In pressure coordinates the derivative operator becomes:

$$\frac{D}{Dt} = \frac{\delta}{\delta t} + \mathbf{v} \cdot \nabla + \omega \frac{\delta}{\delta p} \tag{2.17}$$

where $\mathbf{v}$ is the horizontal velocity and ω is the vertical velocity in pressure coordinates, $\omega = \frac{Dp}{Dt}$. The primitive equations then become:

$$\frac{D\mathbf{v}}{Dt} = -\nabla\phi - f\mathbf{k} \times \mathbf{v} + (D_{\mathbf{v}}) \quad \text{(Horizontal Momentum)} \tag{2.18}$$

$$\frac{\delta\phi}{\delta p} = -\frac{1}{p} \quad \text{(Hydrostatic Balance)} \tag{2.19}$$

$$\nabla \cdot \mathbf{v} + \frac{\delta\omega}{\delta p} = 0 \quad \text{(Mass Conservation)} \tag{2.20}$$

$$\frac{DT}{Dt} = \frac{q}{c_p} + \frac{\omega}{\rho c_p} + (D_{\mathbf{T}}) \quad \text{(Energy Conservation)} \tag{2.21}$$

where for a constant pressure surface, ∇ is the horizontal gradient, $\Phi = gz$ is the geopotential, $f = 2\Omega\sin(\phi)$ is the coriolis parameter, $\mathbf{k}$ is the local vertical unit vector, p is the pressure, ρ is the density, T is the temperature, q is the thermodynamic heating rate and c_p is the specific heat capacity. The last of these primitive equations is more commonly written in terms of the potential temperature $\theta = T(p/p_0)^{R/c_p}$, giving equation 2.14.

$D_{\mathbf{v}}$ and D_T are parameterisations used to represent dissipation of kinetic energy. The terms are agnostic of the type of dissipation applied. They can be used to parameterise any kind of dissipative drag forces acting on the winds, such as Ohmic dissipation from magnetic drag, shocks or shear-instabilities (discussed further in Section 2.5.2).

Most GCMs do not resolve the physical mechanism which are thought to dissipate kinetic energy within hot Jupiter atmospheres and instead introduce a form of numerical drag, i.e through the use of a Shapiro filter (Shapiro 1970) which we discuss further in Chapter 3, to help equilibrate the kinetic energy with the flow. As numerical drag relies on selected modeling parameters, rather than being physically motivated, there are potential issues with this that have been pointed out on numerous occasions (Cho et al. 2015; Goodman 2009; Heng et al. 2011a; Koll & Komacek 2018; Li & Goodman 2010; Liu & Showman 2013; Mayne et al. 2014; Thrastarson & Cho 2010). However, although the dissipation of kinetic energy within a GCM relies on the numerical drag (if no additional drag mechanisms are included), the state of large-scale dynamical structures relies on the angular momentum budget. As the Shapiro filter is designed to act only on small-scale flows (Shapiro 1970), the angular momentum budget should not be affected by the numerical drag. Koll & Komacek (2018) show is the case for GCMs relying on numerical drag in.

2.5 Dynamics

The primary source of dynamics in tidally locked exoplanets is the contrast between strong day-side heating, forced by irradiation from the host star, and night-side cooling (Heng & Showman 2015; Pierrehumbert & Hammond 2019; Showman & Polvani 2010, 2011; Showman et al. 2013).

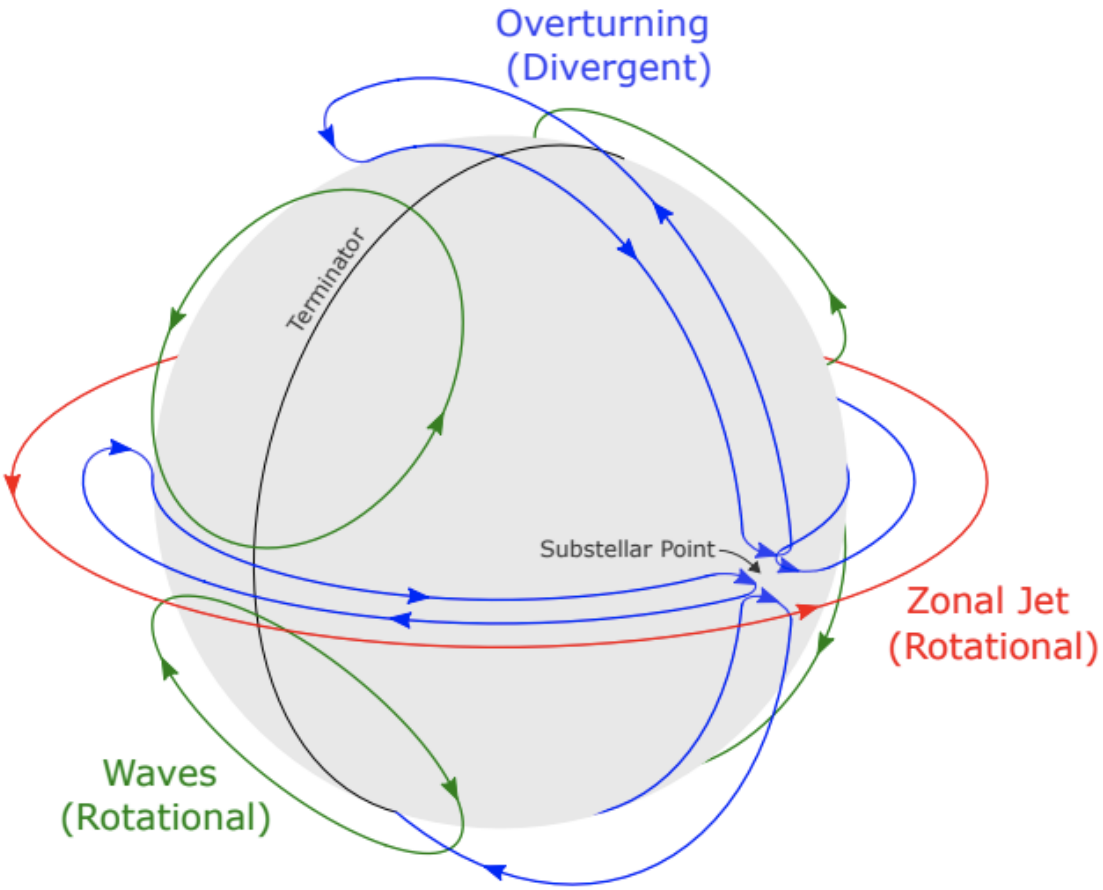


Figure 2.3: This Figure is taken from Hammond & Lewis (2021), and displays a diagram of the different circulation regimes that are present in tidally locked exoplanet atmospheres.

The resulting planetary scale circulation can generally be deconstructed into three components, divergent overturning circulation, rotational circulation from waves and rotational circulation from a zonal jet. Figure 2.3 displays a diagram of these three circulation regimes from Hammond & Lewis (2021).

The planetary scale overturning circulation is caused by gas rising on in the hot day-side, and sinking in the colder night-side (Pierrehumbert & Hammond 2019; Showman & Polvani 2011; Showman et al. 2013). Planetary scale standing waves are excited by the pressure gradient and confined by the rotation (Sardeshmukh & Hoskins 1988; Showman & Polvani 2010), which interact to produce a super-rotating jet at the equator, further advecting energy from day-side to night-side (Hammond & Pierrehumbert 2018; Showman & Polvani 2010, 2011; Tsai et al. 2014). The waves themselves also contribute to the heat transport, cooling

the day-side and warming the night-side.

From both modelling and theory, we see consensus in the presence of super-rotating jets at the equator, reaching many kms^{-1}, and divergent day-night direct flows over the poles (Charbonneau et al. 2008; Cooper & Showman 2005; Cowan et al. 2007; Crossfield et al. 2010; Dobbs-Dixon & Agol 2013; Guillot & Showman 2002; Heng et al. 2011b; Knutson et al. 2007, 2009; Mayne et al. 2014; Menou & Rauscher 2009; Perna et al. 2012; Rauscher & Menou 2012; Showman & Guillot 2002; Showman et al. 2008, 2015; Tan & Komacek 2019). I will now describe these circulation regimes and their origins in more detail.

2.5.1 Super-rotation & Formation of the Jet

When a planet's atmosphere has more angular momentum in the same direction as the surface below it, this is known as a state of atmospheric super-rotation. Many solar system gas giant planets exhibit fast eastward moving super-rotating jets, such as Jupiter and Saturn. However, their origin in these planets is still not fully understood. Super-rotation is not necessarily expected for planets, as the equator is already the region with the highest angular momentum due to the rotation. Thus, super-rotation requires transferring momentum from regions with low momentum (mid-latitudes) to regions of high momentum (equator). Diffusion alone would have the opposite effect, therefore there must be some underlying mechanism causing organised transfer of momentum in this way. For hot Jupiters, the most plausible explanation to date was proposed by Showman & Polvani (2011), and relies on the interaction between planetary scale standing waves, namely Rossby and Kelvin-like waves (Showman & Polvani 2010, 2011; Tsai et al. 2014).

For tidally locked planets, the strong gradient between day-side heating and night-side cooling applies a roughly wavenumber-1 forcing to the atmosphere, i.e with one maximum at the substellar and one minimum at the antistellar point. This causes gas to rise on the day-side and sink on the night-side thus driving planetary scale overturning circulation away from the substellar point in all directions (i.e see Figure 2.3) (Hammond & Lewis 2021; Showman & Polvani 2011; Showman et al. 2013).

This forcing also generates planetary scale stationary waves. Away from the equator Rossby waves are formed, as overturning gas is propagated westwards due to the coriolis force. This in turn induces latitudinal oscillation in the gas, as Rossby waves are transverse waves and therefore induce motion perpendicular to the direction of travel. Due to variation in the Coriolis effect with latitude and the conservation of potential vorticity, the gas must then rotate forming latitudinal eddies. At the equator, stationary waves are balanced by non-linear terms in the material derivative (Hammond et al. 2020) and propagate eastwards. These waves are not balanced by linear drag and are therefore not true Kelvin waves. However, these equatorial standing waves have the same morphology as Kelvin waves and produce a similar effect. They are therefore commonly referred to as 'Kelvin-like' waves.

The combination between these two oppositely propagating waves then tilts the latitudinally rotating eddies formed by the Rossby waves, with the lower latitude portions of the eddies pushed eastwards by the Kelvin waves and the higher latitudinal portions pushed westward by the Rossby waves. These tilted eddies in the mid-latitude regions of the atmosphere then pump zonal-mean momentum towards the equator, thus forming an equatorial super-rotating jet in the atmosphere. Vertical transport of gas at the equator then becomes important in balancing the jet as it accelerates (Debras et al. 2020; Hammond et al. 2020). The frequency of the stationary Rossby and Kelvin-like waves are then Doppler shifted as

the jet accelerates. This shifts the waves eastwards (Hammond & Pierrehumbert 2018; Tsai et al. 2014), and modifies the momentum transport towards the equator in non-trivial ways. Additionally, further non-linear interactions between the overturning and rotational circulation modifies them in non-trivial ways which are still poorly understood (Hammond & Lewis 2021).

The overall resulting circulation structure of hot Jupiters is commonly observed as a night-side gyre and day-side chevron-like structure in the atmosphere, which are particularly efficient at pumping momentum. An example of this circulation pattern is seen displayed in Figure 2.4. The strong super rotating jet is also clearly visible at the equator, and overturning circulation at higher latitudes, with a planetary hot spot which is shifted eastwards of the substellar point.

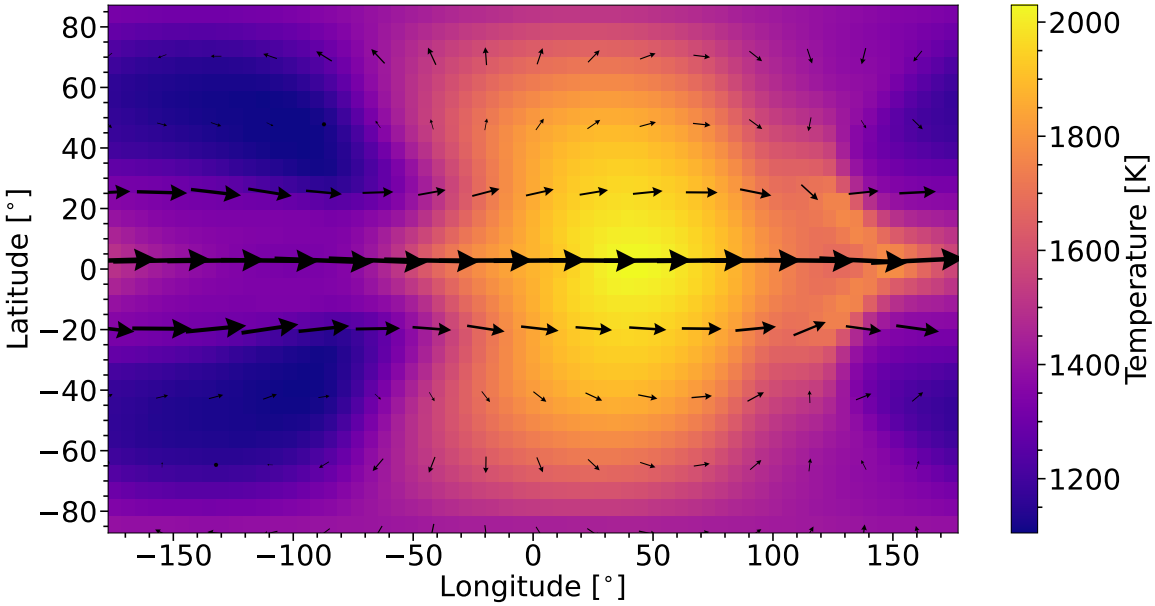


Figure 2.4: Latitude vs longitude thermal structure at the 0.1 bar pressure level for a model with $T_{eq} =$ 1600K at solar metallicity from our grid of models, generated with the SPARC/MiTgcm (Showman et al. 2009). The arrows display the magnitude and direction of the zonal winds.

This mechanism to form the super-rotating jets can only work if the Rossby and Kelvin-like waves are capable of efficiently transporting energy, i.e if the radiative timescale is low then the atmosphere will lose energy to space before it can be transported by the waves. Equally, the jet formation will also be inhibited if the planetary waves are sufficiently damped by a source of atmospheric drag, although Showman & Polvani (2011) show how tilted eddies can form even when drag is present. The day-to-night overturning circulation is therefore dominant when the radiative or dynamical drag is too large for formation of the jet.

These jets were first predicted to be found in hot Jupiter atmospheres through modelling (Cooper & Showman 2005; Dobbs-Dixon & Agol 2013; Guillot & Showman 2002; Heng et al. 2011b; Mayne et al. 2014; Menou & Rauscher 2009; Perna et al. 2012; Rauscher & Menou 2012; Showman & Guillot 2002; Showman et al. 2008, 2015; Tan & Komacek 2019), before later being inferred through observation (Charbonneau et al. 2008; Cowan et al. 2007; Crossfield et al. 2010; Knutson et al. 2007, 2009).

2.5.2 Drag Mechanisms

Although we have a qualitative understanding of how super-rotating jets form in tidally locked exoplanets, there is no general theory which can explain the magnitude of these jets across the observed population. This is because, as we have discussed, the final state of the jet depends on complex interactions between standing waves and rotational eddies, which are poorly understood. We know that in steady-state, the kinetic advection of heat in an atmosphere is balanced by the dissipation of kinetic energy through drag on the winds. However, this problem is further complicated by the fact that the mechanisms through which hot Jupiters primarily dissipate kinetic energy are still a topic of debate (Goodman 2009). Therefore, to accurately constrain the wind speeds on hot Jupiters we must first understand which dissipation mechanisms dominate.

There are currently three theories for the dissipation mechanisms in hot Jupiter atmospheres. Magnetic drag can be induced when the temperature is high enough to ionise chemicals, particularly sodium and potassium, in an atmosphere. The magnetic field generated by the planet can then interact with these charged particles, creating an additional source of drag and releasing energy through Ohmic dissipation (Batygin et al. 2013; Beltz et al. 2022; Koll & Komacek 2018; Menou 2012; Perna et al. 2010a; Rauscher & Menou 2013; Rogers 2017; Rogers & Komacek 2014; Rogers & Showman 2014). The drag is therefore increasingly strengthened in hotter atmospheres, as the ionisation fraction increases. Perna et al. (2010a) predicts that the effects of magnetohydrodynamical (MHD) drag would act as a bulk Lorentz force drag on the winds, and has been shown capable of significantly disrupting the circulation on hot Jupiters (Batygin et al. 2013; Beltz et al. 2022; Koll & Komacek 2018; Menou 2012; Perna et al. 2010a,b; Rauscher & Menou 2013; Rogers 2017; Rogers & Komacek 2014; Rogers & Showman 2014). This could cause time variable, or even westward, winds (Hindle et al. 2019, 2021a,b; Rauscher & Menou 2013; Rogers 2017; Rogers & Komacek 2014; Rogers & Showman 2014), shifting the planetary hot-spot and therefore impacting observable features such as the offset in optical phase curves (Hindle et al. 2019, 2021a,b). However, this effect has been shown to only become significant above temperatures of $\sim$1400K (Koll & Komacek 2018; Menou 2012; Rogers & Showman 2014).

Additional dissipation mechanisms which have been suggested include shocks developed in the supersonic jet (Dobbs-Dixon & Agol 2013; Fromang et al. 2016; Heng 2012; Li & Goodman 2010; Perna et al. 2012), and the turbulence induced by shear-driven instability, such as Kelvin-Helmholtz instability (Fromang et al. 2016; Koll & Komacek 2018; Li & Goodman 2010). Because the magnetic drag has such a strong dependence on temperature, in the magnetic dominated regime we expect drag to increase sufficiently fast with equilibrium temperature for wind speed to decrease with increasing temperature. For hydrodynamic instabilities, however, the dependence on equilibrium temperature is weak enough that we expect wind speed to increase with increasing temperature (Koll & Komacek 2018).

2.5.3 Length Scales

In order to characterise the atmosphere of a planet it is important to first know the scale over which primary atmospheric adjustments take place. If the main source of energy transport is that of large atmospheric structures, then lower resolution models will still be capable of providing insight. However, if this is not the case then increasingly high resolution models must be used to determine the atmospheric circulation. From the governing momentum

equations (see Section 2.4 for these equations), we know that the balance between the inertial force, i.e advection, and Coriolis force is the main factor in shaping atmospheric dynamics. The Rossby number is a measure of this balance and can be expressed as:

$$R_o = \frac{U}{fL}, \tag{2.22}$$

where U is the characteristic wind speed, L is the characteristic length scale and f is the Coriolis parameter, $f = 2\Omega \sin\phi$. When $R_o << 1$, it signifies that the pressure gradient will balance the coriolis force, rather than advection. In this case, the atmosphere is in geostrophic balance. When $R_o >> 1$, the effects of planetary rotation are negligible, and the force balance is between the pressure gradient and advection. In typical hot Jupiters, the Rossby number at the photosphere R_o varies between $\sim 0.1 < R_o <\sim 1$, with variation depending on planetary parameters such as the temperature, rotation period, gravity, metallicity and atmospheric drag (see Showman et al. (2010) for a review). Importantly, this means that hot Jupiters can exist in diverging circulation regimes, depending on the planetary conditions. We discuss this in more detail, and link to observation, in Chapter 4.

For the characteristic length scale, L, the Rossby deformation radius is typically used. This is a measure of the distance at which the Coriolis force begins to prevent the smoothing of atmospheric pressure gradients via wave adjustment mechanisms:

$$L_D = \frac{ND}{f}, \tag{2.23}$$

where D is the vertical length scale of the atmosphere, usually one scale height, and N is the Brunt-Väisälä frequency. For an isothermal atmosphere, $N = \sqrt{c_p}k_B\sqrt{g/H}$ where c_p is the heat capacity at constant pressure, k_B is the Boltzmann constant, g is the gravity and H is the vertical scale height. For hot Jupiters, the Rossby deformation radius is usually on the order of the planetary radius, signifying that large scale structures will dominate atmospheric circulation (Showman & Guillot 2002).

Another useful tool for characterizing atmospheric flow in hot Jupiters is the Rhines scale:

$$L_{Rh} = \pi\sqrt{\frac{U}{\beta}}, \tag{2.24}$$

where $\beta = 2\Omega\cos\phi/R_p$ is known as the beta-effect, which describes the meridional gradient in coriolis force. The transition between non-linear advection and linear advection being dominant for atmospheric vortices occurs at L_{Rh}, marking the point at which small scale vortices can no longer cascade into larger ones. Again this length scale is typically of the same order as the planetary radius for hot Jupiters, signifying that a low number of zonal jets are expected to be present.

The combination of both Rhines scale and Rossby deformation radius being similar to the planetary radius predicts that the majority of energy and therefore heat is transported within hot Jupiter atmospheres via large planetary scale structures, which has two important consequences. Firstly, this means that circulation models with lower spatial resolutions are still capable of characterising the atmospheric circulation in hot Jupiters. Secondly, it means that we can still draw meaningful insights into the circulation from spatially averaged observations of their atmospheres.

We also note that both the Rossby number and Rhines scale depend on the planetary rotation rate, Ω, and therefore on the orbital period in a tidally locked regime. As such we expect the dynamics within hot Jupiter atmospheres to vary with orbital period.

2.5.4 Timescales

The balance between the radiative timescale, Equation 2.1, and the timescales over which the advection and wave adjustment mechanisms occur are also incredibly important in determining the mean atmospheric state. Gravity waves, generated via the horizontal temperature and pressure variations, cause the vertical stretching and contraction of air columns. This motion vertically shifts the plane of constant potential temperature in the atmosphere, i.e the isentropes across which an adiabatically heated or cooled air parcel will move. If the coriolis force is comparatively weak then these waves are able to radiate infinitely and the resulting final state is one with constant isobaric temperature. These wave-adjustment mechanisms have been shown to act not only locally but also over planetary scales in exoplanets (Perez-Becker & Showman 2013; Showman & Polvani 2011), and are therefore capable of smoothing out large scale horizontal temperature gradients. The wave timescale can be defined as the timescale at which energy transporting gravity waves can travel across a hemisphere of the planet, in the isothermal case (Parmentier et al. 2021; Perez-Becker & Showman 2013):

$$\tau_{\text{wave}} \sim \frac{\pi R_p}{\sqrt{k_b T_{\text{photo}}/\mu}} \propto \frac{1}{\sqrt{T_{\text{photo}}}}, \tag{2.25}$$

where R_p is the planetary radius, μ the mean molecular weight, k_b the Boltzmann constant and T_{photo} the photospheric temperature.

The advective timescale can be defined as the timescale it takes for a parcel of gas to be advected across one hemisphere by the equatorial zonal jet (Parmentier et al. 2021):

$$\tau_{\text{adv}} \sim \frac{\pi R_p}{U_{\text{jet}}} \propto \frac{1}{T_{\text{eq}}}. \tag{2.26}$$

where U_{jet} is the mean wind speed at the equator and T_{eq} the equilibrium temperature. Parmentier et al. (2021) show that U_{jet} itself scales in an affine manner (i.e linear minus a constant) based on the temperature, which is important for our analysis in Chapter 4.

Comparison between these characteristic timescales can be used to estimate if equatorial super-rotation is inhibited, i.e if τ_{rad} or $\tau_{\text{drag}} << \tau_{\text{wave}}$ then the jet cannot form (Showman et al. 2013), and the overturning circulation will dominate. A rough estimate for the point at which this occurs comes from comparing the group and phase velocity of Kelvin and Rossby waves to the planetary radius (Showman et al. 2013):

$$\tau_{\text{rad}}, \quad \tau_{\text{drag}} << \frac{R_p}{NH}. \tag{2.27}$$

For a typical hot Jupiter $R_p/\text{NH} \sim 10^5$s.

Similar comparison can be used to predict the day-night temperature difference for hot Jupiters. From Komacek & Showman (2016),

$$\tau_{\text{wave}}(p) \sim \begin{cases} \sqrt{\tau_{\text{drag}}(p)\tau_{\text{rad}}(p)\Delta \ln p}, & \text{if } \tau_{\text{drag}}(p) < f^{-1} \\ \sqrt{f^{-1}\tau_{\text{rad}}(p)\Delta \ln p}, & \text{if } \tau_{\text{drag}}(p) > f^{-1} \end{cases} \tag{2.28}$$

where if τ_{wave} is the larger of these two quantities then the day-night temperature difference will also be small, and vice versa.

In the case of magnetic drag dissipating kinetic energy, the Lorentz drag timescale in an atmosphere can be calculated from (Koll & Komacek 2018; Perna et al. 2010a; Rauscher & Menou 2013):

$$\tau_{\text{mag}} = \frac{4\pi H_e \rho}{B^2}, \tag{2.29}$$

where ρ is the atmospheric gas density, B is the dipole field strength and H_e is the atmospheric electrical resistivity.

2.6 Overall Redistribution of Heat

Heat is transported in hot Jupiter atmospheres via two mechanisms: direct advection of heat by the winds and wave adjustment mechanisms. As the atmosphere tries to move heat from day to night-side, energy is lost by the gas through radiation. The final efficiency of the heat transport is therefore determined by competition between the advective or wave driven transport and radiative losses (Komacek & Showman 2016; Perez-Becker & Showman 2013; Showman & Guillot 2002; Zhang et al. 2018). For example, a lower temperature planet should lose less heat through radiation, increasing the efficiency of heat transport, but this may be counteracted by weaker circulation. Heat advection itself occurs, primarily, via two different and competing methods: rotational circulation, which is dominated in hot Jupiters by the super-rotating equatorial jet, and divergent overturning circulation between the day-side and night-side hemispheres. Hammond & Lewis (2021) show that, for a typical hot Jupiter, these two regimes can both contribute to the heat circulation efficiency equally. As the jet circulation is highly dependent on a host of external factors such as the orbital period of the planet, these components will also have variable relative magnitudes. This means that there are essentially three ways to transport heat: wave adjustment mechanisms, rotational circulation and divergent circulation. Because of this, heat transport varies widely over the observed hot Jupiter population as it is highly dependent on atmospheric thermal and chemical structure.

2.6.1 Expected Scaling of Heat Redistribution

Given the radiative timescale has a much stronger dependency on temperature and gravity than the advective and wave timescales, we expect adjustments to the radiative timescale to dominate changes in the heat redistribution.

Opacity will increase with atmospheric metallicity, as a higher ratio of metals to hydrogen will increase the atomic weighting of the atmosphere. From Equation 2.1, the radiative timescale at the photosphere will therefore reduce with increasing metallicity (Drummond et al. 2018; Kataria et al. 2015), leading to less efficient heat redistribution. However, as P_{phot} also depends on gravity, the scaling with g is not clear until we rewrite Equation 2.1. The

radiative timescale can equally be expressed in terms of the opacity, κ. By first taking the hydrostatic equation and the definition of optical depth, τ:

$$dP = -\rho g dz, \tag{2.30}$$
$$d\tau = \kappa dm, \tag{2.31}$$

then noticing that $\rho dz = dm$, we can rewrite the pressure as:

$$dP = \frac{g d\tau}{\kappa}, \tag{2.32}$$

where $\tau \sim 2/3$ is the optical depth at the photosphere. Assuming constant gravity and opacity, the photospheric pressure can then be described as:

$$P_{\text{photo}} \sim \frac{2g}{3\kappa}. \tag{2.33}$$

Because pressure and optical depth vary exponentially in our atmosphere, and because the opacity usually increases with pressure, the opacity value that matters to determine the photospheric pressure is the opacity at the photosphere, κ_{photo}. Substituting this back into equation 2.1, the radiative timescale then becomes,

$$\tau_{\text{rad}} \sim \frac{c_p}{6\sigma\kappa(P_{\text{photo}}(g), T_{\text{photo}})T_{\text{photo}}^3}. \tag{2.34}$$

As κ increases with pressure, due to pressure broadening of spectral lines, τ_{rad} will decrease with increasing surface gravity. The exact scaling relation between opacity and pressure can be found in Freedman et al. (2014). In conclusion, we expect planets with high metallicity and high gravity to be the less efficient at transporting heat from day to night. We also expect the heat redistribution to become worse in higher temperature atmospheres, due to the $1/T^3$ dependence. This has been shown to be the case for increasing temperature (Komacek & Showman 2016; Perez-Becker & Showman 2013), and metallicity (Charnay et al. 2015).

2.7 Further Complications to Energy Balance

Particularly for the higher temperature ultra-hot Jupiters, there are multiple further complications to the atmospheric energy balance. In the day-side atmosphere of these planets, temperatures are high enough for thermal dissociation of molecular hydrogen, H_2, into atomic hydrogen, H. This dissociation reaction is endothermic, and therefore removes energy from the day-side atmosphere. The dissociated hydrogen can then be advected onto the night-side by the equatorial jet, where it recombines due to the much colder temperatures (Bell & Cowan 2018; Komacek & Tan 2018; Roth et al. 2021). This recombination reaction is exothermic, and deposits energy into the night-side atmosphere. Overall this process removes energy from the day-side atmosphere and redistribute it into the night-side, and if this energy source/sink is large enough, it will affect the mean temperature state of the atmosphere.

This can affect both emission spectroscopy, producing lower than expected thermal emission from the day-side atmosphere, and transit photometry, as these measurements rely on the relative day-night temperature contrast. The impact of this effect on observable features

has been modelled in numerous studies (Bell & Cowan 2018; Komacek & Tan 2018; Roth et al. 2021). However, the effects of the H2 dissociation are greatly lessened in the presence of TiO/VO, which are likely to be present in the atmosphere at these high temperatures.

Additionally, magnetohydrodynamic drag (discussed in Section 2.5.2) will also have significant implications on the energy balance in hot and ultra-hot Jupiters. Heat generated through Ohmic dissipation can be deposited into the deep layers, thus changing the thermal properties of the atmosphere, disrupting the dynamic flows and altering circulation patterns (Batygin et al. 2013; Beltz et al. 2022; Koll & Komacek 2018; Menou 2012; Perna et al. 2010a; Rauscher & Menou 2013; Rogers 2017; Rogers & Komacek 2014; Rogers & Showman 2014). If this Ohmic dissipation is responsible for radius inflation observed in the population, this could provide a correlation between the hotspot offset and radius inflation and provide a observational test linking exoplanet interiors and atmospheres (Menou 2012). However, Rogers (2017); Rogers & Komacek (2014); Rogers & Showman (2014) use 3D anelastic equations to model magnetic coupling to the atmosphere and show that Ohmic dissipation is not strong enough to explain radius inflation observed in the population. Additionally, Menou (2012) suggests that temperature inversions in the upper atmosphere could result from Ohmic heating even without the presence of strong optical absorbers. As mentioned in Section 2.5.2, this magnetic drag is only significant at temperatures above $\sim$1400K, and is therefore unlikely to affect the entire hot Jupiter population (Beltz et al. 2022; Menou 2012; Rogers 2017; Rogers & Komacek 2014).

One of the most complex complications to the energy balance results from the formation of clouds, which have been shown capable of drastically changing the observable features of hot Jupiter atmospheres (Komacek et al. 2022a; Parmentier et al. 2021). Hot Jupiters are expected to have a thick layer of condensate clouds in their night-side hemisphere. Although (as mentioned in Section 2.2) the flat trend in night-side temperature with equilibrium temperature that has been observed in the population (Beatty et al. 2019; Bell et al. 2021; Keating et al. 2019) has been shown to be a consequence of the strong dependence between radiative timescale and equilibrium temperature (Parmentier et al. 2021), night-side clouds reduce the outgoing longwave radiation and therefore reduce the temperature to lower than expected values (Parmentier et al. 2021). However, this flat trend in night-side temperature breaks in the ultra-hot Jupiter regime (Komacek et al. 2022a; Parmentier et al. 2021; Roman et al. 2021), where it is possible that uniform night-side clouds may dissipate and become patchy. The presence of clouds, particularly if mostly contained on the night-side, can have observable effects on the atmosphere of these planets, increasing the phase curve amplitude and decreasing the phase curve offset. Importantly, the offset is shifted by the hemispherical averaging between cloudy regions with decreased outgoing longwave radiation (OLR) and hot day-side regions, meaning that the hotspot itself is not shifted. This means that the offset does not necessarily track the hottest longitudinal point on the planet (Parmentier et al. 2021). However, in order to understand the role of clouds, one must first understand the cloudless circulation, which will be the topic of the following chapters.

Bibliography

Arcangeli J., et al., 2018, ApJ, 855, L30
Batygin K., Stanley S., Stevenson D. J., 2013, ApJ, 776, 53
Beatty T. G., Madhusudhan N., Tsiaras A., Zhao M., Gilliland R. L., Knutson H. A., Shporer A., Wright J. T., 2017, AJ, 154, 158

Beatty T. G., Marley M. S., Gaudi B. S., Colón K. D., Fortney J. J., Showman A. P., 2019, AJ, 158, 166
Bell T. J., Cowan N. B., 2018, ApJ, 857, L20
Bell T. J., et al., 2021, MNRAS, 504, 3316
Beltz H., Rauscher E., Roman M. T., Guilliat A., 2022, AJ, 163, 35
Burrows A., Hubeny I., Hubbard W. B., Sudarsky D., Fortney J. J., 2004, ApJ, 610, L53
Carone L., et al., 2020, MNRAS, 496, 3582
Charbonneau D., Knutson H. A., Barman T., Allen L. E., Mayor M., Megeath S. T., Queloz D., Udry S., 2008, ApJ, 686, 1341
Charnay B., Meadows V., Misra A., Leconte J., Arney G., 2015, ApJ, 813, L1
Cho J. Y. K., Polichtchouk I., Thrastarson H. T., 2015, MNRAS, 454, 3423
Cont D., et al., 2021, A&A, 651, A33
Cont D., et al., 2022, A&A, 668, A53
Cooper C. S., Showman A. P., 2005, ApJ, 629, L45
Coulombe L.-P., et al., 2023, arXiv e-prints, p. arXiv:2301.08192
Cowan N. B., Agol E., 2011, ApJ, 729, 54
Cowan N. B., Agol E., Charbonneau D., 2007, MNRAS, 379, 641
Crossfield I. J. M., Hansen B. M. S., Harrington J., Cho J. Y. K., Deming D., Menou K., Seager S., 2010, ApJ, 723, 1436
Debras F., Mayne N., Baraffe I., Jaupart E., Mourier P., Laibe G., Goffrey T., Thuburn J., 2020, A&A, 633, A2
Dobbs-Dixon I., Agol E., 2013, MNRAS, 435, 3159
Drummond B., Mayne N. J., Baraffe I., Tremblin P., Manners J., Amundsen D. S., Goyal J., Acreman D., 2018, A&A, 612, A105
Evans T. M., et al., 2016, ApJ, 822, L4
Fortney J. J., Marley M. S., Barnes J. W., 2007, ApJ, 659, 1661
Fortney J. J., Lodders K., Marley M. S., Freedman R. S., 2008, ApJ, 678, 1419
Freedman R. S., Lustig-Yaeger J., Fortney J. J., Lupu R. E., Marley M. S., Lodders K., 2014, ApJS, 214, 25
Fromang S., Leconte J., Heng K., 2016, A&A, 591, A144
Goodman J., 2009, ApJ, 693, 1645
Goody R. M., Yung Y. L., 1989, Atmospheric radiation : theoretical basis
Guillot T., 2010, A&A, 520, A27
Guillot T., Showman A. P., 2002, A&A, 385, 156
Hammond M., Lewis N. T., 2021, Proceedings of the National Academy of Science, 118, e2022705118
Hammond M., Pierrehumbert R. T., 2018, ApJ, 869, 65
Hammond M., Tsai S.-M., Pierrehumbert R. T., 2020, ApJ, 901, 78
Hansen B. M. S., 2008, ApJS, 179, 484
Heng K., 2012, ApJ, 761, L1
Heng K., Showman A. P., 2015, Annual Review of Earth and Planetary Sciences, 43, 509
Heng K., Menou K., Phillipps P. J., 2011a, MNRAS, 413, 2380
Heng K., Frierson D. M. W., Phillipps P. J., 2011b, MNRAS, 418, 2669
Heng K., Morris B. M., Kitzmann D., 2021, arXiv e-prints, p. arXiv:2103.02673
Hindle A. W., Bushby P. J., Rogers T. M., 2019, ApJ, 872, L27
Hindle A. W., Bushby P. J., Rogers T. M., 2021a, ApJ, 916, L8
Hindle A. W., Bushby P. J., Rogers T. M., 2021b, ApJ, 922, 176
Hubeny I., Burrows A., Sudarsky D., 2003, ApJ, 594, 1011
Kalnay E., 2002, Atmospheric Modeling, Data Assimilation and Predictability
Kasper D., Bean J. L., Line M. R., Seifahrt A., Stürmer J., Pino L., Désert J.-M., Brogi M., 2021, ApJ, 921, L18
Kataria T., Showman A. P., Lewis N. K., Fortney J. J., Marley M. S., Freedman R. S., 2013, ApJ, 767, 76
Kataria T., Showman A. P., Fortney J. J., Stevenson K. B., Line M. R., Kreidberg L., Bean J. L., Désert J.-M., 2015, ApJ, 801, 86
Keating D., Cowan N. B., Dang L., 2019, Nature Astronomy, 3, 1092
Knutson H. A., et al., 2007, Nature, 447, 183
Knutson H. A., et al., 2009, ApJ, 690, 822
Koll D. D. B., Komacek T. D., 2018, ApJ, 853, 133
Komacek T. D., Showman A. P., 2016, ApJ, 821, 16
Komacek T. D., Tan X., 2018, Research Notes of the American Astronomical Society, 2, 36
Komacek T. D., Tan X., Gao P., Lee E. K. H., 2022a, ApJ, 934, 79

Komacek T. D., Gao P., Thorngren D. P., May E. M., Tan X., 2022b, ApJ, 941, L40
Kreidberg L., et al., 2014, ApJ, 793, L27
Lacis A. A., Oinas V., 1991, J. Geophys. Res., 96, 9027
Li J., Goodman J., 2010, ApJ, 725, 1146
Line M. R., et al., 2016, AJ, 152, 203
Liu B., Showman A. P., 2013, ApJ, 770, 42
Lothringer J. D., Barman T., Koskinen T., 2018, ApJ, 866, 27
Madhusudhan N., Burrows A., 2012, ApJ, 747, 25
Mansfield M., et al., 2021, Nature Astronomy, 5, 1224
Mayne N. J., et al., 2014, A&A, 561, A1
Menou K., 2012, ApJ, 745, 138
Menou K., Rauscher E., 2009, ApJ, 700, 887
Mihalas D., Mihalas B. W., 1984, Foundations of radiation hydrodynamics
Miller N., Fortney J. J., 2011, ApJ, 736, L29
Mollière P., van Boekel R., Dullemond C., Henning T., Mordasini C., 2015, ApJ, 813, 47
Nugroho S. K., Gibson N. P., de Mooij E. J. W., Herman M. K., Watson C. A., Kawahara H., Merritt S. R., 2020, ApJ, 898, L31
Parmentier V., 2014, PhD thesis, LAGRANGE - Joseph Louis LAGRANGE - Université Nice Sophia Antipolis (UNS); Observatoire de la Côte d'Azur CNRS : UMR7293
Parmentier V., Guillot T., 2014, A&A, 562, A133
Parmentier V., Showman A. P., Lian Y., 2013, A&A, 558, A91
Parmentier V., Guillot T., Fortney J. J., Marley M. S., 2015, A&A, 574, A35
Parmentier V., Fortney J. J., Showman A. P., Morley C., Marley M. S., 2016, ApJ, 828, 22
Parmentier V., et al., 2018, A&A, 617, A110
Parmentier V., Showman A. P., Fortney J. J., 2021, MNRAS, 501, 78
Pelletier S., et al., 2023, arXiv e-prints, p. arXiv:2306.08739
Perez-Becker D., Showman A. P., 2013, ApJ, 776, 134
Perna R., Menou K., Rauscher E., 2010a, ApJ, 719, 1421
Perna R., Menou K., Rauscher E., 2010b, ApJ, 724, 313
Perna R., Heng K., Pont F., 2012, ApJ, 751, 59
Pierrehumbert R. T., Hammond M., 2019, Annual Review of Fluid Mechanics, 51, 275
Piette A. A. A., Madhusudhan N., McKemmish L. K., Gandhi S., Masseron T., Welbanks L., 2020, MNRAS, 496, 3870
Pino L., et al., 2020, ApJ, 894, L27
Powell D., Louden T., Kreidberg L., Zhang X., Gao P., Parmentier V., 2019, ApJ, 887, 170
Prinoth B., et al., 2022, Nature Astronomy, 6, 449
Rauscher E., Menou K., 2012, ApJ, 750, 96
Rauscher E., Menou K., 2013, ApJ, 764, 103
Robinson T. D., Catling D. C., 2012, ApJ, 757, 104
Rogers T. M., 2017, Nature Astronomy, 1, 0131
Rogers T. M., Komacek T. D., 2014, ApJ, 794, 132
Rogers T. M., Showman A. P., 2014, ApJ, 782, L4
Roman M. T., Kempton E. M. R., Rauscher E., Harada C. K., Bean J. L., Stevenson K. B., 2021, ApJ, 908, 101
Roth A., Drummond B., Hébrard E., Tremblin P., Goyal J., Mayne N., 2021, MNRAS, 505, 4515
Roth A., Parmentier V., Hammond M., 2024, MNRAS, 531, 1056
Sardeshmukh P. D., Hoskins B. J., 1988, Journal of the Atmospheric Sciences, 45, 1228
Shapiro R., 1970, Reviews of Geophysics and Space Physics, 8, 359
Showman A. P., Guillot T., 2002, A&A, 385, 166
Showman A. P., Polvani L. M., 2010, Geophys. Res. Lett., 37, L18811
Showman A. P., Polvani L. M., 2011, ApJ, 738, 71
Showman A. P., Cooper C. S., Fortney J. J., Marley M. S., 2008, ApJ, 682, 559
Showman A. P., Fortney J. J., Lian Y., Marley M. S., Freedman R. S., Knutson H. A., Charbonneau D., 2009, ApJ, 699, 564
Showman A. P., Cho J. Y. K., Menou K., 2010, in Seager S., ed., , Exoplanets. pp 471–516, doi:10.48550/arXiv.0911.3170
Showman A. P., Fortney J. J., Lewis N. K., Shabram M., 2013, ApJ, 762, 24

Showman A. P., Lewis N. K., Fortney J. J., 2015, ApJ, 801, 95
Spiegel D. S., Silverio K., Burrows A., 2009, ApJ, 699, 1487
Tan X., Komacek T., 2019, in AAS/Division for Extreme Solar Systems Abstracts. p. 326.03
Thorngren D., Gao P., Fortney J. J., 2019, ApJ, 884, L6
Thrastarson H. T., Cho J. Y.-K., 2010, ApJ, 716, 144
Tsai S.-M., Dobbs-Dixon I., Gu P.-G., 2014, ApJ, 793, 141
White A. A., Staniforth A., Wood N., 2008, Quarterly Journal of the Royal Meteorological Society, 134, 261
Yan F., et al., 2020, A&A, 640, L5
Yan F., et al., 2022, A&A, 659, A7
Zhang M., et al., 2018, AJ, 155, 83

Chapter 3

Creating a Large GCM Model Grid

The material in this chapter is based on Roth et al. (2024):
– Roth A., Parmentier V., Hammond M., 2024, MNRAS, 531, 1056

3.1 Introduction

To characterize the physical, micro-physical and chemical structure of hot Jupiter atmospheres, a hierarchy of 1D, 2D and 3D models have been used. Models in lower dimensions are generally much more computationally efficient. These models often couple a treatment for radiative transfer with advanced chemical networks (e.g. Tsai et al. (2017); Venot et al. (2019)), to determine self consistent chemical abundances within the atmosphere (Baeyens et al. 2021; Goyal et al. 2020; Tsai et al. 2021). 3D global circulation models (Arcangeli et al. 2019; Charnay et al. 2015a,b; Dobbs-Dixon & Agol 2013; Drummond et al. 2018c; Kataria et al. 2015; Kreidberg et al. 2018; Lee et al. 2016, 2017; Line et al. 2014; Lines et al. 2018, 2019; Mayne et al. 2014; Parmentier et al. 2018, 2021; Showman et al. 2009; Steinrueck et al. 2019) are able to capture the full longitudinal and latitudinal complexities of dynamical modelling for planets with such disparate hemispherical conditions, but are very computationally expensive and offer limited chemical complexity in comparison. As mentioned in Chapter 2, these models have been used to explain the high speed, super-rotating, jets caused by interactions between the atmospheric flow and standing waves (Hammond & Lewis 2021; Showman & Polvani 2011; Tsai et al. 2014), and eastward shifts of the highest temperature point observed in many hot Jupiters. There are clear merits to using 3D models for hot Jupiter atmospheres. These models show that the dynamics in hot Jupiters are indeed three-dimensional, mid-latitude Rossby gyres and super-rotating jets, for example, which cannot be captured properly in 1D or 2D models using parameterisations. Additionally, 3D models are the only way to predict day-to-night heat transport from first principles, rather than selecting an a-priori input parameter.

As discussed in detail throughout Chapter 1, in order to both improve characterisation of individual hot Jupiters and clarify which formation mechanisms are responsible for the observed population, we must first gain an understanding of how their atmospheres are affected by planetary parameters. 1D and 2D radiative-convective model grids have been widely used to better understand hot Jupiter atmospheres (Baeyens et al. 2021, 2022; Baxter et al. 2021; Goyal et al. 2020, 2021; Mansfield et al. 2021; Molaverdikhani et al. 2019). A number of 3D GCM grids have also been used to identify the importance of planetary parameters in shaping the atmospheric circulation in hot Jupiters. The day-to-night temperature contrast, location of photosphere and longitudinal position of the atmospheric hot spot have all be shown to depend on the intrinsic properties of a planet Drummond et al. (2018a); Kataria et al. (2015, 2016); Komacek & Showman (2016); Komacek et al. (2017, 2022); Perna et al. (2012); Showman et al. (2009, 2015). However, as discussed in Chapter 1, the observed hot Jupiter population spans a wide parameter space, varying by orders of magnitude in instellation, surface gravity and rotation period. Parameters such as atmospheric metallicity and mechanisms causing dynamic drag are also largely unconstrained. In conjunction with

the high cost of running GCM models, this means that until now no study has utilised non-grey 3D modelling to investigate the impact of systematically and jointly varying all of these intrinsic planetary properties on an atmosphere, which is the ultimate goal for this study.

As such, we begin this chapter by outlining important results from 3D modelling studies in more detail (Section 3.2). We then describe the SPARC/MiTgcm in detail (Section 3.3), including treatment for dynamics, radiative transfer, dissipation schemes and limitations of the model. We then move on to describing the creation of a large GCM model grid (Section 3.4). This includes a brief discussion on each of the free parameters, why certain values have been selected and how we expect them to affect an atmosphere.

3.2 Important Results from 3D Modelling Studies

The first 3D global circulation model was applied to hot Jupiters in (Showman & Guillot 2002), using the EPIC (Explicit Planetary Isentropic Coordinate) model (Dowling et al. 1998). Showman & Guillot (2002) were the first to identify the strong day-night temperature contrast at the photosphere, and concluded that this would drive strong equatorial rotation in the form of a super-rotating jet, propagating eastwards due to force balancing arguments. The numerical simulations showed that the day-night temperature distribution would be highly dependent on the dynamics, which are determined by the competition between radiative cooling and heat transport through the winds and planetary scale standing waves.

As spectroscopic and photo-metric data from the Spitzer and Hubble space telescopes began to provide spatially resolved temperature constraints and confirmed the presence of strong winds and super-rotating jets (Charbonneau et al. 2008; Cowan et al. 2007; Crossfield et al. 2010; Knutson et al. 2007, 2009), many 3D atmospheric models began to be published (Cooper & Showman 2005, 2006; Dobbs-Dixon & Lin 2008; Dobbs-Dixon et al. 2010; Heng et al. 2011; Lewis et al. 2010; Menou & Rauscher 2009; Perna et al. 2010; Rauscher & Menou 2010; Showman & Guillot 2002; Showman et al. 2008, 2009; Thrastarson & Cho 2010). These models were also applied to specific hot Jupiter targets, such as HD 209458 b (Cooper & Showman 2005, 2006; Dobbs-Dixon et al. 2010; Showman et al. 2008, 2009), HD 189733 b (Showman et al. 2008, 2009), and even hot Neptunes such as GJ 436 b (Lewis et al. 2010). All these models found largely similar results, large day-night temperature contrast and dynamics dominated by equatorial super-rotation, with an atmospheric hotspot shifted eastwards of the substellar point.

The first GCM to incorporate non-grey radiative transfer modelling was the SPARC/MiTgcm (Showman et al. 2009). A number of models later went on to adopt this method and were applied to specific targets (e.g Charnay et al. (2015a,b); Dobbs-Dixon & Agol (2013); Drummond et al. (2018c); Kataria et al. (2015); Kreidberg et al. (2018); Lee et al. (2016, 2017); Lewis et al. (2014, 2017); Lines et al. (2018, 2019); Mayne et al. (2014); Parmentier et al. (2018); Steinrueck et al. (2019); Venot et al. (2020)). However, many were found to overestimate the eastwards shift of the hotspot and underestimate the phase curve amplitude (Kataria et al. 2015; Lewis et al. 2017; Parmentier & Crossfield 2018; Parmentier et al. 2021; Zhang et al. 2018), leading to night-sides being modelled as hotter than found in observation (Keating et al. 2019). Through modelling efforts many theories for this discrepancy were put forward, such as higher than expected metallicities (Drummond et al. 2018a; Kataria et al. 2015; Showman et al. 2009), disequilibrium chemistry (Baxter et al. 2021; Knutson et al. 2012; Mendonça et al. 2018b), and magnetic drag disrupting the circulation (Komacek et al. 2017; Perna et al.

2010; Rauscher & Menou 2013; Showman et al. 2013). Both disequilibrium chemistry and higher than expected metallicity were later shown to have an insufficiently large effect to explain the observed data (Drummond et al. 2018a; Kataria et al. 2015; Mendonça et al. 2018b; Steinrueck et al. 2019).

As discussed throughout Chapter 2, magnetic drag in planets with equilibrium temperatures above ∼1400K has been shown capable of modifying the thermo-dynamical structure in hot Jupiters, altering circulation patterns and affecting the atmospheric energy balance (Batygin et al. 2013; Beltz et al. 2022; Koll & Komacek 2018; Menou 2012; Perna et al. 2010; Rauscher & Menou 2013; Rogers 2017; Rogers & Komacek 2014; Rogers & Showman 2014). However, this does not explain the discrepancies between modelling and observation at the cooler end of the hot Jupiter parameter space.

A more recently proposed explanation is that of night-side clouds reducing the thermal radiation (Beatty et al. 2019; Kataria et al. 2015; Keating et al. 2019; Lines et al. 2019; Mendonça et al. 2018b; Oreshenko et al. 2016; Parmentier et al. 2021; Showman et al. 2009). The presence of night-side clouds was shown in Parmentier et al. (2021) to significantly increase the amplitude and offset of planetary phase curves for hot Jupiters. This result also implies that phase curve offset does not necessarily track the planetary hot spot offset when clouds are present.

There are now many GCMs based on different dynamical cores and radiative transfer schemes i.e THOR (Mendonça et al. 2016), the Unified Model (UM) (Mayne et al. 2014), EXO-FMS (Lee et al. 2021), and SPARC/MiTgcm (Showman et al. 2009) just to name a few. These GCMs have been used to show how the atmospheres of hot Jupiters depend on an array of other parameters. Day-to-night temperature contrast has been shown to depend heavily on irradiation received, rotation period and atmospheric composition (Kataria et al. 2016; Komacek & Showman 2016; Komacek et al. 2017; Perna et al. 2012; Showman et al. 2015). Super-solar metallicities are also found to increase the day-to-night temperature contrast at the photosphere and reduce eastward hot-spot offset (Drummond et al. 2018a; Kataria et al. 2015, 2016; Showman et al. 2009). Additionally, Kataria et al. (2016); Komacek et al. (2022) show how surface gravity plays an important role when determining the photospheric pressure in the atmosphere.

3.3 The SPARC/MiTgcm

In this study, we use the non-grey SPARC/MITgcm global circulation model (Showman et al. 2009), which has been widely applied to modelling the atmospheric dynamics for hot, Jupiter sized planets in tidally locked orbits (Kataria et al. 2015, 2016; Lewis et al. 2017; Parmentier et al. 2013, 2016, 2018, 2021; Showman et al. 2009, 2015; Steinrueck et al. 2019). This model couples the dynamical code from the MITgcm (Adcroft et al. 2004), with the plane-parallel radiative transfer code of Marley & McKay (1999). The GCM calculates the dynamical structure in an atmosphere by solving the four hydrostatic primitive dynamical equations, which can be derived from the full set of dynamical equations (see Kalnay (2002) and Section 2.4) on a cubed sphere grid. To do this the model makes four main assumptions about an atmosphere (Mayne et al. 2013; Parmentier 2014): The primitive set from Table 2.1 plus the hydrostatic approximation.

3.3.1 Radiative Transfer with EGP

Within the SPARC/MiTgcm, radiative transfer is handled via the plane-parallel radiative transfer code of Marley & McKay (1999). Although this code was first developed to study Titan's atmosphere (McKay et al. 1989), it has previously been used to study both hot Jupiters (Fortney et al. 2005, 2008; Parmentier et al. 2021), and ultra-hot Jupiters (Parmentier et al. 2018). This code uses the two-stream approximation method of Toon et al. (1989) to solve the radiative transfer equation (2.5) in local thermodynamic equilibrium for all frequencies, ν, and directions, μ (Chandrasekhar 1960).

The non-grey opacities are modelled through the correlated-k distribution method (Goody & Yung 1989; Lacis & Oinas 1991), as described in Section 2.3. The GCM uses 11 spectral bins of 8 k-coefficients (Kataria et al. 2013), and the spectral calculation use 196 bins of 8 k-coefficients. This is possible as the Planck function can be approximated to be constant over certain spectral intervals, meaning the exact position of spectral lines within these intervals is unimportant. For the opacities, we use those detailed in Freedman et al. (2008), including updates from Freedman et al. (2014). For the stellar spectra we use the NextGen stellar models (Hauschildt et al. 1999).

During this study we will use EGP in two formats. For the computation of secondary eclipse spectra, the incident angle of stellar irradiation, μ, is calculated as coming from a given direction, hence automatically accounting for limb-darkening effects (Fortney et al. 2006; Parmentier et al. 2016, 2021). For calculations where the total flux emitted from the planet is required rather than the flux emitted in a specific direction, in bond albedo calculations for example, we use a constant value of of $\mu = 2/3$. This format means the total flux coming from each individual column is calculated whilst assuming a mean value of μ, which provides a good estimation of the integration over μ calculation that would normally need to be done for each column.

3.3.2 Geometric & Bond Albedos

By outputting the integrated reflected flux from EGP we can also compute values for both geometric and bond albedo within the grid. The bond albedo is calculated using the 'constant μ' version of EGP, whilst the geometric albedo is calculated suing the 'variable μ' format.

In order to test that we recover a reasonable result for both the geometric and bond albedos, we have compared them with analytical trends. The left panel of Figure 3.1 shows a comparison between the geometric albedo from EGP as it varies with the single scattering alebdo vs the analytical predictions from Madhusudhan & Burrows (2012). The right panel of Figure 3.1 shows a comparison between the bond albedo from EGP as it varies with the single scattering albedo vs the analytical predictions from Heng et al. (2021). As we can see, the values from EGP match the analytical very well in both cases.

3.3.3 Dissipation

As discussed in Chapter 2, dissipation within the GCM can be added through the $D_{\mathbf{v}}$ and D_T terms from Equations 2.18 and 2.21 respectively. Numerical dissipation within our GCM is done via a 4th order Shapiro filter (Shapiro 1970), applied to the temperature and velocity fields, which dissipates kinetic energy by damping the highest wavenumber component of

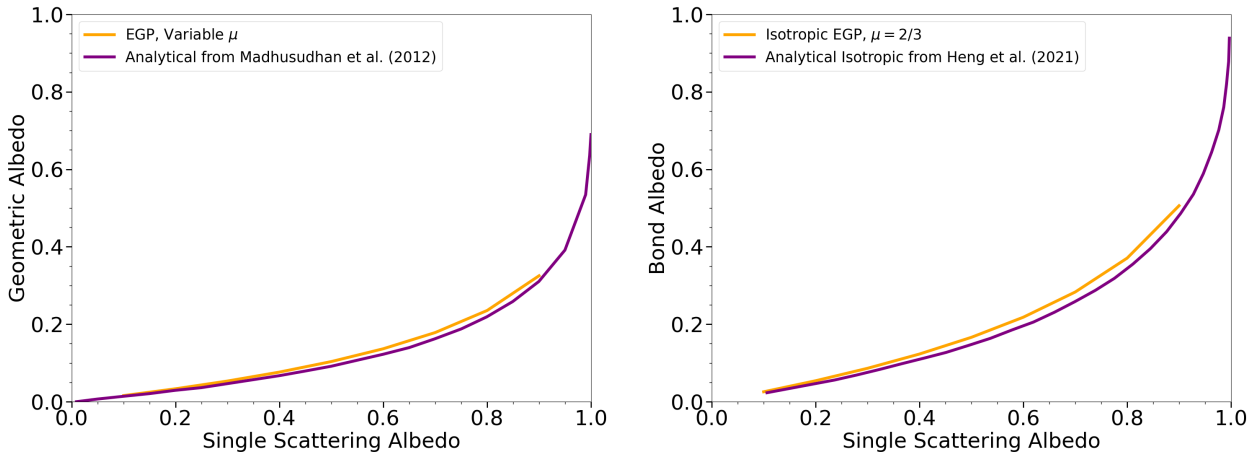


Figure 3.1: Left Panel: Shows a comparison between the geometric albedo vs single scattering albedo for an isothermal model run through EGP and the analytical predictions of Madhusudhan & Burrows (2012). **Right Panel:** Shows a comparison between the bond albedo vs single scattering albedo for an isothermal model run through EGP and the analytical predictions of Heng et al. (2021)

the flow in the GCM, effectively smoothing the horizontal gradients between grid points. From (Koll & Komacek 2018) (see their equation 5), the rate at which numerical drag dissipates kinetic energy is:

$$W_{\text{num}} = \frac{U^2 p}{\tau_{shap} g}, \tag{3.1}$$

where U is the wind speed, p the pressure, g the gravity and τ_{shap} is the damping timescale of the Shapiro filter. If τ here is fixed and we ignore the $\frac{p}{g}$ factor, U^2 and therefore the numerical dissipation should be proportional to the kinetic energy. Alternatively, τ can be scaled depending on the grid spacing within the GCM, Δx, as $\tau \sim \Delta x / U$. This makes the final numerical dissipation timescale:

$$W_{\text{num}} = \frac{U^3 p}{\Delta x g}. \tag{3.2}$$

Dissipation through non-numerical drag, i.e that of Ohmic dissipation or Kelvin-Helmholtz instabilities, can be represented as Rayleigh drag through the dissipation terms. In this case the drag timescale, τ_{drag}, is related to the dissipative term as:

$$\tau_{drag} = -\frac{\mathbf{v}}{D_{\mathbf{v}}}. \tag{3.3}$$

If we assume that all kinetic energy is *locally* dissipated into heat we then get (Parmentier 2014):

$$D_T = \frac{\mathbf{v}^2}{2 c_p \tau_{drag}} \tag{3.4}$$

However, this assumption of local dissipation of kinetic energy is not always true. For instance, as we discussed in Chapter 2, in the case of magnetic drag, kinetic energy is con-

verted into electrical currents and the resulting Ohmic dissipation can occur in different areas of the atmosphere. (Batygin et al. 2013; Beltz et al. 2022; Koll & Komacek 2018; Menou 2012; Perna et al. 2010; Rauscher & Menou 2013; Rogers 2017; Rogers & Komacek 2014; Rogers & Showman 2014).

3.3.4 Model Limitations

Due to the complexity of atmospheric modelling there are certain atmospheric effects that are not included in the SPARC/MiTgcm. Firstly, the effects of hydrogen dissociation and recombination, discussed in 2.7, are not included in the model. This could potentially lead to over-predictions of the day-side and under-predictions of the night-side temperature. As a result, predicted phase curve amplitudes may be too large.

Additionally, the SPARC/MiTgcm does not include any MHD effects on the atmosphere that we have discussed in Sections 2.5.2 and 2.7. 3D and shallow water MHD models have been used to show how these effects could cause time variable wind speeds in hot Jupiter atmospheres, potentially leading to time variability, and westwards shifts, in the hotspot and therefore in the observed phase curves (Rogers 2017; Rogers & Komacek 2014; Rogers & Showman 2014). This happens as a strong magnetic field can disrupt the mid-to-high latitude geostrophic circulation, which normally drives the eastwards energy transfer. Lorentz forces can then drive the hotspot westward (Hindle et al. 2021a). This theory has been applied to select hot Jupiter data sets in order to constrain the magnetic field strength required to cause westward hotspot shifts (Hindle et al. 2021b), and to identify potential targets displaying the westward shifts in future observations (Hindle et al. 2019). However, to date these MHD models have not been coupled with any rigorous treatment for radiative transfer within a planet's atmosphere, which could significantly alter predictions and is a particularly interesting avenue of potential future research on the topic.

For this study, we also choose to model cloudless atmospheres. Clouds, particularly if mostly contained on the night-side, have been shown capable of drastically changing the observable features of hot Jupiter atmospheres (Parmentier et al. 2021) (as discussed in Section 2.7). However, estimating the effect of clouds, MHD and hydrogen dissociation on the population of planets requires us to first estimate the effect of all planet parameters on the population, without the involvement of these effects, which is the topic of the following chapter.

3.4 Creating a Large GCM Model Grid

For our grid, all models assume an internal heat flux corresponding to a temperature of 100K. Although it has been shown that internal heat flux probably increases with equilibrium temperature (Thorngren et al. 2019), the effect of the internal heat on the wind and thermal structure at the photosphere is not yet fully understood (Komacek et al. 2022). We therefore leave such study for future work and choose to keep the internal heat constant here. All of our models also use a fixed planetary radius of $1.3R_j$, where R_j is the equatorial radius of Jupiter at the 1 bar pressure level ($71,492km$). Despite the radii of hot Jupiters varying by around a factor of two across the population, this was done in order to minimize the number of parameter dimensions within this study. We assume a specific heat capacity of the atmosphere $C_p = 1.3 \times 10^4 Jkg^1K^{-1}$, with a specific heat capacity ratio of $\gamma = 1 + 2/7$

and a mean molecular weight of $\mu = 2.3mH$ - which is valid for the H_2-dominated atmospheres we are simulating. Other prescribed model parameters are changed on a model to model basis, including: equilibrium temperature, atmospheric metallicity, rotation period (changed with stellar parameters following Kepler's 3rd law), surface gravity, Rayleigh drag timescale, and the inclusion of certain molecular species, see Section 3.4 for details.

In the drag-free models, we purposely do not add a Rayleigh drag parameterisation as has been done in the past by e.g. Komacek & Showman (2016) and most dissipation is due to the 4th order Shapiro filter applied to the temperature and velocity fields, which dissipates kinetic energy by smoothing the horizontal gradients between grid points (Koll & Komacek 2018). We use a fixed dissipation timescale of τ_{shap}=50s for all models, meaning that the numerical dissipation is proportional to the kinetic energy of each model (Koll & Komacek 2018). This provides us with the least dissipative models that can be obtained at the spatial resolution we are using, while being numerically stable.

We additionally run a smaller grid across a range of effective prescribed Rayleigh drag timescales. For this drag grid, we no longer vary the surface gravity and the sampling of equilibrium temperatures is reduced compared to the drag-free grid. Details on the drag timescales selected and the exact model parameters used in the drag grid can be found in Section 3.5.6.

We use an initial pressure-temperature profile, at all grid points, from the non-grey analytical model of Parmentier & Guillot (2014) (which is itself based on the semi-grey analytical model of Guillot (2010)). The atmosphere was allowed to evolve for 150 days, 300 days for the 1000-1200K models, with all quantities being averaged over the final 50 days for the output. This is enough integration time for a pseudo-steady state to be reached at the photospheric pressure level (Showman et al. 2009), although not enough to reach a fully converged state which would take several thousand days (Mayne et al. 2017; Mendonça 2020; Mendonça et al. 2018a; Wang & Wordsworth 2020). As shown in Section 3.4.3, running for much longer times does not significantly change the observable properties of the planets we are interested in. Given that the interactions between the deep interior and upper atmosphere are still not fully understood for hot Jupiter exoplanets, we are assuming that the deep layers are quiet as they don't have time to develop winds, giving us the same solution as a photosphere equilibriated with a quiet deep interior and meaning that our choice of deep boundary condition has no effect on the final result. The models were run at a horizontal resolution of C32, which corresponds to an approximate resolution of 128 longitudinal and 64 latitudinal cells. The atmosphere is split into 53 pressure levels, between 2×10^{-6} - 200 bars. For low metallicity models the time-step was set to 25 s, which was decreased to 12.5 s at higher metallicities in order to stabilize the simulations. Running the GCM for 300 days with a time step of 25 s, or for 150 days with a 12.5 s time step, requires roughly 48 hours on 48 CPU cores. This means that each model requires between ∼1100-2300 CPU hours depending on the parameters. Our full grid of 516 models (345 drag-free and 171 drag models), therefore, required ∼1 million CPUh to run.

3.4.1 Spectral Calculations for the Grid

To additionally speed up post-processing of the grid, the temperature structure from the models was recalculated with a lower spatial resolution of C16, equivalent to 64 longitude and 32 latitude cells. This is done as an insignificant portion of the spectral information is lost when decreasing the spatial resolution in this manner, whilst a significant amount of

time is saved in the calculations (Robbins-Blanch et al. 2022). The effect that reducing the spacial resolution in this way has on the radiance can be seen Figure 3.2

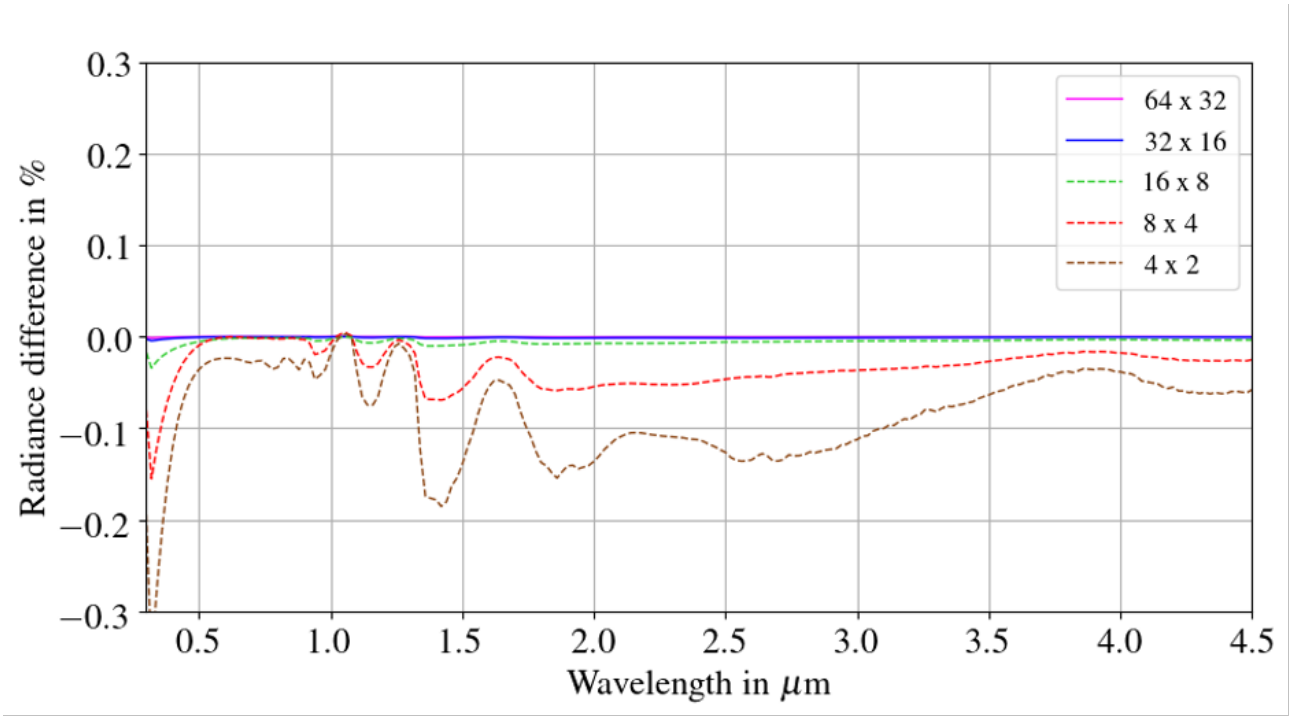


Figure 3.2: This figure shows the percentage difference in output radiance, over the HST and JWST main observing wavelengths, after post-processing a GCM model with different spacial resolutions of pressure-temperature information, with respect to the 128x62 case. The different spacial resolutions are seperated by color. Resolutions of 64x32 and 32x16 are displayed in solid lines whilst all lower resolutions are all displayed with dashed lines. All credit for this image goes to Victor Trees, Vivien Parmentier's previous DPhil student.

3.4.2 Chemistry

In our models we assume local chemical equilibrium with local rain-out of condensate materials (Visscher et al. 2006, 2010), and a solar C/O ratio of 0.46 (Lodders et al. 2009). Both molecular and atomic chemical abundances are calculated using a version of the NASA CEA Gibbs minimisation scheme (Gordon & McBride 1994), assuming solar elemental abundances and local chemical equilibrium, developed to study gas and condensate equilibrium chemistry under different atmospheric conditions (Kataria et al. 2015; Marley et al. 2017; Moses et al. 2013; Parmentier et al. 2018; Skemer et al. 2016; Wakeford et al. 2017). Chemical equilibrium is far from a safe assumption in hot Jupiter atmospheres, where the extreme conditions cause effects such as photochemistry and chemical quenching which smooths out the very large day to night chemical gradients (Cooper & Showman 2006; Drummond et al. 2018b; Mendonça et al. 2018b; Steinrueck et al. 2019). However, although non-equilibrium abundances (through quenching) can change the overall heat transport and the observables in specific band-passes (i.e temperature changes of ∼100-200K can lead to a ∼20% change in the spectra (Steinrueck et al. 2019)), the effects of disequilibrium chemistry on the overall atmospheric energy balance is small compared to the population trend (Drummond et al. 2016;

Steinrueck et al. 2019). The approximation of chemical equilibrium relies on the assumption that the chemical reaction timescales are much shorter than the dynamical timescales. This approximation therefore becomes better for the hottest planets, as chemical reaction rates are generally proportional to temperature.

For the models with increased metallicity, we multiply the elemental abundances of all elements apart from hydrogen and helium by the metallicity factor and adjust the H/He abundance to ensure that the sum of all mixing ratios is equal to 1. To the first order, atmospheric metallicity increases the abundance of all molecules present in the atmosphere, overall increasing the opacity of the atmosphere. At second order, atmospheric metallicity can change the balance between molecules in chemical equilibrium and, for example, favour CO instead of CH_4 in cool planets (JWST Transiting Exoplanet Community Early Release Science Team et al. 2023). Additionally, we include models both with and without TiO and VO in the grid, more details on these species can be found in Section 3.5.5.

3.4.3 Model Convergence

As mentioned in Section 3.4, as our models only evolve for between 150-300 days (depending on the equilibrium temperature) they are not in a fully converged state. The primary cause for incomplete model convergence is parameter dependant flux transformed into kinetic energy to drive winds in the model. To fully converge the deep atmosphere, i.e for the global kinetic energy of the simulation to be converged with the instellation flux, would take potentially tens of thousands of CPU hours (see Figure 3 in Mendonça (2020)), making the costs and time for running the grid completely unreasonable and seemingly unnecessary. However, as the radiative timescale at the photosphere is much smaller than that of the deep atmosphere, the photospheric level will converge substantially faster. For this study, as we are primarily interested in the trends due to planetary parameters rather than specific atmospheric characterisation, it is important that these quantities have reached a steady state within our model run time rather than 'full convergence' being achieved. To test this, we allow models at four equilibrium temperatures to evolve for 900 days. We then sample the redistribution factor (see Section 4.3) at a number of different time steps to check if it has achieved steady state. This can be seen in Figure 3.3. From this we find that initially the planet rapidly warms over a short period of time. This is due to the radiative timescales being much shorter than the dynamical timescales at the photosphere. Heat redistribution then starts to affect the atmospheric state, moving the heat away from the day-side atmosphere. The redistribution factor is found to have a negligible change after the 150 day mark, suggesting that we have in fact reached a pseudo steady-state at the photospheric pressure level in these models. In addition to flux losses through unconverged deep layers, a small portion of flux is systematically lost due to truncation of the stellar spectrum.

3.5 Grid Parameters

In the grid, we have six free planetary parameters which are varied: equilibrium temperature ($T_{\rm eq}$), atmospheric metallicity (Log(M/H)), rotation period (determined via the stellar parameters), surface gravity (Log(g)), Rayleigh drag timescale and the presence of strongly absorbing chemicals TiO and VO. We separate the combinations of these parameters into two separate grids for comparison purposes, a drag-free model grid with $\tau_{drag} = \infty$ and a

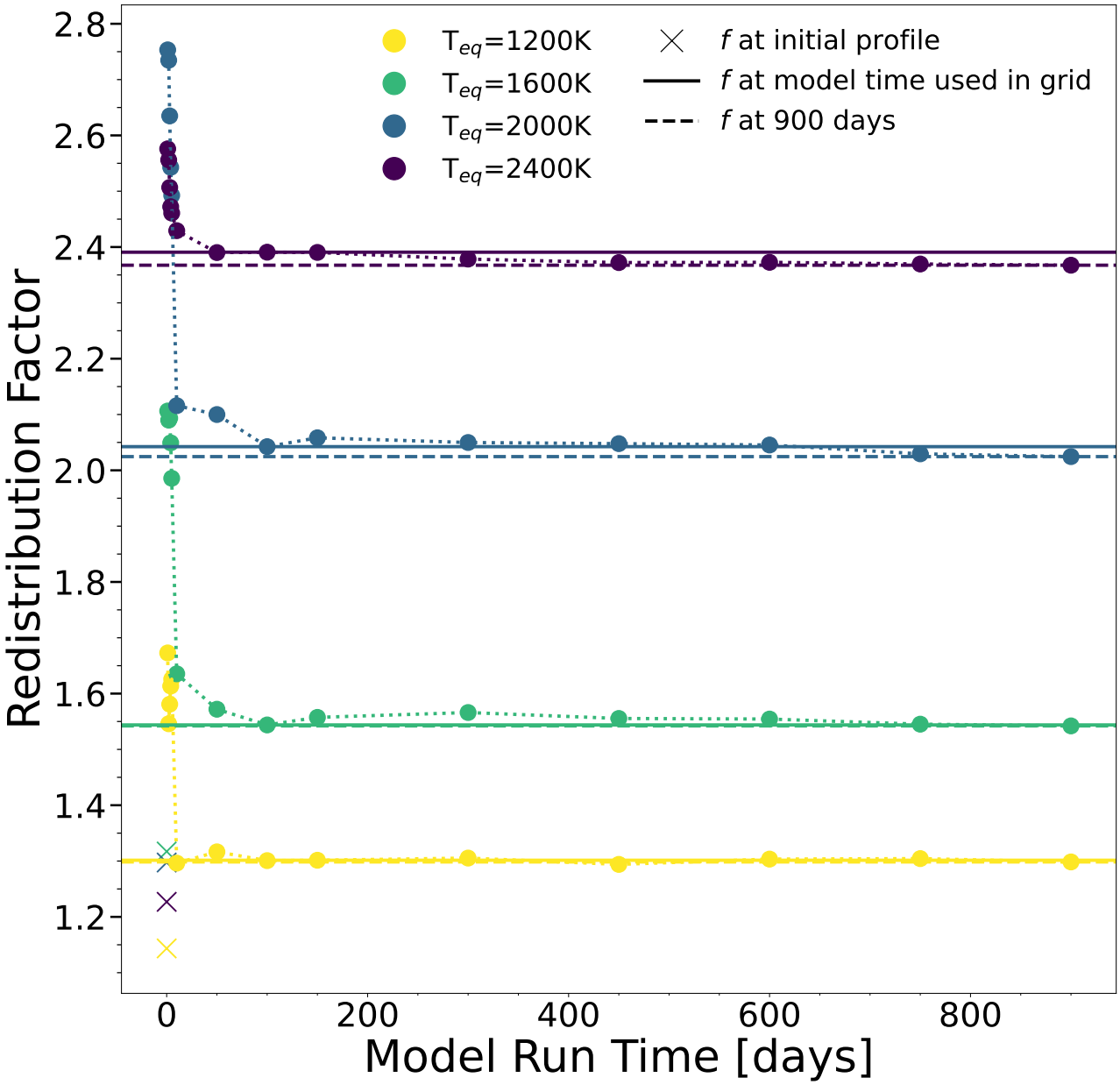


Figure 3.3: Redistribution factor as a function of model run time for a range of equilibrium temperatures in the model grid. The dashed lines show the value after 900 days and the solid lines the value at the integration time within the grid (150 days for models with equilibrium temperatures above 1400K and 300 days for models below). The points marked with a cross show the redistribution factor of the initial profile.

grid with prescribed Rayleigh drag timescales. The full range of values used for the drag-free grid can be seen in Table 3.1. The values used in the drag model grid can be seen in Table 3.3. Any other necessary model parameters (i.e C/O ratio, planet radius, internal temperature) remain consistent across the grid. The values used for these fixed parameters can be seen in Section 3.4. Combinations of these free parameters were used to run a total of 345 drag-free simulations, with an additional 171 simulations including finite drag. The extent of our model grid when compared to the observed exoplanet population can be seen in Figure 3.4. From this, we note that the population scatter is well covered within the grid,

with the vast majority of planets within our equilibrium temperature range having a closely analogous model.

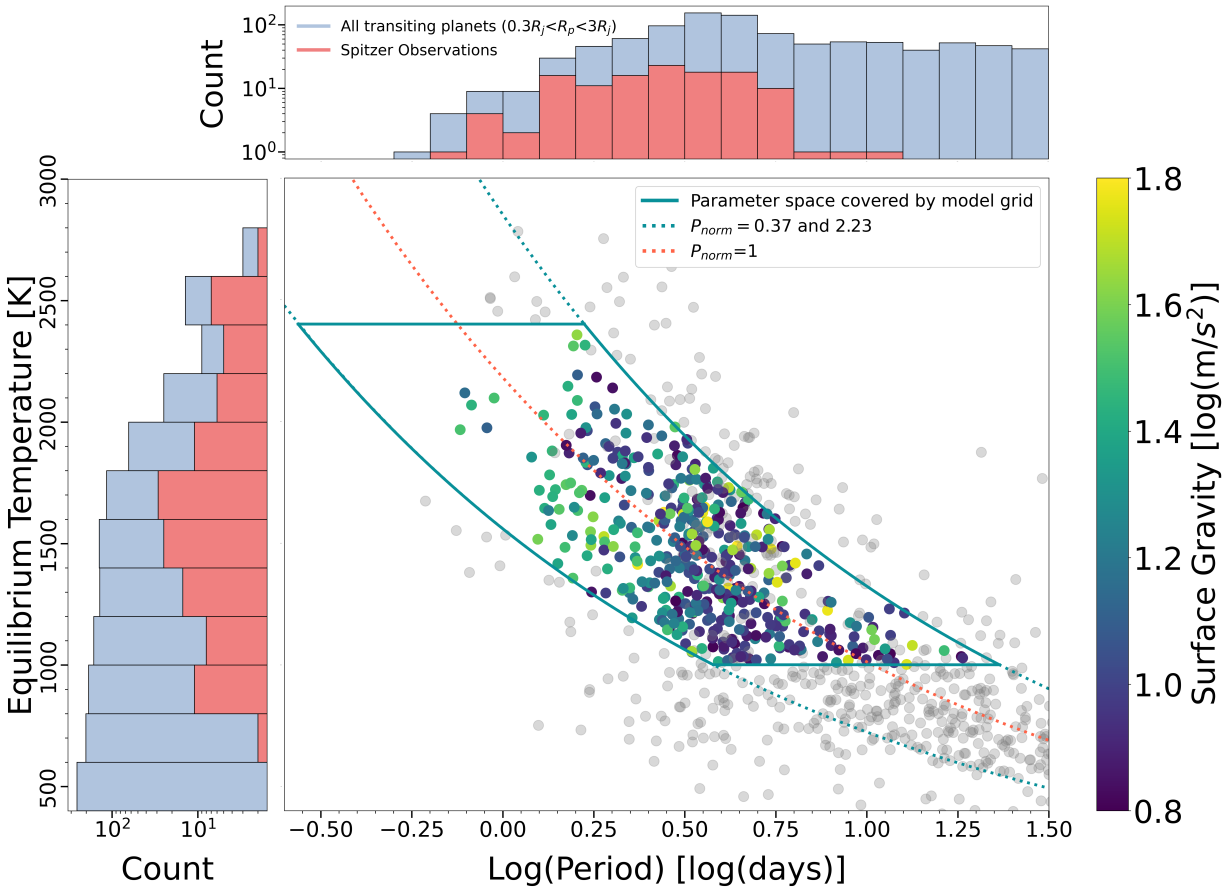


Figure 3.4: Distribution of known exoplanets ($0.3 < R_p < 3R_j$) with equilibrium temperature vs orbital period. Planets that fall within our grid boundaries, as described in Sections 3.5.1 and 3.5.2, are colour-coded by their gravity. Planets that fall outside our grid boundaries are left grey. The blue dashed lines on the scatter plot represent the minimum and maximum values of constant period multiplicity for our model grid, as defined in Section 3.4. The outlined solid blue shape shows the area that is covered by our model grid in the equilibrium temperature vs log(period) space. The histogram to the left of the scatter plot displays the distribution of planets in the equilibrium temperature space (blue bars) when compared to the distribution of the measured Spitzer population from Deming et al. (2023) (red bars). The histogram above the scatter plot shows the same population level comparison for the period distribution.

3.5.1 Equilibrium Temperature

The equilibrium temperature, $T_{\rm eq}$, is a measure of the stellar irradiation received by an atmosphere. It is defined as the effective temperature that a homogeneous planet with zero albedo would have. This temperature is incredibly important for the atmospheric structure, as it affects the dynamical, radiative and chemical timescales significantly. In our grid we have selected a wide range of equilibrium temperatures, from 1000K (which is on the lower end for hot Jupiter exoplanets) to 2400K. We sample every 200K giving us eight values. We

Table 3.1: Free parameters used in the drag-free 3D GCM grid.

T_{eq} [K]	Log(M/H)	Normalised Period Multiplier	Log(g[SI])	Molecular Species
1400-2400 (200K intervals)	0.0, 0.7, 1.5	0.37, 1, 2.23	0.8, 1.3, 1.8	C_2H_2, C_2H_4, C_2H_6, CaH, CH_4, CO, CO_2, CrH, FeH, H_2O, H_2S, HCN, K, Li, LiCl, MgH, N_2, Na, NH_3, OCS, PH_3, SiO, TiO, VO
1000-2400 (200K intervals)	″	″	″	No TiO, VO

don't use temperatures higher than 2400K as above this molecular dissociation (Parmentier et al. 2018), transport of heat through H2 dissociation (Bell & Cowan 2018; Komacek & Tan 2018; Roth et al. 2021), and atomic iron opacities (Lothringer et al. 2018) start to cause significant complications to the planetary energy balance. Magnetic drag may also start to disrupt the equatorial jet (Beltz et al. 2022; Rogers 2017; Rogers & Komacek 2014). On the other end, we don't use temperatures lower than 1000K as for these planets the assumption of tidally locked orbits starts to break down (Parmentier et al. 2015; Showman et al. 2014).

The distribution of temperature from the known planet population observed is displayed in Figure 3.4. From this we can see that the majority of hot Jupiters have equilibrium temperatures between ∼1000-1800K, with a lower number at higher temperatures, and that our population range covers most of the observed atmospheres.

3.5.2 Orbital Period

In order to stay close to the observed population, we decided to run models for planets orbiting three different stellar types. A K2 dwarf, similar to HD 189733, a G0V dwarf, similar to HD 209458 and a F6 dwarf similar to HAT-P-7. The influence of different stellar spectra on planet atmospheres, and particularly the sensitivity of temperature inversions to the spectral type, have been previously studied using 1D models for both hot (Mollière et al. 2015) and ultra-hot Jupiters (Lothringer & Barman 2019). Associated stellar spectra come from the NextGen stellar model archive (Hauschildt et al. 1999). As such, $M_{\rm star}$, $T_{\rm star}$ and $R_{\rm star}$ all vary between the different model tracks. Even though the exact stellar spectrum surely has an effect on the radiative energy balance of the atmosphere, the main effect of changing stellar parameters that we are interested in is the related change of orbital period. Because we assume that our planets are tidally locked, their rotation period is directly determined by the equilibrium temperature and stellar parameters:

$$P = \left(\frac{R_{\rm star}}{R_{\rm sun}}\right)^{\frac{3}{2}} \left(\frac{T_{\rm star}}{T_{\rm sun}}\right)^{3} \left(\frac{M_{\rm sun}}{M_{\rm star}}\right)^{\frac{1}{2}} \left(\frac{1991.5\text{K}}{T_{\rm eq}}\right)^{\frac{1}{3}} \text{days}. \tag{3.5}$$

As shown in Table 3.2, our three stars correspond to three model tracks with periods shifted by 0.37 and 2.23 compared to our nominal case. Thus, at a given equilibrium temperature our grid has rotation period varying by a factor of 6. The goal of varying the orbital period in this way is to compare how the atmosphere varies when looking at different planets around the same stellar type. The distribution of observed orbital periods for the hot Jupiter population is displayed in Figure 3.4. We note that for high temperature models

(>2000K), we do model some orbital periods that are lower than observed in the population, which was done to maintain the completeness of the grid.

Table 3.2: Free parameters used in the 3D GCM grid.

M_{star} [M_{sun}]	R_{star} [R_{sun}]	T_{star} [K]	Normalised Period Multiplier	Absolute Period Range [days]
0.8	0.8	4875	0.37	0.27 - 3.79
1.1	1.18	5920	1	0.75 - 10.36
1.5	2	6259	2.23	1.67 - 23.13

3.5.3 Metallicity

We define the planetary metallicity here as the atomic molar mixing ratio of all other chemical elements to hydrogen and helium in the atmosphere. Elemental abundances are scaled from solar composition (Lodders et al. 2009), with all atoms other than H and He multiplied by the metallicity value. For the grid we have selected three values to sample in the metallicity: Log(M/H)=0.0, 0.7 and 1.5. These range from solar to roughly 30-times solar metallicity.

We do not explore very high values of metallicity, ensuring that our approximation of a constant mean molecular weight and heat capacity throughout the population stay correct (see Zhang & Showman (2017)). The main effect of metallicity is therefore to increase the molecular opacities of the atmosphere, which leads to lower photospheric pressures.

3.5.4 Surface Gravity

The surface gravity of a planet is dependent on the mass and radius, and displays order of magnitude variations in the hot Jupiter mass regime. For example WASP-18 b (Hellier et al. 2009) is a very high density planet with a surface gravity of log(g)=∼2.2 (158.5 ms^{-2}), whilst there are also very low density planets, such as WASP-39 b (Maciejewski et al. 2016), which has a surface gravity of log(g)=∼0.63 (4.3 ms^{-2}). We therefore sample three values for the surface gravity, representing close to the extremes in the hot Jupiter population: log(g[SI])=0.8, 1.3, 1.8 (g=6.31, 19.95, 63.10 ms^{-2}). As shown in Thomson & Vallis (2019); Zhang & Showman (2017), gravity naturally cancels out in the dynamic equations. However, the role of gravity is important in setting the pressure of the infrared photosphere and thus the opacities at the photosphere.

3.5.5 TiO & VO

Here, we decide to be agnostic about the transition from an atmosphere containing TiO/VO to one without. We therefore run both a set of models at chemical equilibrium (and thus containing TiO/VO) between 1000-2400K, and a set of models where the elemental abundances of Ti and V have been artificially set to zero, mimicking the disappearance of TiO/VO due to condensation processes in the deep layers (Parmentier et al. 2016; Spiegel et al. 2009), or in the night-side atmopshere (Beatty et al. 2017; Parmentier et al. 2016; Pelletier et al. 2023), between equilibrium temperatures of 1400-2400K.

3.5.6 Drag Timescale

For the drag models we choose to be agnostic on the type of atmospheric drag. Dissipation is included in the model via the $D_{\mathbf{v}}$ and D_T terms in the hydrostatic primitive equations, 2.18 and 2.21 respectively. The drag is modelled as a bulk Rayleigh drag, assuming local dissipation of kinetic energy (see Section 3.3.3). This is physically different to numerical drag through the Shapiro filter (Shapiro 1970), which has different scaling based on the grid spacing and wind speed.

We use drag timescales of $\tau_{drag} = 10^5$, 10^4 and 10^3s. We don't use values larger than 10^5s because, as shown in Showman et al. (2013) and discussed in Chapter 2, drag with longer timescales will be insufficient to inhibit the formation of equatorial super-rotating and therefor have a limited effect on the dynamical structure for a typical hot Jupiter. Additionally, for drag timescales longer than 10^6s dissipation via the Shapiro filter will be dominant. On the other end, we do not use timescales shorter than 10^3 s as circulation is already expected to be almost completely dampened at this level of drag and shorter timescales would therefore have insignificant effects on an atmosphere. This selection of drag timescales, in addition to our drag-free (i.e $\tau_{drag} = \infty$) models, is in line with other modelling studies investigating the effects of variable drag in hot Jupiters (i.e Koll & Komacek (2018)).

We sample the normalised period and atmospheric metallicity over the same range and intervals as the drag-free grid. In order to reduce the number of free parameters, we choose to fix the surface gravity at its median value of log(g[SI])=1.3 (g=19.95 ms^{-2}). We also reduce the sampling of equilibrium temperatures, now at 400K intervals between 1000-2200K. Models are still produced both with and without the presence of TiO and VO. The full range of parameters used for the drag model grid can be found in Table 3.3. In total, the drag model grid comprises of 171 models. By sampling the drag model grid in this way, we can still easily compare it to models of equivalent parameters from the drag-free grid.

Table 3.3: Free parameters used in the 3D GCM drag grid.

T_{eq} [K]	Log(M/H)	Normalised Period Multiplier	Log(τ_{drag}[s])	Molecular Species
1400-2400 (400K intervals)	0.0, 0.7, 1.5	0.37, 1, 2.23	3, 4, 5	C_2H_2, C_2H_4, C_2H_6, CaH, CH_4, CO, CO_2, CrH, FeH, H_2O, H_2S, HCN, K, Li, LiCl, MgH, N_2, Na, NH_3, OCS, PH_3, SiO, TiO, VO
1000-2400 (400K intervals)	″	″	″	No TiO, VO

Bibliography

Adcroft A., Campin J.-M., Hill C., Marshall J., 2004, Monthly Weather Review, 132, 2845
Arcangeli J., et al., 2019, A&A, 625, A136
Baeyens R., Decin L., Carone L., Venot O., Agúndez M., Mollière P., 2021, MNRAS, 505, 5603
Baeyens R., Konings T., Venot O., Carone L., Decin L., 2022, MNRAS, 512, 4877
Batygin K., Stanley S., Stevenson D. J., 2013, ApJ, 776, 53
Baxter C., et al., 2021, A&A, 648, A127
Beatty T. G., Madhusudhan N., Tsiaras A., Zhao M., Gilliland R. L., Knutson H. A., Shporer A., Wright J. T., 2017, AJ, 154, 158

Beatty T. G., Marley M. S., Gaudi B. S., Colón K. D., Fortney J. J., Showman A. P., 2019, AJ, 158, 166
Bell T. J., Cowan N. B., 2018, ApJ, 857, L20
Beltz H., Rauscher E., Roman M. T., Guilliat A., 2022, AJ, 163, 35
Chandrasekhar S., 1960, Radiative transfer
Charbonneau D., Knutson H. A., Barman T., Allen L. E., Mayor M., Megeath S. T., Queloz D., Udry S., 2008, ApJ, 686, 1341
Charnay B., Meadows V., Leconte J., 2015a, ApJ, 813, 15
Charnay B., Meadows V., Misra A., Leconte J., Arney G., 2015b, ApJ, 813, L1
Cooper C. S., Showman A. P., 2005, ApJ, 629, L45
Cooper C. S., Showman A. P., 2006, ApJ, 649, 1048
Cowan N. B., Agol E., Charbonneau D., 2007, MNRAS, 379, 641
Crossfield I. J. M., Hansen B. M. S., Harrington J., Cho J. Y. K., Deming D., Menou K., Seager S., 2010, ApJ, 723, 1436
Deming D., Line M. R., Knutson H. A., Crossfield I. J. M., Kempton E. M. R., Komacek T. D., Wallack N. L., Fu G., 2023, arXiv e-prints, p. arXiv:2301.03639
Dobbs-Dixon I., Agol E., 2013, MNRAS, 435, 3159
Dobbs-Dixon I., Lin D. N. C., 2008, ApJ, 673, 513
Dobbs-Dixon I., Cumming A., Lin D. N. C., 2010, ApJ, 710, 1395
Dowling T. E., Fischer A. S., Gierasch P. J., Harrington J., LeBeau R. P., Santori C. M., 1998, Icarus, 132, 221
Drummond B., Tremblin P., Baraffe I., Amundsen D. S., Mayne N. J., Venot O., Goyal J., 2016, A&A, 594, A69
Drummond B., Mayne N. J., Baraffe I., Tremblin P., Manners J., Amundsen D. S., Goyal J., Acreman D., 2018a, A&A, 612, A105
Drummond B., et al., 2018b, ApJ, 855, L31
Drummond B., Mayne N. J., Manners J., Baraffe I., Goyal J., Tremblin P., Sing D. K., Kohary K., 2018c, ApJ, 869, 28
Fortney J. J., Marley M. S., Lodders K., Saumon D., Freedman R., 2005, ApJ, 627, L69
Fortney J. J., Cooper C. S., Showman A. P., Marley M. S., Freedman R. S., 2006, ApJ, 652, 746
Fortney J. J., Lodders K., Marley M. S., Freedman R. S., 2008, ApJ, 678, 1419
Freedman R. S., Marley M. S., Lodders K., 2008, ApJS, 174, 504
Freedman R. S., Lustig-Yaeger J., Fortney J. J., Lupu R. E., Marley M. S., Lodders K., 2014, ApJS, 214, 25
Goody R. M., Yung Y. L., 1989, Atmospheric radiation : theoretical basis
Gordon S., McBride B. J., 1994, NASA Reference Publication, 1311
Goyal J. M., et al., 2020, MNRAS, 498, 4680
Goyal J. M., Lewis N. K., Wakeford H. R., MacDonald R. J., Mayne N. J., 2021, ApJ, 923, 242
Guillot T., 2010, A&A, 520, A27
Hammond M., Lewis N. T., 2021, Proceedings of the National Academy of Science, 118, e2022705118
Hauschildt P. H., Allard F., Baron E., 1999, ApJ, 512, 377
Hellier C., et al., 2009, Nature, 460, 1098
Heng K., Menou K., Phillipps P. J., 2011, MNRAS, 413, 2380
Heng K., Morris B. M., Kitzmann D., 2021, arXiv e-prints, p. arXiv:2103.02673
Hindle A. W., Bushby P. J., Rogers T. M., 2019, ApJ, 872, L27
Hindle A. W., Bushby P. J., Rogers T. M., 2021a, arXiv e-prints, p. arXiv:2107.07515
Hindle A. W., Bushby P. J., Rogers T. M., 2021b, ApJ, 916, L8
JWST Transiting Exoplanet Community Early Release Science Team et al., 2023, Nature, 614, 649
Kalnay E., 2002, Atmospheric Modeling, Data Assimilation and Predictability
Kataria T., Showman A. P., Lewis N. K., Fortney J. J., Marley M. S., Freedman R. S., 2013, ApJ, 767, 76
Kataria T., Showman A. P., Fortney J. J., Stevenson K. B., Line M. R., Kreidberg L., Bean J. L., Désert J.-M., 2015, ApJ, 801, 86
Kataria T., Sing D. K., Lewis N. K., Visscher C., Showman A. P., Fortney J. J., Marley M. S., 2016, ApJ, 821, 9
Keating D., Cowan N. B., Dang L., 2019, Nature Astronomy, 3, 1092
Knutson H. A., et al., 2007, Nature, 447, 183
Knutson H. A., et al., 2009, ApJ, 690, 822
Knutson H. A., et al., 2012, ApJ, 754, 22
Koll D. D. B., Komacek T. D., 2018, ApJ, 853, 133
Komacek T. D., Showman A. P., 2016, ApJ, 821, 16
Komacek T. D., Tan X., 2018, Research Notes of the American Astronomical Society, 2, 36

Komacek T. D., Showman A. P., Tan X., 2017, ApJ, 835, 198
Komacek T. D., Gao P., Thorngren D. P., May E. M., Tan X., 2022, ApJ, 941, L40
Kreidberg L., et al., 2018, AJ, 156, 17
Lacis A. A., Oinas V., 1991, J. Geophys. Res., 96, 9027
Lee E., Dobbs-Dixon I., Helling C., Bognar K., Woitke P., 2016, A&A, 594, A48
Lee E. K. H., Wood K., Dobbs-Dixon I., Rice A., Helling C., 2017, A&A, 601, A22
Lee E. K. H., Parmentier V., Hammond M., Grimm S. L., Kitzmann D., Tan X., Tsai S.-M., Pierrehumbert R. T., 2021, MNRAS, 506, 2695
Lewis N. K., Showman A. P., Fortney J. J., Marley M. S., Freedman R. S., Lodders K., 2010, ApJ, 720, 344
Lewis N. K., Showman A. P., Fortney J. J., Knutson H. A., Marley M. S., 2014, ApJ, 795, 150
Lewis N. K., Parmentier V., Kataria T., de Wit J., Showman A. P., Fortney J. J., Marley M. S., 2017, arXiv e-prints, p. arXiv:1706.00466
Line M. R., Knutson H., Wolf A. S., Yung Y. L., 2014, ApJ, 783, 70
Lines S., et al., 2018, A&A, 615, A97
Lines S., Mayne N. J., Manners J., Boutle I. A., Drummond B., Mikal-Evans T., Kohary K., Sing D. K., 2019, MNRAS, 488, 1332
Lodders K., Palme H., Gail H. P., 2009, Landolt Börnstein, 4B, 712
Lothringer J. D., Barman T., 2019, ApJ, 876, 69
Lothringer J. D., Barman T., Koskinen T., 2018, ApJ, 866, 27
Maciejewski G., et al., 2016, Acta Astron., 66, 55
Madhusudhan N., Burrows A., 2012, ApJ, 747, 25
Mansfield M., et al., 2021, Nature Astronomy, 5, 1224
Marley M. S., McKay C. P., 1999, Icarus, 138, 268
Marley M. S., Saumon D., Fortney J. J., Morley C., Lupu R. E., Freedman R., Visscher C., 2017, in American Astronomical Society Meeting Abstracts #230. p. 315.07
Mayne N. J., et al., 2013, arXiv e-prints, p. arXiv:1311.2083
Mayne N. J., et al., 2014, A&A, 561, A1
Mayne N. J., et al., 2017, A&A, 604, A79
McKay C. P., Pollack J. B., Courtin R., 1989, Icarus, 80, 23
Mendonça J. M., 2020, MNRAS, 491, 1456
Mendonça J. M., Grimm S. L., Grosheintz L., Heng K., 2016, ApJ, 829, 115
Mendonça J. M., Malik M., Demory B.-O., Heng K., 2018a, AJ, 155, 150
Mendonça J. M., Tsai S.-m., Malik M., Grimm S. L., Heng K., 2018b, ApJ, 869, 107
Menou K., 2012, ApJ, 745, 138
Menou K., Rauscher E., 2009, ApJ, 700, 887
Molaverdikhani K., Henning T., Mollière P., 2019, ApJ, 883, 194
Mollière P., van Boekel R., Dullemond C., Henning T., Mordasini C., 2015, ApJ, 813, 47
Moses J. I., et al., 2013, ApJ, 777, 34
Oreshenko M., Heng K., Demory B.-O., 2016, MNRAS, 457, 3420
Parmentier V., 2014, PhD thesis, LAGRANGE - Joseph Louis LAGRANGE - Université Nice Sophia Antipolis (UNS); Observatoire de la Côte d'Azur CNRS : UMR7293
Parmentier V., Crossfield I. J. M., 2018, in Deeg H. J., Belmonte J. A., eds, , Handbook of Exoplanets. p. 116, doi:10.1007/978-3-319-55333-7˙116
Parmentier V., Guillot T., 2014, A&A, 562, A133
Parmentier V., Showman A. P., Lian Y., 2013, A&A, 558, A91
Parmentier V., Showman A. P., de Wit J., 2015, Experimental Astronomy, 40, 481
Parmentier V., Fortney J. J., Showman A. P., Morley C., Marley M. S., 2016, ApJ, 828, 22
Parmentier V., et al., 2018, A&A, 617, A110
Parmentier V., Showman A. P., Fortney J. J., 2021, MNRAS, 501, 78
Pelletier S., et al., 2023, arXiv e-prints, p. arXiv:2306.08739
Perna R., Menou K., Rauscher E., 2010, ApJ, 719, 1421
Perna R., Heng K., Pont F., 2012, ApJ, 751, 59
Rauscher E., Menou K., 2010, ApJ, 714, 1334
Rauscher E., Menou K., 2013, ApJ, 764, 103
Robbins-Blanch N., Kataria T., Batalha N. E., Adams D. J., 2022, ApJ, 930, 93
Rogers T. M., 2017, Nature Astronomy, 1, 0131

Rogers T. M., Komacek T. D., 2014, ApJ, 794, 132
Rogers T. M., Showman A. P., 2014, ApJ, 782, L4
Roth A., Drummond B., Hébrard E., Tremblin P., Goyal J., Mayne N., 2021, MNRAS, 505, 4515
Roth A., Parmentier V., Hammond M., 2024, MNRAS, 531, 1056
Shapiro R., 1970, Reviews of Geophysics and Space Physics, 8, 359
Showman A. P., Guillot T., 2002, A&A, 385, 166
Showman A. P., Polvani L. M., 2011, ApJ, 738, 71
Showman A. P., Cooper C. S., Fortney J. J., Marley M. S., 2008, ApJ, 682, 559
Showman A. P., Fortney J. J., Lian Y., Marley M. S., Freedman R. S., Knutson H. A., Charbonneau D., 2009, ApJ, 699, 564
Showman A. P., Fortney J. J., Lewis N. K., Shabram M., 2013, ApJ, 762, 24
Showman A. P., Lewis N. K., Fortney J. J., 2014, arXiv e-prints, p. arXiv:1411.4731
Showman A. P., Lewis N. K., Fortney J. J., 2015, ApJ, 801, 95
Skemer A. J., et al., 2016, ApJ, 817, 166
Spiegel D. S., Silverio K., Burrows A., 2009, ApJ, 699, 1487
Steinrueck M. E., Parmentier V., Showman A. P., Lothringer J. D., Lupu R. E., 2019, ApJ, 880, 14
Thomson S. I., Vallis G. K., 2019, Quarterly Journal of the Royal Meteorological Society, 145, 2627
Thorngren D., Gao P., Fortney J. J., 2019, ApJ, 884, L6
Thrastarson H. T., Cho J. Y.-K., 2010, ApJ, 716, 144
Toon O. B., McKay C. P., Ackerman T. P., Santhanam K., 1989, J. Geophys. Res., 94, 16287
Tsai S.-M., Dobbs-Dixon I., Gu P.-G., 2014, ApJ, 793, 141
Tsai S.-M., Lyons J. R., Grosheintz L., Rimmer P. B., Kitzmann D., Heng K., 2017, ApJS, 228, 20
Tsai S.-M., Malik M., Kitzmann D., Lyons J. R., Fateev A., Lee E., Heng K., 2021, arXiv e-prints, p. arXiv:2108.01790
Venot O., Bounaceur R., Dobrijevic M., Hébrard E., Cavalié T., Tremblin P., Drummond B., Charnay B., 2019, A&A, 624, A58
Venot O., et al., 2020, ApJ, 890, 176
Visscher C., Lodders K., Fegley Bruce J., 2006, ApJ, 648, 1181
Visscher C., Lodders K., Fegley Bruce J., 2010, ApJ, 716, 1060
Wakeford H. R., Visscher C., Lewis N. K., Kataria T., Marley M. S., Fortney J. J., Mandell A. M., 2017, MNRAS, 464, 4247
Wang H., Wordsworth R., 2020, ApJ, 891, 7
Zhang X., Showman A. P., 2017, ApJ, 836, 73
Zhang M., et al., 2018, AJ, 155, 83

Chapter 4

A Large Grid of GCM Models: Atmospheric Diversity

The material in this chapter is based on Roth et al. (2024):
– Roth A., Parmentier V., Hammond M., 2024, MNRAS, 531, 1056

4.1 Introduction

As we have discussed throughout the previous chapters, intrinsic properties of hot Jupiter exoplanets are expected to have a profound effect on their atmospheric state. Additionally, there are order of magnitude variations in these intrinsic properties across the observed hot Jupiter population (as displayed in Figure 3.4).

Numerous modelling and observational studies have identified some of the inherent trends between the planetary properties and the atmospheric state. The efficiency of heat redistribution within their atmospheres has been shown to decrease with increasing temperature (Komacek & Showman 2016; Perez-Becker & Showman 2013), and with increasing metallicity (Charnay et al. 2015). Both metallicity and gravity are expected to play a key role in determining the photospheric pressure, and the temperature contrast at the photosphere will therefore depend on these parameters. The phase curve amplitude, which generally tracks heat redistribution, has been shown to increase with temperature (Komacek & Showman 2016; Parmentier et al. 2021) and be correlated to the phase curve offset (Schwartz et al. 2017). The magnitude of eastward shifts in atmospheric hotspot, and resulting phase curve offset, are also expected to reduce for super solar metallicities (Kataria et al. 2015). Additionally, the phase curve offset has been shown to vary non-monotonically with temperature (Komacek & Showman 2016; Zhang et al. 2018), and both phase curve offset and amplitude have been shown to vary with rotation period (Stevenson et al. 2014).

However, due to the computational cost associated with the complexity of non-grey 3D modelling, combined with the wide parameter space spanned by the hot Jupiter population, no study has produced a model grid both systematically and jointly varying parameters to the extent of our grid described in Chapter 3. In this chapter we use our grid of 345 drag-free models to explore the a-priori scatter in the population created by the different responses of atmospheric circulation to planetary parameters.

Beginning with an overview of the thermal and dynamical structure (Section 4.2), we then discuss the wide variation in day-to-night heat redistribution within the grid (Section 4.3). We then move on to an overview of the secondary eclipse spectra and phase curves (Section 4.4), including more detailed discussion on the trends between offset and period and correlation between the amplitude and offset. We then discuss temperature variation between the limbs (Section 4.5), before summarising our conclusions (Section 4.6).

4.2 Atmospheric Characteristics for a Range of Planetary Parameters

For much of the analysis in this investigation we will be boiling the atmosphere down into a series of characteristic observable features. However, we show in Figure 4.1 the wide range of diversity displayed by our models. This shows the temperature structure, normalised by the equilibrium temperature, at the pressure level closest to the 1.4 micron photospheric pressure for all the models within our grid. Water has a strong molecular feature peaking at 1.4 microns. The shape of an emission spectrum in the HST/WFC3 bandpass ($\sim 1.1 - 1.7\mu m$) therefore depends heavily on water abundance and the atmospheric thermal structure, hence the use of the 1.4 micron photospheric pressure here. The 1.4 micron photospheric pressure can be calculated as (Parmentier et al. 2018):

$$P_{\text{photo(1.4 micron)}} = \frac{2}{3}\frac{g\mu}{\sigma_{H_2O}A_{H_2O}}, \tag{4.1}$$

where σ_{H_2O} is the absorption cross section of water at $1.4\mu m$, which we assume to be constant, A_{H_2O} is the volume mixing ratio of water, g is the gravity and μ is the mean molecular weight. In principle A_{H_2O} should vary longitudinally, however, we ignore this here so that the photospheric pressure can be calculated as an isobar. so that This can be scaled by our model parameters as:

$$P_{\text{photo(1.4 micron)}} = \left(\frac{g}{2046.2ms^{-2}}\right)\left[\frac{M}{H}\right]^{-1} \text{bars}. \tag{4.2}$$

This method of calculating photospheric pressure works well for lower temperature planets. However, it does become less accurate for higher temperatures as it does not include any treatment for water dissociation. Each model is sorted into columns and rows based on their grid parameters. Gaps in the grid shown in Figure 4.1 are due to models that are unable to converge. This is due to numerical instabilities within the GCM i.e if the time-step is too long. This can be solved by further reducing the time-step, although this significantly increases the CPUh required to run a model. It is therefore impracticable to reduce the time-step sufficiently for very high temperature, high metallicity and fast rotation rates when producing the number of models within our grid.

The temperature structure in our models varies drastically based on the prescribed model parameters. Surface gravity and metallicity alter the location of the photospheric pressure level, orbital period changes the width and strength of equatorial jet circulation and TiO/VO create temperature inversions. From these temperature maps we can already start to see some trends among the models. The equatorial jet structure is clearly visible in many. This jet becomes narrower in latitude for models with higher temperatures, which are rotating much faster than their cooler counterparts in the grid, and for models with lower metallicity. High latitude Rossby waves are also visible for many of the models. The day-to-night temperature contrast can clearly be seen to increase with the equilibrium temperature.

Figure 4.2 shows the zonal-mean zonal wind speed with pressure for the grid arranged in the same format. Again there are some clear trends that emerge with our model parameters. The strength of the super-rotating jet is clearly increased with the equilibrium temperature. The jet also extends to deeper pressures in the atmosphere as the surface gravity is increased.

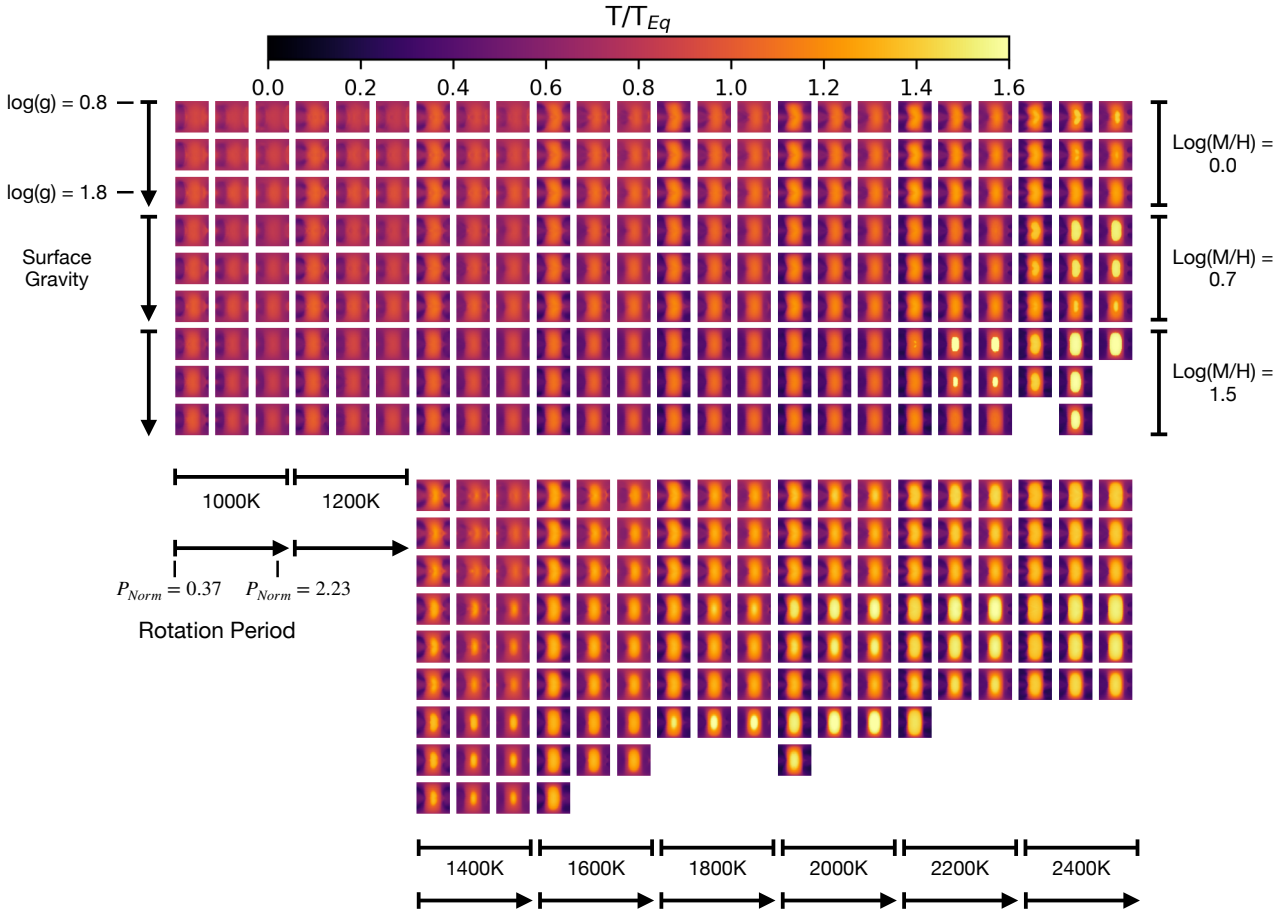


Figure 4.1: Latitude vs longitude thermal structure, temperature normalised by equilibrium temperature, for all models within the grid, at the pressure level closest to the 1.4 micron photospheric pressure. Equilibrium temperature is sorted into columns and atmospheric metallicity into rows. The surface gravity increases between the values seen in Table 3.1 down each bracket of rows and the normalised orbital period increases in the same manner along columns. Models excluding TiO/VO are separated into the top half, with models including the two species in the bottom half.

As the normalised rotation period is increased, the jet also clearly becomes wider, and the flow structure transitions from multiple jets to a single one for higher temperature models.

To show how the secondary eclipse spectra vary with our model parameters, we include Figure 4.3. Here we can see that increasing metallicity and surface gravity act to increase the thermal flux, with increasing normalised period having the opposite effect. This is caused by the effect of parameters on the heat redistribution, which is discussed in detail throughout Section 4.3. It is interesting to note here that the metallicity appears to have a larger effect on the flux within the emission bands, surface gravity has a larger effect outside of the bands and the normalised period has a fairly constant effect across the spectra. The bottom right panel of Figure 4.3 shows how the presence of TiO and VO affect the emission spectra. In particular, the molecular bands which show absorption features in the absence of TiO/VO switch to emission features when these species are present.

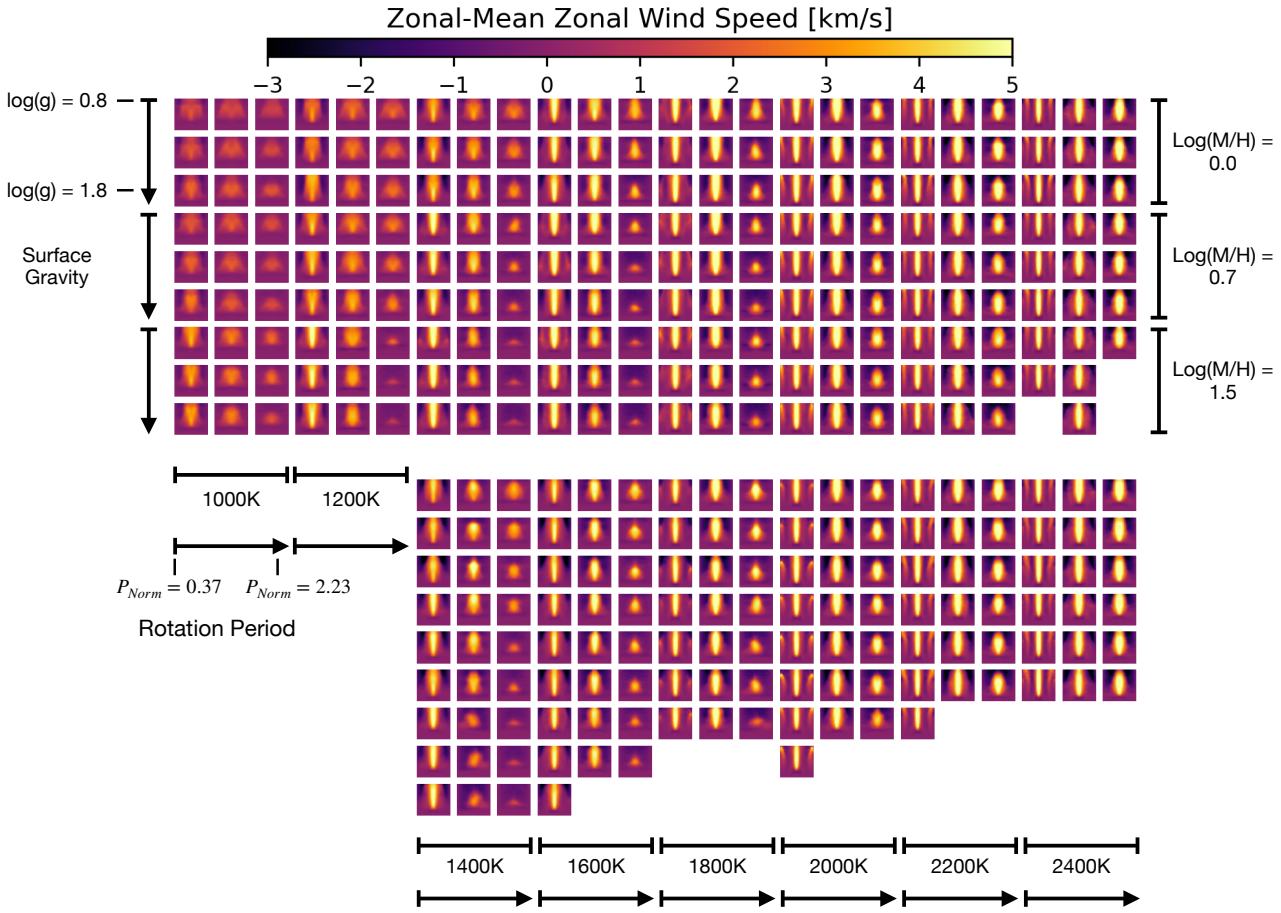


Figure 4.2: Zonal-mean zonal wind speed for all models within the grid. Equilibrium temperature is sorted into columns and atmospheric metallicity into rows. The surface gravity increases between the values seen in Table 3.1 down each bracket of rows and normalised orbital period increases in the same manner along columns. Models excluding TiO/VO are separated into the top half, with models including the two species in the bottom half.

4.3 Heat Redistribution

As described in Chapter 2, stellar flux incident on a planet's atmosphere has two main pathways. It is either reflected back into space or deposited in the day-side atmosphere. The energy can then be re-radiated into space from the day-side, or advected onto the night-side before being re-radiated (Cowan & Agol 2011).

The ratio between energy radiated from the day-side and that advected onto the night-side can be described as the heat redistribution efficiency. Ideally, measurements of the emitted light from a planet at all phases is necessary to estimate the heat redistribution efficiency. However, for planets with a small albedo, this efficiency can be determined by comparing the incoming radiation ($\sigma T_{\rm eq}^4$) to the outgoing longwave radiation from the planetary day-side ($\sigma T_{\rm day}^4$). Thus we define the heat redistribution efficiency, or f-factor, as (Arcangeli et al.

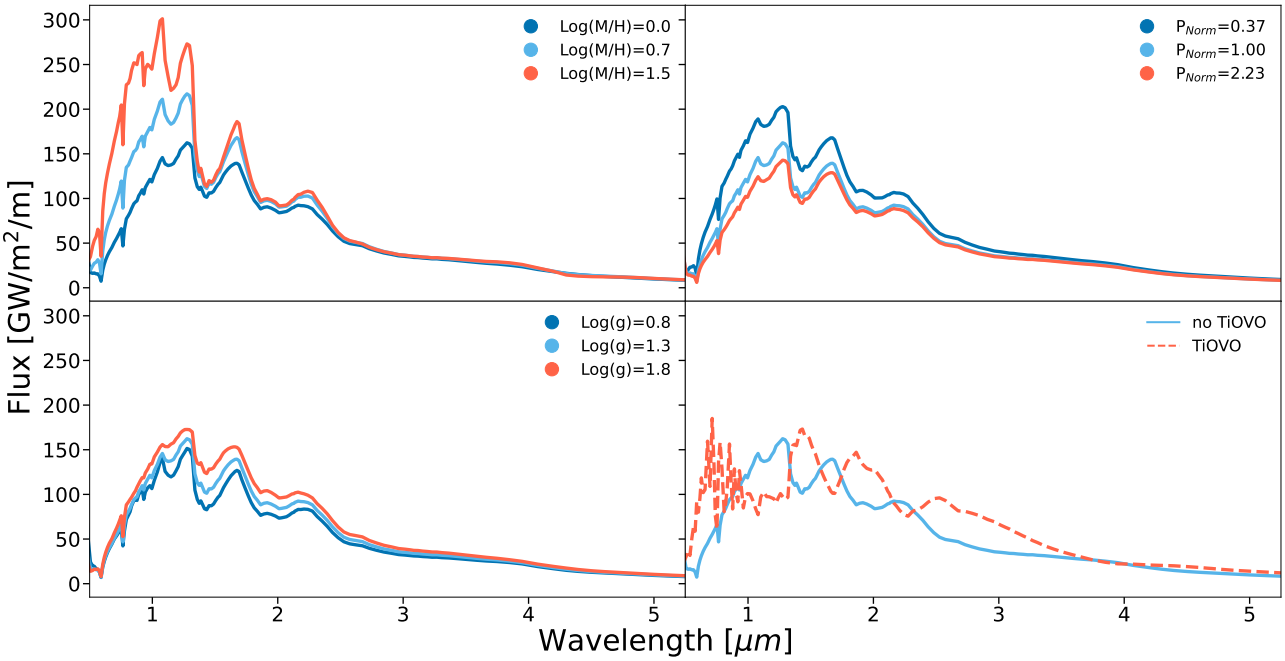


Figure 4.3: Secondary eclipse spectra for a number of 1800K T_{eq} models within the grid. **Upper Left Panel:** Shows the variation in atmospheric metallicity. **Upper Right Panel:** Shows the variation in normalised orbital period. **Lower Left Panel:** Shows the variation in atmospheric surface gravity. **Lower Right Panel:** Shows the difference between spectra for models containing and not containing TiO and VO.

2018):

$$f = \left(\frac{T_{\rm day}}{T_{\rm eq}} \right)^4, \tag{4.3}$$

where $T_{\rm day}$ is the temperature of the equivalent blackbody emitting as much energy in our direction as the planetary day-side. Following this definition, the redistribution factor (f-factor) has a minimum value of $f = 1$, corresponding to a case of maximum planet wide heat redistribution where the atmospheric temperature is fully homogenised between the day and night-sides, and a maximum value of $f = 2.66$ where there is zero heat redistribution between the two hemispheres. These limits only apply when considering the bolometric flux. A value of $f = 2$ corresponds to a theoretical case where there is day-side only heat redistribution. These f-factor values are related to the ϵ values defined in (Cowan & Agol 2011) by $\epsilon = 1 + 0.6(1 - f)$. Equation 4.3 is used to calculate the heat transport in our cloudless models, using the same method as described in Parmentier et al. (2021), since the albedos are always small (as shown in the following section). This will further enable a direct comparison with secondary eclipse data.

4.3.1 Geometric & Bond Albedo

The bond albedo, A_b, of a planetary body is a measure of the fraction of incident radiation that is reflected back into space without being absorbed over all wavelengths and viewing angles. Because of this it is crucial in working out planetary energy balance. The spherical albedo is this same measurement, but for a singular wavelength. The geometric albedo,

related to the spherical albedo via Equation 2.4, is the albedo measured when the light source is between the observer and the planet. Figure 4.4 displays the bolometric geometric and bond albedos for our grid of models. All models within the grid have a geometric albedo of $\leq$ 0.1 and a bond albedo of $\leq$ 0.15. The albedo also decreases at higher equilibrium temperatures. This distribution confirms our expectation that cloudless hot Jupiter models have low albedos.

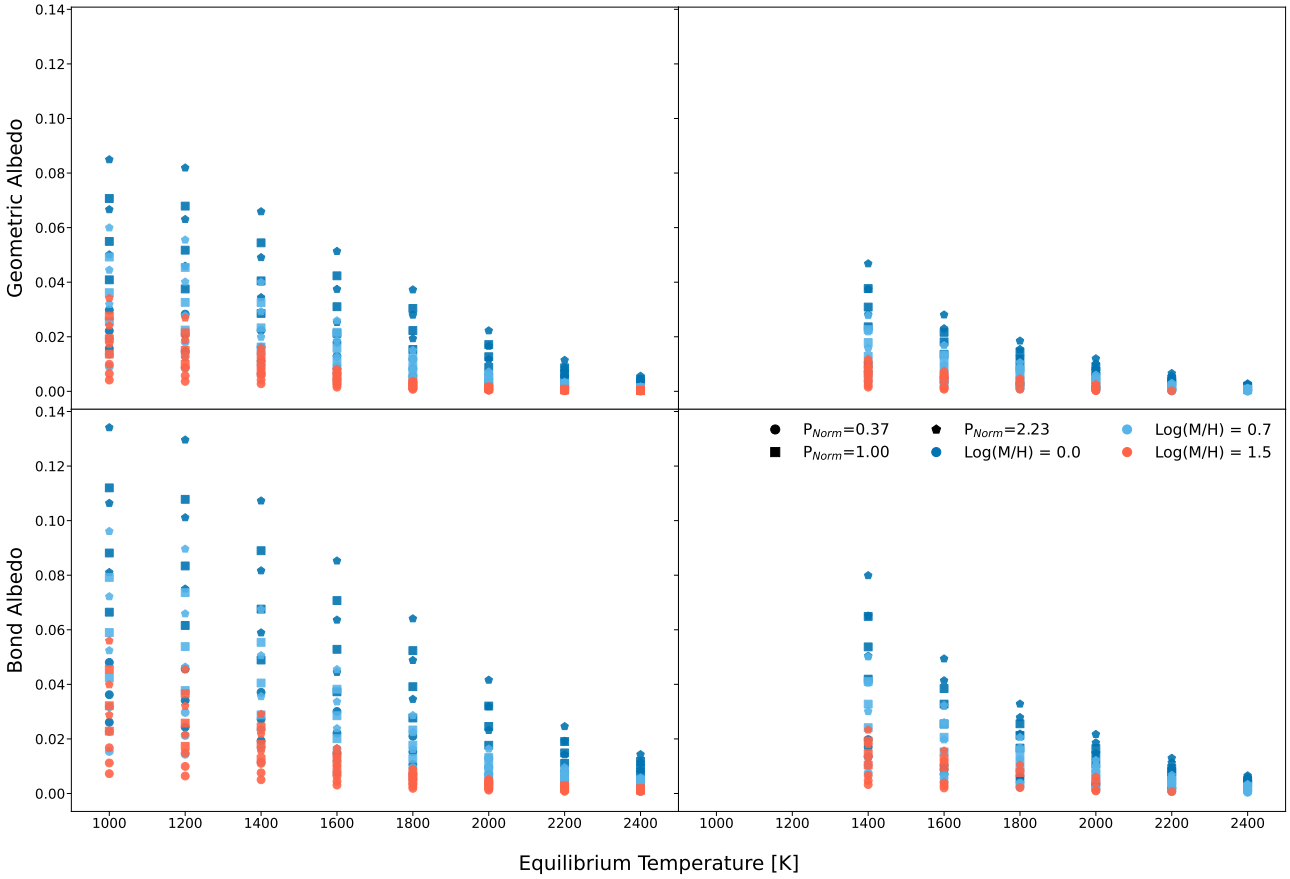


Figure 4.4: Calculated values for the bolometric geometric (**Top Panels**) and bond (**Bottom Panels**) albedos from the model grid plotted against the equilibrium temperature. **Left Panels:** Show models not containing TiO/VO. **Right Panels:** Show models containing TiO/VO. The shape of each point depicts the orbital period, and the colour depicts the metallicity of the model.

4.3.2 Expected Scaling for the Heat Redistribution Factor with the Jet

Parmentier et al. (2021) find the speed of the equatorial jet, $U_{\rm jet}$, to increase linearly (minus a constant) with equilibrium temperature in their cloudless GCM models, which we also find for our models, as seen in Figure 4.5.

$U_{\rm jet}$ also increases linearly with increasing surface gravity. Increasing atmospheric metallicity slightly increases $U_{\rm jet}$ at lower $T_{\rm eq}$, but reduces it at higher $T_{\rm eq}$. Additionally, increasing rotation period decreases $U_{\rm jet}$, although this relationship is non-linear. However, order of magnitude variations in these parameters change $U_{\rm jet}$ by at most a factor of 2.

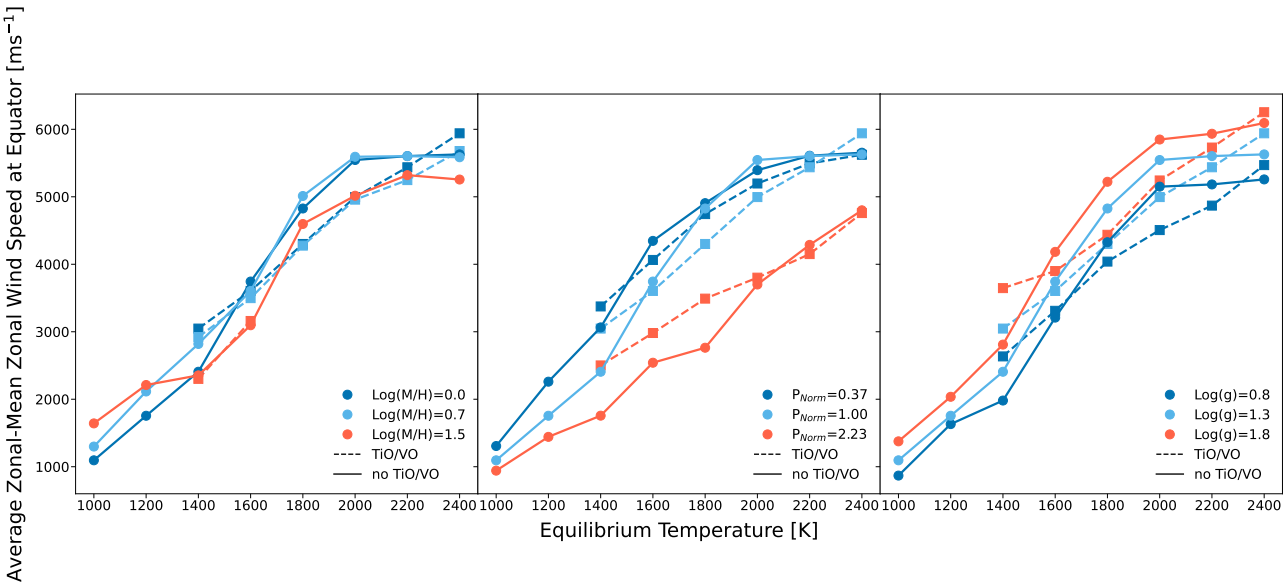


Figure 4.5: Zonal-mean zonal wind speed at the equator averaged over pressure for a subset of models within the grid. Each panel displays the variation with $T_{\rm eq}$ due to one of: rotation period, surface gravity and metallicity, whilst the other two parameters are kept constant (when constant Log(M/H)=0.0, P_{Norm}=1, log(g)=1.3). Cross-terms between parameters are not included. Models excluding and including TiO/VO are displayed with solid and dashed lines respectively. **Left Panel:** Variation in zonal-mean zonal wind speed at the equator whilst changing metallicity. **Middle Panel:** Variation in zonal-mean zonal wind speed at the equator with different normalised orbital period. These tracks corresponds to planets tidally-locked around different stellar types. **Right Panel:** Variation in zonal-mean zonal wind speed at the equator whilst changing surface gravity.

4.3.3 Overall Model Distribution

The bolometric redistribution factor values for all models in the grid are shown in Figure 4.6, with those models containing TiO/VO on the right and those without on the left. There is a trend towards higher f-factor values (meaning weaker day-night heat redistribution) at higher equilibrium temperature models in our grid. This is a well documented result that has been previously shown in both non-grey (Parmentier et al. 2021) and semi-grey modelling (Komacek et al. 2017; Perna et al. 2012), and also predicted with energy balance models (Cowan & Agol 2011). The scaling is caused by the strong temperature dependency of the radiative timescale (T^3 from equation 2.34) compared to the scaling of the wind and wave speeds (T and $\sqrt{T}$ from equations 2.26 and 2.25 respectively). The linear scaling of wind speeds with temperature can also be seen displayed in Figure 4.5. Overall, hot planets do not move heat around fast enough compared to the time needed for a parcel of gas to cool down radiatively. This naturally explains why the night-sides of hot Jupiters are almost independent of the equilibrium temperature (Parmentier et al. 2021).

There is also a noticeable kink in the distribution of f-factors for models not containing TiO/VO. This is due to the competition between the radiative, advective and wave timescales. Below ∼1600K the photospheric pressure stays roughly constant (see Figure 4 in (Parmentier et al. 2021)), as opacity is increasing with the temperature but the Plank function is shifting to shorter wavelengths. Over this range of temperature, the f-factor does not vary strongly with $T_{\rm eq}$. Over the same range of $T_{\rm eq}$, the radiative and advective timescales stay

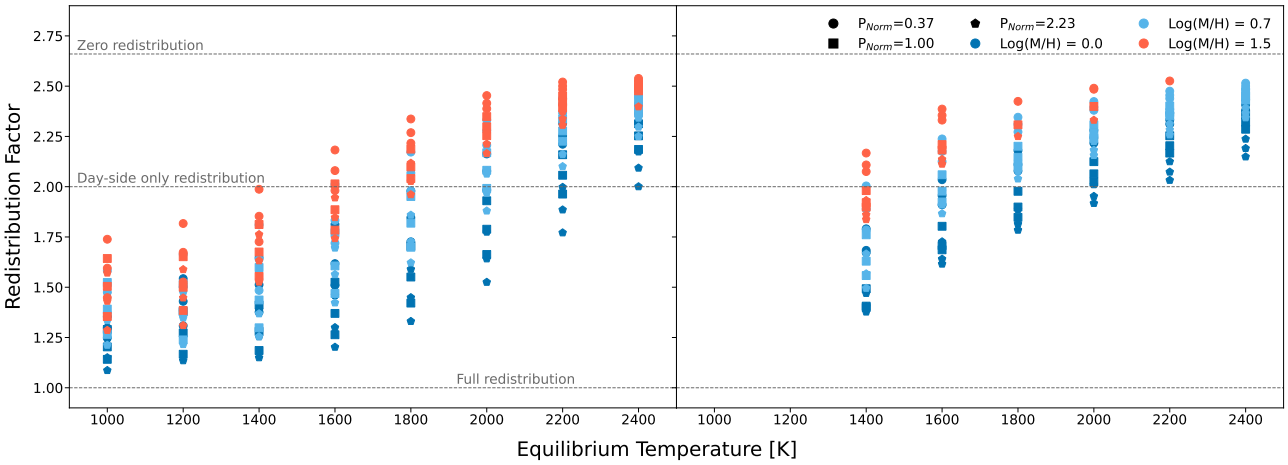


Figure 4.6: Bolometric redistribution factor, f-factor, a measure of the day-night atmospheric heat redistribution, for the model grid vs equilibrium temperature. **Left Panel:** Shows models with TiO/VO removed. **Right Panel:** Shows models containing TiO/VO. The shape of each point depicts the orbital period and the colour depicts the metallicity of the model. The grey dashed lines are drawn at key values corresponding to specific redistribution regimes.

very close to each other. This is because the advective timescale is not inversely linear but inversely *affine* (linear minus constant alpha, due to the scaling of U_{jet} with temperature, see Parmentier et al. (2021) equation 6). As a consequence, when both radiative and advective timescales cross each other they do not scale as T^2 but $T^3/(T_{\rm eq} - \alpha)$, which shows a much weaker variation with $T_{\rm eq}$.

When TiO and VO are present (right panel of Figure 4.6), the heat redistribution is worse, making the f-factor larger. The reason is multi-fold. First, the opacities do not decrease with decreasing wavelength anymore, meaning that (contrary to the case without TiO) as the temperature increases the photospheric pressure decreases, leading to shorter radiative timescales. Second, a portion of the stellar energy is absorbed at very low pressure and re-emitted directly from the stratosphere, rather than transported to the IR-photosphere, hence decreasing the overall rate of day-night heat transport.

The main takeaway here, however, is that at each equilibrium temperature we find that there is a significantly large spread in the heat redistribution based on the other planetary parameters. When gravity, period and metallicity are varied together, they can alter the efficiency of the heat redistribution as much as the equilibrium temperature itself. If we compare the spread in these values to that found in Parmentier et al. (2021), showing the change in redistribution factor between cloudless and cloudy atmosphere models when altering only the equilibrium temperature, we find that the intrinsic properties of the planet are having a comparable effect on the atmosphere to that of night-side clouds. The spread is also equivalent to that found in Komacek et al. (2017) between models with very low drag timescales ($\tau_{\rm drag} = 10^3 s$) and infinite drag timescales. In our own drag models, discussed in Chapter 6, we display that this spread is also equivalent to the effects of order of magnitude increases in magnetic field strength and the resulting magnetic drag timescales (see Section 6.4)

The spread in heat redistribution factor at a given equilibrium temperature in our models, due to the combined variability of rotation period, gravity and metallicity, is well in line with the spread observed by May et al. (2022), who measure a heat redistribution fac-

tor varying between 0.6 and 2.6 for planets between 1100-2400K (in the Spitzer bands the f-factor can be below 1). May et al. (2022) also display the heat redistribution to have a very wide range within a narrow variation of equilibrium temperatures (f=0.6-2.4 between 1100-1700K). This is an important point to note, as due to the wide range of effects that different parameters have on the redistribution, there is a large amount of degeneracy between the efficiency of heat redistribution between cases. This greatly complicates the characterisation of hot Jupiter atmospheres, as the intrinsic properties of the planet, chemical constituents of the atmosphere and the presence of night-side clouds all act to affect the redistribution in a wide range of potentially offsetting ways.

4.3.4 Specific Trends with Parameters

We now look into more detail at the trends with each parameter and discuss whether it is in agreement with simple timescale analysis. To take a closer look at how each planetary parameter is individually affecting heat redistribution, we can plot the f-factor as a function of temperature for a subset of models within our grid (ignoring cross-terms between the parameter space for now). This can be seen in Figure 4.7.

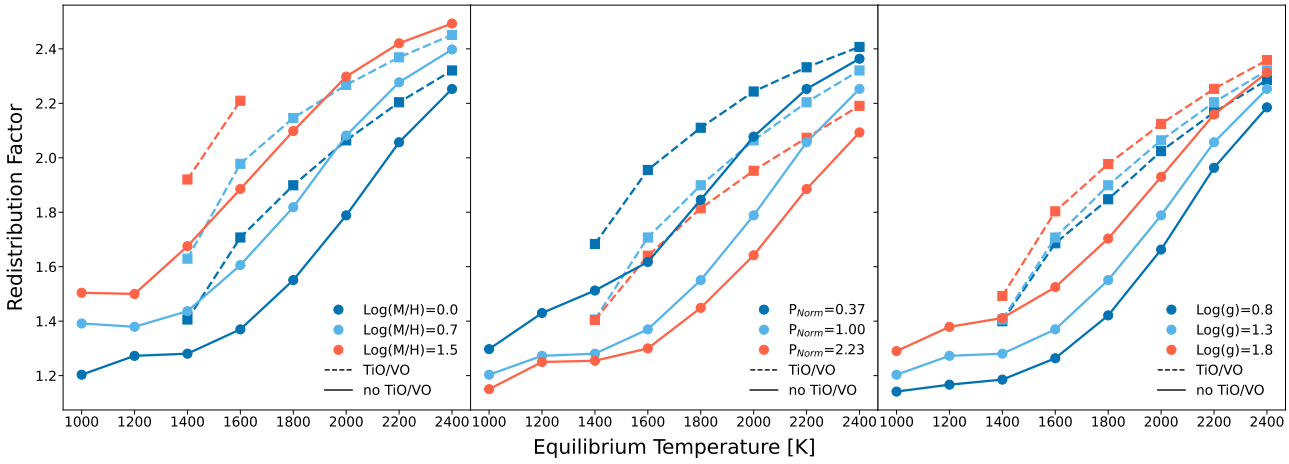


Figure 4.7: Calculated bolometric f-factor values for a subset of models within the grid. Each panel displays the variation in f-factor with $T_{\rm eq}$ due to one of: metallicity, orbital period and surface gravity, whilst the other two parameters are kept constant (when constant Log(M/H)=0.0, P_{norm}=1, log(g)=1.3). Cross-terms between parameters are not included. Models excluding and including TiO/VO are displayed with solid and dashed lines respectively. **Left Panel:** Variation in f-factor with metallicity. **Middle Panel:** Variation in f-factor with different normalised orbital period. These tracks correspond to planets tidally-locked around different stellar types. **Right Panel:** Variation in f-factor with surface gravity.

The change in f-factor with atmospheric metallicity is found in the left panel of Figure 4.7. Here, we find the calculated f-factor increases with higher atmospheric metallicity. This is caused by higher metallicity increasing the opacity, and therefore shifting the photosphere to a lower pressure (as explained in Section 2.6.1). This reduces the radiative timescale at the photosphere, which increasingly outweighs the dynamical timescale in the atmosphere and therefore reduces the day-night heat redistribution efficiency.

In the right panel we see that the f-factor increases with surface gravity. From the re-written radiative timescale equation (see Equation 2.34), we show that, as the photospheric pressure increases with surface gravity, leading to increased opacities due to the pressure

broadening of spectral lines, the radiative timescale at the photosphere decreases with surface gravity. This therefore leads to a decrease in heat redistribution (again see Section 2.6.1).

At a given equilibrium temperature, a longer orbital period is shown to increase the heat redistribution efficiency (decrease the f-factor) in the middle panel of Figure 4.7. This is caused by the increased strength of the combined rotational and divergent components of the circulation, as both transport heat from the day to the night-side and are both dependent on rotation period (Hammond & Lewis 2021; Lewis & Hammond 2022). As we will see in more details in Section 4.4.1, the opposite is true for the offset, for which it is the *relative* strength of divergent and rotational components of the circulation that matter.

Comparing the models excluding and including TiO/VO shows us that the presence of these species reduces redistribution across the board. Strong absorption in the near UV/optical range by these species in the high altitude day-side atmosphere, where the radiative timescale is short, reduces the efficiency of energy redistribution and significantly increases the temperature compared to the night-side. The average effect of the TiO/VO on the heat redistribution is $\Delta f = 0.216$, but this varies significantly with temperature.

4.3.5 Combined Parameter Trends: Heat Redistribution

We now discuss the quantitative effect that each parameter has on the heat redistribution. Because the change of heat transport with, for example, period, depends on the other parameters, such as temperature, we propose to look at both the average effect of the parameters and the variation of this average effect within the grid. For this, we measure the difference in heat redistribution between two models when varying only one parameter and keeping the other ones constant:

$$\Delta f_{P_{1,2}(T_{\rm eq},\log(M/H),\log(g))} = \frac{f_{P_2,\rm all} - f_{P_1,\rm all}}{\log(P_2) - \log(P_1)}. \tag{4.4}$$

Here P_1 is our model with a period normalisation factor of $P_{\rm norm} = 0.37$ and P_2 the model with $P_{\rm norm} = 1$. We then take the statistical mean between all the Δ values for the combinations of $T_{\rm eq}$, log(M/H) and log(g). This gives us the statistical average for the change we would expect to see in the heat redistribution when transitioning between consecutive grid points for the period, i.e $\Delta f_{P_{1,2}}$. This process is then repeated for each of the other parameters. The standard deviation in the Δf values is also calculated, i.e $\sigma f_{P_{1,2}}$. The mean and standard deviation for each parameter Δf is shown in Figure 4.8.

The size of the bars is the averaged change of the heat redistribution parameter when changing metallicity, pressure or gravity. The size of the error bars is the variation of this change when evaluated at different values of the other parameters. For example, one can see that the impact of period on the heat redistribution is similar for all metallicities and gravities. Hence it has a small variance. On the contrary, the change of heat redistribution due to a change of period depends strongly on the specific metallicity and gravity of the planet, hence the larger variance.

Overall, we see for the case without TiO/VO that gravity, period and metallicity have a quantitatively similar effect on the heat redistribution at a given equilibrium temperature. For the case with TiO/VO (right panel), the variation with gravity has a much smaller effect than the other parameters but both metallicity and period contribute in a similar way. However, atmospheric metallicity is largely unconstrained in comparison to period and gravity, which vary by no more than an order of magnitude within the population (see Figure 3.4). If

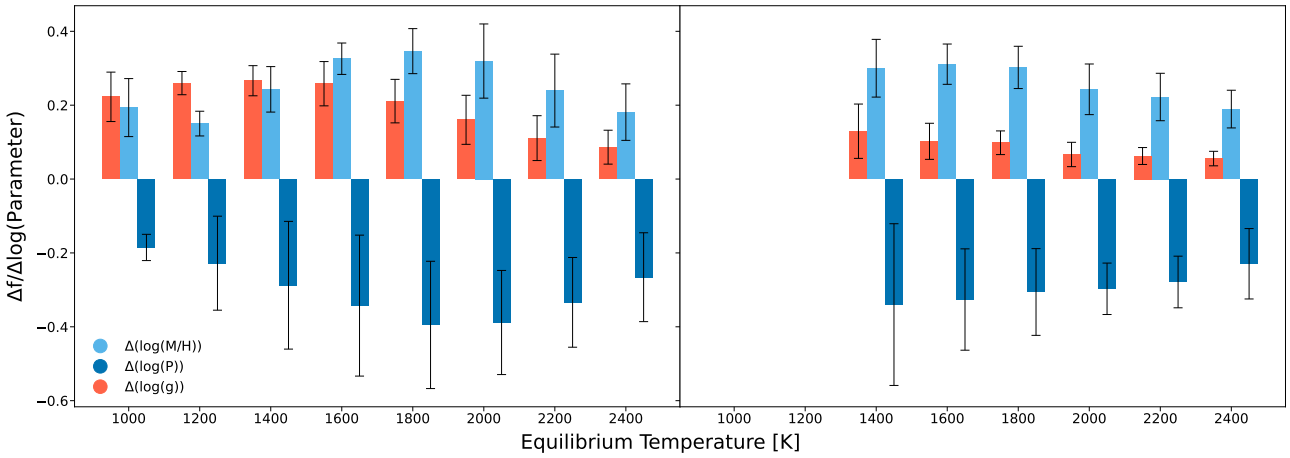


Figure 4.8: Relative impact of each planetary parameter on heat redistribution. The y-axis of each plot is the change in the f-factor divided by the change in the log of each planetary parameter. The x-axis is the equilibrium temperature. Light blue denotes the change due to metallicity, dark blue the change due to period and red the change due to surface gravity. The error bars display the standard deviation in the impact of each parameter. **Left Panel:** Models with TiO/VO removed. **Right Panel:** Models containing TiO/VO.

the metallicity variation is strong enough across the population, its heat redistribution trend could therefore dominate the observed population trend.

4.4 Bolometric Phase Curves

The phase curve of a planet, characterised as the change in brightness temperature observed during a full orbit, contains information about the longitudinal structure of the planet's atmosphere. As the phase curve amplitude and shape are determined by longitudinal inhomogeneities for transiting planets, they contain useful information about the 3D nature of planets. This includes the contrast in brightness temperature between day and night-sides, which is directly linked to the phase curve amplitude, and the asymmetry of the brightness distribution, which is directly obtained by measurement of the phase curve offset (in the cloud-free case).

4.4.1 Offset

Over the population of planets, phase curve offset is firstly determined by equilibrium temperatures, with offsets varying between 50° in the colder cases to a few degree (and even negative values) for the hottest planets (Bell et al. 2021). Within each temperature bin, however, the variation of the phase curve offset is extremely large. For example, for planets at 1400K it ranges between 50° for low gravity, low metallicity cases to 10° for high metallicity, high gravity cases. Additionally, the phase curve offset is predicted to vary in a non-monotonic way with temperature (Komacek & Showman 2016; Zhang et al. 2018).

The bolometric phase curve offsets for a subset of our models are displayed in Figure 4.9. For the most part, the trends we find can be explained using the same logic as that of the heat redistribution. A reduction in the efficiency of heat redistribution naturally leads

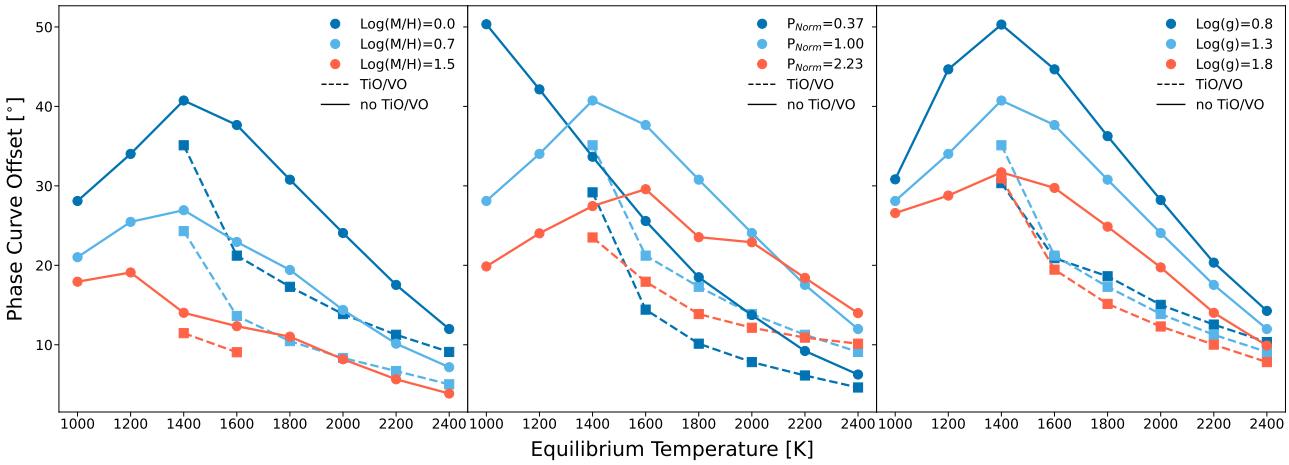


Figure 4.9: Phase curve offset for a subset of models within the grid. Each panel displays the variation in offset with $T_{\rm eq}$ due to one of: orbital period, surface gravity and metallicity, whilst the other two parameters are kept constant (when constant Log(M/H)=0.0, P_{Norm}=1, log(g)=1.3). Cross-terms between parameters are not included. **Left Panel:** Variation in offset whilst changing metallicity. **Middle Panel:** Variation in offset with different normalised orbital period. These tracks corresponds to planets tidally-locked around different stellar types. **Right Panel:** Variation in offset whilst changing surface gravity.

to lower phase offsets at higher temperatures. The trends in both increasing metallicity and surface gravity can again be explained by the reduced pressure of the photosphere, where a shorter radiative timescale will result in a lower hotspot shift from the substellar point. The presence of TiO and VO significantly reduce the phase offset in all cases, again due to the reduction in heat redistribution efficiency caused by the strong near UV/optical absorption in the upper atmosphere of the day-side. The presence of TiO/VO causes a portion of the energy to re-emitted directly from the stratosphere instead of the IR-photosphere, which leads to a smaller hotspot offset.

The phase offset appears to peak between equilibrium temperatures of 1400-1600K, with models at lower temperatures having reduced offsets. This behaviour is also found in Komacek et al. (2017) (see their Figure 9). This is due to homogenisation of temperature at these lower equilibrium temperatures, caused by longer radiative timescale, which can be seen in Figure 4.1. Because of this, their phase offset is determined by small, wavenumber-2 variations of the thermal structure. The effect of rotation period on the phase offset (via the implied planetary rotation rate) is more complex, which we discuss in the next section.

4.4.2 Offset Trend with Period

As we saw in Section 4.3.4, larger rotation period leads to more efficient heat redistribution (smaller f-factor). Based on simple energy balance models (Cowan & Agol 2011), which assume heat is transported by a jet and that advection is balanced by radiative cooling, we would therefore expect phase curve offsets to increase with increasing period, as was proposed by May et al. (2022) based on Spitzer phase curve observations.

However, as shown in Figure 4.10, systematically in our models the offset first increases with period then, at long period past a critical point, *decreases* with period. This shows a very different behaviour than for the heat redistribution which varies monotonically with period (see Figure 4.7). We also notice that the position of this turning point in period appears to be

a function of equilibrium temperature.

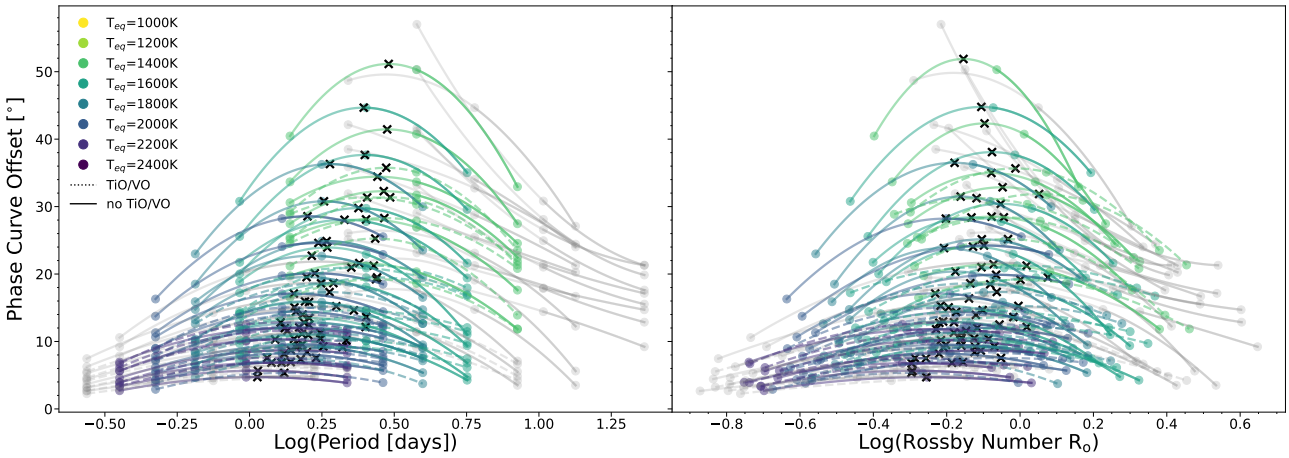


Figure 4.10: Left Panel: Phase curve offset for all models plotted against log(period). **Right Panel:** Phase curve offset for all models plotted against log(Ro_T). In both plots, models with a larger offset at P_{Norm}=1 than at P_{Norm}=0.37 or 2.23 are colour coded in equilibrium temperature. Any models that do not satisfy this criteria are in grey. The black crosses display the maxima of the curve fitted to these models. Models with TiO and VO are shown in dashed lines and those without in filled lines.

We can explain this trend, and the fact that heat redistribution and phase curve offsets behave differently, by considering the competition between the divergent and the rotational component of the circulation (as in Hammond & Lewis (2021); Lewis & Hammond (2022)) and their impact on the Doppler shifting of Rossby waves. Whereas both components contribute to the heat redistribution, only the rotational component contributes to the phase curve offset. Therefore, planets with a strong divergent component can have a small phase curve offset despite having a significant heat transport efficiency. The position of the peak of the rotational circulation is approximated by Equation 12 of Hammond & Pierrehumbert (2018), from which we derive the following expression for the longitudinal shape $R(\theta)$ of the wavenumber-1 rotational circulation:

$$R(\theta) = \mathbb{R}\mathrm{e}\left\{\frac{\cos(\theta) + i\sin(\theta)}{(1/\tau_{\mathrm{rad}}) - i\,(\omega_m - \bar{U})}\right\} \tag{4.5}$$

where θ is longitude (with $\theta = 0$ at the substellar point), τ_{rad} is the radiative timescale, ω_m is the Rossby wave frequency (which increases with increasing Ω), and $\bar{U}$ is the jet speed.

This equation is valid only in the rotationally dominated regime (e.g. for short rotation periods). It shows the balance between the radiative damping ($1/\tau_{\mathrm{rad}}$ term), that tends to drag the offset towards zero, the Rossby wave ($-i\omega_m$ term), that tends to drive the offset towards negative values, and the jet speed ($+i\bar{U}$ term), that tends to increase the hot spot offset. For a given equilibrium temperature (and thus a given radiative timescale), a change in rotation period would change both terms in the imaginary part of the denominator. In our grid, as the rotation period increases from $P_{\mathrm{norm}} = 0.37$ to $P_{\mathrm{norm}} = 1$, the coriolis force decreases and ω_m decreases. At the same time, the strength of the wind speed stays roughly constant, but the size of the equatorial jet increases (see Figure 4.2), so the term $+i\bar{U}$ increases. Overall, this means that the eastward shift from the jet becomes larger than the westward shift from the Rossby waves, leading to an increase of the eastward shift with increasing period.

When the normalised period goes from P_{norm} =1 to 2.23, both the jet speed and the Rossby wave speed reduce significantly. Therefore the divergent circulation (Hammond & Lewis 2021; Lewis & Hammond 2022), which by definition has no offset, becomes more and more dominant compared to the rotational circulation. This leads to an offset that decreases with increasing period.

In summary we find that for a given equilibrium temperature, at short orbital periods the circulation is dominated by the rotational component, which, because the Rossby wave speed decreases with increasing period while the jet becomes wider, leads to an offset that increases with period. Then, for larger rotation periods, the divergent circulation becomes more and more dominant, leading to an offset that decreases with increasing period.

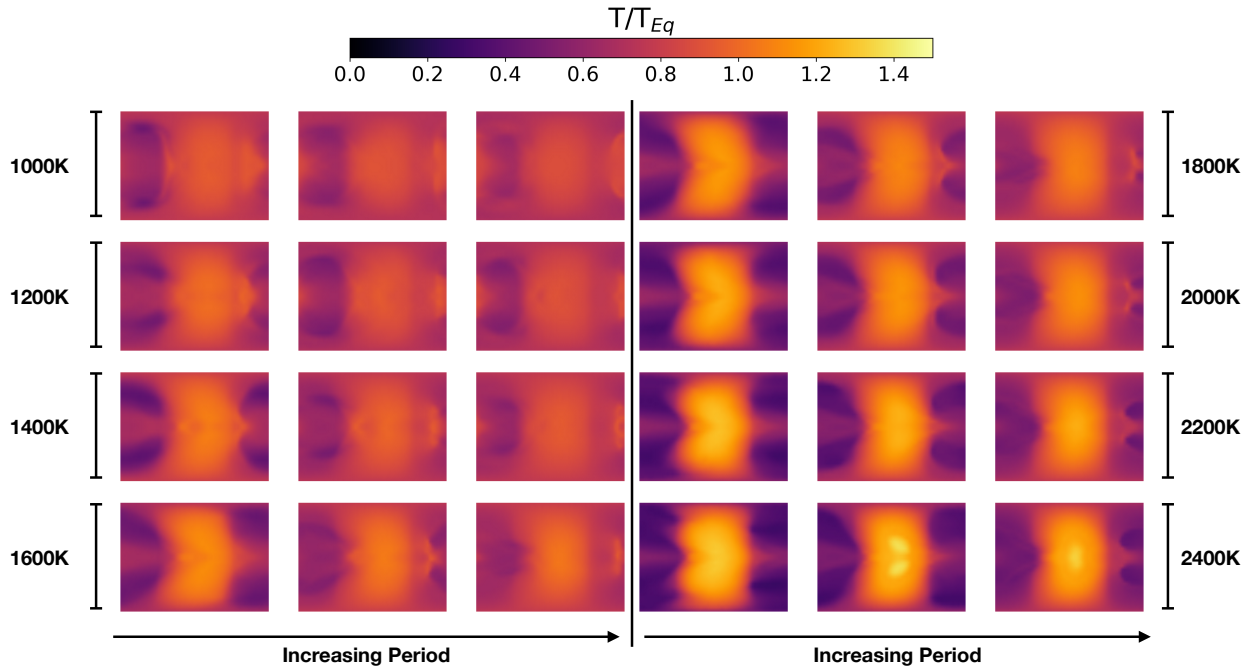


Figure 4.11: Latitude vs longitude thermal structure, at the 1.4 micron photosphere, for the subset of models displayed with solid lines in the middle panel of Figure 4.9. Equilibrium temperature increases down columns and orbital period increases along rows.

To illustrate this behaviour, the thermal structure at the photosphere for our models at differing periods is plotted in Figure 4.11. Taking the 1800K row, in the leftmost plot we can clearly see the circulation Doppler-shifting, according to the terminology in Hammond & Pierrehumbert (2018), the Rossby wave towards the evening terminator, with the divergent circulation present at higher latitudes. In the centre column, the Doppler shift has increased, shifting the overall hot-spot further eastward. In the rightmost column, the magnitude of the rotation has now decreased to the point where the divergent circulation is now pulling the hot-spot back towards 0°.

Figure 4.10 shows that the maximum phase offset occurs at different orbital periods for different equilibrium temperatures. We can explain this by estimating that the peak phase shift will occur when $\bar{U}$ is larger than ω_m in Equation 4.5. We estimate the ratio of these two quantities as the Rossby number, Equation 2.22, using the jet speed as the characteristic velocity scale.

The right panel of Figure 4.10 displays the phase curve offset plotted against R_o. For those sets of models which display turning points, the maxima of the fitted curves are all found between values of $R_o \sim 0.5 - 1$, supporting the argument that the rotational phase shift depends on the balance of the jet speed and Coriolis parameter. This trend breaks down for lower equilibrium temperatures. However, as explained in the previous section, these planets have a very uniform brightness temperature due to their long radiative timescale, and so their phase offset is determined by small variations in the thermal structure.

It should be noted that although all of the offset values calculated for our model grid are positive, negative values of the phase curve offset have been previously observed in certain wavelength bands (Dang et al. 2018; Esteves et al. 2015). Westwards optical phase offset can be explained by clouds on the western limb (Parmentier et al. 2016). MHD has also been suggested as a potential cause for westwards offsets (Hindle et al. 2021; Rogers & Komacek 2014).

4.4.3 Combined Parameter Trends: Offset

To investigate the combined effect of the parameters we perform the same calculation from Section 4.3.5 for the phase curve offset. The mean and standard deviation for each parameter Δ is shown in Figure 4.12. The offset, as expected, has a much more complex dependency on the parameters. Increasing both surface gravity and metallicity reduces the offset across the board, with the metallicity having the larger impact of the two. Whereas increasing period first increases the offset then reduces it, as explained in the previous section. However, the standard deviation in the impact of period is large, indicating that cross parameters can drastically affect this relationship.

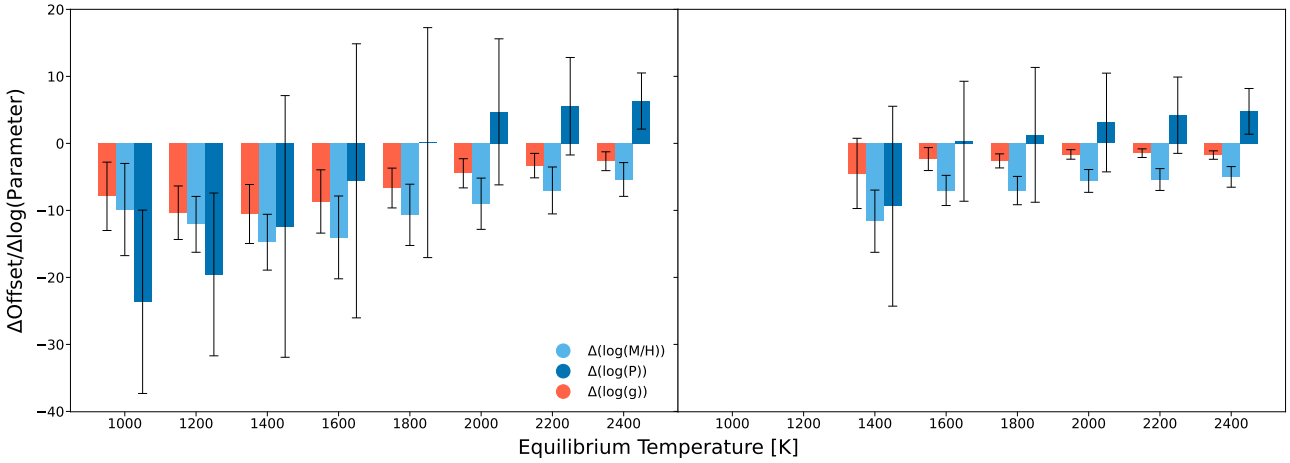


Figure 4.12: Relative impact of each planetary parameter on phase curve offset. The y-axis of each plot is the change in the offset divided by the change in the log of each planetary parameter. The x-axis is the Equilibrium temperature. Light blue denotes the change due to metallicity, dark blue the change due to period and red the change due to surface gravity. The error bars display the standard deviation in the impact of each parameter. **Left Panel:** Models with TiO/VO removed. **Right Panel:** Models containing TiO/VO.

Phase curve offsets are most sensitive to gravity, metallicity and periods in the 1000-1600K range. The same trends can be seen in the models containing TiO/VO, although

notably here the offset is much less significantly affected by the parameters, due to the substellar temperature inversion having a dominating effect on the hotspot position.

4.4.4 Amplitude

The relative amplitude is a measure of the maximum brightness contrast between hemispheres, and so is intrinsically linked to the heat redistribution which we discuss in Section 4.3. It has been defined in a few different ways throughout literature. When investigating atmospheric energy balance (i.e (Cowan et al. 2012; Komacek & Showman 2016; Komacek et al. 2017; Schwartz & Cowan 2015)) it is often defined as the day-night brightness temperature contrast. Here we define the relative amplitude in terms of the phase curve fluxes (Parmentier & Crossfield 2018; Perez-Becker & Showman 2013):

$$A = \frac{F_{p,\max} - F_{p,\min}}{F_{p,\max}}. \tag{4.6}$$

Figure 4.13 displays the phase curve amplitude tracks at different grid parameters, in the same way as Figures 4.7 and 4.9 do for the redistribution factor and offset respectively. The less efficient that day-to-night heat redistribution is, the larger the phase curve amplitude is expected to be. Because of this, it follows the same trends as the heat redistribution - increasing with temperature (Komacek & Showman 2016; Pluriel et al. 2020), metallicity and surface gravity, but decreasing with orbital period.

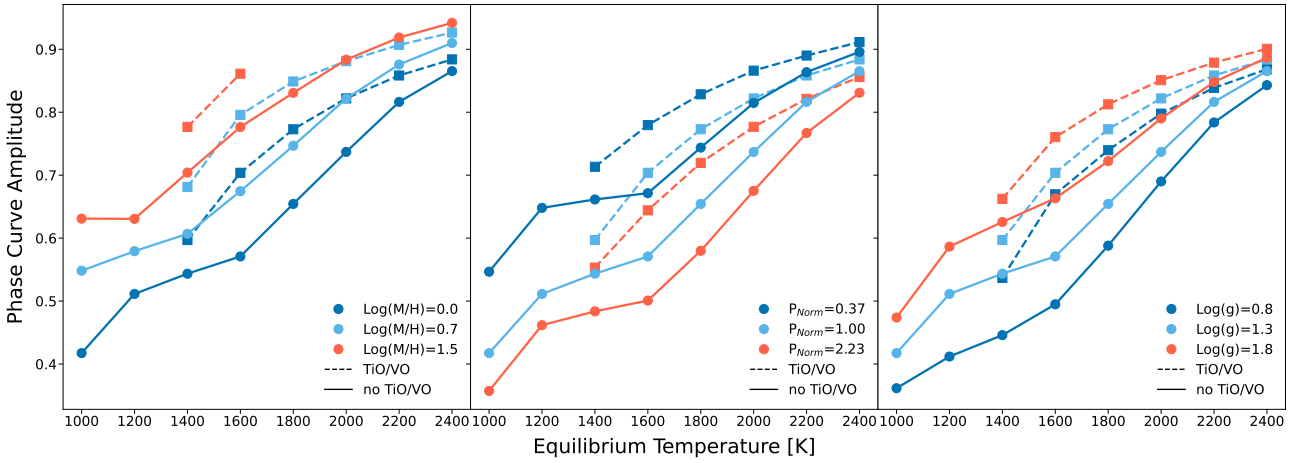


Figure 4.13: Phase curve amplitude for a subset of models within the grid. Each panel displays the variation in offset with $T_{\rm eq}$ due to one of: rotation period, surface gravity and metallicity, whilst the other two parameters are kept constant (when constant Log(M/H)=0.0, P_{Norm}=1, log(g)=1.3). Cross-terms between parameters are not included. Models excluding and including TiO/VO are displayed with solid and dashed lines respectively. **Left Panel:** Variation in amplitude whilst changing metallicity. **Middle Panel:** Variation in amplitude with different normalised orbital period. These tracks corresponds to planets tidally-locked around different stellar types. **Right Panel:** Variation in amplitude whilst changing surface gravity.

4.4.5 Amplitude and Offset are Set by Different Mechanisms

Energy balance models based on advection of heat by a jet would lead to the conclusion that phase curve offset and amplitude should directly correlate with each other, with high

winds expected to produce efficient heat redistribution and a large phase shift. However, Figure 4.14 shows that the amplitude in our models decreases monotonically with increasing period. This is in direct contrast to the non-monotonic trend found for the offset (Figure 4.10).

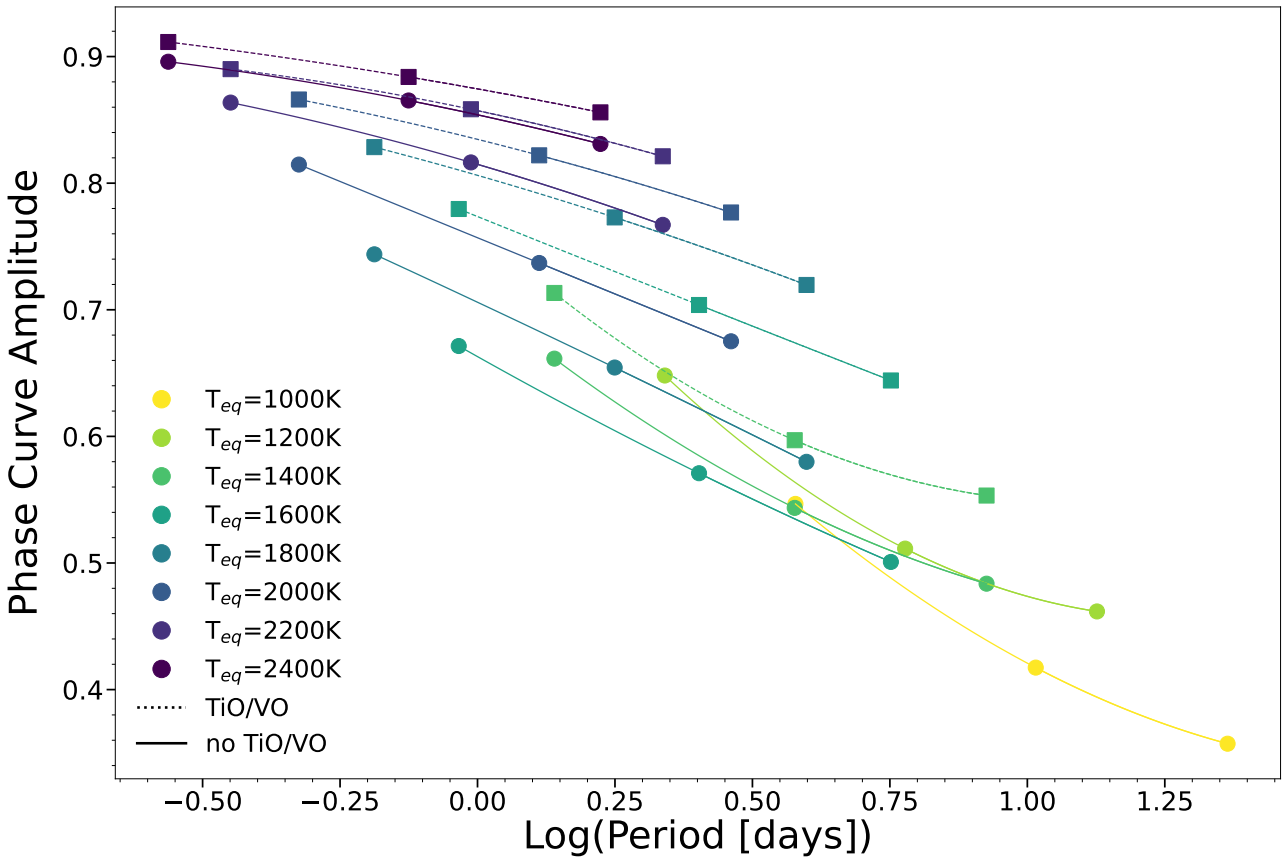


Figure 4.14: Phase curve amplitude for the subset of models shown in Figure 4.11 (Log(M/H)=0.0, log(g)=1.3)) plotted against log(period).

This highlights that phase curve offset and phase curve amplitude are not set by the same component of the atmospheric circulation. The amplitude of the phase curve increases when heat redistribution becomes less efficient. As both the jet and the day-to-night flow contribute to the heat transport, the phase curve amplitude is sensitive to the sum of the rotational and divergent components of the circulation. On the contrary, rotational and divergent parts of the circulation affect the phase curve offset in opposite directions. The rotational part tends to increase the offset whereas the divergent part tends to reduce it. As a consequence, the offset depends on the *relative* strength of divergent and rotational flow whereas the amplitude depends on the *combined* strength of divergent and rotational circulation.

This means that the relationship between phase curve offset and amplitude should not necessarily be linear, which we can see in Figure 4.15 where there are two clear regimes in the amplitude vs offset trend based on the Rossby number (discussed in Section 4.4.1). For planets with short periods ($R_o \leq 1$) the amplitude increases when offset decreases. For those with long periods ($R_o > 1$) it is the opposite. We do see that a linear relationship holds for fast rotating planets, the low ($R_o \leq 1$) branch in Figure 4.15, with offset=$-103.5° \times$amplitude$+99.6°$.

However, this relationship does not hold for larger rotation periods (those with $R_o > 1$). The models deviating from the linear trend are those with $P_{norm} = 1$ (planets around ∼G0 stars, Table 3.2) between $T_{eq} = 1000 - 1600K$ and those with $P_{norm} = 2.23$ (planets around ∼F6 stars, Table 3.2) between $T_{eq} = 1000 - 2200K$. However, we expect the linear relationship between amplitude and offset to hold for planets around ∼K2 dwarfs.

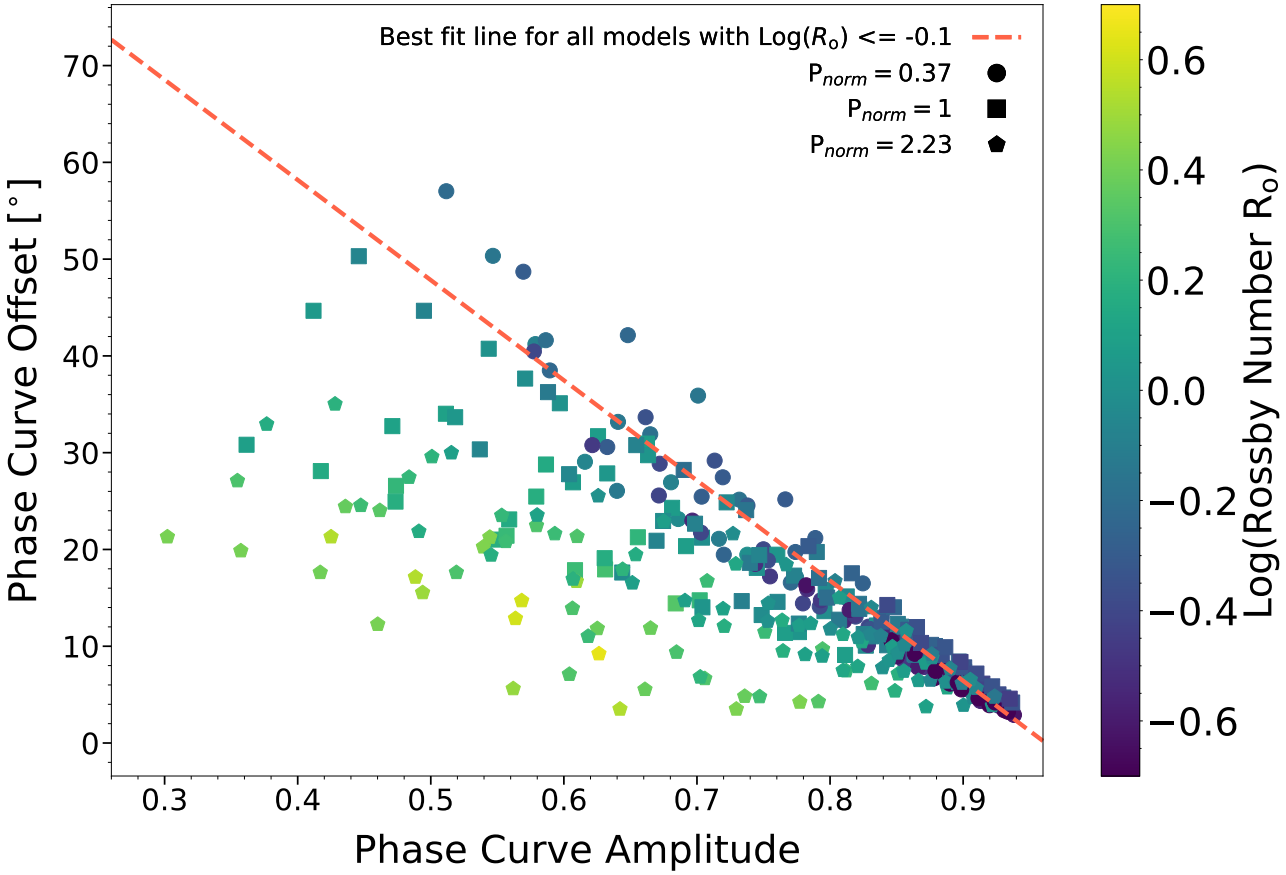


Figure 4.15: Phase curve offset plotted against amplitude for all models within the grid. Colour denotes the Rossby number of the model and shape denotes the normalised period. The red dashed line displays the best fit to the models with value of log(Ro_T)≤-0.1.

There are, however, some processes our models omit which could alter the relationship between phase curve offset and amplitude. As mentioned in Section 3.3.4, our model does not include H2 dissociation, which can have a non-negligible impact on the phase curve offset and day-night temperature contrast below 2400K (Tan & Komacek 2019). H2 dissociation reduces the day-night contrast and resulting phase curve amplitude, by transporting additional heat from the day to the night-side (Bell & Cowan 2018; Komacek & Tan 2018; Roth et al. 2021). This can reduce the speed of winds at a constant rotation period and reduce the phase-offset. Including this additional heating source could change the non-monotonic trend found between offset and rotation period to a linearly increasing trend for high temperature models. However, the effects of the H2 dissociation are greatly lessened in the presence of TiO/VO, which are likely to be present in the atmosphere at these high temperatures. Additionally, for the high temperature models, MHD effects could reduce the phase curve offsets (Beltz et al. 2022; Rogers 2017; Rogers & Komacek 2014), potentially altering the location of the turning point. Our models also do not include any clouds, which

have been shown capable of drastically changing the observable features of hot Jupiter atmospheres (Parmentier et al. 2021). The presence of clouds, particularly if mostly contained on the night-side, can increase the phase curve amplitude and decrease phase curve offset.

4.5 Temperature Contrast Between the Limbs

During transit spectroscopy one probes the limbs of a planet. Limb-to-limb variation in temperature can lead to variations in chemistry and cloud coverage. All of these lead to potential bias when interpreting transmission spectra (Line & Parmentier 2016; MacDonald & Madhusudhan 2017; Pluriel et al. 2020) and can have specific signatures in the transit light curve both at low spectral resolution (Line & Parmentier 2016) and at high spectral resolution (Ehrenreich et al. 2020; Wardenier et al. 2021).

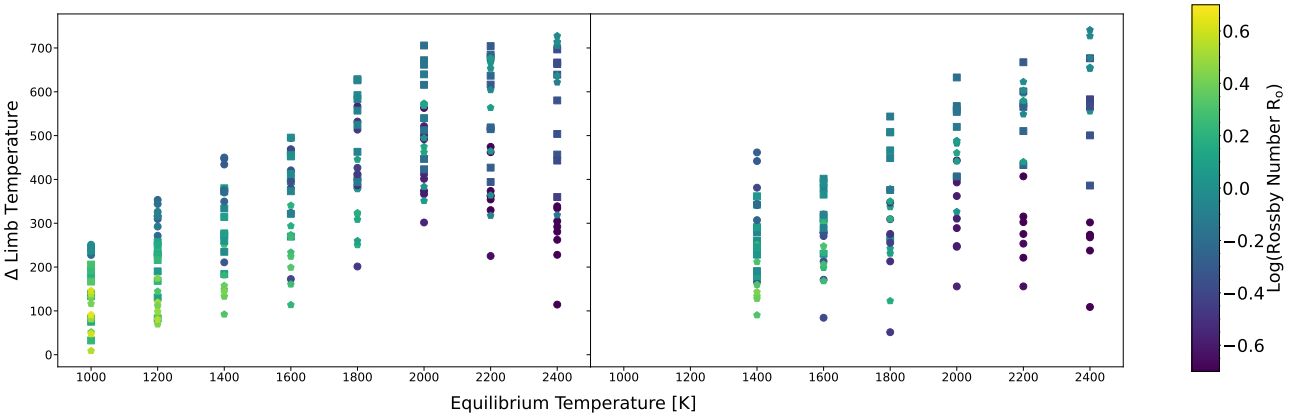


Figure 4.16: Temperature difference between the evening and morning limb pressure-temperature profiles at the transit photospheric pressure level plotted against equilibrium temperature. Each model is color coded by its Rossby number. **Left Panel:** Without TiO/VO. **Right Panel:** With TiO/VO.

Figure 4.16 shows the temperature contrast between the east and west limbs of out models at the photospheric pressure level, corrected for the transit chord optical depth by the geometric factor $\sqrt{2\pi R_p/H}$ (Fortney 2005). The temperature is calculated as the average over all latitudes and $\pm 20^\circ$ of longitude, in order to take into account the line-of-sight effect and the planet rotation during transit (Wardenier et al. 2022). A positive value here denotes an evening limb that is hotter than the morning limb. We can see that the temperature contrast does become increasingly large, although the upwards trend begins to flatten out at higher equilibrium temperatures. This is due to the combined effects of both the heat redistribution and hotspot offset. In Section 4.3 we see that heat redistribution becomes increasingly less efficient at higher equilibrium temperatures, which will naturally lead to a hotter evening limb and colder morning limb. Then, in Section 4.4.1 we see that the phase curve offset, which tracks the hotspot offset in the case of a cloudless atmosphere, reduces with equilibrium temperature. This will naturally lead to a more symmetrical structure and thus a smaller east/west contrast.

As the phase offset peaks for models with $R_o \sim 1$, models with $R_o < 1$ or > 1 will have lower phase offset and therefore more symmetrical atmospheres. At low equilibrium temperatures (T_{eq} <1600K), the heat redistribution efficiency is strong and most models have $R_o > 1$, so the limb temperature contrast is small. As the equilibrium temperature increases,

the efficiency of heat redistribution reduces, but the offset also reduces. In our models we find the limb temperature differences starts to increase, implying that the reduction to heat redistribution with equilibrium temperature must be more impactful on the limb temperatures in this regime than the offset reducing with equilibrium temperature. This behaviour is maintained between 1000-2000K. Above 2000K, the heat redistribution trend with temperature flattens out as it reaches close to its minimum (e.g large f-factor). However, the offset is still reducing with $T_{\rm eq}$, so the limb temperature difference stops increasing for models with $R_{\rm o} \sim 1$ and even decreases for those with $Ro_T < 1$.

In the presence of TiO/VO, the heat redistribution is much worse at lower temperatures. The offset is also significantly reduced. From the right panel of Figure 4.16, we can see that in this case the relationship between the limb temperature contrast appears to flatten at much lower temperatures, which is likely due to the decrease in variation for both the heat redistribution and offset when TiO/VO are present.

4.6 Summary & Conclusion

In this chapter, we show how the atmospheric circulation of hot Jupiters is affected by the large variation in planetary parameters across the population. We use our large drag free-model grid to explore the effects of these parameters on the heat redistribution, observable quantities from bolometric phase curves and limb-to-limb temperature contrast.

We show that the day-night heat redistribution in hot Jupiter atmospheres is as sensitive to the combined effects of atmospheric metallicity, rotation period and surface gravity as it is to the equilibrium temperature. We therefore expect a large scatter along the general trend of increasing heat redistribution with temperature. As a consequence, a large sample of planets will be needed to measure any trends in the hot Jupiter population by observation, unless one can control some of these parameters through careful target selection.

We find the relationship between phase curve offset and orbital period is non-monotonic within our models. With an offset that generally increases with rotation period for slowly rotating planets and decreases with rotation period for fast rotating planets. We propose that the turning point is due to the balance between the rotational circulation (i.e. the jet) and the overturning circulation, and can be characterised by the Rossby number of the atmosphere (see Equation **??**). This relationship breaks down for low equilibrium temperature models which are in a different circulation regime than the hotter planets.

We further find that phase curve offset and phase curve amplitude do not necessarily track each other. That is because the rotational and divergent part of the atmosphere both advect heat from the day to the night-side of the planet, but have counteracting effects on the hot spot offset. This competition between the rotational and divergent effects create two clear regimes within our models. For those with low periods ($R_{\rm o} \leq 1$) the amplitude increases when offset decreases, and those with long periods ($R_{\rm o} > 1$) the opposite is found. This produces a scatter in the relationship between the offset and amplitude.

We find that the combined effects of the heat redistribution and phase shift also impacts the temperature contrast between the planetary limbs. As heat redistribution becomes increasingly less efficient at higher temperatures, the evening limb becomes increasingly hotter than the morning limb, increasing the east/west temperature contrast. For the hottest planets, however, the reduced hot spot shift reduces the limb temperature asymmetries. We predict the largest limb-to-limb temperature differences for planets with $T_{\rm eq} \approx 2000K$.

Overall, we show that the combined effects of our grid parameters introduce a large degeneracy in the atmospheric state of hot Jupiters, with both the heat redistribution (which tracks phase curve amplitude) and phase curve offset shown to have a large variance depending on the specific planetary parameters. This makes attaining observational constraints for these atmospheres very complex, as multiple axis of observation are required. Our best avenue to characterize these atmospheres is therefore with broad wavelength coverage from multiple instruments, in both emission and transmission, alongside optical phase curves.

Bibliography

Arcangeli J., et al., 2018, ApJ, 855, L30
Bell T. J., Cowan N. B., 2018, ApJ, 857, L20
Bell T. J., et al., 2021, MNRAS, 504, 3316
Beltz H., Rauscher E., Roman M. T., Guilliat A., 2022, AJ, 163, 35
Charnay B., Meadows V., Misra A., Leconte J., Arney G., 2015, ApJ, 813, L1
Cowan N. B., Agol E., 2011, ApJ, 729, 54
Cowan N. B., Machalek P., Croll B., Shekhtman L. M., Burrows A., Deming D., Greene T., Hora J. L., 2012, ApJ, 747, 82
Dang L., et al., 2018, Nature Astronomy, 2, 220
Ehrenreich D., et al., 2020, Nature, 580, 597
Esteves L. J., De Mooij E. J. W., Jayawardhana R., 2015, ApJ, 804, 150
Fortney J. J., 2005, MNRAS, 364, 649
Hammond M., Lewis N. T., 2021, Proceedings of the National Academy of Science, 118, e2022705118
Hammond M., Pierrehumbert R. T., 2018, ApJ, 869, 65
Hindle A. W., Bushby P. J., Rogers T. M., 2021, ApJ, 922, 176
Kataria T., Showman A. P., Fortney J. J., Stevenson K. B., Line M. R., Kreidberg L., Bean J. L., Désert J.-M., 2015, ApJ, 801, 86
Komacek T. D., Showman A. P., 2016, ApJ, 821, 16
Komacek T. D., Tan X., 2018, Research Notes of the American Astronomical Society, 2, 36
Komacek T. D., Showman A. P., Tan X., 2017, ApJ, 835, 198
Lewis N. T., Hammond M., 2022, ApJ, 941, 171
Line M. R., Parmentier V., 2016, ApJ, 820, 78
MacDonald R. J., Madhusudhan N., 2017, MNRAS, 469, 1979
May E., et al., 2022, arXiv e-prints, p. arXiv:2203.15059
Parmentier V., Crossfield I. J. M., 2018, in Deeg H. J., Belmonte J. A., eds, , Handbook of Exoplanets. p. 116, doi:10.1007/978-3-319-55333-7˙116
Parmentier V., Fortney J. J., Showman A. P., Morley C., Marley M. S., 2016, ApJ, 828, 22
Parmentier V., et al., 2018, A&A, 617, A110
Parmentier V., Showman A. P., Fortney J. J., 2021, MNRAS, 501, 78
Perez-Becker D., Showman A. P., 2013, ApJ, 776, 134
Perna R., Heng K., Pont F., 2012, ApJ, 751, 59
Pluriel W., Zingales T., Leconte J., Parmentier V., 2020, A&A, 636, A66
Rogers T. M., 2017, Nature Astronomy, 1, 0131
Rogers T. M., Komacek T. D., 2014, ApJ, 794, 132
Roth A., Drummond B., Hébrard E., Tremblin P., Goyal J., Mayne N., 2021, MNRAS, 505, 4515
Roth A., Parmentier V., Hammond M., 2024, MNRAS, 531, 1056
Schwartz J. C., Cowan N. B., 2015, MNRAS, 449, 4192
Schwartz J. C., Kashner Z., Jovmir D., Cowan N. B., 2017, ApJ, 850, 154
Stevenson K. B., et al., 2014, Science, 346, 838
Tan X., Komacek T., 2019, in AAS/Division for Extreme Solar Systems Abstracts. p. 326.03
Wardenier J. P., Parmentier V., Lee E. K. H., Line M. R., Gharib-Nezhad E., 2021, MNRAS, 506, 1258
Wardenier J. P., Parmentier V., Lee E. K. H., 2022, MNRAS, 510, 620

Zhang M., et al., 2018, AJ, 155, 83

Chapter 5

A Large Grid of GCM Models: Spectra and the Onset of TiO/VO Revealed

The material in this chapter is based on Roth et al. (2024):
– Roth A., Parmentier V., Hammond M., 2024, MNRAS, 531, 1056

5.1 Introduction

Throughout Chapter 4 we have used our drag-free model grid to show how variations in intrinsic planetary properties can affect the thermal and dynamical structure of hot Jupiter atmospheres. However, the heat redistribution, phase curve offsets and amplitudes discussed so far have all been bolometric quantities. Observations of exoplanet atmospheres do not generally probe the bolometric quantities described above, but band averaged or spectrally resolved properties of an atmosphere. Because different band-passes probe different atmospheric depth, the band-averaged quantities can be different from the bolometric ones. For example, eclipse measurements taken via the Spitzer space telescope provide the brightness temperature of a planet's day-side in a given band-pass, which can be used to measure a 'band averaged' heat redistribution parameter (Baxter et al. 2020; Deming et al. 2023; Garhart et al. 2020).

A number of investigations have already used model grids in conjunction with observational data to better understand trends in the hot Jupiter population. Mansfield et al. (2021) use a 1D model grid to explore trends in the strength of water absorption and emission in HST/WFC3 observations, revealing the equilibrium temperature at which spectra transition from absorption to emission. Goyal et al. (2020, 2021) generate a 1D-2D model grid with a range of re-circulation factors, metallicities and C/O ratios and use this to explore population trends in the observed Spitzer thermal emission.

Therefore, in order to compare our model grid with observational data, we must take another look at the observable features from our model grid in select band-passes. To this end, we now look at two different types of population level eclipse observations: the population of planets observed with the Spitzer Space Telescope and the one observed with the Wide Field Camera 3 on board the Hubble Space Telescope and compare them to our population of modelled planets.

We provide an explanation for the sharp jump in brightness temperature that is seen by Spitzer observations of the population of hot Jupiter atmospheres (Deming et al. 2023) (Section 5.2). We then move on to inferences from investigating spectral indices for water in HST/WFC3 observations (Mansfield et al. 2021) (Section 5.3), before comparing predictions from our grid to the Spitzer phase curve observations (Section 5.4). Finally, we summarize our findings in Section 5.5.

5.2 Spitzer Band Secondary Eclipse

Over its lifetime Spitzer observed 457 eclipses of 122 hot Jupiters in its 3.6 and 4.5 microns observing modes (Deming et al. 2023). Eclipses from both channels spectra, where CH_4 and CO features are expected to be present, depending on the planets equilibrium temperature, have been re-analysed in homogeneous ways by several authors (Baxter et al. 2020; Deming et al. 2023; Garhart et al. 2020). The distribution of planet parameters observed matches well with the overall transiting planet population, as seen in Figure 3.4, making it a good representation for diversity in population level studies. Baxter et al. (2020) find that there is a transition between seeing CO in absorption to CO in emission at $T_{eq} = 1600 \pm 100$K, and are the first to attribute this to a switch to a transition between non-inverted and inverted temperature profiles. We hereafter use the recent re-analyses of Deming et al. (2023), because it is the most recent and comprehensive one. Deming et al. (2023) identify a statistically significant unexpected and sudden rise in the brightness temperatures of the population, with the brightness temperature increasing by 291±41 K between equilibrium temperatures of 1714-1818 K. Both Baxter et al. (2020) and Deming et al. (2023) therefore agree on a transition in the atmospheric state at this temperature. The primary difference is that Baxter et al. (2020) find a smooth transition in contrast to the sharp one found by Deming et al. (2023). Deming et al. (2023) propose a few explanations for this sudden rise in brightness temperature - such as the onset of magnetic drag which would inhibit longitudinal heat redistribution or the rapid dissipation of day-side clouds at these temperatures.

Here we propose a novel mechanism to explain this rise in temperature: that the sudden appearance of TiO and VO changes the thermal structure of the atmosphere and therefore alters the apparent heat redistribution efficiency. Indeed, as shown in Figure 4.6, the presence of TiO and VO in a planet's atmosphere reduces the apparent heat transport and thus increases the heat redistribution factor ($\Delta f_{\rm avg} = 0.216$). We will now look at the specific effect of TiO/VO on the brightness temperature of the Spitzer band-pass.

For this, we calculate the brightness temperature in the Spitzer band-pass in our grid of models by first fitting a blackbody to the spectral region of the Spitzer band-passes. We can then use the temperature of this blackbody as the brightness temperature and compare with the equilibrium temperature of our models.

We show the difference between day-side brightness temperature and equilibrium temperature in Figure 5.1. This difference would be zero for a planet with full heat redistribution, and would be $(2.66^{1/4} - 1) \times T_{\rm eq}$ for a planet with no heat redistribution. In between these two extremes, the band averaged redistribution value depends on both the day-to-night heat transport and on the spatially varying chemical composition of the planet, thus sometimes leading to negative values (Dobbs-Dixon & Cowan 2017). Figure 5.1 shows two tracks in the brightness temperature versus equilibrium temperature, corresponding to models in chemical equilibrium and to models where TiO/VO have been artificially removed from the atmosphere. Both tracks have a brightness temperature that increases relative to the equilibrium temperature as the equilibrium temperature gets larger. This is a direct consequence of the heat redistribution parameter that increases with equilibrium temperature, as shown in Figure 4.6.

Additionally, we can see that the with and without TiO/VO model tracks are offset by ∼50-300K depending on the equilibrium temperature. This was discussed in Section 4.3 and is due to TiO/VO intercepting and re-radiating part of the stellar flux at very low pressures, where the radiative timescales are very short. Overall, this reduces the heat transport to the

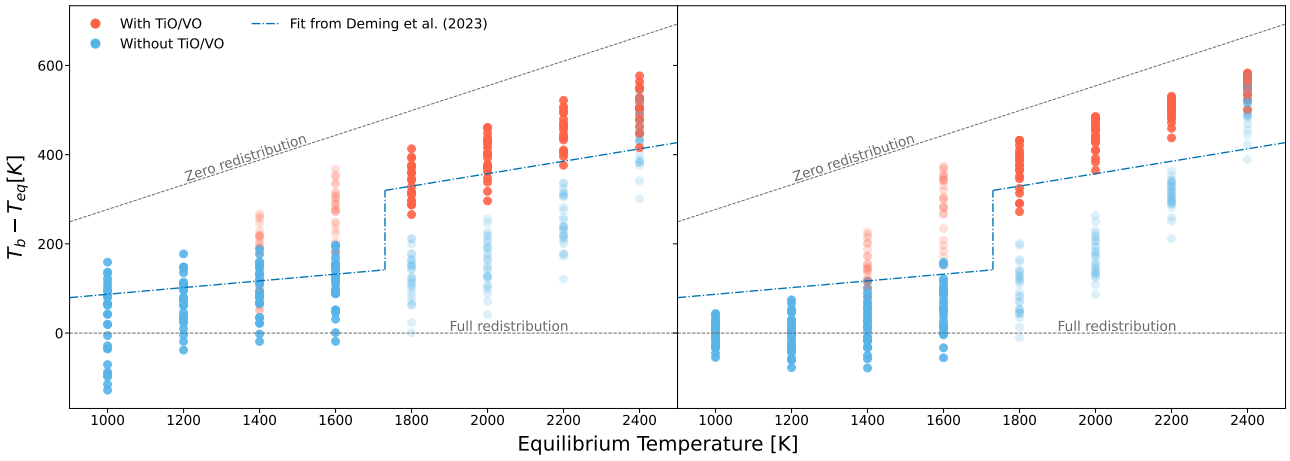


Figure 5.1: Comparison between the Spitzer band-pass brightness temperatures and model equilibrium temperatures. The opacity of points containing TiO/VO with equilibrium temperatures below the transition temperature found in Deming et al. (2023), and points not containing TiO/VO above the transition temperature, have been reduced to emphasise the transition. The blue dashed line corresponds to the fits seen in Figure 3 of Deming et al. (2023). **Left Panel:** Spitzer 1 (3.6 microns). **Right Panel:** Spitzer 2 (4.5 microns).

planetary night-side and increases the planet brightness temperature.

Figure 5.1 also compares our population of models with the best fit to the population of planets proposed by Deming et al. (2023), which consists of a rising slope at low equilibrium temperature, a jump around 1714-1818 K, and a gentle slope at high equilibrium temperature. Without any adjustment, we can see that the best fit to the observed population of planets falls right inside our population of models, with the low temperature fit corresponding to the models without TiO/VO and the high temperature fit corresponding to the models with TiO/VO. We do note, however, that towards very high temperatures the Deming et al. (2023) fit lies slightly below the TiO/VO models. Given that the parameter distribution of the Spitzer observations is representative of the wider hot Jupiter population (see Figure 3.4 for this comparison), and not weighted towards planets with parameters that would give lower values here, one possible cause is partial depletion of TiO/VO in these atmospheres, which we discuss with more detail in Section 5.2.

We now show in Figure 5.2 the brightness temperature difference between models with and without TiO/VO, with all other parameters being constant (e.g. size of the 'jump' in Figure 5.1 between equivalent models). We see that the position and amplitude of the jump observed by Deming et al. (2023) (black cross in Figure 5.2) aligns very well with the model predictions if the population of planets jumps from the models with TiO/VO to the ones without TiO/VO at around 1800K. We therefore conclude that the appearance of TiO/VO between 1714K and 1818K can explain the jump in brightness temperature observed in the population of hot Jupiters.

This would align well with observational evidence suggesting the appearance of gaseous TiO/VO in atmospheres at around this temperature range. Parmentier et al. (2016), for instance, predict the transition to occur at $\leq$1900K based on the large apparent albedos for Kepler-76 b and HAT-P-7 b , and improved fitting of Kepler light-curves for planets above this temperature. This transitional temperature is consistent with cold trap models (Beatty et al. 2017; Parmentier et al. 2013, 2016) and the temperature predicted for deep cold traps

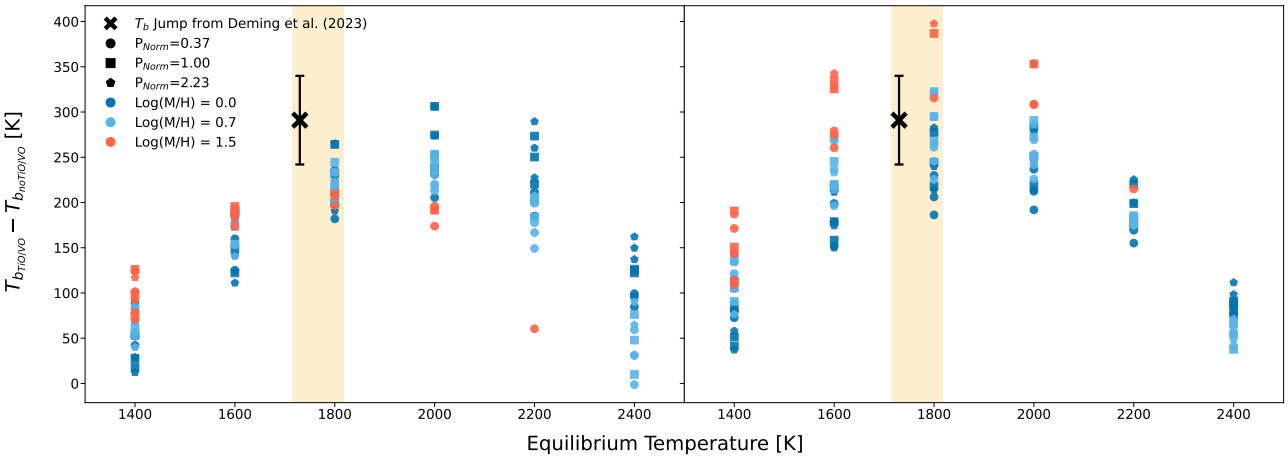


Figure 5.2: Difference between the day-side brightness temperature for models containing and not containing TiO/VO. The yellow shaded region displays the temperature range of the abrupt increase in emergent flux from Deming et al. (2023). The black cross shows the exact value found in Deming et al. (2023). **Left Panel:** Spitzer 1 (3.6 microns).**Right Panel:** Spitzer 2 (4.5 microns).

to possibly occur from micro-physical cloud models (Powell et al. 2018). Importantly, the trends shown in Figure 5.1 and 5.2 do not rule out the smooth transition found in Baxter et al. (2020). In fact, Figure 5.1 in particular can explain both trends. If the appearance of TiO/VO at the transition temperature is modified by partial depletion, the transition between the non-inverted to inverted regimes may well be smoothed out as the fractions of TiO/VO in the atmospheres naturally increase with increasing temperature.

We further note that, although our modelled planets have a large scatter along the temperature trend ($\sigma \sim 104$K, which increases to $\sigma \sim 166$K when the error bars from the observed Spitzer population are included), this scatter is significantly smaller than the one seen in the population of Spitzer data points ($\sigma \sim 221$K). We conclude that either additional mechanisms lead to an additional scatter around the mean value compared to our expectation (e.g. chemical disequilibrium, presence of night-side clouds, atmospheric drag), or that the Spitzer IRAC instruments have additional noise that increases the scatter of the population (Hansen et al. 2014).

We now wonder whether this jump would be seen with other instruments, such as HST/WFC3. We show in Figure 5.3 the difference between the brightness temperature minus the equilibrium temperature for a single model at 1800K, with and without TiO/VO, as a function of wavelength. We can see that the size of the jump is highly dependent on the wavelength. This is because different wavelengths probe different depths in the atmosphere. Because TiO/VO changes both the heat redistribution and the vertical structure of the thermal profile, at some wavelengths (or some pressure levels) the reduction of the heat redistribution (due to the presence of TiO/VO) is compensated by the cooling of the atmosphere below the thermal inversion due to the anti-greenhouse effect (Parmentier & Guillot 2014). This is particularly prevalent in the WFC3 band-pass, where no specific jump in the population would be expected.

We would therefore predict that if a similar population study using HST/WFC3 observations were to be carried out, then the brightness temperature increase would be absent altogether. However, over a wavelength range such as that probed by the JWST/NIRSPEC/G395 instrument (2.87–5.14μm) or by JWST/MIRI (5-28μm) the signature of this tran-

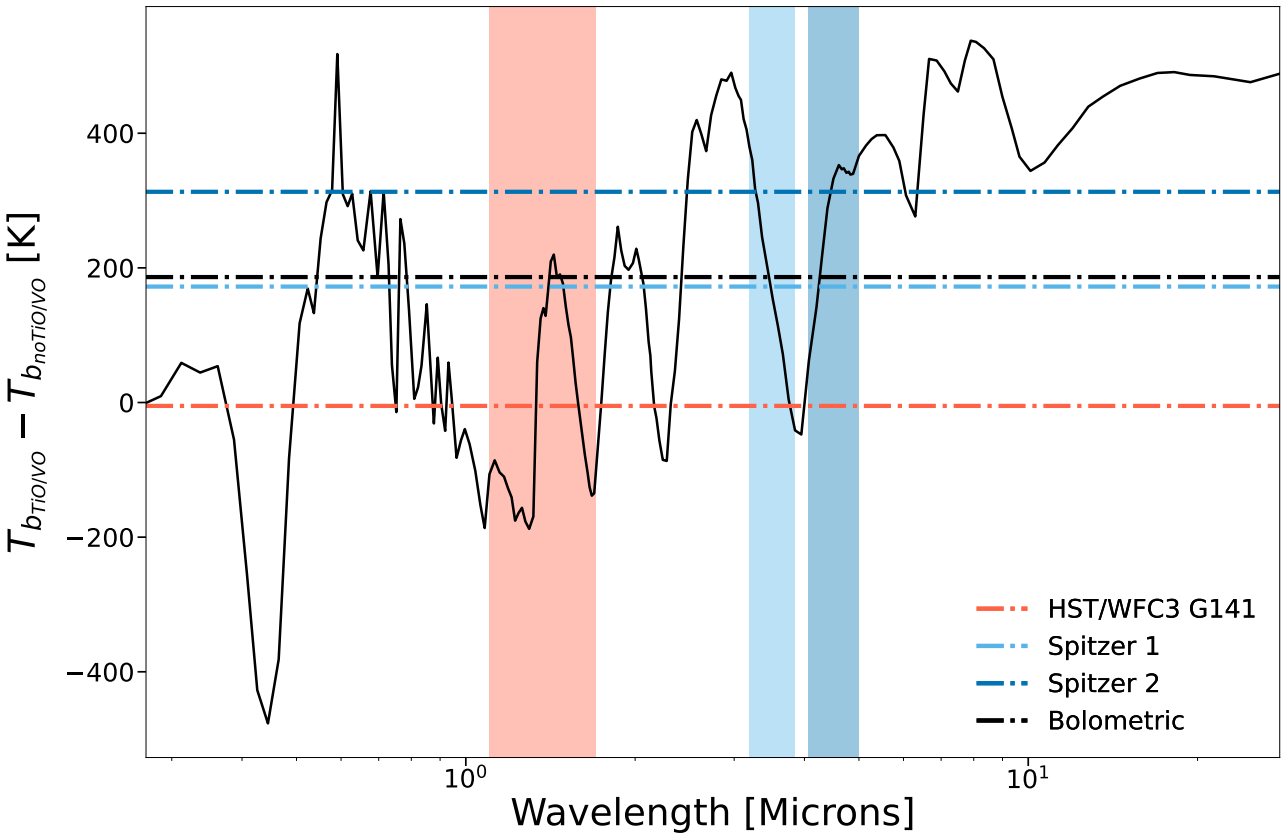


Figure 5.3: This figure shows $T_{b_{TiO/VO}} - T_{b_{noTiO/VO}}$ for an 1800K model over all wavelengths. The red, light blue and dark blue shaded regions show the HST/WFC3, Spitzer 1 and Spitzer 2 band-passes respectively. Dashed lines of the same colors represent the average value within each band-pass.

sition would be larger.

5.3 Spectral Feature Strength

The thermal flux emitted by a planet's day-side can be measured by observing its eclipse behind the star. When the spectroscopic eclipse is measured, the spectra can provide insights into the thermal profile of the planet. In particular, the spectra can be used to determine whether the thermal profile is increasing with decreasing pressure (an inverted atmosphere that produces emission features) or whether it is decreasing with decreasing pressure (a non-inverted atmosphere with absorption features). Therefore, another way to probe the TiO/VO to no TiO/VO transition at the population level is to look at the spectral variation of the water feature within the HST/WFC3 band-pass, where water has a strong molecular feature between 1.35-1.48μm. When this feature transitions from absorption to emission, it indicates that a temperature inversion is present in the atmosphere. For hotter planets the combination of thermal dissociation and the appearance of H- opacities reduces the spectral feature of water and brings the spectrum close to a blackbody. If the transition from TiO/VO to no TiO/VO happens at cooler temperatures than the onset of dissociation, we would expect a sharp transition between planets with inverted thermal profile and thus emission features (such as Cont et al. (2022); Coulombe et al. (2023); Evans et al. (2016)) to planets with

non-inverted thermal profile and thus absorption features (such as Kreidberg et al. (2014); Line et al. (2016)).

The Hubble Space Telescope has observed the eclipse of 21 planets with the WFC3 instruments. A spectral index was determined by Mansfield et al. (2021) in order to reduce these points (Initially 19 in Mansfield et al. (2021), with later additions in Fu et al. (2022); Mansfield et al. (2022)) into a single index value. The WFC3 index measures the departure of the 1.4 micron feature (usually due to water) to the underlying continuum. To calculate it we first fit a a blackbody to two 'out-of-band' regions between 1.22-1.33μm and 1.53-1.61μm, where water absorption in the band-pass is minimal. The temperature of this blackbody is then referred to as the observed day-side temperature, T_{day}. The water feature strength in the 1.35-1.48μm 'in-band' region is then calculated by (Mansfield et al. 2021):

$$S_{H_2O} = \log\left(\frac{F_{\text{blackbody,in-band}}}{F_{\text{planet,in-band}}}\right). \tag{5.1}$$

Based on this definition, positive values correspond to a water feature observed in absorption, and negative values to a water feature observed in emission.

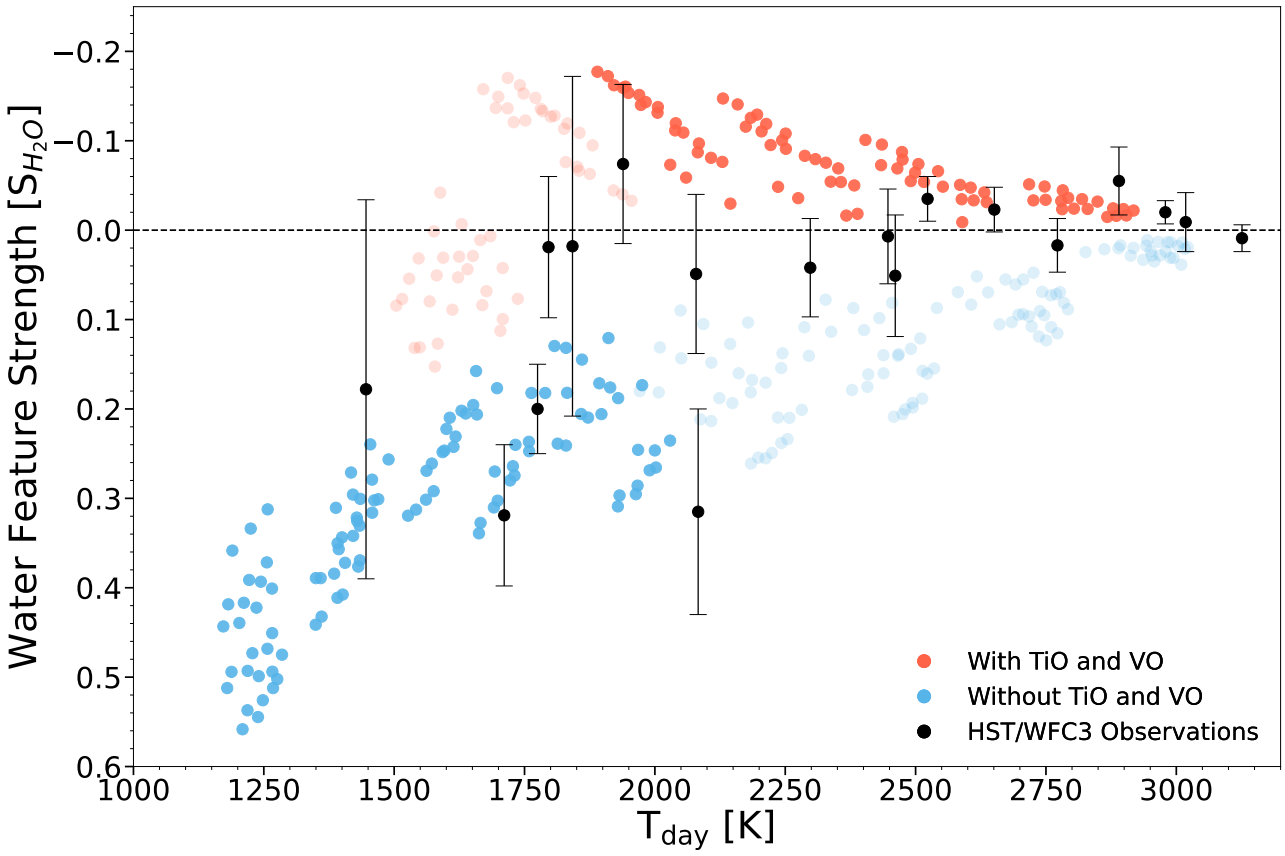


Figure 5.4: This figure shows a comparison between the water feature strength calculated for the drag-free 3D GCM grid and observational data. The opacity of points containing TiO/VO with equilibrium temperatures below the transition temperature found in Deming et al. (2023), and points not containing TiO/VO above the the transition temperature, have been reduced to emphasise the transition. The blue points are models without TiO/VO, the red points are the models with TiO/VO and the black points with error-bars are the observational data from Fu et al. (2022); Mansfield et al. (2021, 2022).

In Figure 5.4 the water feature strength for all models within the grid can be seen when compared to observations from HST/WFC3 seen in Fu et al. (2022); Mansfield et al. (2021, 2022). In our models we see that, when TiO/VO are absent from the models, the water feature is seen in absorption (negative index value) and the strength of the water feature decreases with increasing temperature as the day-side thermal profile becomes more isothermal for more irradiated planets. When TiO/VO are present, the water feature is initially seen in absorption below $T_{\rm day} \sim 1700$K, where the TiO/VO begin to condense out of the atmosphere in chemical equilibrium. The feature rapidly swaps to emission above this temperature, with the strength of emission decreasing towards higher temperature models. Both models containing TiO/VO, and those without, are seen to converge towards the zero line at high day-side temperatures. This occurs as increasing quantities of water are thermally dissociated in the atmosphere at high temperatures and H- opacities start filling the gap in the water bands (Parmentier et al. 2021).

Figure 5.4 further shows that our models are able to encompass all the observed datapoints. Particularly, we see that the spread of the water feature strength index becomes smaller at high equilibrium temperatures, where the dissociation of water and the H- opacity reduce the water feature strength in all planets.

Looking in more details, we see that the observations seem to lie in between the models with TiO/VO and those without TiO/VO for the 1800-2500K T_{day} range. Particularly, we do not see the large emission features that should be prominent for planets in the 1800K-2000K range. Similarly, we do not see the strongly absorbing water features expected by the no TiO/VO models in that specific range of temperatures.

One possible explanation is that TiO/VO is indeed present in these atmospheres, but at a smaller abundance than in the chemical equilibrium prediction. This could happen due to deep or day/night partial cold trap mechanisms (Beatty et al. 2017; Parmentier et al. 2016; Pelletier et al. 2023; Spiegel et al. 2009), which are omitted from our 3D models, or to original elemental Ti and V depletion. Pelletier et al. (2023), for instance, recently detected VO but no TiO in WASP-76 b ($T_{\rm eq} = 2228$K), and suggest condensation of TiO to be responsible. Such a partial depletion of TiO/VO would naturally bring the models between the TiO/VO and no TiO/VO tracks in Figure 5.4, allowing a closer match to the data.

We note that the partial reduction of TiO/VO, which we argue can explain the HST data set, does not necessarily rule out our explanation for the sharp increase in brightness temperature in the Spitzer data set. Indeed, the TiO/VO models in Figure 5.1 lie above the observations, and partial depletion of TiO/VO could easily lower the model track and lead to a better agreement with the observations. To determine if this works quantitatively would require models with partial TiO/VO abundances, which are out of the scope of the current study. Nonetheless, we believe that the current Spitzer data provides compelling argument for future ground-based optical high-resolution observations in order to determine the TiO and VO abundances in these atmospheres.

Another possible explanation for the damped features in the HST/WFC3 band-pass would be that the H- abundance is larger than expected by our models. This could be due to an increase in alkali abundances, which are the prime source of electrons for the H-. As for the partial TiO/VO abundance scenario, we leave this for a future study.

5.4 Spitzer Phase Curve Offset & Amplitude

Spitzer observed 21 phase curves of hot Jupiters in its 3.6 μm and 4.5 μm bands. For those planets within the equilibrium temperature bounds of our grid, we use the uniform re-analysis of Bell et al. (2021) where available (for the 4.5 μm band). For those not included in Bell et al. (2021), we use the values summarised in May et al. (2022) for Qatar-2 b, WASP-34 b, WASP-52 b and WASP-104 b. We also exclude HD 149458 b from our data set, as done in Zhang et al. (2018).

Figure 5.5 displays the phase curve offsets and amplitudes calculated from the model grid compared to the Spitzer/IRAC 4.5μm band observations. The model grid shows the amplitude to increase with the equilibrium temperature and decrease with orbital period. Overall, the trend with equilibrium temperature matches the observations quite well, with a few outliers at lower temperatures. These outliers (Qatar-2 b, WASP-34 b (May et al. 2022), CoRoT-2 b, Qatar-1 b (Bell et al. 2021) and WASP-43 b (May & Stevenson 2020)), with amplitudes close to unity, are likely due to night-side clouds, which are omitted from our models and would significantly reduce the night-side brightness temperature and increase observed amplitude. In particular, for WASP-43 b, night-side clouds have been postulated to be the reason for the observed amplitude (Kataria et al. 2015; Parmentier et al. 2021; Venot et al. 2020). One feature that seems to be present in the data and not in the models is the sudden jump to lower amplitudes for planets with orbital periods larger than 1 day. However, we do not have an explanation for this potential jump.

As our model grid omits all processes which could cause negative phase curve offsets, we will focus on comparison only to ones with positive values. The trend in offset with equilibrium temperature is remarkably consistent between the models and observations, decreasing for higher equilibrium temperatures. The observational data also matches the model grid well when compared by period. In our models we clearly see the turning point behaviour detailed in Section 4.4.1. However, there is no observed data beyond periods of $\sim$4 days for which the offset would begin to noticeably decrease if following the model grid trend.

Overall, from this comparison we can see that the spread of values observed for both phase curve amplitude and (positive) offset can be induced by the varying planetary parameters within our model grid.

5.4.1 Spitzer 3.6 micron Phase Curve Data Comparison

For the 3.6 μm band, we take the values of phase curve offset and amplitudes from Parmentier & Crossfield (2018) with a correction for HAT-P-7 b found in Parmentier et al. (2021). We take the values of May et al. (2022) for Qatar-2 b, WASP-52 b, Beatty et al. (2019) for KELT-1 b. For WASP-43 b we use the most resent re-analysis of May & Stevenson (2020).

Figure 5.6 displays a comparison between the model grid and phase curve offsets and amplitudes observed in the Spitzer/IRAC 3.6μm band-pass. The results here follow much the same trends as the 4.5μm data found in Section 5.4, with the trends and scatter in the observational data well produced by the model grid. We also find the noticeable turning point in the phase curve offset for the model grid, but lack the planetary observational data with long enough periods to observe this. In the 3.6μm band-pass we also observe a turning point in the amplitude with both increasing equilibrium temperature and period.

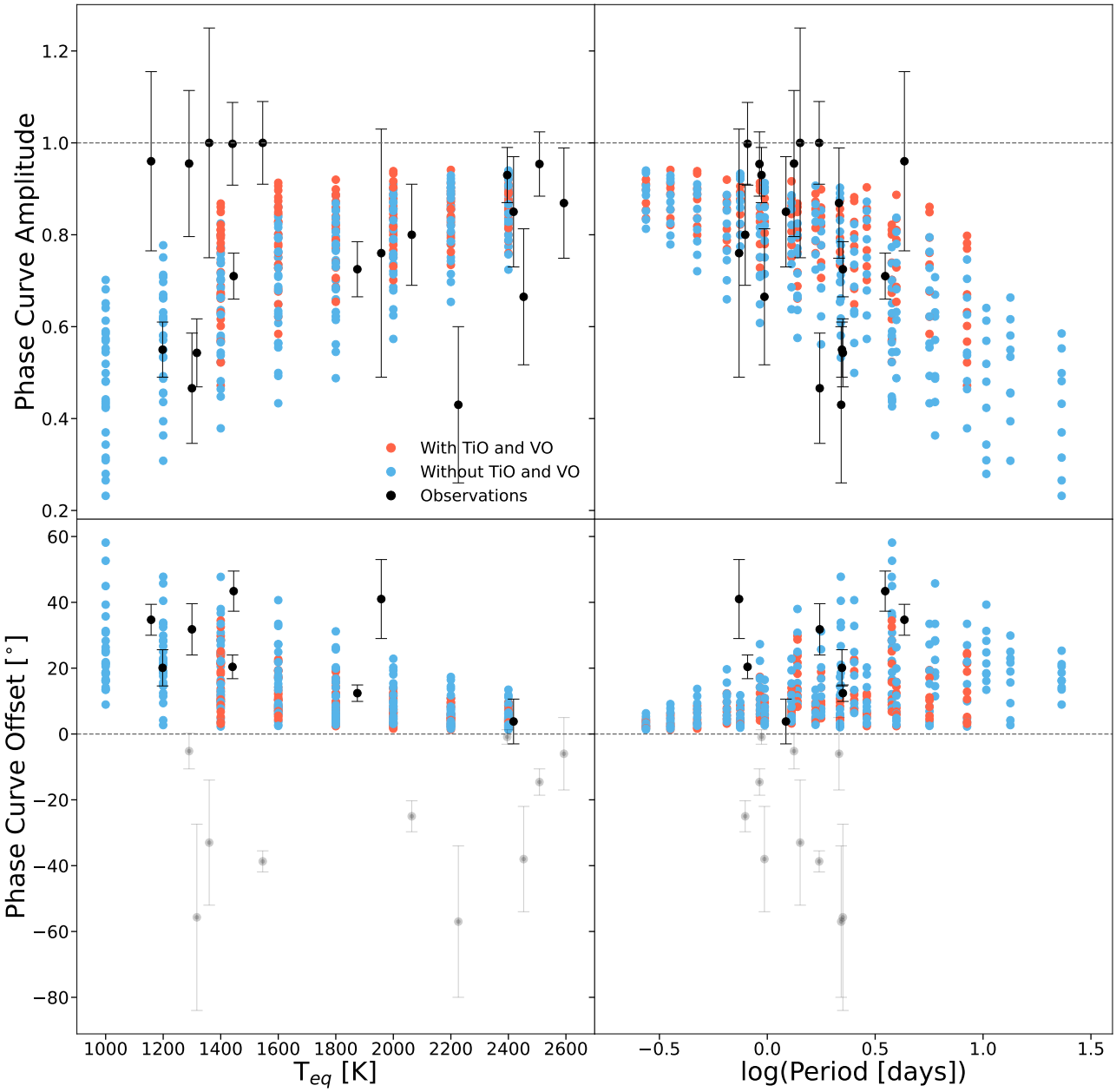


Figure 5.5: This figure shows a comparison between the phase curve offset and amplitudes in the Spitzer/IRAC 4.5μm band calculated for the 3D GCM grid and the observational data. The blue points are models without TiO/VO, the red points are the models with TiO/VO and the black points with error-bars are the observational data. **Left Panels:** shows the offset and amplitude vs equilibrium temperature. **Right Panels:** shows the offset and amplitude vs orbital period.

5.5 Summary & Conclusion

In this chapter, we have focused on comparison between the observable features of our drag-free grid spectra and phase curves in specific band-passes and population level observations.

By comparing our spectra to the re-analysed Spitzer/IRAC secondary eclipse data from Deming et al. (2023), we propose a novel mechanism that explains quantitatively the abrupt

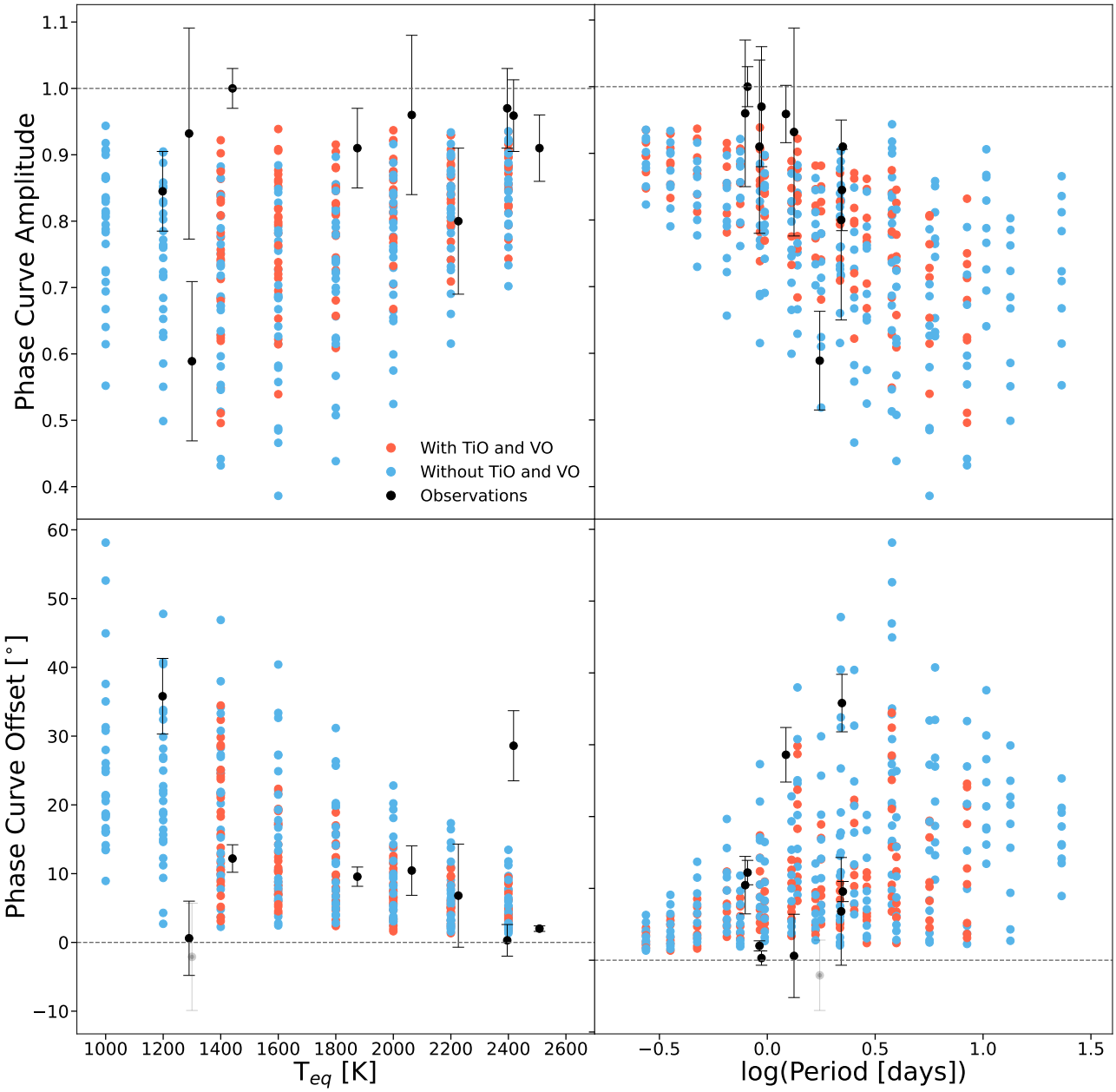


Figure 5.6: This figure shows a comparison between the phase curve offset and amplitudes in the Spitzer/IRAC $3.6\mu m$ band calculated for the 3D GCM grid and the observational data. The blue points are models without TiO/VO, the red points are the models with TiO/VO and the black points with error-bars are the observed data. **Left Panels:** Shows the offset and amplitude vs equilibrium temperature. **Right Panels:** Shows the offset and amplitude vs orbital period.

increase in the brightness temperature seen in this population: the appearance of TiO/VO in the atmosphere at $T_{\rm eq} \approx 1800K$ which reduces the efficiency of heat transport and creates a sudden brightening of the flux in the Spitzer band-pass.

Further comparing our models to the spectral variation of the water feature strength observed within the HST/WFC3 band-pass (Mansfield et al. 2021), we find that most observation between 1400-2200K are poorly matched by our grid of models. We suggest that this could be due to the partial depletion of TiO/VO due to non local condensation processes.

We leave the question on whether an atmosphere partially depleted of TiO/VO can indeed fit both Hubble and Spitzer population level trends for future work.

Finally, by looking at observed phase curve parameters, we find that the intrinsic scatter of our model grid aligns well with the observed spread in the data. We also find that the trend that phase curve amplitude increases with equilibrium temperature is well matched by our models. However, we do not predict the possible sudden jump towards lower phase curve amplitudes for planets with period larger than 1 day. We also find that the offset trends in both equilibrium temperature and period are well matched with our models, but that our model is unable to reproduce any of the observed negative offsets.

Bibliography

Baxter C., et al., 2020, A&A, 639, A36
Beatty T. G., Madhusudhan N., Tsiaras A., Zhao M., Gilliland R. L., Knutson H. A., Shporer A., Wright J. T., 2017, AJ, 154, 158
Beatty T. G., Marley M. S., Gaudi B. S., Colón K. D., Fortney J. J., Showman A. P., 2019, AJ, 158, 166
Bell T. J., et al., 2021, MNRAS, 504, 3316
Cont D., et al., 2022, A&A, 668, A53
Coulombe L.-P., et al., 2023, arXiv e-prints, p. arXiv:2301.08192
Deming D., Line M. R., Knutson H. A., Crossfield I. J. M., Kempton E. M. R., Komacek T. D., Wallack N. L., Fu G., 2023, arXiv e-prints, p. arXiv:2301.03639
Dobbs-Dixon I., Cowan N. B., 2017, ApJ, 851, L26
Evans T. M., et al., 2016, ApJ, 822, L4
Fu G., et al., 2022, ApJ, 925, L3
Garhart E., et al., 2020, AJ, 159, 137
Goyal J. M., et al., 2020, MNRAS, 498, 4680
Goyal J. M., Lewis N. K., Wakeford H. R., MacDonald R. J., Mayne N. J., 2021, ApJ, 923, 242
Hansen C. J., Schwartz J. C., Cowan N. B., 2014, MNRAS, 444, 3632
Kataria T., Showman A. P., Fortney J. J., Stevenson K. B., Line M. R., Kreidberg L., Bean J. L., Désert J.-M., 2015, ApJ, 801, 86
Kreidberg L., et al., 2014, ApJ, 793, L27
Line M. R., et al., 2016, AJ, 152, 203
Mansfield M., et al., 2021, Nature Astronomy, 5, 1224
Mansfield M., et al., 2022, AJ, 163, 261
May E. M., Stevenson K. B., 2020, AJ, 160, 140
May E., et al., 2022, arXiv e-prints, p. arXiv:2203.15059
Parmentier V., Crossfield I. J. M., 2018, in Deeg H. J., Belmonte J. A., eds, , Handbook of Exoplanets. p. 116, doi:10.1007/978-3-319-55333-7˙116
Parmentier V., Guillot T., 2014, A&A, 562, A133
Parmentier V., Showman A. P., Lian Y., 2013, A&A, 558, A91
Parmentier V., Fortney J. J., Showman A. P., Morley C., Marley M. S., 2016, ApJ, 828, 22
Parmentier V., Showman A. P., Fortney J. J., 2021, MNRAS, 501, 78
Pelletier S., et al., 2023, arXiv e-prints, p. arXiv:2306.08739
Powell D., Zhang X., Gao P., Parmentier V., 2018, ApJ, 860, 18
Roth A., Parmentier V., Hammond M., 2024, MNRAS, 531, 1056
Spiegel D. S., Silverio K., Burrows A., 2009, ApJ, 699, 1487
Venot O., et al., 2020, ApJ, 890, 176
Zhang M., et al., 2018, AJ, 155, 83

Chapter 6

A Large Grid of GCM Models: The Effects of Dynamic Drag

6.1 Introduction

In our drag-free models discussed so far, kinetic energy is dissipated through numerical dissipation. This conforms to observed data, and conserves energy within the system, but is a non-physical approximation to a complex dynamical process. However, the specific dissipation mechanisms which act as the primary cause of atmospheric drag in hot Jupiters are still under investigation (Goodman 2009). Magnetic drag (Menou 2012; Perna et al. 2010; Rauscher & Menou 2013; Rogers & Showman 2014), shear instability induced turbulence (Fromang et al. 2016; Koll & Komacek 2018; Li & Goodman 2010) and shocks (Dobbs-Dixon & Agol 2013; Fromang et al. 2016; Heng 2012; Li & Goodman 2010; Perna et al. 2012) have all been suggested as possible dissipation mechanisms. The best way to investigate the viability of these mechanisms is by comparing the predictions from different dissipation models to observed data.

As such, there have been a number of studies modelling drag mechanisms for hot Jupiter atmospheres. Rauscher & Menou (2013) model hot Jupiters HD 189733 b and HD 209458 b over a range of magnetic field strengths. They find that even at a magnetic field strength of 3 Gauss, the winds on HD 209458 b are strongly influenced by the magnetic drag, whereas HD 189733 b has a temperature too low to be influenced by a realistic magnetic field. Yadav & Thorngren (2017) use dynamo scaling laws to show that the magnetic fields of hot Jupiters increase with increasing incident flux. The radii is also shown to increase the magnetic field, leading to predictions of dipole magnetic fields strengths between 50-100G for the most inflated hot Jupiters. The intrinsic link between instellation flux received and rotation period, due to tidal locking of hot Jupiters, also implies that the magnetic fields will generally be larger for faster rotating hot Jupiters across the population. Koll & Komacek (2018) come to a similar conclusion on the potential influence of magnetic drag in HD 189733 b and HD 209458 b. By modelling hot Jupiter atmospheres as planetary heat engines and applying this theory to observed wind speeds from Doppler spectroscopy, Koll & Komacek (2018) find that although magnetic drag can explain the winds observed in HD 209458 b, it is likely too weak for HD 189733 b, unless the magnetic field is much larger than expected. They also find that drag from both shocks and shear instabilities are capable of matching the wind speeds observed for both planets. Beltz et al. (2022) model WASP-76 b with spatially variable drag (rather than uniform) and compare the observable predictions to Spitzer phase curves, finding that a minimum magnetic field of 3G would be required to match observation. They additionally find that stronger global magnetic field strength affects increasingly deeper pressure levels within the atmosphere.

Regardless of the drag mechanism, a reduction in longitudinal offset of the planetary hotspot, compared to drag-free prediction, could provide evidence of drag affecting winds at the thermal photosphere in an atmosphere. However, in order to interpret observable fea-

tures in relation to kinetic dissipation we must first understand how drag on the winds will affect these observable features in the spectra and phase curves of these planets. As such, in this chapter we are largely agnostic about the specific mechanism causing atmospheric drag and treat it as a bulk Rayleigh drag, as described in Chapter 3.

We begin by discussing the general atmospheric characteristics of the models in our drag grid (Section 6.2), the setup of which is described (Section 3.5.6). To investigate the effects of this drag on observable features we then look back at the metrics used in Chapters 4 and 5 for the drag-free grid, to see how these will change under the influence of variable atmospheric drag timescale. This includes analysis of the emission spectra, spectral indices and phase curve offset and amplitude (Section 6.3). We then explore the effects of magnetic drag on the planetary heat redistribution over a range of magnetic field strengths (Section 6.4), before concluding our findings (Section 6.5).

6.2 General Atmospheric Characteristics for a Range of Drag Strengths

As with the drag-free model grid in Chapters 4 and 5, we will primarily be focusing on atmospheric changes in our models across smaller slices of the drag grid, and in characteristic observable features, rather than the grid as a whole. However, we include Figure 6.1 to display the diversity in the full drag model grid. This shows the temperature structure, normalised by the equilibrium temperature, at the pressure level closest to the 1.4 micron photospheric pressure (see Equation 4.2) for models with prescribed Rayleigh drag timescales in addition to the equivalent drag-free models. As the drag timescale is decreased, the super-rotating jet can clearly be seen to be suppressed. The relative day-to-night temperature difference also clearly increases with decreasing drag timescale, indicating less efficient heat redistribution, which would be expected due to a decrease in planetary scale advection. Interestingly, by comparing the drag-free models to those with $\tau_{\text{drag}} = 10^5$s we can see that in some cases high latitude reverse jets appear to form, increasing the temperature towards the morning limb and significantly shifting the atmospheric hotspot westwards. However, this feature is not present in the $\tau_{\text{drag}} = 10^4$s models, implying that increasing strength drag has non-linear effects on an atmosphere. This can lead to non-monotonic shifts in the planetary hotspot with drag timescale, and even small negative phase curve offsets in certain models, which we discuss further in Section 6.3.3.

These reverse jet features can be even more clearly seen in Figure 6.2, which displays the zonal-mean zonal wind speed with pressure for the drag models arranged in the same format. Whilst the equatorial confined jet speed clearly decreases with increasing drag strength in all cases, the winds at high latitudes appear to strengthen between $\tau_{\text{drag}} = \infty$ to $\tau_{\text{drag}} = 10^5$s before again decreasing for lower timescales. The direction of these high latitude winds appears to be dependent on the planetary rotation period, primarily eastwards in slow rotators and westwards in faster ones. Notably, the transition between drag-free and dragged models also marks a transition between an atmosphere dominated by a single super-rotating jet and that of one with multiple jets of similar magnitudes.

If the atmospheric Rayleigh drag is the dominant factor in determining the wind speeds then the speed should scale as (Koll & Komacek 2018):

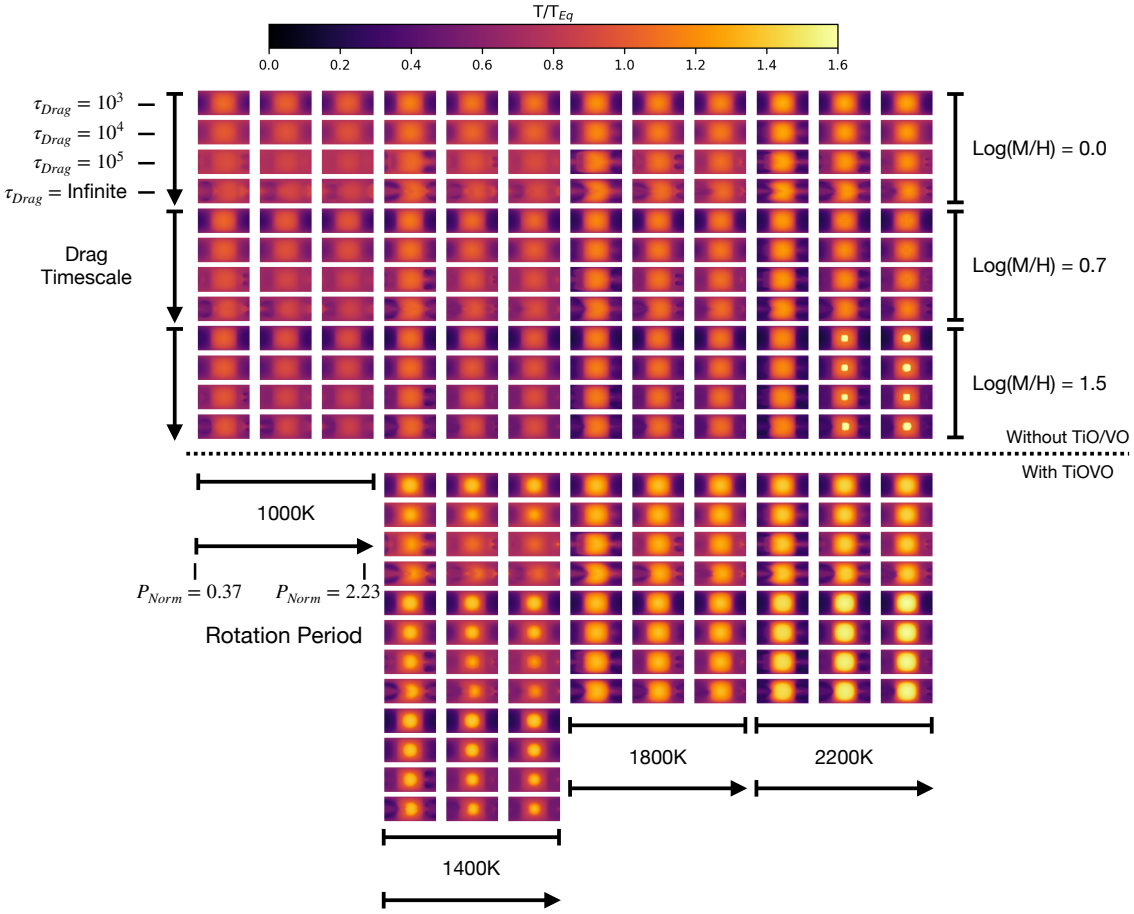


Figure 6.1: Latitude vs longitude thermal structure, temperature normalised by equilibrium temperature, for models within the drag timescale grid in addition to the equivalent drag-free models, at the pressure level closest to the 1.4 micron photospheric pressure. Equilibrium temperature is sorted into columns and atmospheric metallicity into rows. The drag timescale increases between values seen in Table 3.3 down each bracket of rows. The normalised orbital period increases in the same manner along columns. Models excluding TiO/VO are separated into the top half, with models including the two species in the bottom half

$$U_{\text{Rayleigh}} = k_0 \left(\tau_{\text{drag}} \eta \sigma T_{\text{eq}}^4 \frac{g}{p} \right)^{\frac{1}{2}}, \tag{6.1}$$

where η is the efficiency of the atmospheric Ericsson cycle, g is the gravity, p the pressure and k_0 is fitting constant. If numerical drag is the dominant factor in determining the wind speeds then the speed should scale as (Koll & Komacek 2018):

$$U_{\text{Numerical}} = k_1 \left(\Delta x \eta \sigma T_{\text{eq}}^4 \frac{g}{p} \right)^{\frac{1}{3}}, \tag{6.2}$$

where Δx is the spacing of the latitude/longitude grid at the equator and k_1 is the fitting constant. Figure 6.3 shows a comparison between the zonal-mean zonal wind speed of a subsection of our GCM drag models at the photosphere, compared to the predicted

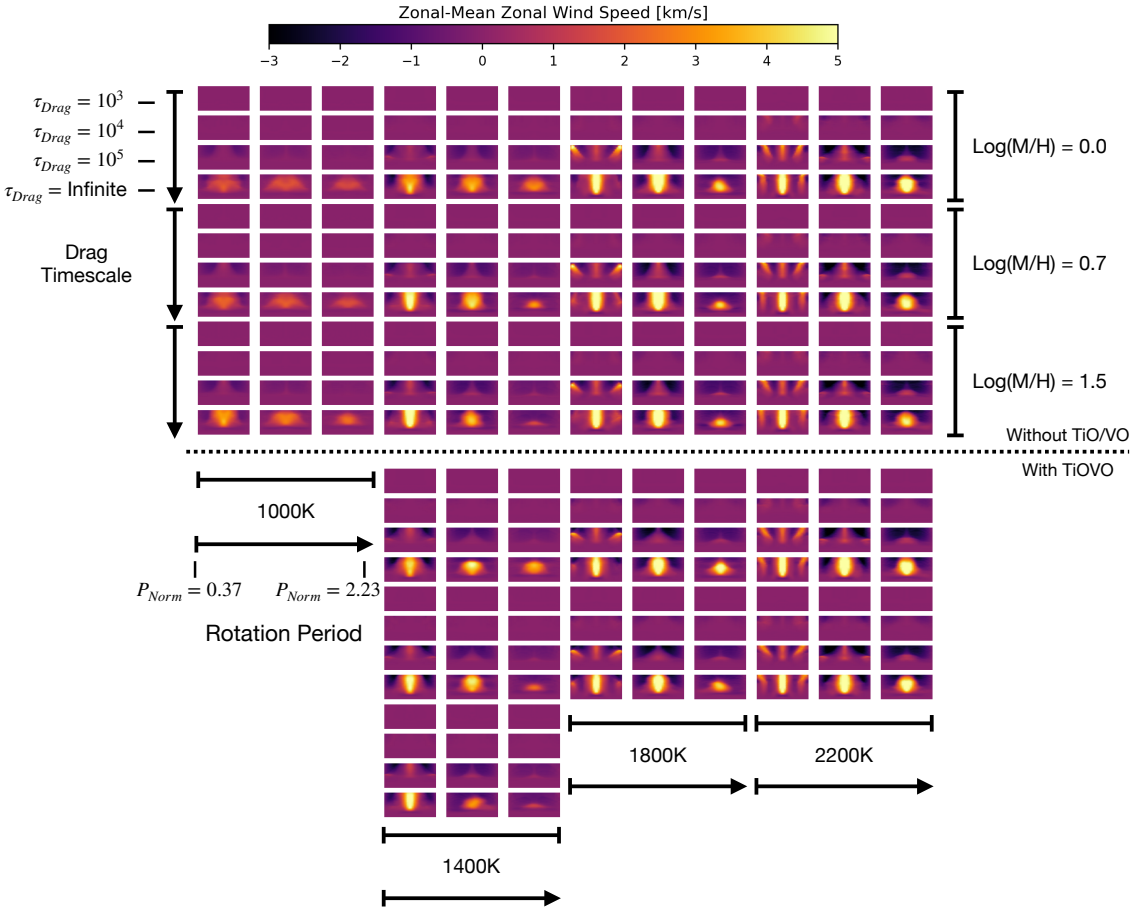


Figure 6.2: Zonal-mean zonal wind speed for all models within the drag timescale grid in addition to the equivalent drag-free models. Equilibrium temperature is sorted into columns and atmospheric metallicity into rows. The drag timescale increases between values seen in Table 3.3 down each bracket of rows. The normalised orbital period increases in the same manner along columns. Models excluding TiO/VO are separated into the top half, with models including the two species in the bottom half.

Rayleigh wind speed. We cannot show this comparison for all models as the wind speed predictions depend on all of our planetary parameters (i.e temperature, photospheric pressure and period). However, the comparison here is representative of the grid as a whole. For this comparison we use a k_0 value of 0.25 (model has $T_{\rm eq} = 1400K$, log(M/H)=0, $P_{\rm norm}$=1). This k_0 value is adjusted to fit our data rather than using the value quoted in (Koll & Komacek 2018), k_0=0.3, which is for a model with slightly different parameters. This fitting value should account for the assumptions which go into calculating $U_{\rm Rayleigh}$, such as the exact pressures over which the Ericsson cycle acts, and that a parcel of gas traverses two scale heights vertically every time it fully travels around the planet horizontally. The fitting factor should also account for methods used to estimate the day-side and night-side temperatures from the GCM model, which can be done in a variety of ways. Here we choose to use the temperature calculated from the bolometric spectra at phases of 0° and 180°. We choose to plot our drag-free models at a drag timescale of 10^7s in this comparison for the sake of easy visualisation. Koll & Komacek (2018) show that, at this drag timescale, the Rayleigh drag accounts for less than 10% of their energy dissipation (see their Figure 1). From this

comparison we can see that the wind speed in our models with drag match the Rayleigh drag prediction very well, implying that the atmospheric circulation is correctly being balanced by the Rayleigh drag. Contrary to this, our $\tau_{\text{drag}} = \infty$ model has a much higher wind speed than the Rayleigh drag prediction, even at very long drag timescales.

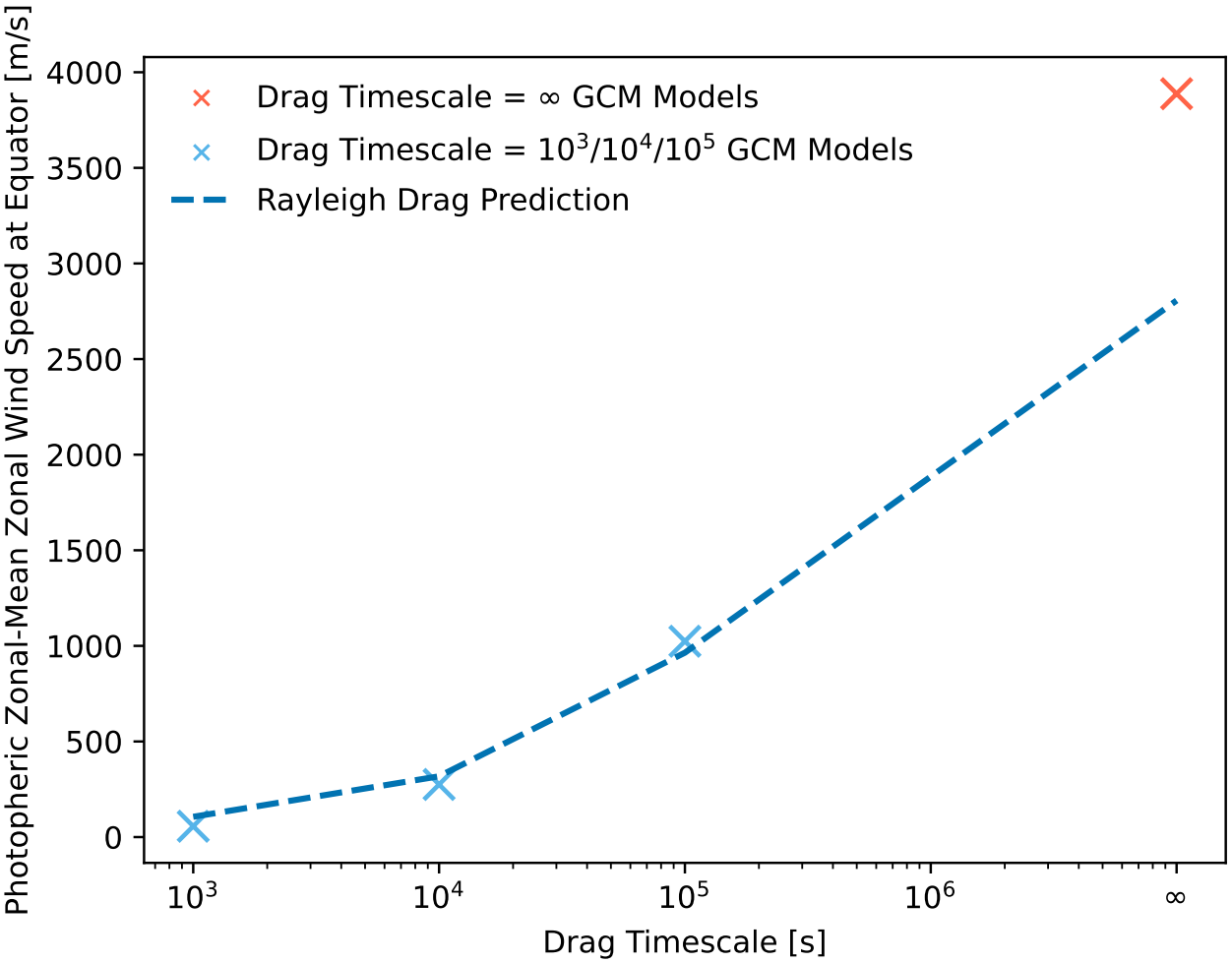


Figure 6.3: Comparison between the zonal-mean zonal wind speed at the photosphere of GCM models with $T_{\text{eq}} = 1400K$, Log(M/H)=0, P_{norm}=1 and different drag timescales to predicted wind speed, $U_{Rayleigh}$, from Equation 6.1. The dashed line shows the predicted value of $U_{Rayleigh}$ and crosses mark the values derived from the GCM models. The colour of the crosses also separate the drag-less (i.e $\tau = \infty$) model and those with finite drag timescales.

6.3 The Effects of Drag on Emission Spectra & Phase Curves

6.3.1 Emission Spectra

Figure 6.4 displays a comparison between models at different drag timescales when TiO/VO are absent or present in the atmosphere. From this we can immediately identify a stark contrast between the behaviour of the spectra at different drag timescales in these two cases. When TiO/VO are absent, the flux increases at all wavelengths for lower drag timescales.

This flux increase is more prominent outside of molecular bands, meaning that the molecular features are strongest in cases of more intense drag.

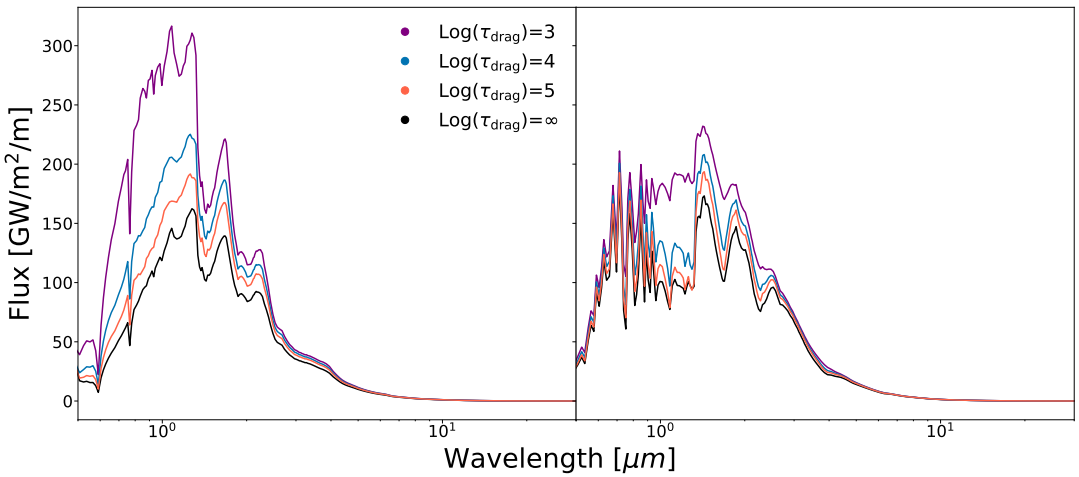


Figure 6.4: Comparison of secondary eclipse spectra for models from the dragged GCM grid with T_{eq}=1800K, log(M/H)=0.0, $P_{norm} = 1$ at varying drag timescales. **Left Panel:** Shows the spectra for models with TiO/VO removed. **Right Panel:** Shows the spectra for models containing TiO/VO. In both panels the drag timescale is denoted by the colour of the line.

This can be explained by looking at the day-side average pressure-temperature profiles, which are found in Figure 6.5. Here, we find that increasing drag drag increases the day-side vertical temperature contrasts. The effects of drag are also found to be most prevalent deeper in the atmosphere. This is caused by the damping of the advective wind speeds with drag, which results in less efficient redistribution of energy deposited in the day-side atmosphere onto the night-side. As a result, the day-side atmosphere is higher temperature when Rayleigh drag is strongest, which is seen in the spectra of Figure 6.4 as an overall flux increase. This can be thought of as competition between the radiative, advective and wave driven transport timescales and the drag timescale. When drag increases, it first affects the deep layers, where the radiative damping is comparatively long. Because of this, at these pressures the drag timescale is the dominating factor in determining the temperature, meaning that the day-to-night heat transport is most strongly inhibited in this region. The effects of drag are therefore more pronounced at shorter wavelengths, as these generally probe deeper pressure levels. The same argument can be applied to the variable effect inside and outside of the molecular bands. Outside of the bands we probe deeper into the atmosphere, where the drag timescale is dominant in determining the atmospheric structure, whereas inside the bands we are probing shallower levels, where the radiative timescale stays dominant for the values of drag we choose to model.

When TiO/VO are present in the atmosphere, we still find that the flux increases as the drag timescale reduces *at longer wavelengths* (i.e between ∼1-3 μm). However, the flux appears to be independent of the drag timescale at shorter wavelengths. This is because in an inverted atmosphere the shorter wavelengths will probe *low* pressure levels, where the radiative timescale is much shorter. The drag will therefore have very little effect at these pressures, which can be seen in the right hand panel of Figure 6.5, and so the spectra is largely unaffected by the drag timescale.

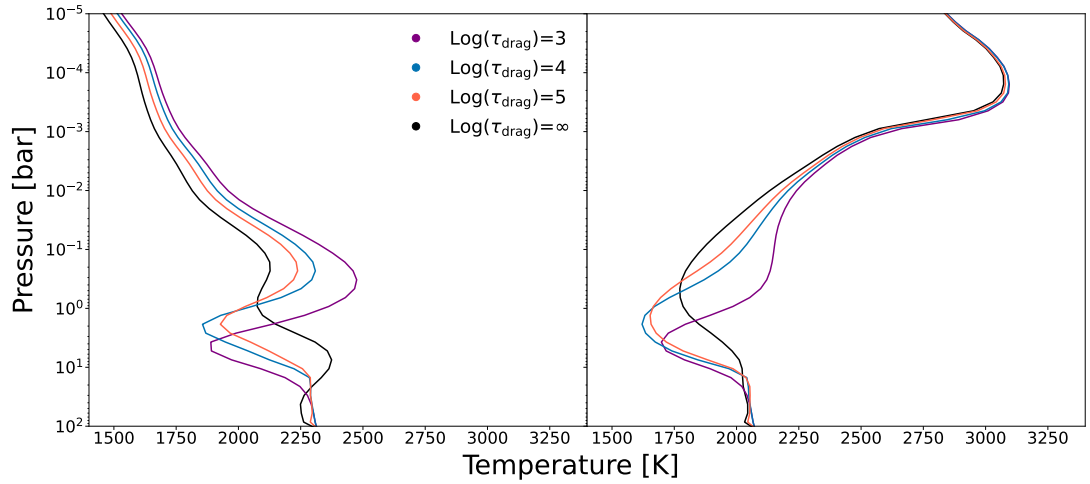


Figure 6.5: day-side average pressure-temperature profiles for models with 1800K T_{eq}, log(M/H)=0.0, $P_{norm} = 1$ at varying drag timescales within the grid. **Left Panel:** Shows the PT profiles for models with TiO/VO removed. **Right Panel:** Shows the PT profiles for models containing TiO/VO. In both panels the drag timescale is denoted by the colour of the line.

6.3.2 Phase Curve Offset

In Figure 6.6 we present colour maps displaying the variation in phase curve offset with metallicity and drag timescale. We see that phase curve offset usually decreases with decreasing drag timescale (increasing drag strength) and with increasing metallicity. Importantly, the drag seems to have a much larger effect on the offset than the metallicity. Additionally, the variation in offsets due to metallicity are stronger for weak drag than for strong drag. We also see that multiple combination of drag and metallicity can lead to a similar phase curve offset for a given planet. When observing exoplanet phase curves, a link between atmospheric metallicity and phase curve offset is often brought up (e.g (Kempton et al. 2023)). This degeneracy between drag and metallicity paints a more complex picture. However, we can wonder whether looking at the offset of the spectral phase curves, rather than the bolometric ones, could distinguish between high drag or high metallicity for a given observed planet.

To investigate this we select two pairs of models in our grid which appear to have roughly the same overall offset, Log(M/H)=1.5, $\tau_{drag} = 10^5$s / Log(M/H)=0.7, $\tau_{drag} = 10^4$s and Log(M/H)=0.7, $\tau_{drag} = 10^5$s / Log(M/H)=0, $\tau_{drag} = 10^4$s. By plotting the offset of these models against wavelength, which can be seen in Figure 6.7, we find that although the overall values of the bolometric offset are very similar, the wavelength dependence of the offset varies drastically based on the combination of drag and metallicity. Between the $\tau_{drag} = 10^5$s, Log(M/H)=0.7 and $\tau_{drag} = 10^5$s, Log(M/H)=0.0 models the wavelength dependence of the offset is clearly flatter in the higher drag timescale and metallicity case. However, when comparing the $\tau_{drag} = 10^5$s, Log(M/H)=1.5 and $\tau_{drag} = 10^4$s, Log(M/H)=0.7 models, these parameters appear to have more of a pivoting effect on the wavelength dependence, with the later case having lower offset at shorter wavelengths and larger offset at longer wavelengths. Unfortunately, due to the constraints of our model grid, we are presently unable to disentangle the exact nature of this wavelength dependence between varying drag

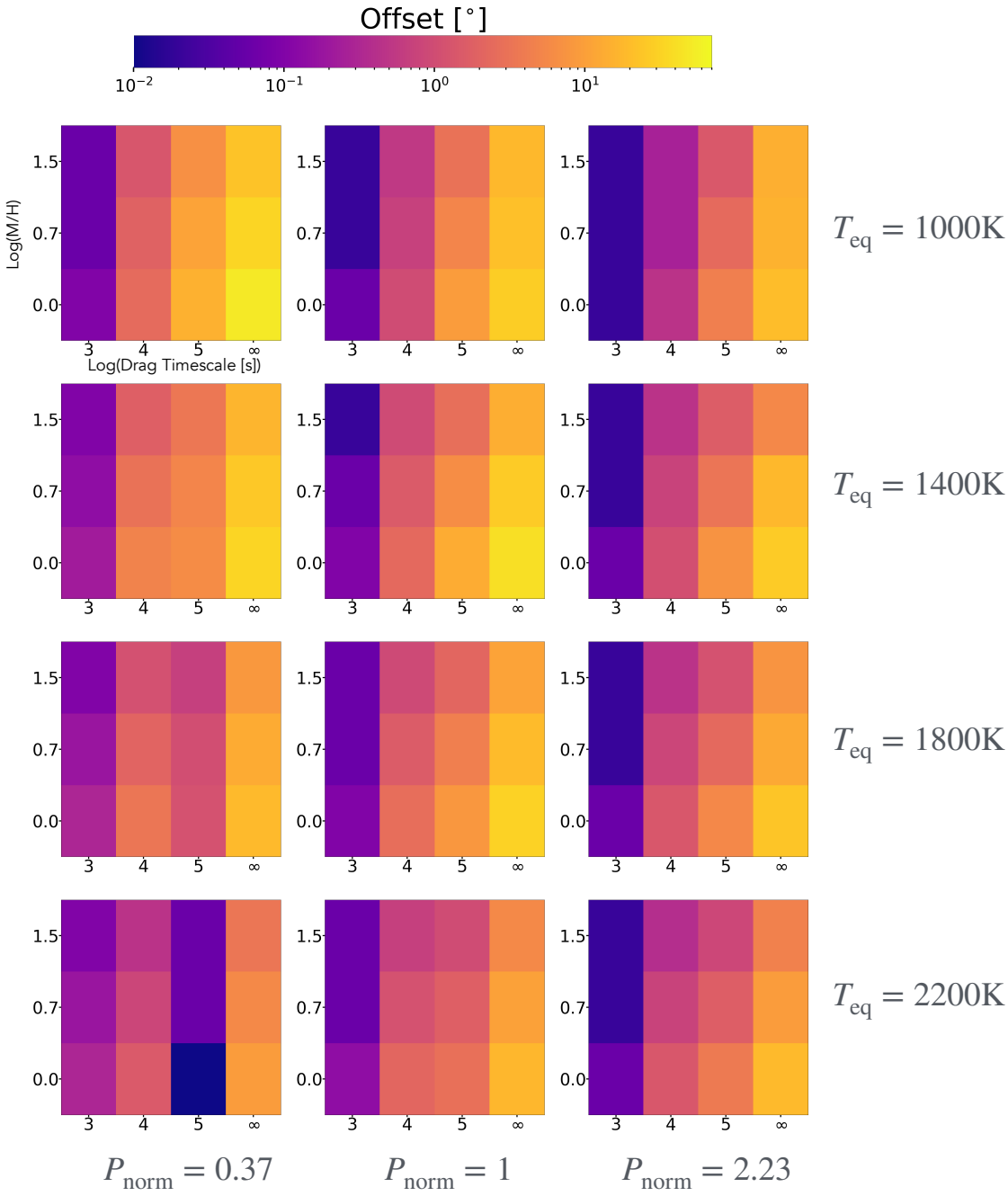


Figure 6.6: Colour maps displaying the phase curve offset as a function of both metallicity and drag timescale for models within the drag grid at different temperatures (separated into rows of subplots) and normalized periods (separated into columns of subplots). In each subplot, going down columns decreases metallicity (from log(M/H)=1.5 to 0) and across rows increases the drag timescale (from log($\tau_{\rm drag}$)=3 to ∞).

timescale and metallicity. We simply don't have enough models of differing parameters which happen to have the same overall offsets to make any meaningful grid wide comparison. However, the drag timescale has clearly been shown here to have an effect on the wavelength dependence of the phase curve offset. This provides a compelling reason to observe

optical phase curves, or a broader wavelength coverage with multiple instruments, for hot Jupiters when trying to distinguish between metallicity and drag effects in characterising their atmospheres.

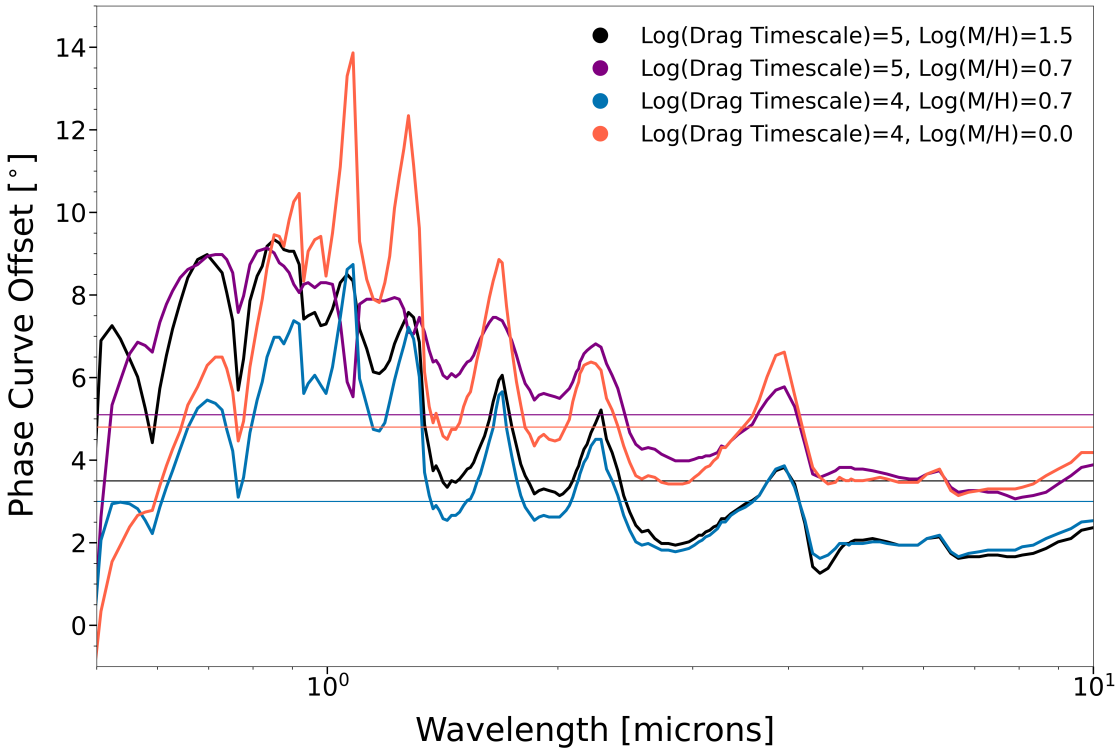


Figure 6.7: Phase curve offset as a function of wavelength for a specific set of models within the drag grid with $T_{\rm eq}$ = 1400K, $P_{\rm norm}$=0.37 (and Log(g)=1.3). The combination of drag timescale and metallicity is displayed by colour. The solid lines of matching colour represent the bolometric value of the offset.

6.3.3 Non-Monotonically Decreasing Offset

Although in most cases we find a phase curve offset which decreases monotonically as the drag timescale decreases, there are a small number of models within the drag grid where this is not the case. Figure 6.8 shows the phase curve offset as it varies with wavelength for a subset of models within the grid ($T_{\rm eq}$ = 1800K, Log(M/H) = 0, $P_{\rm norm}$ = 0.37). For these particular models we can see that as the drag timescale decreases there is a large westward shift in offset between $\tau_{\rm drag} = \infty$ and $\tau_{\rm drag} = 10^5$s. Between $\tau_{\rm drag} = 10^5$s and $\tau_{\rm drag} = 10^4$s the offset then shifts back eastwards, at a much reduced strength from the $\tau_{\rm drag} = \infty$ case, before then decreasing to near 0 at all wavelengths in the $\tau_{\rm drag} = 10^3$s case. A very small number of models with shorter drag timescales within the grid even have negative, and therefore overall westwards shifted hotspots at certain wavelengths.

To explain this effect we look at Figure 6.9 which shows the temperature structure, normalised by the equilibrium temperature, for the models from Figure 6.8 at different pressure levels. As the drag timescale decreases we can see the strength of heat advection by the jet

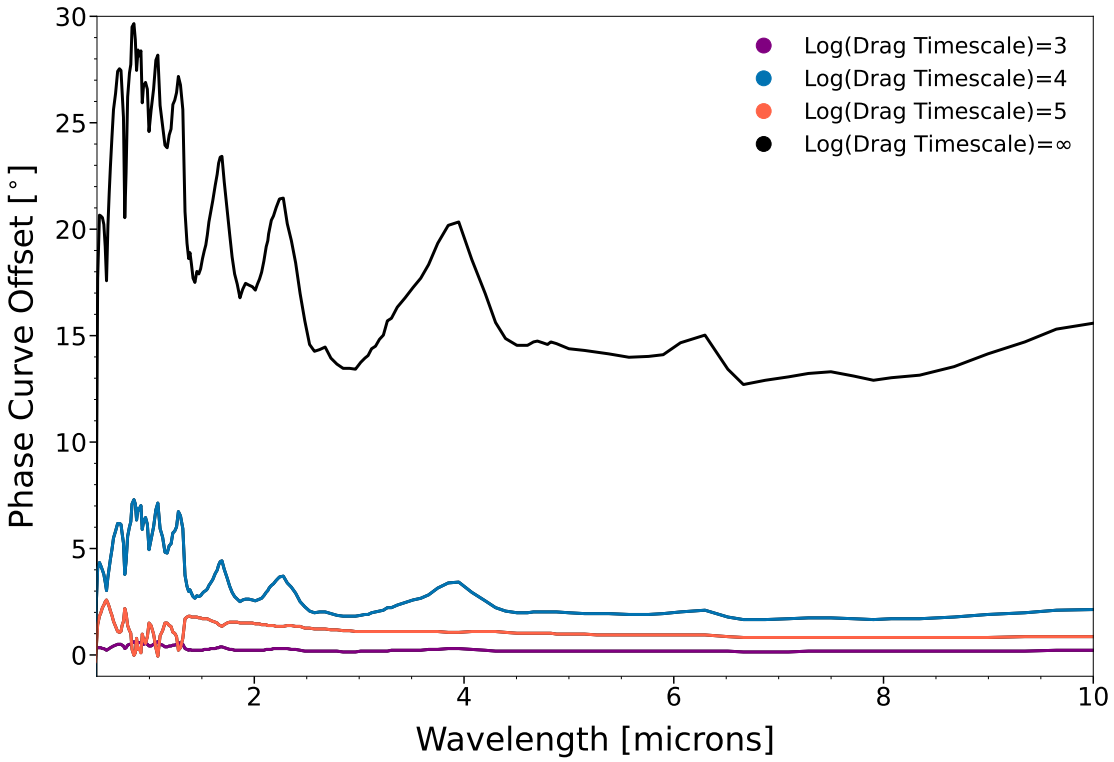


Figure 6.8: Phase curve offset vs wavelength for models with $T_{\rm eq}$ = 1800K, Log(M/H)=0, $P_{\rm norm}$=0.37 (and Log(g)=1.3) at different drag timescales. These models also have TiO/VO removed from the atmosphere. The colour denotes the drag timescales.

decreasing, which will naturally shift the hotspot towards the substellar point. However, it appears that the high latitude reverse jets are largely unaffected between the drag $\tau_{\rm drag} = \infty$ and $\tau_{\rm drag} = 10^5$s cases, before being suppressed in the $\tau_{\rm drag} = 10^4$s case. This is the cause of the non-monotonic hotspot and resulting phase curve offset shift with Rayleigh drag in addition to this, we see that at lower pressures the day-side limb can even increases in temperature between the $\tau_{\rm drag} = \infty$ and $\tau_{\rm drag} = 10^5$s cases, which is a likely candidate for the negative offsets we find at certain wavelengths in a small number of cases. It should be noted, however, that these high temperature, rapidly rotating planets (in which we see non-monotonically decreasing and westwards shifted offsets within the grid) are, in reality, very rare as evidenced by Figure 1.1 in Chapter 1.

6.3.4 Drag Dependent Phase Curve Offset & Amplitude Relationship

The reduced strength of the phase curve offset with drag also drastically changes the relationship between the phase curve offset and amplitude. Figure 6.10 displays the phase curve offset plotted against the amplitude and Rossby number. We now see two clear regimes, the drag-free models which display turning points in the offset with period as the Rossby number changes (as displayed in Section 4.4.2), and the models with drag having a much more shallow dependence between the phase curve offset and amplitude. For the drag models,

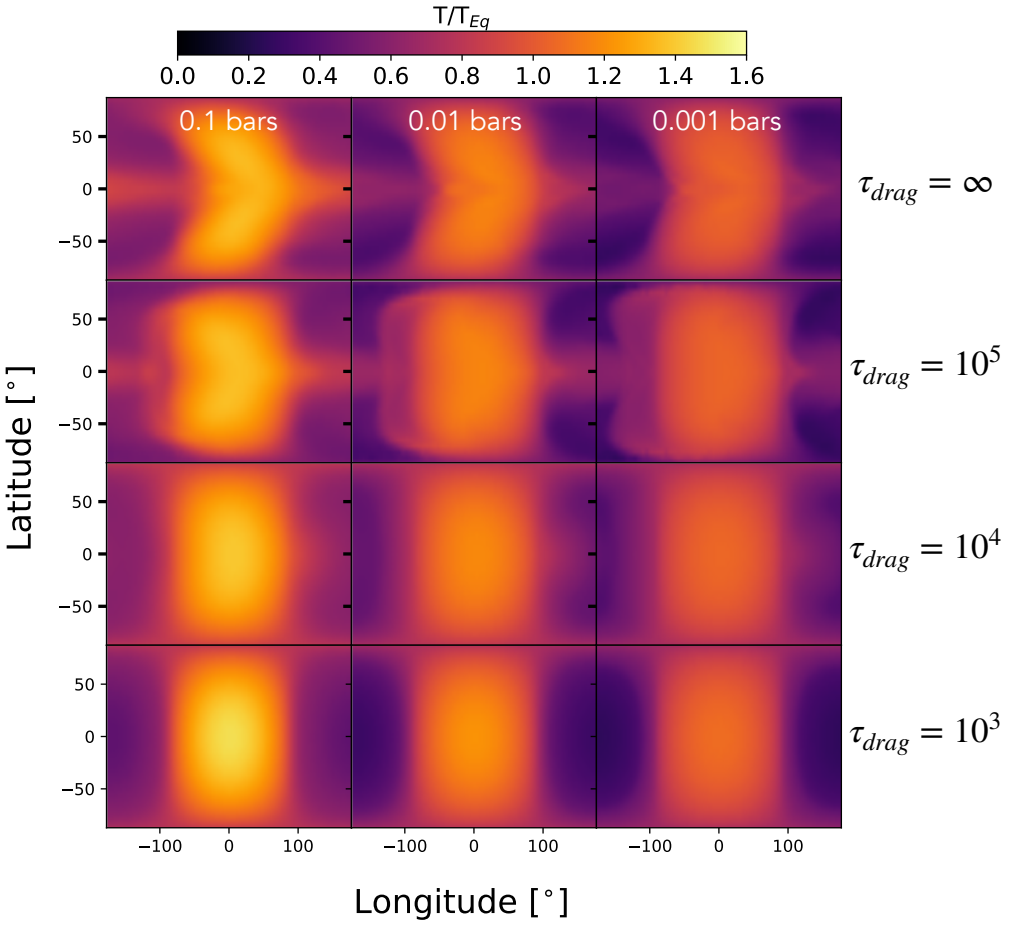


Figure 6.9: Latitude vs longitude thermal structure, temperature normalised by equilibrium temperature, for the models displayed in Figure 6.8. The drag timescale decreases down columns and across rows the pressure is decreased by an order of magnitude.

where the Rayleigh drag is generally stronger than the coriolis force, the Rossby number no longer works as a turning point metric. In this case, the drag is an extra component not accounted for in the calculation and the atmospheric state is now determined by a three-way force balance between the drag, advection and coriolis force. In the left hand panel of Figure 6.10 we can see how the offset vs amplitude relationship changes as the drag timescale is changed, sharply decreasing from the drag-free to $\tau_{\rm drag} = 10^5$s models and then trending towards the new line of best fit for the drag models.

We can explain this track using the same logic as in Section 6.3.3. Figure 6.11 shows a comparison between the RMS of the overall zonal wind speeds and the RMS of the separated negative/positive components for the model track in Figure 6.10. Although the positive and overall zonal wind speeds do decrease as the drag timescale decreases, we find that the negative wind speed increases between the $\tau_{\rm drag} = \infty$ and $\tau_{\rm drag} = 10^5$s cases. This is evidence of strong westward jets forming at higher latitudes. These westward jets will counteract the eastward jet, which in combination with a reduction to the eastward jets magnitude leads to a large reduction in the phase curve offset. However, the westward jets still carry energy from the day-to-night side, meaning that the heat redistribution efficiency and resulting phase curve amplitude is affected far less. Then, between the $\tau_{\rm drag} = 10^5$s

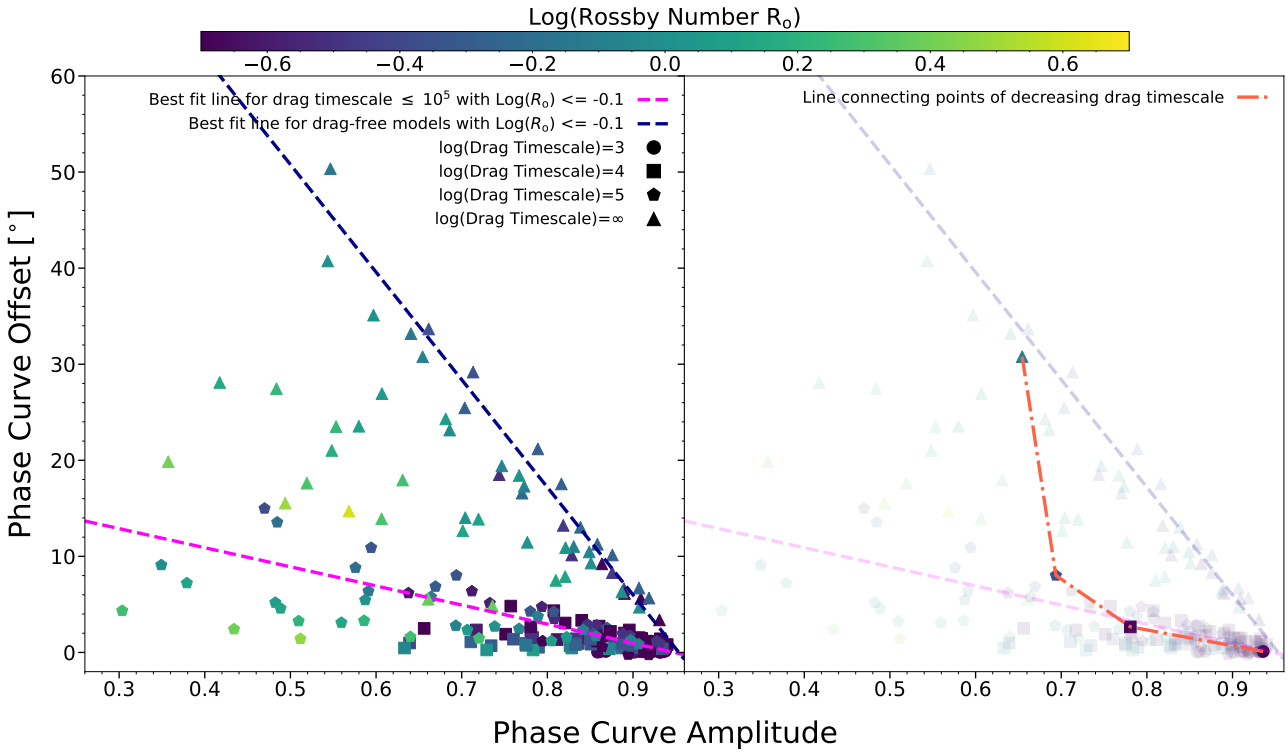


Figure 6.10: Phase curve offset plotted against amplitude for all models within the drag grid. Colour denotes the Rossby number of the model and shape denotes the drag timescale. **Left Panel:** The dark blue dashed lines display the best fit to the drag-free models with log(Ro_T)≤-0.1 (as in Figure 4.15), whilst the magenta dashed line displays the best fit to the models with finite Rayleigh drag timescales under the same Rossby number condition. **Right Panel:** Displays the same data (with increased transparency), in addition to a line joining models without TiO/VO, $T_{\rm eq} = 1800$, log(M/H) $= 0$ and $P_{\rm norm} = 1$ at varying drag timescales.

and $\tau_{\rm drag} = 10^4$s cases *both* the westward and eastward jets are suppressed, meaning the energy transport is more significantly reduced and the phase curve amplitude is decreased more than the already small offset. This is another example of the relationship we discussed in Chapter 4, again showing that the phase curve offset and amplitude are set by different mechanisms in the atmosphere.

6.3.5 Spectral Indices

Figure 6.12 displays the water feature index, as previously described in Section 5.2, for all models within the drag grid and their drag-free counterparts. Here we show this index plotted against the day-side temperature, as in (Mansfield et al. 2021), rather than the equilibrium temperature as done in Section 5.2. This is done to better distinguish the combined effects of drag on the temperature structure and on the water band. As expected, based on Figure 6.4 - where the depth of the 1.4 micron water band has very little variation with drag timescale - the dependence of the water feature strength on the drag is fairly low. However, when combined with the increase in day-side temperature for lower drag timescale models there is a clear trend in this index. For low, $\leq\sim 1600K$ and high, $\geq\sim 2600K$, day-side temperatures, decreasing drag timescale has very little effect on the water feature strength

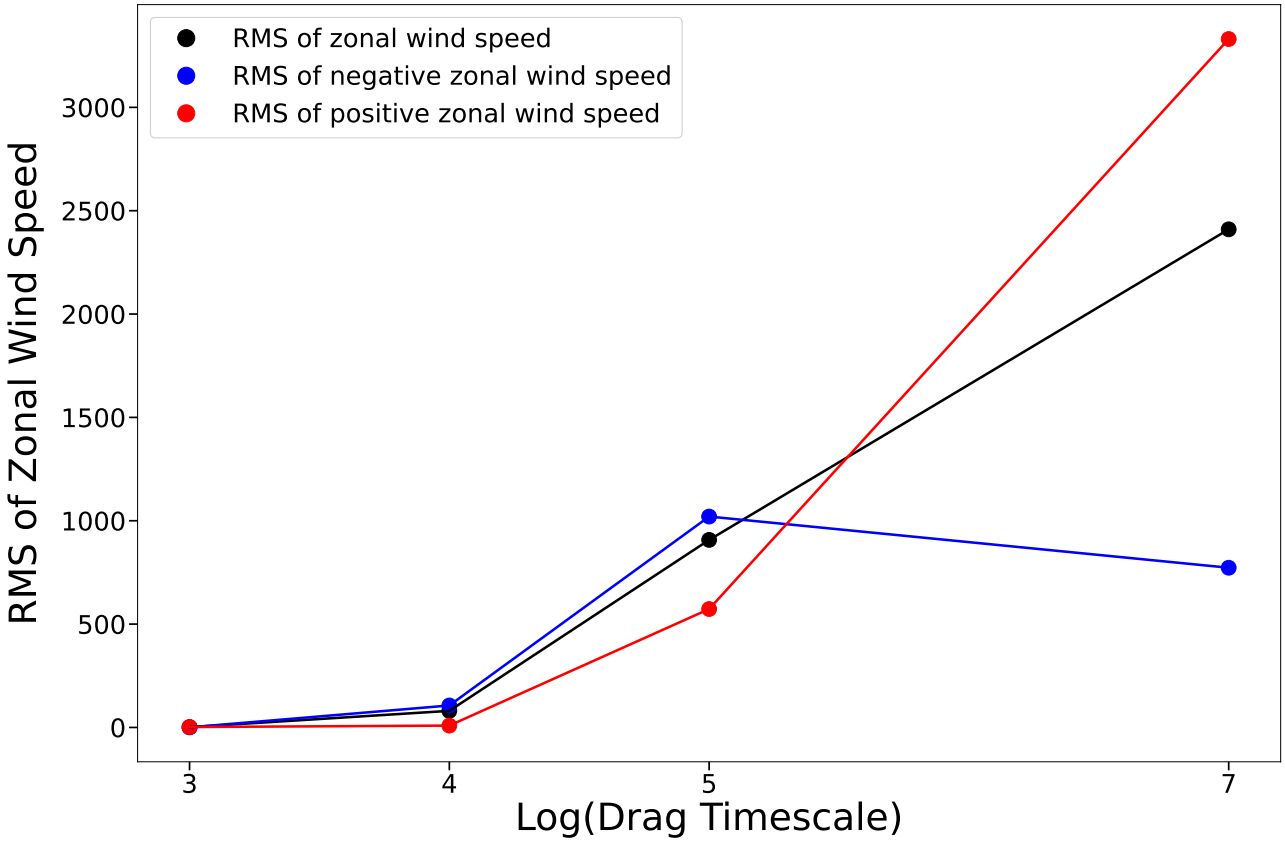


Figure 6.11: RMS of the zonal-mean wind speeds plotted against drag timescale, for the 1800K model track shown in Figure 6.10. The overall, negative and positive components of the RMS in the wind speeds are separated by colour.

whilst increasing the day-side temperature - leading to fairly flat relationship shifting points to the right in Figure 6.12. However, for temperatures between these values, decreasing drag timescale clearly reduces the value of the water feature index (i.e increasing water absorption or decreasing emission) whilst increasing the day-side temperature. This shows that a planet with a hotter day-side due to an increased drag has a vertical thermal structure that is more isothermal than a planet with a hotter day-side, due to a higher equilibrium temperature. This leads to a diagonal trend away from the drag-free models. Although we do not have the specific models with parameters to match the observed data from Fu et al. (2022); Mansfield et al. (2021, 2022), this could be a further potential explanation for *some* of the data points poorly matched by our model grid in Section 5.2.

6.4 The Effects of Drag on Planetary Heat Redistribution

Figure 6.13 shows colour maps for the redistribution factor of models within the drag grid as a function of both the atmospheric metallicity and drag timescales. By looking across the rows in each sub-plot, we can see that, as also shown for the phase curve offset, higher metallicity models show a more narrow range in redistribution factor across the range of drag timescales. Again, this is degenerate between the metallicity and drag timescale.

In order to investigate how the redistribution factor might vary across the population

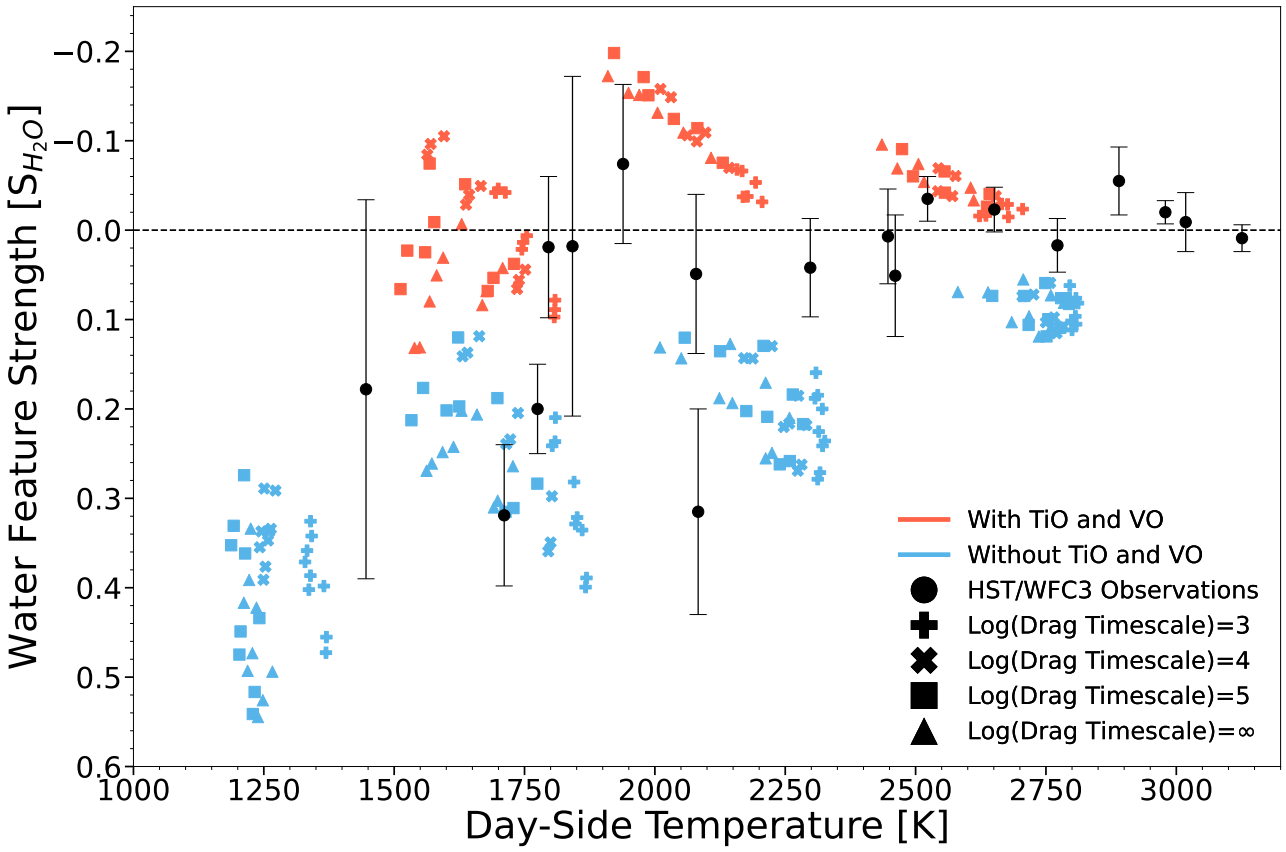


Figure 6.12: This figure shows a comparison between the water feature strength calculated for the GCM drag grid and observational data. The blue points are models without TiO/VO, the red points are the models with TiO/VO and the black points with error bars are the observational data from Fu et al. (2022); Mansfield et al. (2021, 2022). The drag timescale of each model is shown by the shape of the marker

based on the magnetic field of hot Jupiters, we calculate interpolated redistribution factor values based on estimations for the drag timescale under differing magnetic field strengths. The Lorentz drag timescale, Equation 2.29, scales based on the electrical resistivity, H_e and magnetic field, B, of an atmosphere. The electrical resistivity is related to the ionisation fraction, x_e (Menou 2012; Rauscher & Menou 2013):

$$H_e = 230 \frac{\sqrt{T}}{x_e} \mathrm{cm}^2 \mathrm{s}^{-1}, \tag{6.3}$$

where T is the temperature. We calculate the ionisation fraction, assuming $x_e \ll 1$, from a form of the Saha equation as detailed in (Rauscher & Menou 2013):

$$n_i = \left(\frac{a_i}{a_H}\right) n_H \tag{6.4}$$

$$\frac{x_{e,i}^2}{1 - x_{e,i}^2} = \frac{1}{n_i} \left(\frac{2\pi m_e k_b T}{h^2}\right)^{\frac{3}{2}} \frac{-\epsilon_i}{k_b T} \tag{6.5}$$

$$x_e = \sum_{i=1,28} \left(\frac{n_i}{n}\right) x_{e,i}. \tag{6.6}$$

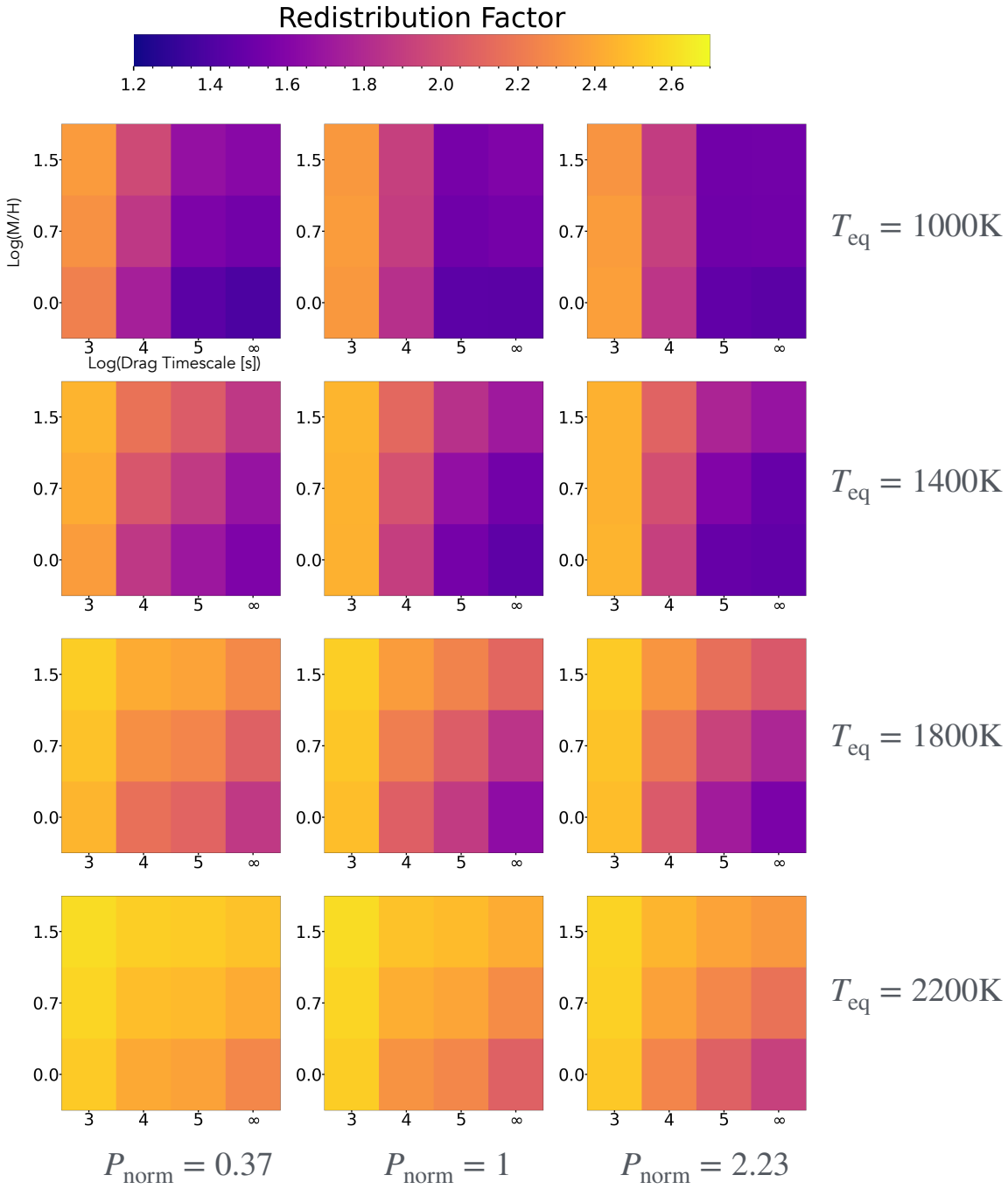


Figure 6.13: Colour maps displaying the redistribution factor as a function of both metallicity and drag timescale for models within the drag grid at different temperatures (separated into rows of subplots) and normalised periods (separated into columns of subplots). In each subplot, going down columns decreases metallicity (from log(M/H)=1.5 to 0) and across rows increases the drag timescale (from log($\tau_{\rm drag}$)=3 to ∞).

Here n_i is the number density, a_i the solar abundance and ϵ_i the first ionisation potential of each element. m_e is the electron mass, k_b the Boltzmann constant. We use the first 28 elements from hydrogen to nickel, as in (Rauscher & Menou 2013).

Figure 6.14 displays the interpolated redistribution factor from the scaling of magnetic drag timescale with our grid parameters at six magnetic field strengths from B=0-30G. It should be noted that in some cases the interpolated value of the magnetic drag will be outside of the range of our model grid. In these cases the value is plotted at the minimum or maximum value within the grid rather than extrapolating. This can be seen to occur at low temperature for weak magnetic fields and high temperature for strong magnetic fields. Importantly, we note that the variation in redistribution factor with equilibrium temperature is fairly smooth at all magnetic field strengths. This implies that the change in drag timescale at constant, or even small changes in, magnetic field strength is unlikely to be the cause of the step function behaviour we see in the Spitzer band emission in Deming et al. (2023), as discussed in Chapter 5. However, this does not entirely rule out magnetic drag as an explanation for the sudden rise in brightness temperature. If the magnetic field were to suddenly increase by multiple orders of magnitude at the temperature of the observed the brightness temperature increase, then this could account for the step function like behaviour observed. It also doesn't rule our clouds dissipating on the day-side as a further possible explanation for the brightness temperature increase.

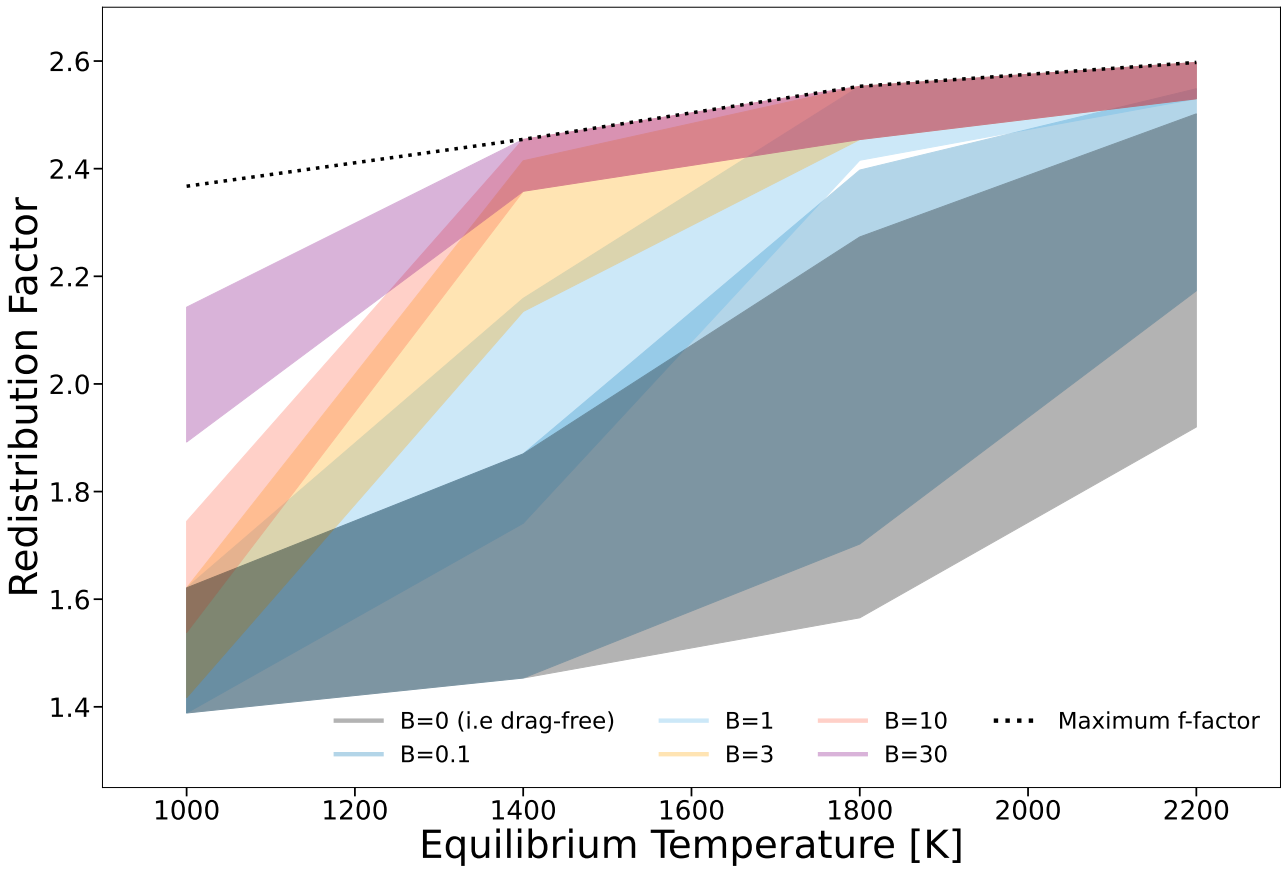


Figure 6.14: Interpolated bolometric redistribution factor from the scaling of magnetic drag timescale with our grid parameters. Magnetic field strength is denoted by colour. The shaded regions show the range of redistribution values based on the period and metallicity. The dotted lines show the absolute maximum and minimum values for the redistribution.

6.5 Summary & Conclusion

In this section we explore the effects of atmospheric drag, in conjunction to our other model grid parameters, on the temperature structure, phase curves and spectra of hot Jupiter exoplanets.

We show that drag has a decreasing effect on secondary eclipse spectra at longer wavelengths, and a more significant effect outside of spectral bands. This is due to the different pressure levels probed by the spectra at different wavelengths. Deeper in the atmosphere, the drag timescale is dominant and so the temperature - and therefore flux - increases dramatically on the day-side for stronger drag. At more shallow levels, the radiative timescale is dominant, and the drag therefore has a relatively small effect.

We find that, in addition to the damping of the equatorial super-rotating jet for increasing drag, the formation of strong reverse jets at higher latitudes (in certain drag regimes) can lead to non-monotonic shifts in the atmospheric hotspot with increasing drag. This results in a non-monotonically decreasing (and even negative in rare cases) phase curve offset with drag timescale.

Additionally, we find that variation in the phase curve offset is dampened at higher metallicities, and that the value of the phase curve offset can be degenerate depending on the combination of atmospheric metallicity and drag strength. We show that, although the overall value of offset can be degenerate between these parameters, the wavelength dependence of the offset will change in different ways, depending on the metallicity and drag regime, supporting the need for spectral phase curve observations of these planets.

We further show that, due to the formation of these strong reverse jets, the phase curve offset and amplitude are affected independently when increasing atmospheric drag. Suppression of the equatorial jet and strengthening of reverse jets will drastically reduce the phase curve offset. However, as the reverse jets still carry heat from the day-to-night side, the amplitude can remain largely unchanged. This is further reinforcement of our findings from Section 4.4.2, where we indicate how phase curve offset and amplitude are set by different mechanisms within the atmosphere.

We find that, for certain day-side temperatures between $\sim$ 1600K and $\sim$ 2600K, the combination of increasing day-side temperature and increasing absorption/decreasing emission of the 1.4 micron water feature leads to a diagonal trend in the water feature strength - away from the drag-free models, towards higher day-side temperature and towards/away from a blackbody in inverted/non-inverted atmospheres respectively. We hypothesise that this may account for some of the observed data that our drag-free grid is unable to match in Section 5.2.

Finally, we explore the effects of drag on atmospheric heat redistribution. Again, we find that this is degenerate between the metallicity and drag regime. We further investigate how different magnetic field strengths could impact the redistribution of heat across our parameter space. By interpolating values of the redistribution factor based on a range of magnetic field strengths, we find that there is a smooth decrease in heat redistribution towards higher temperatures for constant magnetic fields. We go on to conclude that constant magnetic fields are unlikely to cause the sudden brightness temperature increase observed in Deming et al. (2023), although sudden changes in magnetic field strength cannot be ruled out as an explanation.

Bibliography

Beltz H., Rauscher E., Roman M. T., Guilliat A., 2022, AJ, 163, 35
Deming D., Line M. R., Knutson H. A., Crossfield I. J. M., Kempton E. M. R., Komacek T. D., Wallack N. L., Fu G., 2023, arXiv e-prints, p. arXiv:2301.03639
Dobbs-Dixon I., Agol E., 2013, MNRAS, 435, 3159
Fromang S., Leconte J., Heng K., 2016, A&A, 591, A144
Fu G., et al., 2022, ApJ, 925, L3
Goodman J., 2009, ApJ, 693, 1645
Heng K., 2012, ApJ, 761, L1
Kempton E. M. R., et al., 2023, Nature, 620, 67
Koll D. D. B., Komacek T. D., 2018, ApJ, 853, 133
Li J., Goodman J., 2010, ApJ, 725, 1146
Mansfield M., et al., 2021, Nature Astronomy, 5, 1224
Mansfield M., et al., 2022, AJ, 163, 261
Menou K., 2012, ApJ, 745, 138
Perna R., Menou K., Rauscher E., 2010, ApJ, 719, 1421
Perna R., Heng K., Pont F., 2012, ApJ, 751, 59
Rauscher E., Menou K., 2013, ApJ, 764, 103
Rogers T. M., Showman A. P., 2014, ApJ, 782, L4
Yadav R. K., Thorngren D. P., 2017, ApJ, 849, L12

Chapter 7

A Large Grid of GCM Models: Comparison with 1D Radiative-Convective Thermochemical Equilibrium Models

7.1 Introduction

In the era of the Hubble and Spitzer space telescopes, 1D models have been able to adequately explain low resolution space-based observations (Baeyens et al. 2021; Mansfield et al. 2021; Wiser et al. 2024). Additionally, 1D and 2D radiative/convective model grids have been widely used to explore how the observational properties of hot Jupiters vary across the observed population of planets (Baeyens et al. 2021, 2022; Goyal et al. 2020, 2021; Mansfield et al. 2021; Molaverdikhani et al. 2019).

However, as we discussed in Chapter 1, hot Jupiters have intrinsically 3D atmospheres, with large spatial variations in thermo-chemical structure (Caldas et al. 2019; Feng et al. 2016; MacDonald et al. 2020; Pluriel et al. 2020; Taylor et al. 2020). This has been shown (numerous times) to cause strong biases in 1D retrieval models applied to hot Jupiters, for both transmission (Caldas et al. 2019; Lacy & Burrows 2020; Line & Parmentier 2016; MacDonald & Madhusudhan 2017; MacDonald et al. 2020; Pluriel et al. 2020) and emission spectroscopy (Blecic et al. 2017; Feng et al. 2016; Taylor et al. 2020). Furthermore, Feng et al. (2016) suggest that in some cases these biases can lead to incorrect molecular detection.

However, if these biases are well understood then there is potential for them to be mitigated whilst still enabling the use of less computationally expensive, lower dimensionality models for hot Jupiter characterisation. Taylor et al. (2020), for example, show that applying a dilution or 'scaling' factor parameter to a single averaged pressure-temperature profile can perform as well as a double temperature profile approach (i.e one day-side and one night-side temperature profile). This dilution factor is a measure of how homogeneous the day-side atmosphere is, and accounts for the wavelength dependent slope induced in the spectra, due to averaging of the temperature profile in a 1D model (see Taylor et al. (2020) Figure 9).

However, in the era of JWST and improving ground-based observation capabilities with increased spectral resolution and wavelength coverage, the biases already observed in current data will only become stronger (Feng et al. 2016). This necessitates a closer look into the potential pitfalls of modelling 3D atmospheres without using 3D models.

In this chapter, we compare our large drag-free grid of 3D hot Jupiter general circulation models to an equivalent grid of 1D radiative-convective equilibrium atmosphere models. No such direct comparison between 1D and 3D models has previously been performed on this scale. By performing this comparison across a wide parameter space, we aim to identify planetary regimes in which the differences between 1D and 3D model assumptions may be detectable by JWST observations.

We begin by describing the creation of the 1D model grid (Section 7.2), and benchmarking between the 3D GCM and 1D grid (Section 7.3). We then describe the general trends between 1D and 3D pressure-temperature profiles and spectra (Section 7.4), before moving on to the differences observed in spectral indices (Section 7.5). We then take a closer look at the wavelength dependence of differences between the 3D and 1D spectra (Section 7.6), before examining the role of a dilution factor slope between the spectra (Section 7.6.3), finally presenting our conclusions (Section 7.7).

7.2 1D Model Grid

One-dimensional, self-consistent, day-side atmosphere models are provided by Lindsey Wiser, produced using the ScCHIMERA code described in detail in Wiser et al. (2024) (additionally used in, e.g. Arcangeli et al. (2018); Iyer et al. (2023); Kreidberg et al. (2018); Mansfield et al. (2018, 2020)). Models are 1D with altitude, cloud-free, and rely on radiative-convective-thermochemical equilibrium (1D-RCTE). ScCHIMERA uses a two-stream approach (Toon et al. 1989) to calculate layer-by-layer fluxes from an internal source function and incident stellar flux, and models are computed over the pressure range 10^{2}-10^{-5} bars in layers that are equally spaced in log-pressure. For consistency with the GCM grid, atmosphere internal temperature is fixed to 100K. Radiative-convective equilibrium pressure-temperature profiles are found using a Newton–Raphson iteration method (McKay et al. 1989). Opacities are computed using the correlated-K framework (Amundsen et al. 2017; Goody & Yung 1989; Lacis & Oinas 1991) at R=50. Molecular abundances are interpolated from the same abundance tables used by the SPARC/MITgcm (Freedman et al. 2008, 2014), which provides molecular abundances given pressure and temperature in each atmosphere layer.

The 1D model grid is generated by varying the same input parameters as the drag-free SPARC/MITgcm 3D model grid: $T_{\rm eq}$, planet log(g), log(M/H), $T_{\rm star}$, $M_{\rm star}$, and $R_{\rm star}$ (See Section 3.5). We additionally produce 1D models both with and without the high-altitude absorbers TiO and VO.

As we aim to compare the shape of the 1D and 3D day-side spectra for the grid of planets, we require that the 1D and the 3D day-side spectra have the same total outgoing thermal flux. Thus, we adjust the irradiation temperature of the 1D models based on the heat redistribution parameter from the GCM's (Arcangeli et al. 2018) (see Equation 4.3). In the 1D model, the heat redistribution parameter adjusts the instellation flux, so by using the f-factors from the 3D models we are fixing the incident stellar flux at the top of the atmosphere to be equal between the models. This means that the 1D and the 3D models have similar effective temperatures. For incident stellar flux, we interpolate PHOENIX stellar models (Husser et al. 2013) for a given set of stellar parameters.

7.3 Benchmarking of the 1D Grid

Whilst the 1D-RCTE grid has been adapted to interpolate molecular abundances from the same reference tables used by the GCM grid, there is some variation in the opacity files used. Unfortunately, it was not possible to change the opacity files used by ScCHIMERA (Wiser et al. 2024) to those used by the SPARC/MiTgcm (Freedman et al. 2008, 2014) due to

external constraints. We also cannot retroactively change the files used when creating the GCM grid. It is therefore important that we determine any differences that could arise in the spectra between these two models due to the different opacities. It is also important that we understand any differences due to potential numerical errors (i.e small numerical differences due to the way in which the radiative transfer is coded) before trying to interpret the results from a comparison between the two grids.

Table 7.1: Benchmark models.

T_{eq} [K]	Log(M/H)	Normalised Period Multiplier	Log(g[SI])	TiO/VO Present
1000	1.5	0.37	1.8	No
1400	1.5	1	0.8	Both
1800	0.7	0.37	1.3	Both
1800	0.0	2.23	1.8	Both

To do this we selected a range of models from the GCM grid (see Table 7.1) to benchmark. These models were selected so that the entire parameter space range of the grid was covered. To produce a GCM benchmark spectrum, i.e. to approximate 1D by removing any contributions from geometry, we create a geometrically homogeneous model by replacing the temperature profile with the substellar temperature profile from the equilibriated GCM at all latitudes and longitudes. We then run this through the radiative transfer code with a fixed viewing angle of $\mu = 0.5$, and generate the resulting secondary eclipse spectrum. We fix the viewing angle in this way to have a one-to-one comparison between ScCHIMERA and our processing of the GCM spectra. By fixing the viewing angle and the temperature profile in our GCM calculation we are doing the exact same calculation at every latitude/longitude and then taking the average of it. To produce an equivalent 1D ScCHIMERA spectrum benchmark, we turn off ScCHIMERA's radiative-convective equilibrium solver and instead input the same substellar temperature profile, again with $\mu = 0.5$. When comparing these two spectra, the only differences should be the result of differing line lists used between the 1D and 3D models and any rounding errors in the numerical solvers.

Figure 7.1 displays the secondary eclipse spectra for the 'substellar homogeneous' GCM benchmark model and the 1D-RCTE model produced in this manner (alongside the residual between the two) for the models with TiO/VO removed. The residuals show that, above $\sim 1\mu m$, the 1D and 3D spectra agree reasonably well, with relative flux differences of at most 5% in certain molecular bands for low temperature models. The residuals clearly decrease with increasing wavelength and temperature, lying below $\sim 2.5\%$ in most cases. Below $1\mu m$ the residuals are far worse, this is likely due to the poor convergence of the 3D models in the high pressure layers. As such, we will discard any spectral comparison between the 1D and 3D models below wavelengths of $1\mu m$, in the models with TiO/VO removed, for the remainder of this study.

7.3.1 Adjustment for TiO Opacities

So far we have only discussed the benchmarks between 1D-RCTE and GCM models with TiO/VO removed from their atmospheres. Unfortunately, the line lists used for these species are the most disparate between the 1D-RCTE and GCM models. The GCM uses the opacities listed in Freedman et al. (2008, 2014), which come from Allard et al. (2000); Schwenke (1998)

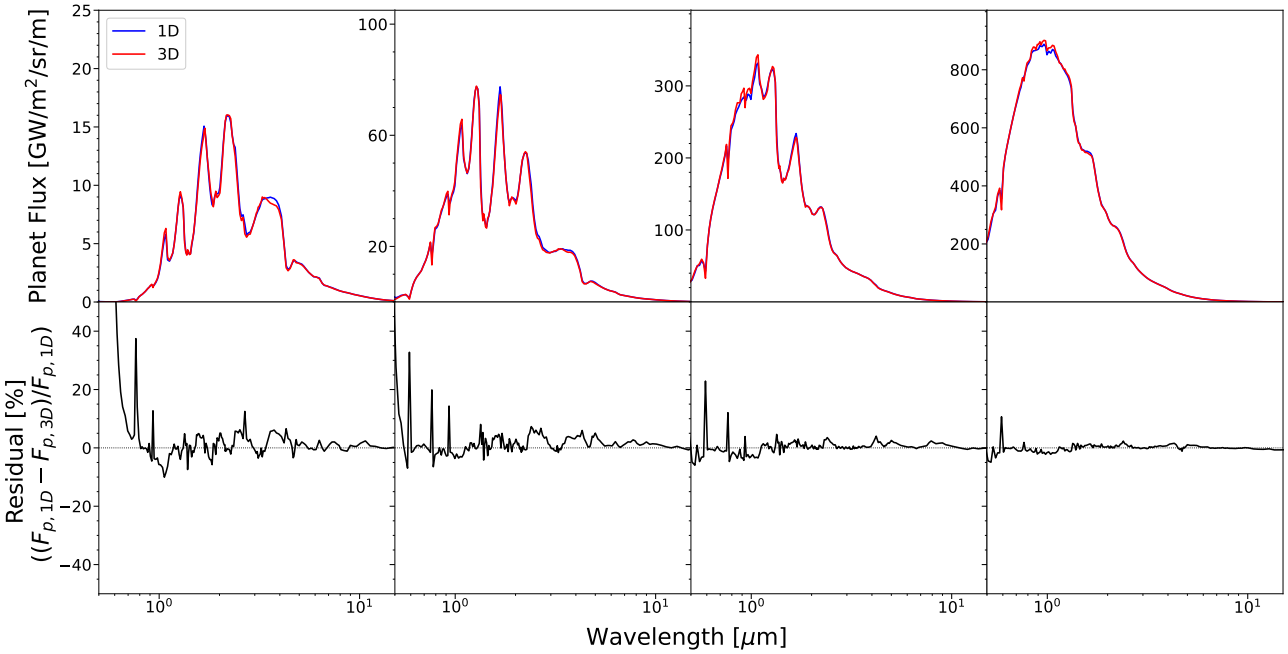


Figure 7.1: Upper Panels: Benchmark secondary eclipse spectra for models with parameters listed in Table 7.1 and TiO/VO removed. 1D and 3D spectra are separated by colour. The equilibrium temperature of the benchmark models used increases across the row from left to right. **Lower Panels:** Residuals between the 1D and 3D benchmark spectra, calculated as $(F_{p,1D} - F_{p,3D}/F_{p,1D})$, corresponding to the upper panels.

for TiO and Alvarez & Plez (1998) for VO. The 1D model uses those of McKemmish et al. (2019) for TiO and McKemmish et al. (2016) for VO. Rather than discard these models in our comparison, we are able to scale the TiO and VO opacities used in the 1D-RCTE models to roughly match those used in the GCM, as the difference is a systematic one due to the different line lists used.

From Equation 4.2, we know that the photospheric pressure is directly related to the opacity at the photosphere, which in models containing TiO/VO will be dominated by the TiO/VO opacities. Therefore, we can determine the differences in the TiO and VO line lists by calculating the difference between the pressures at which these species are emitting in the benchmark spectra. In order to do this we calculate a brightness temperature from the flux emitted in the TiO and VO bands below $1\mu m$. This will be the temperature at the photosphere, assuming that the TiO/VO opacities are dominant at the photospheric pressure level. We then determine the pressure level at which this temperature corresponds to in the vertical profile.

Performing this process for a range of models within our grid, including the benchmark models shown here and additional models run in the same manner, we find a fairly constant ratio between the 1D and GCM photosphere of $P_{phot,1D}/P_{phot,3D} \sim 1.3$. Therefore, by *increasing* the 1D-RCTE TiO/VO opacities by a scaling factor of 1.3 they will better match the GCM opacities.

Figure 7.2 displays the secondary eclipse spectra and residual for the GCM and 1D benchmark models with TiO/VO present in the atmosphere, both before and after this opacity adjustment has been made. As with the models without TiO/VO, we again see that the residuals are much lower above $\sim 1\mu m$. Above this wavelength the residuals are all well

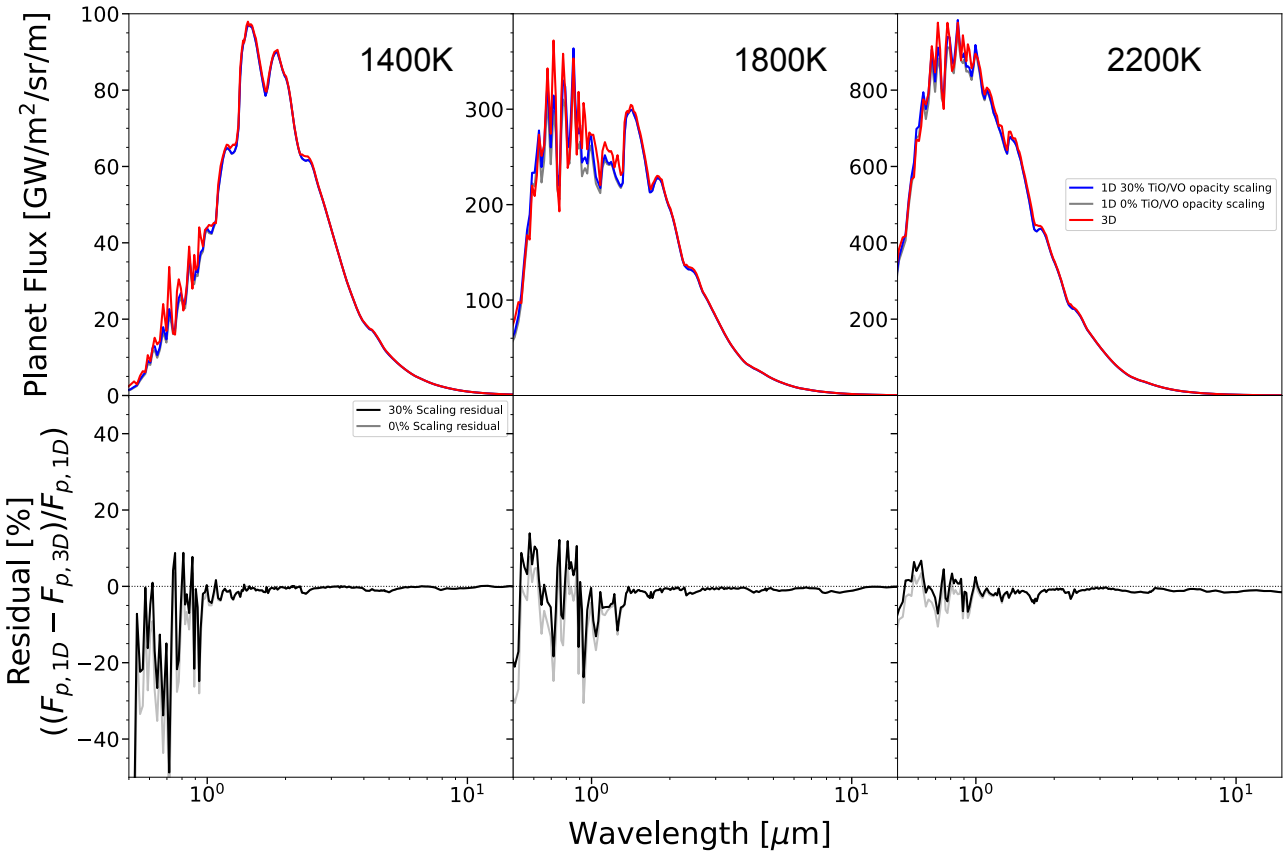


Figure 7.2: Upper Panels: Benchmark secondary eclipse spectra for models with parameters listed in Table 7.1 and TiO/VO present in the atmosphere. 1D and 3D spectra are separated by colour. The equilibrium temperature of the benchmark models used increases across the row from left to right. **Lower Panels:** Residuals between the 1D and 3D benchmark spectra, calculated as $(F_{p,1D} - F_{p,3D}/F_{p,1D})$, corresponding to the upper panels. The residual between the 0% and 30% scaling cases are both displayed and separated by colour.

within an acceptable margin, less than 2.5%. Below $1\mu m$ the residuals are still fairly significant, especially at lower temperatures, although the opacity adjustment has systematically shifted the overall residual in this region towards 0. These remaining differences are likely due to the opacities not having a linear spectral scaling, i.e if there are more individual lines inside the bands compared to outside. For high temperatures, although the residual within individual bands is still quite high, the overall comparison should not suffer as the residual is now split evenly between negative and positive values.

We note that this is not the case at 1400K, where the 3D benchmark model systematically has more flux below $\sim$0.8 μm. However, if the temperature profile of a model falls below the TiO/VO condensation curves then there will be order of magnitude depletion in the TiO/VO abundances. This very strong depletion, over even small temperature adjustments, is large compared to the effects of our 30% opacity scaling. As such, the presence, or lack of, a thermal inversion predicted in chemical equilibrium for models which fall below the TiO/VO condensation curves are robust compared to any scaling of the opacities. When

we later compare the 1D-RCTE and full 3D GCM models (not the 'substellar homogeneous' benchmarks) in Section 7.4.1, we find that a temperature inversion is predicted in chemical equilibrium for the 3D models but not for the 1D models at this temperature. As explained, the relative strengths of depletion and opacity scaling mean that the overall temperature structure is largely unaffected by the 30% increase in opacities for this case, and that the thermal energy comparison between the 1D-RCTE and GCM models is unaffected by the low wavelength differences found in Figure 7.2 for the 1400K benchmark.

7.3.2 Total Flux Integral

Now we are satisfied that the 1D-RCTE benchmark models are able to accurately reproduce spectra of the 'substellar homogeneous' GCM models, the final step is to validate the comparison between the full 3D GCM models and those 1D-RCTE models produced from the planetary parameters, rather than direct input of the substellar GCM temperature profile.

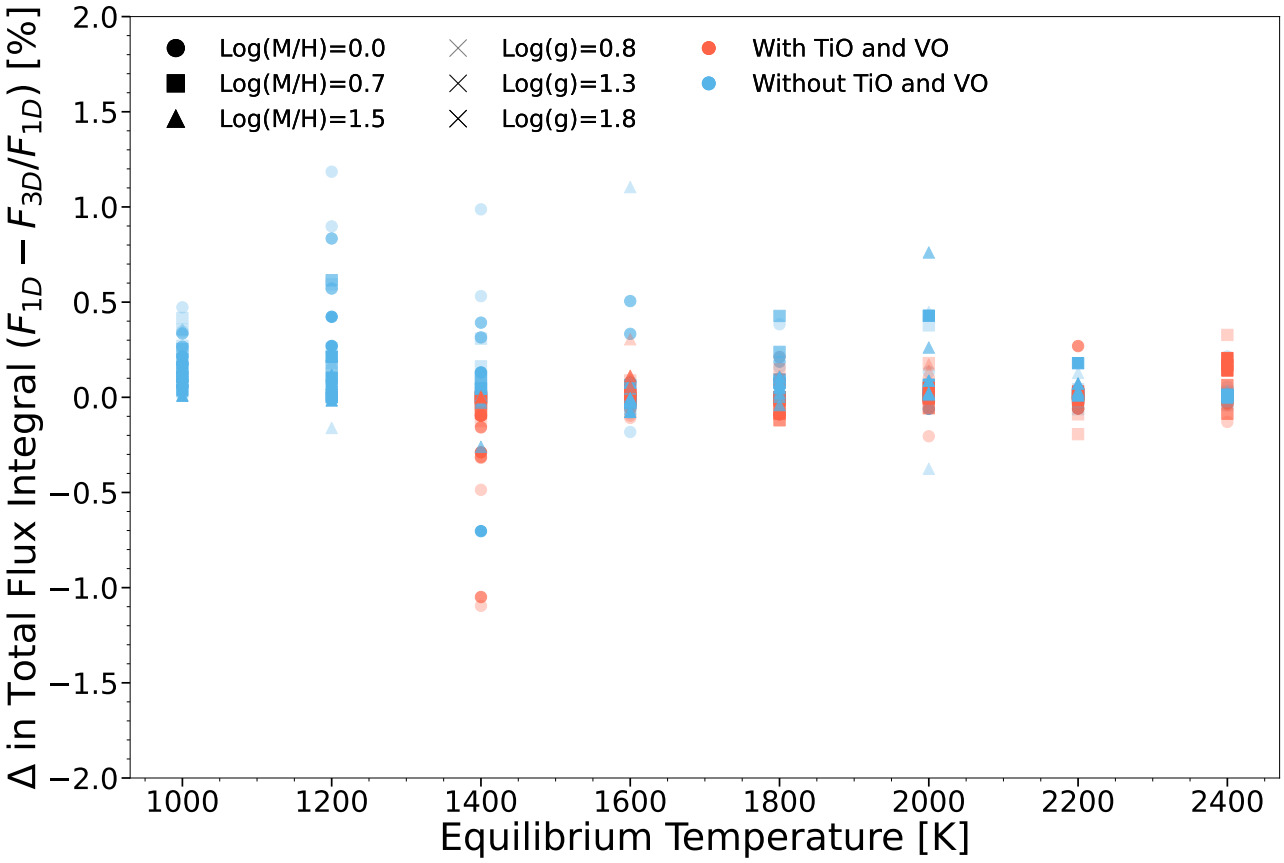


Figure 7.3: Difference in the integral of the secondary eclipse spectra flux over all wavelengths between equivalent 1D and 3D models plotted against equilibrium temperature. The presence or lack of TiO/VO is indicated by colour, log(M/H) is indicated by the shape and log(g) is indicated by the opacity of each point.

In order to do this we look at the total integral of the secondary eclipse spectra flux. Although the 1D-RCTE and GCM models will display differences in the final pressure-temperature profiles, and individual spectral bands, the overall integral of the emitted flux

should be equal as, by definition, we fix the top of atmosphere incident flux to be constant between the models (if the parameters and redistribution factor are set correctly).

Figure 7.3 displays the relative difference between the total flux integral from the 1D and GCM secondary eclipse spectra. This deviation in the flux integral is very low - $\leq$1.5%, even in the worst models. We also notice that, in the majority of cases, the 1D flux integral is slightly higher overall than the GCM.

Overall, the disparity in total flux integral is well within an acceptable margin of error, with the low residual due to any remaining small differences in the opacity line lists used between the two models, and small numerical rounding errors.

7.4 Overview of 1D v 3D

Figure 7.4 displays a representative example comparison between the pressure-temperature profiles and secondary eclipse spectra for equivalent 1D and 3D models. First, looking at the comparison between vertical temperature profiles, we are able to split the atmosphere up into four distinct regions of different behaviour:

1. **Unconverged region**, where the 3D temperature is equilibriated with the initial conditions in the deep layers, due to the very long radiative timescales.
2. **Transport dominated region**, where the 3D temperature is typically colder than the 1D.
3. **Photospheric region**, where the 1D and 3D temperatures are of the same magnitude.
4. **Radiative dominated region**, where the 3D temperature is typically warmer than the 1D.

These regions can be understood as a consequence of the pressure dependency of heat redistribution in the GCM. In region 2 (the converged deep layers), the energy transport is very efficient, whereas it is much less efficient at low pressures. This means that the effective heat redistribution parameter varies with height in an atmosphere. However, for the 1D models, only a single heat redistribution parameter is used, which roughly corresponds to the heat redistribution factor at the photosphere. Consequently, we expect the deeper layers to be colder in the 3D models, as they will always have a heat redistribution that is more efficient than at the photosphere - and vice versa for the shallow layers. In addition to this, the deep layers in the day-side of the GCM must be equilibriated with the cooler night-side, further reducing the temperature in comparison to the 1D.

In the left panel in Figure 7.4 we can see that these differences in temperature profiles have a significant impact on the secondary eclipse spectra, with the 1D models exhibiting much deeper molecular features. This can simply be understood as the spectra probing different pressure levels in the atmosphere with wavelength. Outside of the molecular bands, high pressure regions are probed where the 3D temperature is lower than the 1D. Inside the bands we have the opposite, with low pressure regions being probed where the 3D temperature is higher than the 1D.

Figure 7.5 displays a similar comparison between pressure-temperature profiles and secondary eclipse spectra, for models containing TiO/VO in the atmosphere. From the temperature profiles we find that our four atmospheric regions largely remain, with the 3D temperature being hotter than the 1D above the photosphere and cooler below it. We do note

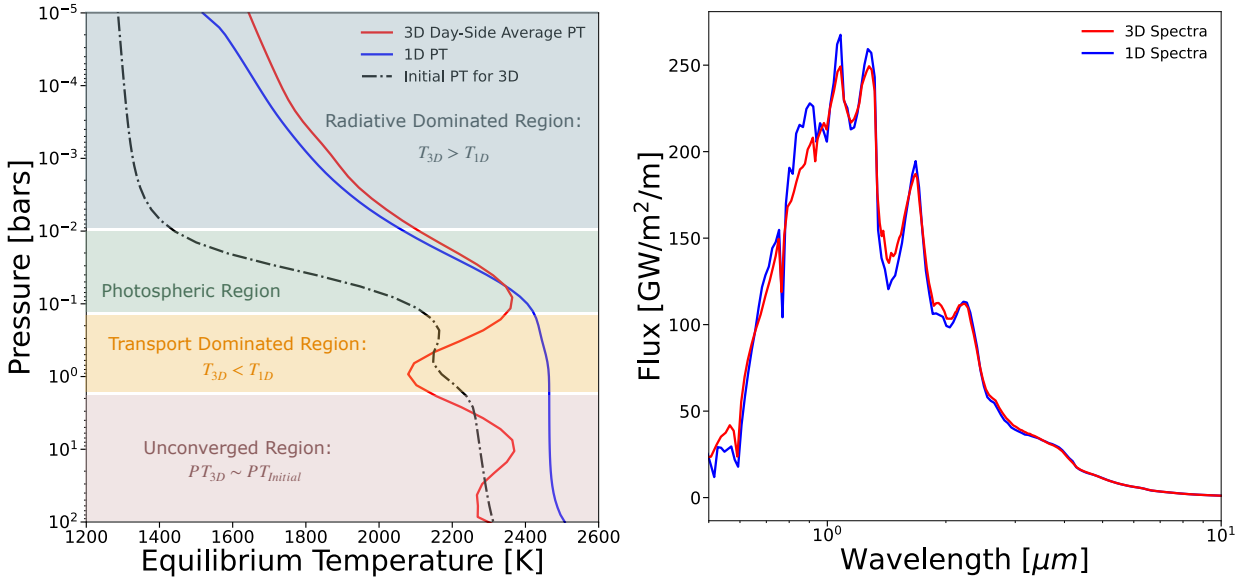


Figure 7.4: Left Panel: Pressure-temperature profiles for 1D and 3D models with $T_{\rm eq}$=1800K, Log(M/H)=0.7, $P_{norm} = 0.37$, Log(g)=1.3 and TiO/VO removed from the atmosphere. The initial profile used in the 3D model is also displayed by the dashed line. Key regions of the atmosphere are shaded in different colours. **Right Panel:** Secondary eclipse spectra for 1D and 3D models with the same parameters as the left panel.

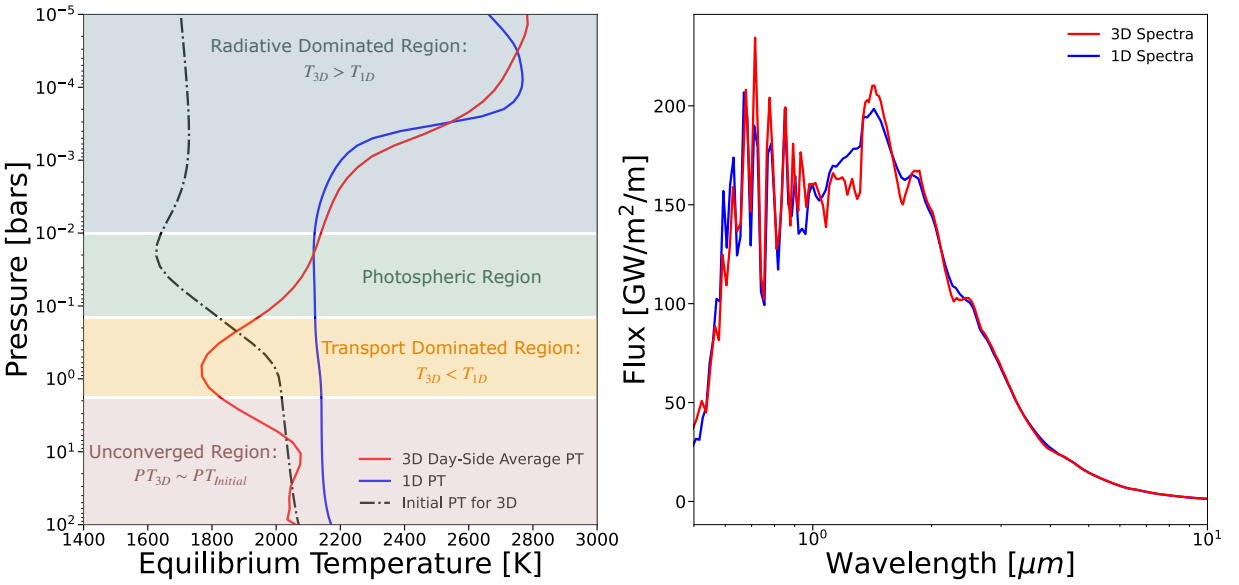


Figure 7.5: Left Panel: Pressure-temperature profiles for 1D and 3D models with $T_{\rm eq}$=1800K, Log(M/H)=0.7, $P_{norm} = 0.37$, Log(g)=1.3 and TiO/VO present in the atmosphere. The initial profile used in the 3D model is also displayed by the dashed line. Key regions of the atmosphere are shaded in different colours. **Right Panel:** Secondary eclipse spectra for 1D and 3D models with the same parameters as the left panel.

that in this case there are some very low pressure regions at $\sim 10^{-4}$ bars, where the 1D temperature becomes hotter than the 3D. This is unexpected, and the exact cause is unknown.

One likely explanation is that the remaining discrepancies in the opacities, which will have a large effect at very low pressures. However, these regions do not have a significant impact on our overall spectral comparison.

In the left panel in Figure 7.4 we find that, in the presence of TiO/VO, differences between the 1D and 3D thermal structures now manifest in a different way on the spectral comparison. Due to the temperature inversion, features are now seen in emission, meaning that the 3D spectra now displays deeper molecular features compared to the 1D.

7.4.1 Special Case: 1400K TiO/VO

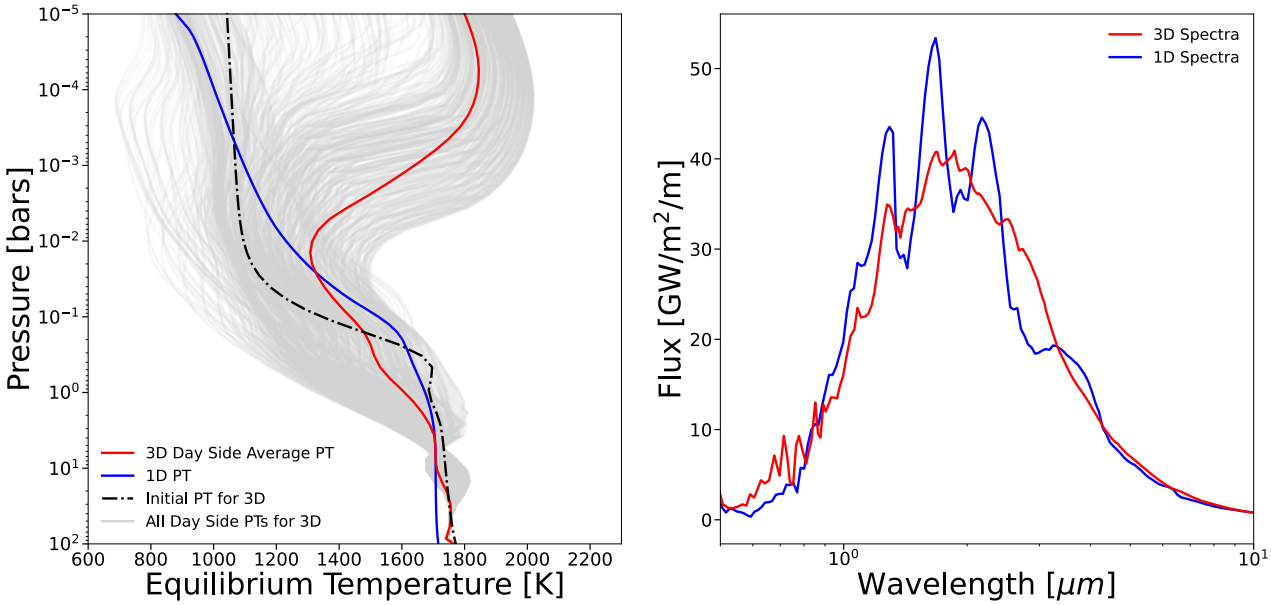


Figure 7.6: Left Panel: Pressure-temperature profiles for 1D and 3D models with $T_{\rm eq}$=1400K, Log(M/H)=0.7, P_{norm} = 0.37, Log(g)=1.3 and TiO/VO present in the atmosphere. The initial profile used in the 3D model is also displayed by the dashed line. All day-side temperature profiles for the 3D model are displayed with reduced opacity. **Right Panel:** Secondary eclipse spectra for 1D and 3D models with the same parameters as the left panel.

The left panel of Figure 7.6 displays the 1D and day-side average 3D temperature profiles for a model at 1400K with TiO/VO present in the atmosphere. Here we note that the average day-side 3D temperature profile displays a temperature inversion, whereas the 1D does not. This is because the substellar temperature profile is always hotter in 3D compared to 1D models, due to the nature of averaging over the planet to produce a single representative profile. Because of this, the 3D temperature profile is able to cross the TiO/VO condensation curves in certain regions of the day-side and produce a thermal inversion in the upper atmosphere. In contrast, the 1D model does not cross these condensation curves, and therefore has no thermal inversion. In the right hand panel of Figure 7.6 we can see that this causes drastic differences to the secondary eclipse spectra. The 1D model displays deep molecular absorption features in comparison to the near blackbody spectra of the 3D, with some small emission features. This highlights the importance of thorough geometrical modelling at the transition between inverted and non-inverted atmospheres.

7.5 Spectral Indices

The top panel of Figure 7.7 displays the water feature strength, as described in Chapter 4, for all the of 1D-RCTE and GCM models within the grid. The bottom panel in this figure displays the logarithmic ratio between the water feature strengths of comparable 1D-RCTE and GCM models, highlighting those with a negative absolute ratio. From this we find a general trend - that the 1D water feature strength is found to have a more positive value than the 3D, although this trend breaks down for the highest temperature models for which both 1D and 3D values become close to that of a blackbody. This means that, in models without TiO/VO, the 1D models display a *stronger* absorption feature, whereas in models with TiO/VO the 1D models have a *weaker* emission feature. This is expected from the spectral comparison in Section 7.4. Spectral features are found to be deeper in the 1D models when TiO/VO are removed and more shallow in 1D models when these species are present. This naturally means that the 3D models will be closer to blackbody emission for a non-inverted atmosphere, whereas the 1D models will be closer to blackbody emission for an inverted atmosphere.

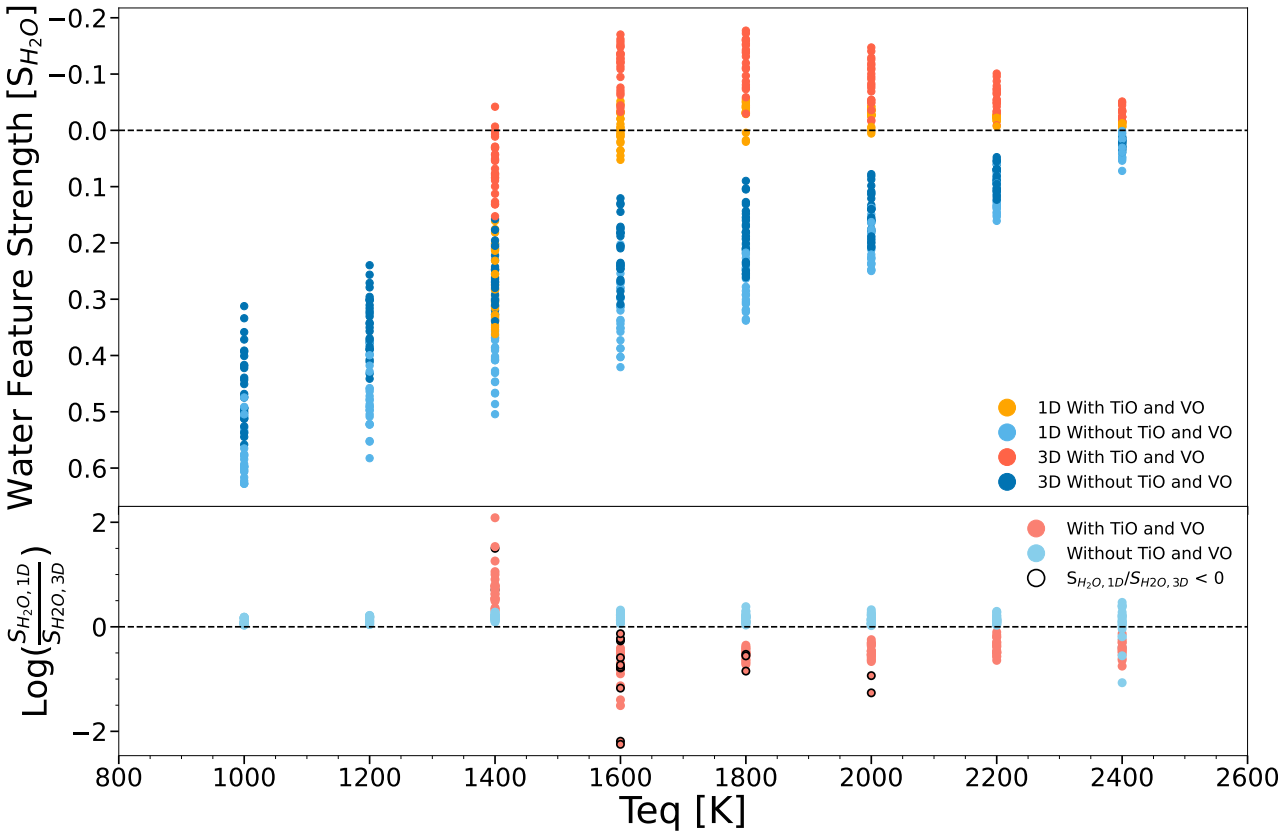


Figure 7.7: This figure shows a comparison between the water feature strength calculated for the 3D GCM grid and 1D grid computed with ScCHIMERA. **Top Panel:** Displays the water feature strength colour coded depending on the dimensionality of the model and the presence or lack of TiO/VO. **Bottom Panel:** Displays the log of the ratio between the water feature strength calculated for 1D models and the equivalent 3D models. Points are colour coded depending on the presence or lack of TiO/VO. Additionally, models with a negative ratio between the water feature strength in 1D and the GCM are given a black border.

We also note that there are a handful of models in which the 3D water feature is displayed in emission, whilst the 1D equivalent is in absorption. This is caused by the models which display temperature inversions in the GCM but not in 1D, as described in Section 7.4.1.

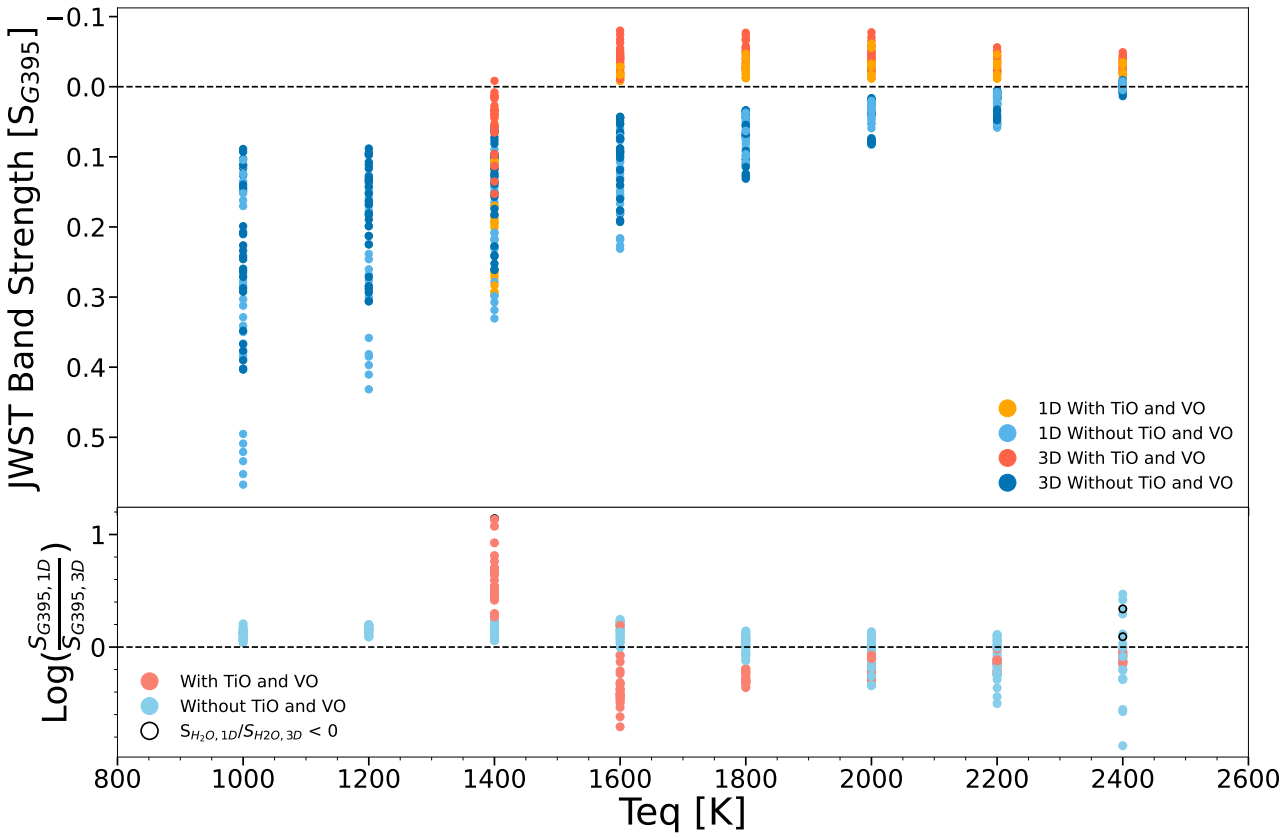


Figure 7.8: This figure shows a comparison between the feature strength calculated in the JWST NIRSpec G395M/G395H band-pass for the GCM grid and 1D grid computed with ScCHIMERA. **Top Panel:** Displays the G395M/G395H feature strength, colour coded depending on the dimensionality of the model and the presence or lack of TiO/VO. **Bottom Panel:** Displays the log of the ratio between the G395M/G395H feature strength calculated for 1D models and the equivalent GCM models. Points are colour coded depending on the presence or lack of TiO/VO. Additionally, models with a negative ratio between the G395 feature strength in 1D and the GCM are given a black border.

We additionally include Figure 7.8, which displays a spectral feature strength, calculated via the same method as the water feature strength for wavelengths in the JWST NIRSpec G395M/G395H band-pass. For this index we take 'in-band' wavelengths of 4.3-4.5 μm and 'out-of-band' wavelengths of 3.9-4.1 and 4.8-5 μm. This spectral index largely displays the same overall trends as the water feature strength index. Although, we note that the temperature at which the index in the band-pass becomes roughly equal for the 1D and 3D models with TiO/VO removed is much lower, at ∼1800K. We primarily include this feature strength here for future use. In the era of Hubble observations, the water feature strength has been the most useful comparison to observation. However, going forward an index within the JWST observing range will become most useful for observational comparison.

7.6 Spectral Dependence of the Flux Residuals

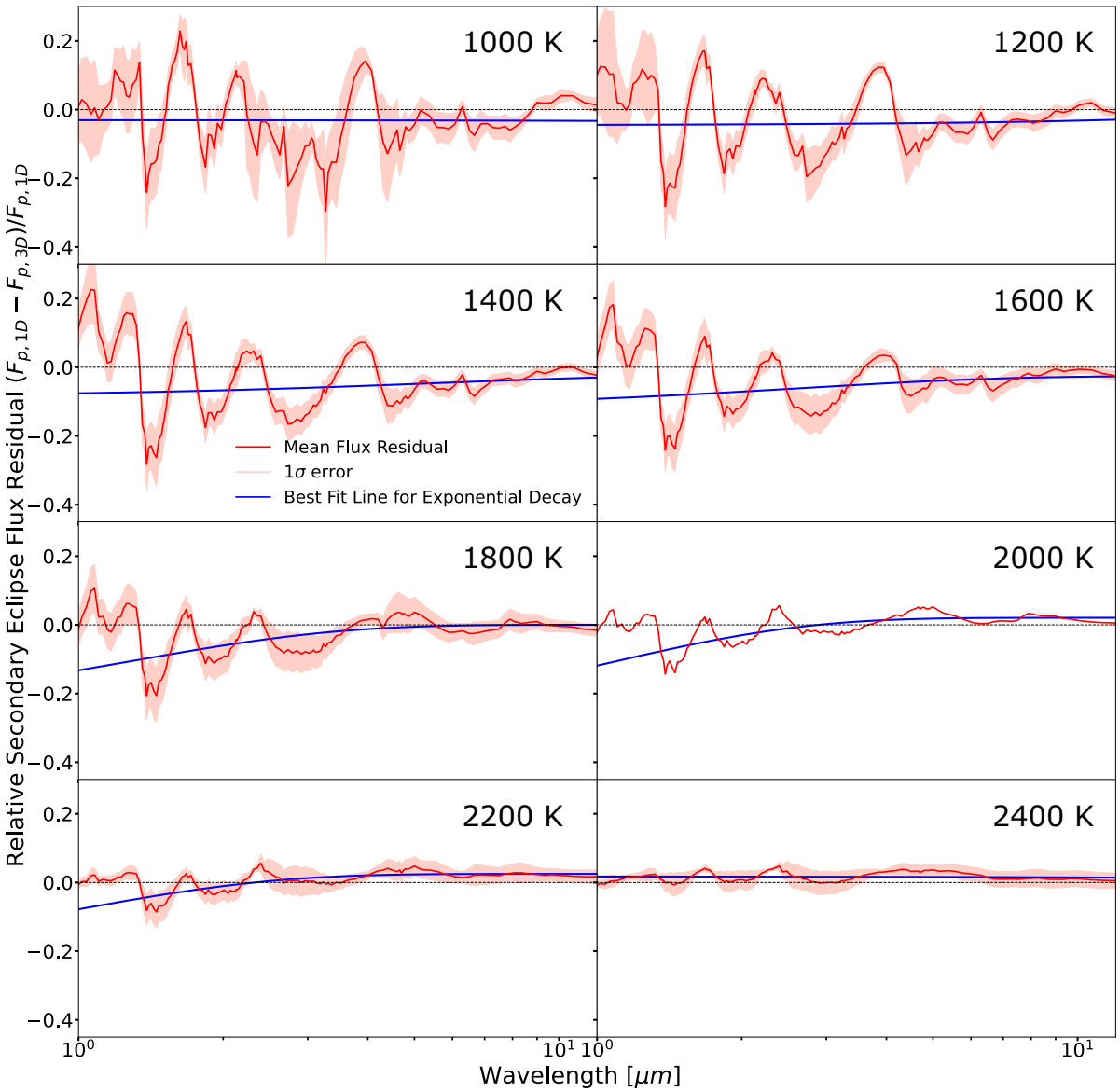


Figure 7.9: Relative secondary eclipse residual vs wavelength, averaged at each temperature across the other parameters within our grid, for models with TiO/VO removed. In addition to the mean we also plot the 1σ error. An exponential decay curve is also plotted, fitted to the mean residual at each temperature. In reference to these residuals, emission spectra observed for WASP-18b (T_{eq} = 2505K (Coulombe et al. 2023a)) via JWST NIRISS/SOSS (0.85-2.85 μm) (Coulombe et al. 2023b) have ∼5-10% error bars at each spectral data point. Emission spectra observed for WASP-77AB (August et al. 2023) ($T_{\rm eq}$ = 1693 (Saha 2024)) via JWST/NIRSpec (2.674-5.173 μm) and HD 149026b (Bean et al. 2023) ($T_{\rm eq}$ = 1694) via JWST/NIRCam (2.349-5.082 μm) have ∼5-10% and ∼15-20% error bars respectively

We now move to investigating the residuals between the 1D and GCM grid over all wavelengths, rather than in specific spectral bands. Figure 7.9 displays the average relative secondary eclipse residual, at each temperature within our grid, calculated as a function of wavelength for the models with TiO/VO removed. From this, we find that the residual

varies significantly with wavelength, increasingly so at lower temperatures. Inside of the spectral bands, the 3D flux is larger than the 1D flux. Outside of the spectral bands we find the inverse relationship, with the 1D flux appearing to be generally larger. Below 1600K, the magnitude of the residual inside and outside of spectral bands is fairly even. At this temperature and above, the residual is clearly more significant within the spectral bands. The magnitude of the residuals both inside and outside of spectral bands also appears to *decrease* overall with wavelength. We discuss this relationship in more detail in Section 7.6.3. Figure 7.10 displays this same metric for models with TiO/VO present in the atmosphere.

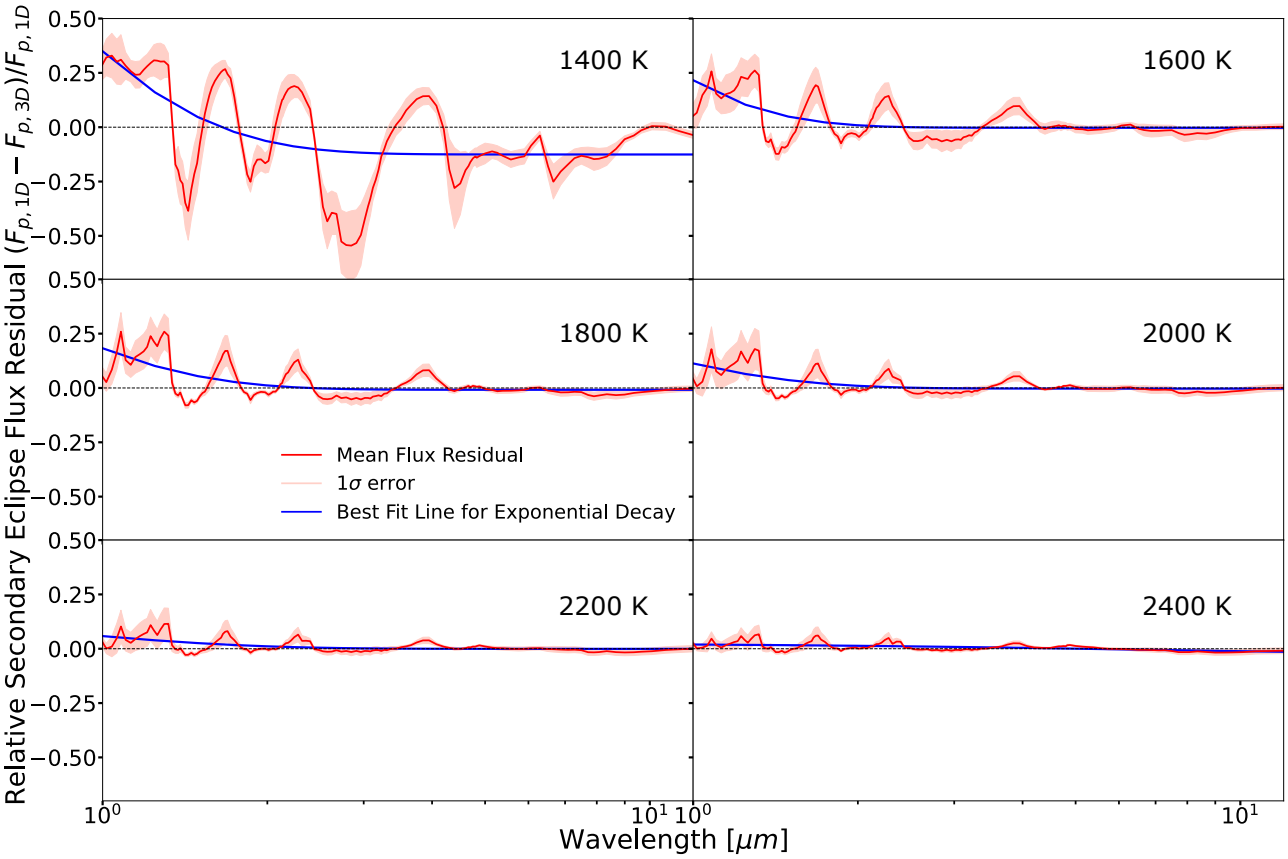


Figure 7.10: Relative secondary eclipse residual vs wavelength, averaged at each temperature across the other parameters within our grid, for models with TiO/VO present in the atmosphere. In addition to the mean we also plot the 1σ error. An exponential decay curve is also plotted, fitted to the mean residual at each temperature.

Significantly, when TiO/VO are present, the relative magnitude of the residuals inside and outside of the bands switch (apart from the 1400K models for which the 1D models produce no inversion, as discussed in Section 7.4.1).

The 3D model flux is still larger than the 1D inside of the bands, and smaller outside of the bands. However, the magnitude of the residual outside of the bands is now much more significant. Additionally, the magnitude of the residual outside of the bands still exhibits a decreasing trend with wavelength. Inside of the bands, the residual is mostly constant at a low negative value.

We now wonder how these residuals compare with data from emission spectra observed via JWST. WASP-18 b (T_{eq} = 2505K (Coulombe et al. 2023a)) observed via JWST NIRISS/-SOSS (0.85-2.85 μm) (Coulombe et al. 2023b) has ∼5% error bars at each spectral data point. This temperature is above the range of our model grid, but inspecting our 2400K averaged residuals shows these errors are likely within the potential discrepancy between 1D and 3D modelling. However, emission spectra observed for WASP-77 Ab (August et al. 2023) ($T_{\rm eq}$ = 1693 (Saha 2024)) via JWST/NIRSpec (2.674-5.173 μm) and HD 149026 b (Bean et al. 2023) ($T_{\rm eq}$ = 1694) via JWST/NIRCam (2.349-5.082 μm) have ∼5-10% and ∼15% error bars respectively. In our average 1600K and 1800K residuals, we find differences of up to 20% over the same wavelength range, implying that the differences between 1D and 3D spectra would likely affect interpretation of these observed spectra.

7.6.1 Overall RMS of the Residuals

To better understand the variation in the overall residuals across our comparison grid parameters, we now look at Figure 7.11, which displays the spectrally averaged RMS of the relative secondary eclipse residual between 1-10μm for each individual model. From this we can clearly see a decreasing trend in the residual RMS with temperature. This is a natural effect of the spectra becoming close to a blackbody at higher temperatures i.e where all molecular features in both absorption and emission are reduced. In addition to this, combinations of our other grid parameters are capable of altering the RMS of the residual by up to 10% at each equilibrium temperature. It should be noted that, as seen in Figures 7.9 and 7.10, the wavelength dependent residual is capable of varying inside and outside of bands by around double the 1-10 μm average. As we have already discussed, from the limited number of observations taken so far, JWST eclipse observation error bars seem to be at $\sim$ 10%. This would imply that caution is required when using 1D radiative-convective equilibrium models for atmospheric characterisation in planets below $\sim$ 2000K.

7.6.2 Parameter Dependence in the RMS of Residuals

To see in more detail how the RMS of the relative secondary eclipse residual between 1-10μm varies across the entire parameter space, we include Figure 7.12, which shows colour maps of this metric for models with TiO/VO removed. Several trends can be found in these colour maps. First, the RMS of the residual clearly decreases with temperature, as already seen in Figure 7.11. The RMS of the residual also generally decreases with shorter normalised period and increases for higher metallicity. Although there are some cases where this trend is broken on a model to model basis. The trend we observe in period is due to the complex relationship between the relative vertical gradients of the 1D and 3D temperature profiles. These are influenced not only by the vertical heat redistribution, but also by changes in the stellar absorption depth, due to the different stellar spectrum used as input parameters. The trend in surface gravity is harder to pinpoint. In higher temperature models the residual generally decreases with increasing gravity, but this relationship is swapped for lower temperature models. Regardless of the trend, the effect of gravity is relatively small compared to our other variables. Additionally, the effect of all other planetary parameters is much lower in the higher temperature models.

Figure 7.13 shows colour maps for the RMS of the relative secondary eclipse residual, between 1-10 μm across the entire parameter space of our comparison grid for models with

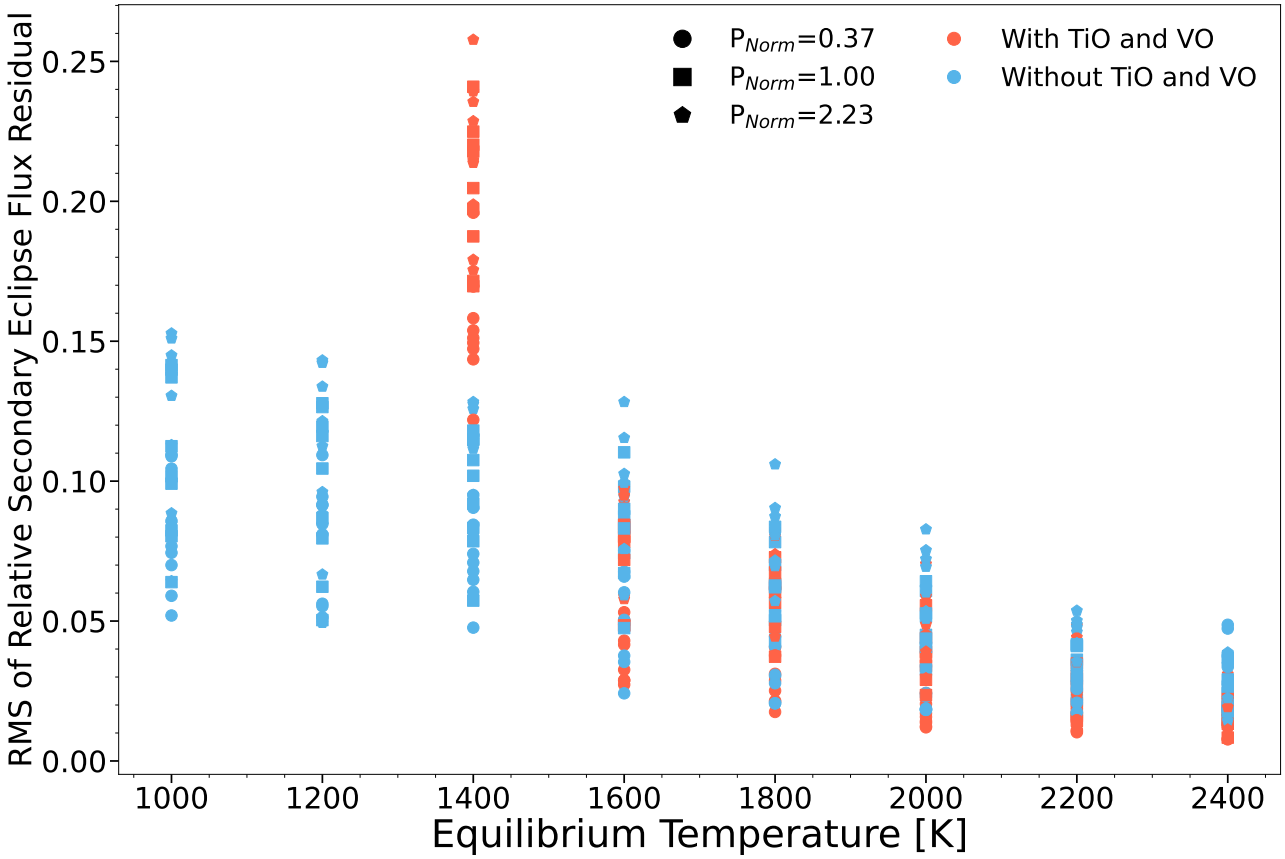


Figure 7.11: RMS of the relative secondary eclipse residual between 1-10μm plotted as a function of temperature for all models within the grid. The presence or lack of TiO/VO in the atmosphere is denoted by the colour of each point.

TiO/VO present in the atmosphere. The clear trends with equilibrium temperature and normalised period remain. Increasing metallicity and surface gravity both appear to reduce the residual in this case (apart from in the 1400K models). However, their effect is very small compared to that of temperature and period.

7.6.3 Dilution Factor Slope

As we have mentioned in Section 7.1, a dilution or 'scaling' factor (Taylor et al. 2020) is sometimes applied to 1D models, in order to adjust the pressure-temperature profile and spectra to better account for inhomogeneous atmospheres. This dilution factor is exhibited in Taylor et al. (2020) as a wavelength dependent slope between retrieved spectra for a 1D model, with and without a dilution factor applied (see their Figure 9).

In Figure 7.9, a line of best fit for the exponential decay of the spectral dependence of the residual can be seen. At temperatures of 1600K and above we can clearly see the slope as described in Taylor et al. (2020), with the magnitude of the *negative* ratio between the flux emitted in the 3D and 1D models decreasing with wavelength, leading to a *positive* slope.

However, this slope clearly does not account for the oscillatory behaviour between regions inside and outside of the bands. Outside of the spectral bands, the ratio between the 3D and 1D emitted flux is reversed, with the 1D emitting more than the 3D. This can also

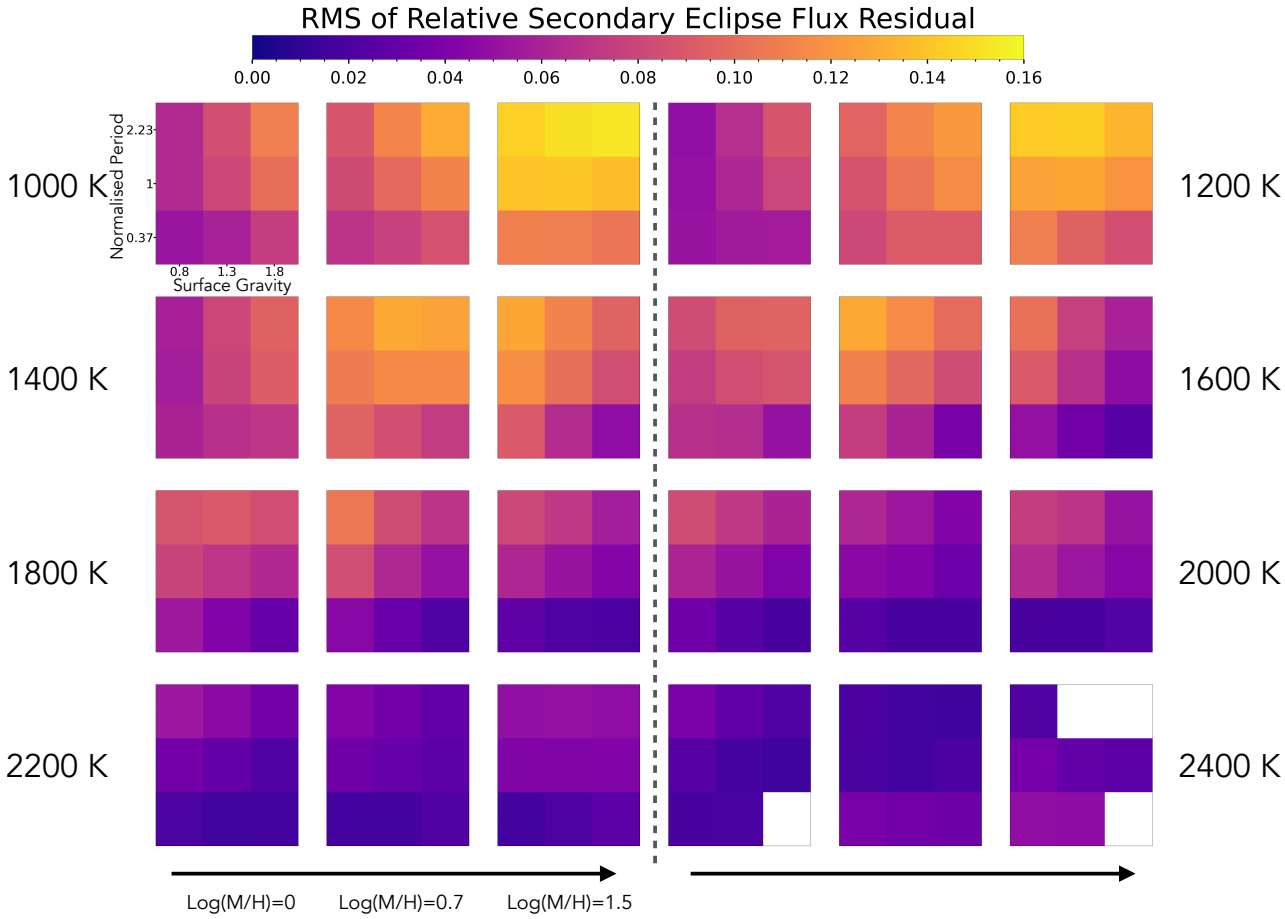


Figure 7.12: Colour maps for the RMS of the relative secondary eclipse residual between 1-10μm for models with TiO/VO removed. Each individual subplot has surface gravity increasing across rows and normalised period decreasing down columns. The overall figure has equilibrium temperature increasing down columns, with the left three plots corresponding to the temperature on the left and vice versa for the right plots. In the same manner, the metallicity increases across rows in the overall plot.

be seen in Figure 7.4, due to the consequences of differing behaviour between the models within the transport dominated region of the atmosphere.

This relationship between regions inside and outside of the bands is further complicated when TiO and VO are present within the atmosphere. From Figure 7.5 we can see that the relationship in the ratio between the 1D and 3D emitted flux is maintained, with the 1D emitting less flux inside of the spectral bands and more outside of them. However, as the features are now in emission, the spectral differences outside of the bands tend to dominate over the differences within the bands, as seen in Figure 7.10. This leads to a *negative* slope, as the ratio of the magnitude of the *positive* ratio between the flux emitted in the 3D and 1D models decreases with wavelength. Again this does not account for the spectral regions inside of molecular bands, where we still generally find a negative ratio between the 3D and 1D flux.

Fitting this dilution factor slope becomes even more complex when individual models within the grids are compared, rather than the temperature averages. Figure 7.14 displays this slope fitted to three individual models which go against the trends observed in the tem-

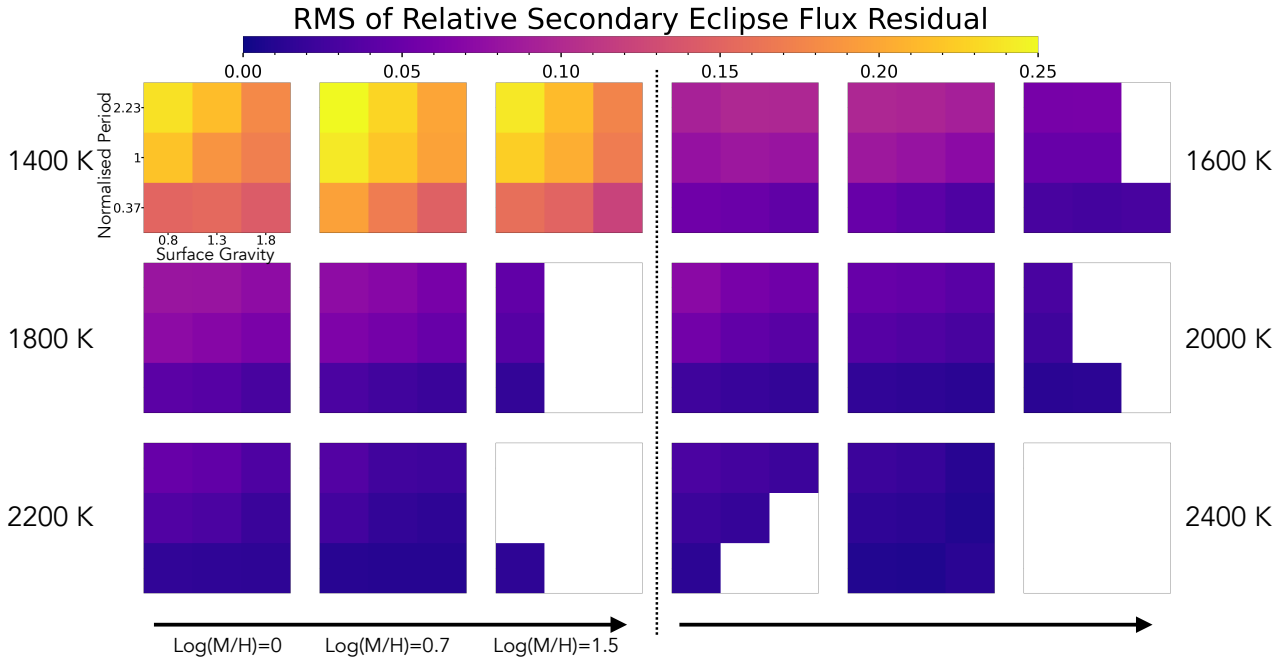


Figure 7.13: Colour maps for the RMS of the relative secondary eclipse residual between 1-10μm for models with TiO/VO present in the atmosphere. Each individual subplot has surface gravity increasing across rows and normalised period decreasing down columns. The overall figure has equilibrium temperature increasing down columns, with the left three plots corresponding to the temperature on the left and vice versa for the right plots. In the same manner, the metallicity increases across rows in the overall plot.

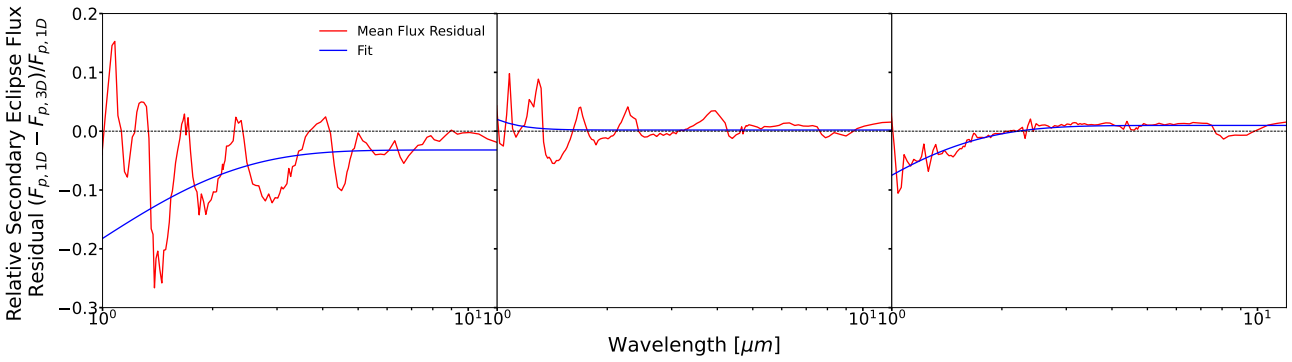


Figure 7.14: Relative secondary eclipse residual vs wavelength and best fit exponential decay curve for individual models with **Left Panel:** $T_{\rm eq}$=1600K, Log(M/H)=1.5 $P_{\rm norm}$=1, Log(g)=1.3 and TiO/VO removed **Middle panel:** $T_{\rm eq}$=1800K, Log(M/H)=1.5 $P_{\rm norm}$=0.37, Log(g)=0.8 and TiO/VO present. **Right Panel:** $T_{\rm eq}$=2200K, Log(M/H)=1.5 $P_{\rm norm}$=0.8, Log(g)=0.8 and TiO/VO present.

perature averaged residuals. The left panel shows a 1600K model, with TiO/VO removed, that has very strong positive slope, despite the temperature average displaying a near-flat, fit. The center panel shows an 1800K model, with TiO/VO present, which displays nearly no slope, despite the temperature average having a clear negative fit. The right panel shows a 2200K model, with TiO/VO present, which displays a *positive* slope, despite the temperature average displaying no slope and TiO/VO models generally having *negative* slopes.

The important take-away is that, although positive or negative slopes can clearly be fitted to the residuals between our 3D and 1D spectra, this slope is a second order effect when compared to the large oscillatory behaviour between different regions of the spectra. This implies that the primary factor which determines this slope in our model comparison is the gradient of the vertical temperature profile (i.e when different pressure levels are probed inside and outside of the spectral bands), rather than dilution of the hotspot. Unfortunately, this means that we cannot easily highlight the precise effect of an inhomogeneous day-side here, as our 1D and 3D models do not have the same temperature gradients. A free retrieval with a 1D model, obtaining a more accurate temperature gradient, would correct for the residuals due to the pressures probed inside and outside of the spectral bands. In this case, the dilution slope could therefore be separately derived.

Due to this large oscillatory behaviour between the molecular bands, we would recommend caution when using a single dilution factor in the characterisation of these atmospheres, as it is only capable of stretching spectral features in one direction (i.e by increasing the flux inside bands more than outside of them). As such, retrievals with a single dilution factor may correctly fit to certain regions of the spectra, whilst worsening the fit to others. One possible approach could be to use a multiple-dilution factor metric, which could be applied separately to the spectral regions inside and outside of bands independently (or even to individual spectral bands). However, this would require a-priori knowledge of the planetary properties and atmospheric chemistry and add significant complexity to numerical models, meaning that a multiple pressure-temperature profile approach may be easier. Improvements to this dilution factor metric are beyond the scope of this study and as such we leave this to future work. However, we highlight the importance of understanding this metric here, and recommend caution when applied in atmospheric retrievals.

7.7 Summary & Conclusion

In this chapter we have compared the thermal structure and secondary eclipse spectra of our drag-free GCM model grid to that of an equivalent 1D-RCTE model grid.

We show how the thermal structure in the models can be split into four distinctive regions of the atmosphere:

- **An unconverged region**, at very high pressures, where the 3D models are still equilibriated with their initial conditions.
- **A transport dominated region**, where the temperature in the 3D models is generally lower than the 1D models, due to increased heat redistribution below the photosphere and equilibriation with the planetary night-side.
- **A photospheric region**, where the temperature structures of the 1D and 3D models are of the same magnitude.

- **A radiative dominated region**, where the temperature in the 3D models is generally higher than in the 1D models due to reduced heat redistribution above the photosphere.

We further investigate how these atmospheric regions lead to differences in the planetary eclipse spectra. In models with TiO/VO removed, we show that the 1D models exhibit much deeper molecular features, due to the different pressures which are probed inside and outside of molecular bands. In the models containing TiO/VO we show that this trend is reversed, due to the temperature inversion causing the molecular features to swap to emission. In this case, the 3D models now display deeper molecular features than the 1D.

We go on to describe how the resulting differences in eclipse spectra will exhibit in spectral indices, including the water feature strength (as described in Sections 5.2 and 6.3.5) and a similar calculation for the JWST NIRSpec G395M/H band-pass. We show that the 1D models are generally found to have more positive spectral indices than the 3D models, meaning that in the case with TiO/VO removed the 3D models are closer to blackbody emission, and vice versa for the case with TiO/VO present.

We discuss the spectral dependence of the residuals between the 1D and 3D models, showing that this varies greatly depending on the wavelengths probed and planetary parameters. Again, we describe how these residuals are generally greater inside molecular bands in non-inverted atmospheres, and greater outside of molecular bands for inverted atmospheres. We compare these residuals to current secondary eclipse observations by JWST, showing that the disparity between 1D and 3D models is often larger than the error bars of these observations within certain spectral regions.

We additionally show the RMS of the spectrally averaged residuals between 1-10 μm, describing in more detail how these vary across our model parameter space. We show that the average residuals decrease as the equilibrium temperature increases and normalised period decreases. The surface gravity and metallicity, however, display no clear population-wide trend in relation to the residuals.

Finally, we discuss the dilution or 'scaling factor' used in atmospheric retrievals using 1D models to adjust for inhomogeneous atmospheres (Taylor et al. 2020). We fit slopes of exponential decay to the spectrally dependent, temperature averaged residuals. We show that these slopes are most prominent between temperatures of $1400 - 2200K$, with models at higher or lower equilibrium temperatures generally having flat fits. We also show how the sign of this slope is generally *positive* in non-inverted atmospheres and *negative* in inverted atmospheres. However, we also show how this slope is likely a second order effect when compared with the large oscillation in the residuals between regions inside and outside of molecular bands. We further show that specific parameter sets can cause these slopes to go against the general trends seen in the temperature averaged residuals. As such we conclude that, although this dilution effect is likely present, more research is required into how this can be robustly applied to atmospheric retrievals.

Bibliography

Allard F., Hauschildt P. H., Schwenke D., 2000, ApJ, 540, 1005
Alvarez R., Plez B., 1998, A&A, 330, 1109
Amundsen D. S., Tremblin P., Manners J., Baraffe I., Mayne N. J., 2017, A&A, 598, A97
Arcangeli J., et al., 2018, ApJ, 855, L30

August P. C., Bean J. L., Zhang M., Lunine J., Xue Q., Line M., Smith P. C. B., 2023, ApJ, 953, L24
Baeyens R., Decin L., Carone L., Venot O., Agúndez M., Mollière P., 2021, MNRAS, 505, 5603
Baeyens R., Konings T., Venot O., Carone L., Decin L., 2022, MNRAS, 512, 4877
Bean J. L., et al., 2023, Nature, 618, 43
Blecic J., Dobbs-Dixon I., Greene T., 2017, ApJ, 848, 127
Caldas A., Leconte J., Selsis F., Waldmann I. P., Bordé P., Rocchetto M., Charnay B., 2019, A&A, 623, A161
Coulombe L.-P., et al., 2023a, arXiv e-prints, p. arXiv:2301.08192
Coulombe L.-P., et al., 2023b, Nature, 620, 292
Feng Y. K., Line M. R., Fortney J. J., Stevenson K. B., Bean J., Kreidberg L., Parmentier V., 2016, ApJ, 829, 52
Freedman R. S., Marley M. S., Lodders K., 2008, ApJS, 174, 504
Freedman R. S., Lustig-Yaeger J., Fortney J. J., Lupu R. E., Marley M. S., Lodders K., 2014, ApJS, 214, 25
Goody R. M., Yung Y. L., 1989, Atmospheric radiation : theoretical basis
Goyal J. M., et al., 2020, MNRAS, 498, 4680
Goyal J. M., Lewis N. K., Wakeford H. R., MacDonald R. J., Mayne N. J., 2021, ApJ, 923, 242
Husser T. O., Wende-von Berg S., Dreizler S., Homeier D., Reiners A., Barman T., Hauschildt P. H., 2013, A&A, 553, A6
Iyer A. R., Line M. R., Muirhead P. S., Fortney J. J., Gharib-Nezhad E., 2023, ApJ, 944, 41
Kreidberg L., et al., 2018, AJ, 156, 17
Lacis A. A., Oinas V., 1991, J. Geophys. Res., 96, 9027
Lacy B. I., Burrows A., 2020, ApJ, 905, 131
Line M. R., Parmentier V., 2016, ApJ, 820, 78
MacDonald R. J., Madhusudhan N., 2017, MNRAS, 469, 1979
MacDonald R. J., Goyal J. M., Lewis N. K., 2020, ApJ, 893, L43
Mansfield M., et al., 2018, AJ, 156, 10
Mansfield M., et al., 2020, ApJ, 888, L15
Mansfield M., et al., 2021, Nature Astronomy, 5, 1224
McKay C. P., Pollack J. B., Courtin R., 1989, Icarus, 80, 23
McKemmish L. K., Yurchenko S. N., Tennyson J., 2016, MNRAS, 463, 771
McKemmish L. K., Masseron T., Hoeijmakers H. J., Pérez-Mesa V., Grimm S. L., Yurchenko S. N., Tennyson J., 2019, MNRAS, 488, 2836
Molaverdikhani K., Henning T., Mollière P., 2019, ApJ, 883, 194
Pluriel W., Zingales T., Leconte J., Parmentier V., 2020, A&A, 636, A66
Saha S., 2024, ApJS, 274, 13
Schwenke D. W., 1998, Faraday Discussions, 109, 321
Taylor J., Parmentier V., Irwin P. G. J., Aigrain S., Lee E. K. H., Krissansen-Totton J., 2020, MNRAS, 493, 4342
Toon O. B., McKay C. P., Ackerman T. P., Santhanam K., 1989, J. Geophys. Res., 94, 16287
Wiser L. S., Line M. R., Welbanks L., Mansfield M., Parmentier V., Bean J. L., Fortney J. J., 2024, ApJ, 971, 33

Chapter 8

Summary & Outlook

8.1 Thesis Summary

The population of hot Jupiters is extremely diverse, with large variations in their irradiation, period, gravity and chemical composition. Their atmospheric metallicity is also largely unconstrained. In this thesis, it was our aim to explore the a-priori scatter in the population created by the different responses of atmospheric circulation to planetary parameters, in order to better understand the intrinsic planet diversity through the observed population level trends.

In **Chapter 2** we introduce the pre-existing theories about hot Jupiter atmospheres. We discuss the heating and cooling of atmospheres through radiation and the methods to model radiative transfer of incident stellar irradiation. Additionally, we discuss the role of strongly absorbing species at low pressure regions in an atmosphere, and their ability to cause temperature inversions. We go on to present the set of dynamical equations which can be used to model these atmospheres, in both spherical and pressure coordinate systems, including common approximations to these equations. We then discuss the dynamics that have been observed in hot Jupiter atmospheres. We present the mechanism thought to lead to formation of super-rotating jets, and discuss the likely contributors to the dissipation of kinetic energy. We further discuss relevant time and length scales for these atmospheres. Additionally, we discuss the overall redistribution of heat within these atmospheres, due to the different components of the circulation, and present the expected scaling of this heat redistribution, due to certain intrinsic planetary parameters. Finally, we discuss complications to the energy balance model of hot Jupiter atmospheres, such as magnetic drag, clouds and hydrogen dissociation.

In **Chapter 3** we introduce the non-grey SPARC/MITgcm global circulation model (Showman et al. 2009). We describe the dynamic modelling by this GCM, in addition to the plane-parallel radiative transfer code of Marley & McKay (1999) for radiative transfer modelling. We also discuss the dissipation schemes used within the GCM, and limitations of this particular model. We go on to describe the creation of the largest library (516 simulations) of 3D hot Jupiter models to date produced with the non-grey SPARC/MITgcm, under the assumption of local chemical equilibrium with local rain-out of condensate materials (Visscher et al. 2006, 2010). We then discuss the selection of free parameters used within the grid. Equilibrium temperature, orbital period, metallicity, surface gravity and Rayleigh drag timescales were all varied throughout the grid, including cross-variation. In addition, models with the strong photo-absorbing molecules TiO and VO artificially removed from chemical equilibrium were also run. These intrinsic planetary properties were varied systematically and jointly over the parameter space.

In **Chapter 4** we use our drag-free GCM grid to begin exploring how the wide range of planetary parameters modelled can cause different responses in the atmospheric circulation. We show that the combined effect of the planetary parameters leads to a large diversity in the ability of atmospheres to transport heat from day-side to night-side at a given equilib-

rium temperature. We further show that the hot-spot offset is a non-monotonic function of planetary rotation period and explain our findings as competition between the rotational and divergent parts of the circulation. As a consequence, we show that phase curve offset and amplitude do not necessarily track each other, as rotational and divergent circulation both advect heat from day-to-night, but have counteracting effects on the offset. We additionally show how this relationship between heat redistribution and hot spot offset, caused by the combined components of divergent and rotational circulation, can impact temperature contrast between the planetary limbs. We find that this temperature contrast is expected to be largest for planets with equilibrium temperatures of $\sim$ 2000K.

In **Chapter 5** we further utilise our drag-free model grid to investigate the effects of planetary parameters on specific spectral band-passes. We compare our findings with the current secondary eclipse data sets observed with Spitzer/IRAC and HST/WFC3. We find that the sudden jump in brightness temperature observed in the Spitzer secondary eclipse measurements (Deming et al. 2023) can be naturally explained by the appearance of TiO/VO at approximately 1800K. We further show that observed spectral variation of the water feature in the HST/WFC3 band-pass (Mansfield et al. 2021) is poorly matched by our model grid between 1400-2200K. We suggest that partial depletion of TiO and VO in the atmosphere could be responsible for this disparity. Finally, we compare our phase curve offset and amplitude with those observed in the Spitzer 3.6 μm and 4.5 μm bands, finding that the intrinsic scatter in our model grid is well aligned with the observed scatter in the data.

In **Chapter 6** we explore the effects of atmospheric drag on the thermal structure and observable features of hot Jupiter atmospheres. We use our drag model grid, with a range of drag timescales, to show that drag has its strongest effect on spectra at short wavelengths and outside of spectral bands. We discuss how this is caused by the different pressures probed by the spectra at different wavelengths, with the drag timescale being dominant deeper in the atmosphere compared to radiative timescale being most dominant at low pressures. We show how, in addition to suppressing the equatorial jet, strong high latitude reverse jets can form in the presence of drag, leading to non-monotonic shifts in the atmospheric hot-spot with drag strength. These strong reverse jets also affect phase curve offset and amplitude independently, as they still advect heat from day-to-night. This further reinforces our discussions in Section 4.4.5, on the complex relationship between these features. Additionally, we show how drag dependent variation in the offset is dampened at higher metallicities, and that the exact value of the offset can be degenerate between the metallicity and strength of drag. We further show that the spectral dependence of the offset is altered by drag and metallicity in different ways, supporting the need for further spectral phase curve observations to disentangle these two effects. By investigating the 1.4 micron water feature strength in our drag models, we find that the effects of drag on the combination of day-side temperature and the strength of the feature can cause a diagonal trend away from drag-free model predictions. We hypothesise that this may account for some of the poorly matched observed data in Section 5.2. Finally, we investigate the effects of magnetic drag on the heat redistribution. We show that the efficiency of redistribution decreases smoothly with temperature for constant magnetic fields, and conclude that it is unlikely for magnetic fields to cause the brightness temperature increase found in (Deming et al. 2023).

In **Chapter 7** we compare our 3D GCM grid to an equivalent 1D-RCTE model grid, in order to investigate the effects of model dimensionality on the thermal structure and spectra of hot Jupiters over a wide parameter space. After describing the benchmarking of these models, we show how comparison between the thermal structures can be split into four dis-

tinctive regions, based on the vertical variation in the efficiency of heat redistribution in the 3D models. We go on to show how these regions lead to clear differences in the secondary eclipse spectra, with 1D models exhibiting much deeper molecular features for non-inverted atmospheres, and vice versa for inverted atmospheres. We further describe how these spectral differences will manifest in observed spectral indices for both the HST/WFC3 water feature and in the JWST NIRSpec G395M/H band-pass, with 1D models generally found to have more positive values in these indices. Next, we discuss the spectral dependence of the residuals between the 1D and 3D spectra. We show how this varies greatly depending on the wavelength, with large oscillations between regions inside and outside of molecular bands. Comparing the magnitude of these residuals to current secondary eclipse observations with JWST, we show that (within certain spectral regions) the disparity between 1D and 3D models are larger than the observational error bars. Additionally, we describe how the spectrally averaged RMS of the residual varies across the parameter space. The residuals are found to vary most with temperature and rotation period. Finally, we discuss the dilution factor used to adjust 1D models for in-homogeneous atmospheres in retrievals. By fitting slopes of exponential decay to our eclipse spectra residuals, we show that the dilution between 1D and 3D models is likely a second order effect when compared to the large oscillations between different spectral regions.

Overall, this GCM library is a powerful tool that can be used to investigate the effects of individual parameters, and a combination of parameters, on thermo-dynamical structure and key observable features in hot Jupiter atmospheres.

8.2 Potential for Future Work

8.2.1 Deconstruction of the Circulation

In Section 4.4.2 and 6.3.4 we display how, due to the differing ways in which divergent overturning circulation and rotational circulation from the jet redistribute energy in an atmosphere, the offset of the atmospheric hotspot and day-to-night temperature difference (traced by the phase curve offset and amplitude) do not necessarily track each other. In Section 4.4.2 we use the thermal Rossby number as a method to asses where the critical point between an atmosphere dominated by rotational heat transport and one dominated by overturning heat redistribution may lie. We additionally use equation 4.5 (Hammond & Pierrehumbert 2018) to approximately explain this behaviour. However, in Section 6.3.4 we show how in the presence of drag the thermal Rossby number is no longer a good measurement for this critical point. A far more robust way to look into how the balance between overturning and rotational heat redistribution is affected with planetary parameters is to decompose the heat redistribution, and separately look at the relative magnitudes of these two competing regimes. Hammond & Lewis (2021) show how contributions from the rotational, i.e the jet and eddies, and divergent overturning circulation can be separated using Helmholtz decomposition, and wrote a code packet which can be applied to GCM simulations to this end. This was adapted from the Helmholtz decomposition from Windspharm (Dawson 2016). Application of this method to the GCM grid provides an interesting avenue for further research into the ways in which hot Jupiter atmospheres redistribute heat, and may provide a more robust insight into the critical point at which atmospheres become dominated by different circulatory mechanisms depending on their parameters.

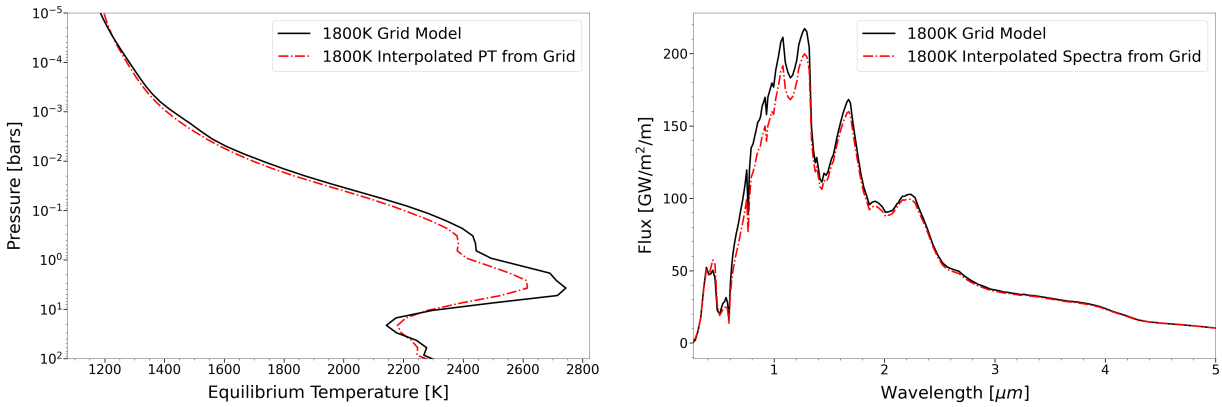


Figure 8.1: Left Panel: Comparison between the evening limb temperature structure of an 1800K equilibrium temperature model (solid black line) and an interpolated temperature structure for the same set of parameters (dashed red line). Right Panel: Comparison between the secondary eclipse spectra of an 1800K equilibrium temperature model (solid black line) and an interpolated spectra for the same set of parameters (dashed red line).

8.2.2 Grid as a Fast Characterisation Tool

One of the most obvious applications for the GCM model grid is as a tool to quickly generate an approximate model for specific planets in order to aid characterisation efforts. The grid is large enough, and sampled at a level which enables fast interpolation to a wide array of planetary parameters. Although bespoke GCM simulations for specific planets will undoubtedly still be required, using the grid in this way will still be useful in providing fast insights into the relevance of 3D effects for specific atmospheres and quick comparisons to observed data.

Figure 8.1 displays the results of an interpolation routine applied to the grid to quickly generate models with a set of new parameters. For this test we removed the 1800K equilibrium temperature point. The basis of this interpolation script was kindly provided by Lindsey Wiser from ASU. We show that the interpolated model matches both the pressure-temperature profile and spectra reasonably well. Of course, this is currently a 'worst-case scenario' for the interpolation routine, as by removing an equilibrium temperature point (the parameter which will have the most drastic effect on the P-T profile and spectra) we have increased the spacing between points in the model grid.

This method has already been used to aid exoplanet characterisation efforts, i.e in Taylor et al. (2023) for early release JWST observations of WASP-96 b.

8.2.3 Grid as a Machine Learning Tool

In addition to being a useful tool for quick characterisation, the model grid is large enough to have potential use as a training set for machine learning algorithms. We have ongoing collaborations with Hamed Valizadegan, Thomas Greene, Miguel Martinho, and Taylor Bell of the NASA Ames research center. The aim of this project is to use our model grid of phase curves and spectra as a training set for a machine learning algorithm to create an emulator which can rapidly and accurately interpolate between the grid models, and which can be

implemented inside atmospheric retrieval routines.

Additionally, we have an ongoing collaboration with Chloe Fisher of the University of Oxford to apply machine learning techniques to the thermo-dynamical structure of our model grid.

8.2.4 Post-Processing of the Grid

A further avenue for research lies in the post-processing of our GCM model grid. Hood & Wardenier (prep) aim to post process models from our GCM grid with the gCMCRT (Lee et al. 2022). The aim of this study will be to better understand where in the parameter space 3D effects matter most, and how they will manifest in observable features and trends, for high resolution observations.

The GCM grid could also be post-processed with cloud micro-physics models. This has applied to a grid of pseudo-2D models (Baeyens et al. 2022) in Helling et al. (2023). However, it is currently unknown how temperature feedback from a cloud layer would affect the atmospheric hot-spot, and this method of post-processing would not allow for self-consistent feedback on the 3D thermo-dynamic structure.

8.3 Sliders and Data Availability

A secondary goal for this study was that, by producing our large grid of GCM models, we could create a resource which can be used by the wider exoplanet community. To this end the entire grid of modelled spectra, phase curves and thermal structures are made available to the community at `https://zenodo.org/doi/10.5281/zenodo.10785320` and `https://3dsim.oca.eu/hot-jupiters-3d-models`.

Additionally, we have developed a quick and easy to run python tool allowing for visualisation of the grid properties (see Figure 8.2 for an example), which is also available for download alongside the GCM grid data.

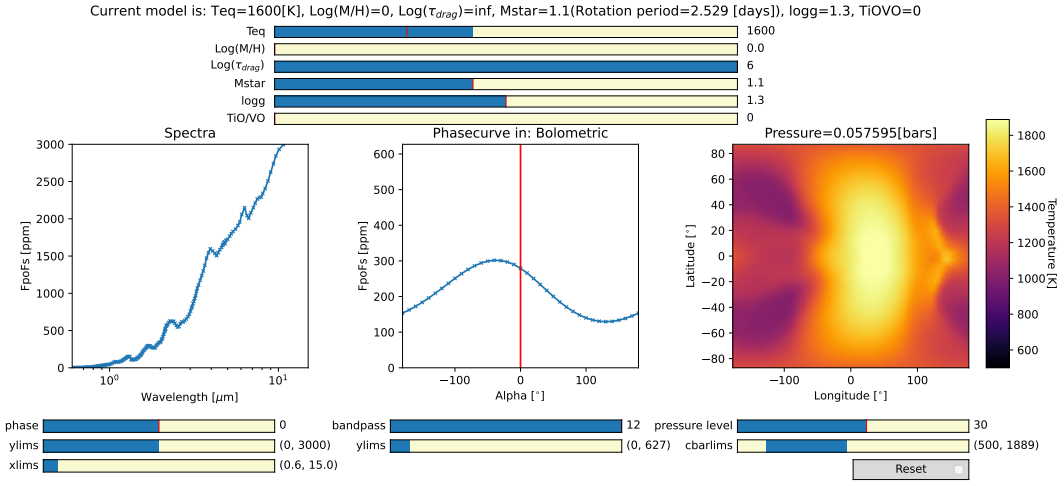


Figure 8.2: Example of the grid visualisation tool for displaying spectra, phase curves and the thermal structure of models in the GCM grid. This tool, along with the grid data, can be found at at `https://zenodo.org/doi/10.5281/zenodo.10785320` and `https://3dsim.oca.eu/hot-jupiters-3d-models`.

Bibliography

Baeyens R., Konings T., Venot O., Carone L., Decin L., 2022, MNRAS, 512, 4877
Dawson A., 2016, Journal of Open Research Software, 4, 31
Deming D., Line M. R., Knutson H. A., Crossfield I. J. M., Kempton E. M. R., Komacek T. D., Wallack N. L., Fu G., 2023, arXiv e-prints, p. arXiv:2301.03639
Hammond M., Lewis N. T., 2021, Proceedings of the National Academy of Science, 118, e2022705118
Hammond M., Pierrehumbert R. T., 2018, ApJ, 869, 65
Helling C., et al., 2023, A&A, 671, A122
Hood T., Wardenier J., 2021-in prep
Lee E. K. H., et al., 2022, ApJ, 929, 180
Mansfield M., et al., 2021, Nature Astronomy, 5, 1224
Marley M. S., McKay C. P., 1999, Icarus, 138, 268
Showman A. P., Fortney J. J., Lian Y., Marley M. S., Freedman R. S., Knutson H. A., Charbonneau D., 2009, ApJ, 699, 564
Taylor J., et al., 2023, MNRAS, 524, 817
Visscher C., Lodders K., Fegley Bruce J., 2006, ApJ, 648, 1181
Visscher C., Lodders K., Fegley Bruce J., 2010, ApJ, 716, 1060

Acknowledgements

I would like to begin by thanking Vivien Parmentier for his supervision during my DPhil project. Your feedback, guidance and support have been invaluable to my development both as an academic and in general throughout the last four years. I would like to thank you and Coline for welcoming us into your home many times, and especially for your continued dedication to my supervision after moving to Nice. I would like to further extend my thanks to Raymond Pierrehumbert, for taking on the role as my formal supervisor after Vivien moved to Nice.

A big thank you also to Lindsey Wiser, without whom I could not have completed large portions of this work. Your tireless efforts running models all hours of the day and night are greatly appreciated. I would also like to thank Xi Zhang, Xianyu Tan and Thaddeus Komacek for their useful conversations pertaining to this work. Additionally, I thank Michael Line and Jingxuan Yang for their help and input in developing the slider visualisation tool. An extra thank you to Mark Hammond, for answering my many, long questions over the years. I would also like to acknowledge the support of the United Kingdom's Science and Technology Facilities Council for funding this research. Additionally, I thank the STFC DiRAC HPC facility, with whom many of the models in this work were run.

Furthermore, I would like to express my gratitude towards all of my colleagues in AOPP. Especially Jake, Joost, Mark, Tobias, Chloe and Jingxuan, with whom I spent many pub trips, formals and other memorable occasions. If you ever need a backup careers, might I suggest forming a troup! Joost, in particular your rendition of *Dancing Queen* in a dingy California dive bar was truly unforgettable. I am also exceptionally grateful for many opportunities to travel during my DPhil. To Jake, for teaching me a valuable lesson about the merits of sunscreen in the Nevada desert. To Joost, Hamish and Jake, for not letting me fall into a canyon. Most of all, to Peter and Joost, for braving forest fires and a bear with me.

A special thank you also goes to all of my friends at St Peter's College. My time here was infinitely more enjoyable knowing you all. In particular, I would like to thank those involved with the SPCBC for providing me with an enjoyable escape from work, and many incredible opportunities. I give an extra thank you to a certain 'zesty' group - Annie, Caroline, Meadow, Wojtek and Alek, for your friendship during lockdown and beyond. An extra thank you to Annie and Ellie. I could not have asked for a better flatmates during my time in Oxford. Memories of countless reality TV shows, one *Sharknado* marathon and a certain drinking game are some of my fondest over the years.

Most importantly I would like to thank my parents, Susie and Steve, for their unwavering support not only through the last four years but my entire life. It is not hyperbolic to say that I would not be here without you both.